

# Metallomics Research

SPECIAL ISSUE

**Selenium Research:  
Integrated Chemistry and Biology**

**Vol. 5/No. 1**  
February 2025



Japan Society for  
Biomedical Research on Trace Elements

---

## Index

---

### Award Review

## Single-Cell Elemental Analysis Using Inductively Coupled Plasma Mass Spectrometry

Yu-ki Tanaka, Yasumitsu Ogra

AWrev01

### SPECIAL ISSUE

## Selenium Research: Integrated Chemistry and Biology

collaboration with Japan Selenium Research Society

### Review

## Selenium-containing $\pi$ -Bond Compounds of Heavier Main-Group Elements

Koh Sugamata, Takahiro Sasamori

rev01

## Mechanisms of Selenoprotein P translation regulation by long noncoding RNA

Yuichiro Mita, Yukihiro Inenaga, Noriko Noguchi

rev19

## Overview of the biochemistry and biology of selenoneine

Takuya Seko, Yumiko Yamashita, Michiaki Yamashita

rev24

Regular article

**Interaction of selenite and arsenite on erythrocytes uptake of each metalloid: Possible mechanism mediated by extracellularly generated selenium-arsenic complexes**

Yayoi Kobayashi, Seishiro Hirano

reg01

**A suppressive effect of selenium on amyloid- $\beta$  plaque deposition in Tg2576 transgenic mice brain**

Sakura Yoshida, Takeshi Fuchigami, Morio Nakayama, Mamoru Haratake

reg13

**The distribution and chemical form of selenium in the tissue of ferns were visualized using a synchrotron radiation X-ray microbeam.**

Shota Yuzawa, Koichi Nambu, Kazuaki Takahashi, Yasumitsu Ogra, Akiko Hokura

reg24

**Phosphine-mediated Reduction of a Selenocysteine Selenenyl Iodide to a Selenocysteine Selenol**

Satoru Kuwano, Ko Fujisaki, Kei Goto

reg39

## Editorial Board

---

[Editor-in-Chief]

**Masahiro KAWAHARA** (Musashino University, Tokyo, Japan)

[Deputy Editor]

**Hisaaki MIHARA** (Ritsumeikan University, Kyoto, Japan)

[Associate Editors]

**Miyuki IWAI-SHIMADA** (National Institute for Environmental Studies, Ibaraki, Japan)

**Masako UEMURA** (Suzuka University of Medical Science, Mie, Japan)

**Tomoko GOTO** (Miyagi Gakuin Women's University, Miyagi, Japan)

**Yayoi KOBAYASHI** (National Institute for Environmental Studies, Ibaraki, Japan)

**Yoshiro SAITO** (Tohoku University, Sendai, Japan)

**Shino HOMMA-TAKEDA** (National Institutes for Quantum Science and Technology, Chiba, Japan)

**Yu-ki TANAKA** (Chiba University, Chiba, Japan)

**Aya TOKUMITSU** (HOKKAIDO RYOIKUEN, Hokkaido, Japan)

**Tomoka TAKATANI-NAKASE** (Mukogawa Women's University, Hyogo, Japan)

**Ayako HASHIMOTO** (Kyoto Women's University, Kyoto, Japan)

**Takafumi HARA** (Tokushima Bunri University, Tokushima, Japan)

**Takehisa MATSUKAWA** (Juntendo University, Tokyo, Japan)

[Advisory Board]

**Md. Khaled Hossain, Ph.D.** (Professor, Department of Biochemistry and Molecular Biology, University of Rajshahi, Rajshahi, Bangladesh)

**Ryszard Lobinski** ( Research Director, French National Centre for Scientific Research (CNRS), Paris, France )  
( Professor, Warsaw University of Technology, Warsaw, Poland )

**Hua Naranmandura** (Professor, School of Medicine and Public Health, Zhejiang University, Hangzhou, China)

## Editorial Office

---

Seishinsha, co. Ltd.,

Japan society for Biomedical Research on Trace Elements

2-8-13 Fukashi, Matsumoto-shi, Nagano 390-0815, Japan

Tel: +81-263-32-2301 Fax: +81-263-36-4691 Editorial Office: brte-post@seisin.cc

URL: <https://www.brte.org/> <https://metallomicsresearch.brte.org/>

### Copyright, Open Access Policy

The journal is fully Open Access and publishes articles under a Creative Commons (CC) license, which allow users to use, reuse and build upon the material published in the journal without charge or the need to ask prior permission from the publisher or author.

# Single-Cell Elemental Analysis Using Inductively Coupled Plasma Mass Spectrometry

Yu-ki Tanaka\*, Yasumitsu Ogra

Graduate School of Pharmaceutical Sciences, Chiba University

## Abstract

Single-cell elemental analysis using inductively coupled plasma-mass spectrometry (ICP-MS) is a rapidly developing field within metallomics, offering the ability to quantify elemental contents in individual cells. Pioneering works have developed diverse sample introduction systems coupled with ICP-MS, enabling high-throughput, precise, and accurate elemental analysis at the single-cell level. These advancements have facilitated applications across medicine and biology, providing insights into elemental metabolism and toxicity. Two prominent approaches have emerged: fast time-resolved analysis of cell suspensions, applicable to a broad range of cell types (bacterial, fungal, plant, and mammalian cells), and laser ablation (LA) for generating aerosols from individual cells. LA is particularly well suited for adherent cultured cells and allows for selective analysis based on cell morphology and size. These complementary techniques provide powerful tools for elucidating the complex interplay between elements and biological systems.

**Keywords:** fast time-resolved analysis, ICP-MS, laser ablation, microdroplet generator, single cell

**Statements about COI:** There are no potential conflicts of interest to be disclosed.

**Award Review:** This review is based on the content of the lecture that won the 2023 JSBRTE Young Investigator Award, and was titled 'Development of applied analytical methods for trace elements by ICP mass spectrometer.'

## Introduction

Living organisms rely on a suite of elements for essential biological functions. While organic molecules are primarily composed of hydrogen, carbon, nitrogen, and oxygen, trace elements, collectively known as minerals, play critical

---

### \*Correspondence

Yu-ki Tanaka

Graduate School of Pharmaceutical Sciences, Chiba University, 1-8-1 Inohana, Chuo, Chiba 260-8675, Japan

**Tel ;** +81 43 226 2945

**E-mail ;** [yu-ki.tanaka@chiba-u.jp](mailto:yu-ki.tanaka@chiba-u.jp)

---

Received: December 19, 2024

Accepted: January 23, 2025

Released online: February 28, 2025

roles in a wide array of processes. Major minerals, including calcium (Ca), phosphorus (P), sulfur (S), sodium (Na), magnesium (Mg), and potassium (K), contribute to diverse functions. Ca, Na, Mg, and K primarily function as electrolytes, regulating fluid balance and facilitating signal transduction. P is covalently incorporated into nucleic acids and lipids, while S is a key component of protein thiol groups, influencing protein structure and function. Trace minerals, including the transition metals iron (Fe), copper (Cu), zinc (Zn), chromium (Cr), cobalt (Co), and molybdenum (Mo), the chalcogen selenium (Se), and the



This work is licensed under a Creative Commons Attribution 4.0 International License.

©2025 THE AUTHORS. [DOI](https://doi.org/10.11299/metallomicsresearch.MR202415) <https://doi.org/10.11299/metallomicsresearch.MR202415>

halogen iodine (I), are essential for maintaining the structure and catalytic activity of numerous enzymes. Because of their diverse involvement in biological processes, imbalance in mineral intake or metabolic disorders can have significantly adverse effects at the organismal level.

The critical roles of minerals in biological systems are evident at the cellular level as well as the organismal level. Intracellular P content, for instance, doubles prior to DNA replication [1]. Similarly, changes in intracellular elemental content are observed during cell differentiation [2], and excessive Ca transport to mitochondria can trigger cell death [3]. These examples underscore the crucial involvement of minerals in essential cellular phenomena such as transcription, translation, metabolism, homeostasis, and programmed cell death. Consequently, elemental analysis at the single-cell level has emerged as a powerful technique in metallomics, offering insights into these critical processes.

High-resolution elemental imaging analysis using particle induced X-ray emission (PIXE) and scanning fluorescence X-ray microscopy (SFXM) provides insights into intracellular distribution and localization of elements [4, 5]. In contrast, inductively coupled plasma (ICP)-based techniques offer high-throughput and quantitative elemental analysis, serving as complementary methods to high-resolution imaging for elucidating intracellular metabolism and the functions of elements. ICP is a powerful ionization source due to its ability to efficiently atomize and ionize a broad range of elements. It offers excellent sensitivity and a wide dynamic range for atomic emission spectrometry (ICP-AES) or mass spectrometry (ICP-MS), both of which are widely used for elemental analysis of biological samples. Recent advances in ICP-MS technology include high matrix tolerance interfaces and collision/reaction cells. These developments have significantly enhanced the detection and quantification of trace minerals in complex biological matrices. These advancements have also paved the way for single-cell elemental analysis using fast time-resolved data acquisition. This technique enables the measurement of elemental content in individual particulate matter, such as nanoparticles (single-particle ICP-MS, spICP-MS) and, importantly, single cells (single-cell ICP-MS; scICP-MS). Introducing particles or cells individually into the ICP, where their constituent elements are ionized and recording the resulting ion signals at 1 ms or shorter intervals make it possible to resolve elemental contents in individual cells. This fast time-resolved approach is crucial because the signals generated from a single cell are typically shorter than 1 ms.

Laser ablation (LA) for sample introduction is an alternative approach to fast time-resolved analysis. LA generates aerosols from solid samples, which are introduced into the ICP-MS, providing two-dimensional elemental distribution data and insights into tissue-level elemental metabolism. While the generated aerosols disperse spatially during transport to the ICP over several seconds, unlike fast time-resolved analysis, which maintains particle/cell integrity until ionization within the ICP, conventional signal integration times (10–100 ms) can be used to resolve signals from individual cells. LA offers several advantages, including eliminating the need for cell suspension preparation for adherent cells and enabling selective analysis based on cell size and morphology. However, the relatively long washout time inherent to LA can limit throughput. Recent development of two-volume cells for rapid washout has significantly mitigated the limitation in LA-based single-cell analysis [6]. Furthermore, the use of galvanometric optics in the solid-mixing method enhanced the accuracy of quantification, ranging from trace to major elements [7].

Both fast time-resolved analysis and LA-based analysis offer powerful capabilities for single-cell elemental analysis, potentially significantly advancing single-cell research in metallomics. More precisely, scICP-MS is a promising technology for elucidating elemental metabolism in toxicology, advancing drug discovery in pharmaceutical sciences, and improving prognosis and diagnosis in medicine. In this review, we provide a comprehensive overview of these complementary approaches and discuss their principles, advantages, limitations, and recent applications.

### Single-cell analysis by fast time-resolved ICP-MS

In ICP-MS analysis, the dwell time, or integration time, for detecting specific ions can be set independently for each element or isotope. Typically, ICP-MS allows for dwell times of 10 ms or longer. While extending the dwell time increases the total number of detected ions, leading to improved precision, it does not always enhance the signal-to-noise ratio significantly. This is because the background signal also accumulates during the extended

integration period, potentially offsetting the benefits of increased ion counts. The development of ICP-MS systems capable of setting dwell times shorter than 10 ms has revolutionized single-particle and single-cell analysis. By enabling fast time-resolved data acquisition, these systems can accurately capture transient signals generated from individual nanoparticles or cells [8]. When samples are introduced into the ICP, their constituent elements are atomized and ionized, subsequently entering the mass spectrometer. Due to the relatively small number of ions generated from a single particle or cell, fast time-resolved data acquisition is crucial to accurately capture the transient signals and extract meaningful elemental information. The acceleration of ions by several hundred volts at the extraction lenses results in the formation of a tightly confined spatial cluster, known as an “ion cloud” or “ion plume”, which rapidly traverses the detector within a fraction of ms. Consequently, the use of conventional dwell times (>10 ms) can result in the simultaneous detection of multiple particles/cells, ultimately leading to content overestimation. While reducing sample density can mitigate this issue, it compromises sample throughput. To overcome such a challenge, setting the dwell time to a value shorter than the detection period of a single ion cloud/plume, typically ranging from 0.2 to 0.6 ms [9], enables high-throughput signal acquisition. Nevertheless, even in the fast time-resolved mode, simultaneous detection may still occur, especially at higher particle or cell densities. Therefore, it is essential to ensure proper sample dispersion and maintain an appropriate density in the suspension to minimize the likelihood of such events.

### Cell suspension preparation

It is vital to prepare a well-dispersed cell suspension while maintaining the structural integrity of the cells in fast time-resolved analysis. Adherent cells require careful dispersion and filtration to isolate individual cells while floating cells can be more readily prepared as single-cell suspensions. In this regard, Á-Fernández García et al. have demonstrated the potential of using single cells isolated from solid tissues by enzymatic digestion for scICP-MS analysis [10]. Our preliminary investigations have shown that human leukemia K562 cells maintain structural integrity in isotonic solutions like phosphate-buffered saline (PBS) and saline (0.9% sodium chloride) but swell in hypotonic solutions like Tris (tris(hydroxymethyl)aminomethane) buffer or rupture in ultrapure water (data not shown). Chemical fixation has been used to preserve cell structure in ultrapure water [11, 12], but our findings suggest that this approach can lead to the leakage of intracellular elements [13]. Bacterial, fungal, and plant cells, with their rigid cell walls, may exhibit greater resistance to osmotic stress than mammalian cells. Moreover, elemental contamination from the cell suspension solution can significantly impact baseline signals in fast time-resolved analysis. Consequently, the use of low-purity reagents should be avoided during sample preparation. High salt concentrations can give rise to several analytical challenges, including nebulizer clogging, interface contamination, mass spectrometric interference, and non-mass spectrometric interference (matrix effects). Preparing isotonic solutions with simple chemical compositions using high-purity reagents is recommended to minimize these issues.

### Quantification protocol

The fast time-resolved analysis enables the acquisition of transient signals, approximately 0.5 ms in duration, from single cells. We can evaluate the elemental content within individual cells by analyzing these transient signals. One potential method involves using reference particle materials containing a known mass of the target element [14]. When these particles are analyzed, the detected transient signals are affected by ion loss within the mass spectrometer during the transmission process. Assuming that the transmission efficiency of the target element is similar for both reference particle materials and cell samples, the elemental content in a cell ( $m_c$ ) can be calculated using the sensitivity factor ( $\alpha$ ; signal intensity per elemental mass) determined from the reference particle materials. This method provides a straightforward approach to quantitative analysis using particulate substances that resemble cells in size and morphology. However, the availability of reference particle materials containing the target element may be limited, particularly for less common elements.

An alternative approach for calculating elemental content relies on the sensitivity factor derived from the signal intensity of ion solutions [14]. While this method may appear similar to the reference particle method, there are

significant differences in the behavior of particles and ionic solutions introduced through the nebulizer. Elements contained within particles are not subject to the same losses as those introduced in solution form and are detected as transient signals. In contrast, ions in the aerosol are subject to losses during transport from the nebulizer to the ICP and are detected as continuous signals rather than transient signals. Therefore, when utilizing a sensitivity factor obtained from ionic solutions, the following steps are necessary: (i) determine the transport efficiency ( $f$ ) of the ions in the aerosol from the nebulizer to the ICP, (ii) measure the ion solution containing the analyte element to calculate the sensitivity factor ( $\alpha$ ) using transport efficiency ( $f$ ), and (iii) calculate the elemental content by dividing the transient signal from the cells by the sensitivity factor ( $\alpha$ ). The detailed calculation is outlined in Equation (1), where  $I_c$ ,  $I_s$ , and  $I_b$  represent the signal intensities from the cells, the ionic solution of the analyte element, and the blank solution, respectively,  $t_d$  denotes the dwell time,  $C_s$  indicates the concentration of the ionic solution, and  $v$  is the sample introduction rate.

$$m_c = \frac{I_c}{I_s - I_b} \times t_d \times f \times C_s \times v \quad (1)$$

We have determined elemental contents in yeast (*Saccharomyces cerevisiae*), green alga (*Chlamydomonas reinhardtii*), and rat red blood cells, ultimately validating the quantification procedure for single-cell analysis [15]. **Fig. 1a** presents the signal profiles of P. For all cell types, dozens of transient signals were detected within a single second of the time-resolved analysis (TRA) profile (**Fig. 1a**). These signals, with a duration of approximately 0.5 ms, strongly suggest that they originated from individual cells. We quantified the intracellular P content using the sensitivity factor derived from ionic P solutions. These values were comparable to those obtained from the bulk concentration analysis following acid digestion (**Fig. 1b**). These findings highlight the potential of fast time-resolved analysis to provide unprecedented insights into cellular heterogeneity and the role of essential elements in cellular processes.

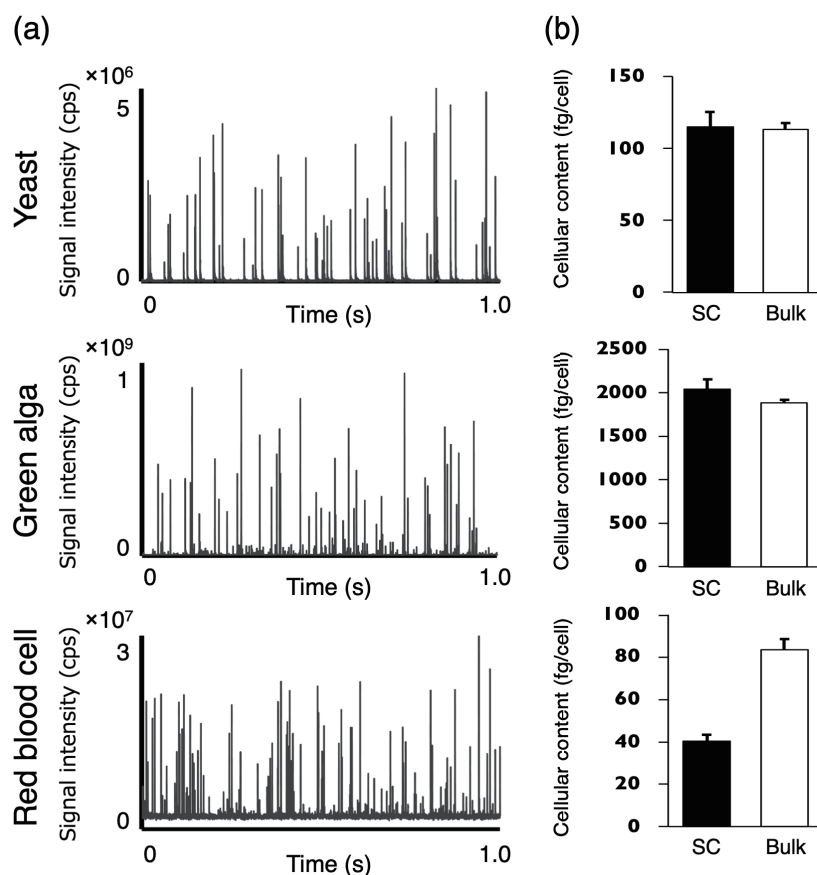


**Fig. 1.** Comparison of intracellular phosphorus (P) content determined by single-cell and bulk analysis (Data from reference [15]).

(a) Time-resolved analysis data for  $^{31}\text{PO}$  with a signal integration time of 0.1 ms. (b) Comparison of P content determined by fast time-resolved single-cell (SC) ICP-MS and bulk solution nebulization ICP-MS following acid digestion (bulk analysis). The higher P content observed in the bulk analysis of red blood cell suggests potential contamination from lysed red blood cells and/or serum components.

### Applications in bacterial cells

Given the diversity of bacteria, including environmental and pathogenic bacteria, gut microbiota, and bacteria used in food processing, they represent promising targets for scICP-MS analysis. Gomez-Gomez et al. investigated the uptake of tellurium (Te) nanoparticles, which are potential environmental contaminants, by *Staphylococcus aureus* (*S. aureus*) and *Escherichia coli* (*E. coli*) [16]. Hellmann et al. also focused on environmental contaminants such as cadmium (Cd), cerium (Ce), and uranium (U) and evaluated the potential of *Streptomyces coelicolor* for bioremediation [17]. Moreover, Xu et al. utilized scICP-MS to investigate the antimicrobial activity of Cu ions against *Legionella pneumophila* [18]. Similarly, Liang et al. employed scICP-MS to detect pathogenic bacterial strains such as *E. coli*, *S. aureus*, *Listeria monocytogenes*, *Shigella dysenteriae*, and *Vibrio parahaemolyticus* using metal-labeled polyclonal antibodies specific to each strain [19].

*E. coli* is a well-established model organism for recombinant protein production. Accordingly, we explored the feasibility of applying single-cell elemental analysis to evaluate the expression of recombinant proteins in *E. coli* [20]. Given the limitations of directly detecting organic molecules using ICP-MS, we labeled proteins with metal ions using a sequence of six histidine residues (His-tag) fused to the protein terminus. The His-tag sequence has a high affinity for divalent transition metal ions such as nickel (Ni) and Co. We utilized a plasmid vector encoding a His-tagged red fluorescent protein, mCherry. To validate the results of ICP-MS, mCherry expression levels were also assessed by flow cytometry. As shown in Fig. 2a, the fluorescence intensity from flow cytometry revealed a time-dependent increase following protein expression induction, indicating increased mCherry expression within the cells. Like the results from flow cytometry, scICP-MS analysis showed an increase in the signal intensity of Co from individual cells following induction (Fig. 2b). Collectively, these findings highlight the potential of scICP-MS to provide quantitative insights into recombinant protein expression at the single-cell level in *E. coli*, thereby aiding the optimization of protein production.

### Applications in mammalian cells

Mammalian cultured cells are the most commonly used cell models in biological research, serving as a preclinical or alternative model to *in vivo* experiments for assessing biological responses,

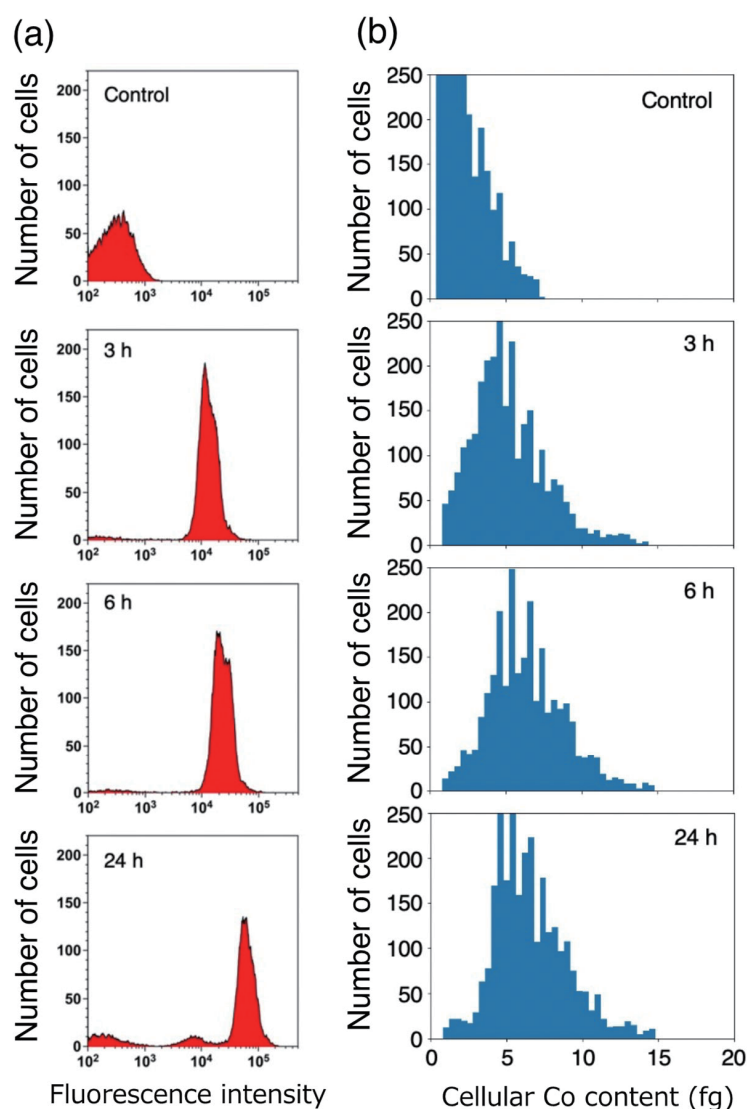


**Fig. 2.** Correlation of mCherry protein expression measured by flow cytometry and scICP-MS (Data from reference [20]).

*E. coli* cells were induced to express mCherry for 0 (control), 3, 6, and 24 h. mCherry expression was quantified by (a) flow cytometry based on fluorescence intensity and (b) scICP-MS by measuring cobalt (Co) signal intensity.

metabolism, and toxicity. From an animal welfare perspective, cultured cell experiments are expected to expand their role in a broader range of research fields, reducing the reliance on animal models.

Recent research has focused on biomedical applications, including the uptake of nanoparticles potentially used as nanomedicine or drug delivery system (DDS) carriers [21–23]. Studies have also evaluated cellular absorption of metal-containing pharmaceuticals such as platinum-based anticancer agents [24–26], gadolinium-containing anticancer drugs [24], and arsenic-based pharmaceuticals for leukemia [27]. These studies demonstrate the expanding role of scICP-MS analysis with cultured cells in medical and pharmaceutical research.

Several research groups have developed microfluidic-based sample introduction systems for efficient and controlled delivery of cultured cells to the ICP-MS instrument, ultimately validating elemental quantification employing the protocol described in the previous section [28–30]. Furthermore, developing hyphenated techniques integrating fluorescence detection prior to ICP-MS has enabled simultaneous spectroscopic and mass spectrometric analyses at the single-cell level. These techniques provide complementary information on cellular elemental composition and function [31, 32]. These hyphenated techniques have facilitated detailed studies of intracellular processes at the single-cell level. For instance, the impact of Ag ion and AgNP exposure has been assessed by quantifying GFP-labeled metallothionein and Ag concentrations within individual cells [33]. This approach has also been extended in mammalian cells to combine fluorescence-activated cell sorting (FACS) with scICP-MS. Gutierrez-Romero et al., for instance, used this combined approach to isolate apoptotic, necrotic, and viable human ovarian cancer cells (A2780 and OVCAR-3) by FACS and subsequently analyze cisplatin prodrug uptake in each cell population [26].

Despite significant advances in single-cell analysis technologies and their applications, a key analytical challenge persists, particularly for mammalian cultured cells. These cells are inherently fragile owing to their large size compared with microorganisms and the lack of a rigid cell wall. This fragility can significantly impact analytical performance. For example, we previously demonstrated that the human myelogenous leukemia K562 cell structure is damaged during nebulization, leading to lower transport efficiency than similarly sized silica particles (**Fig. 3**) [13]. To address these challenges, we employed a microdroplet generator, a technique previously employed in various cell types, including yeast [34], bovine red blood cells [35], and mouse lung cells [36]. Efficient desolvation

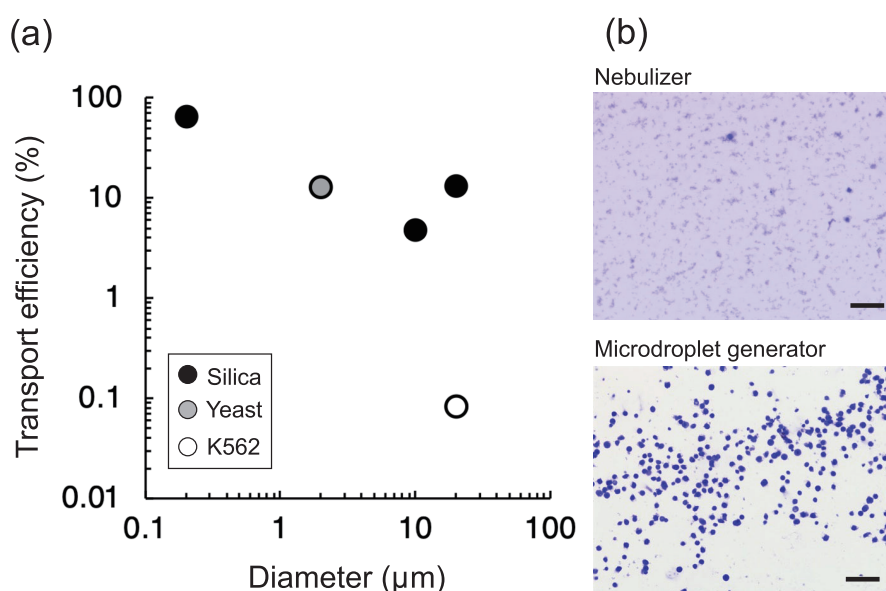


**Fig. 3.** Effect of nebulization on mammalian cell transport and integrity (Data from reference [13]).

(a) Comparison of transport efficiency from the nebulizer to the ICP for differently sized silica particles, yeast, and K562 cells. The significantly low transport efficiency observed for K562 cells is attributed to cell disruption caused by the pneumatic nebulizer. (b) Preservation of cell structure using a microdroplet generator for sample introduction, contrasting with the disruptive effects of nebulization. Scale bars represent 150 μm.

of the generated droplets is crucial for achieving high ionization efficiency, and this is typically accomplished using nitrogen or helium gas [37–39], sometimes in conjunction with heating devices [36] or membrane desolvators [35]. Although we did not utilize these additional desolvation methods, the microdroplet generator alone proved sufficient to maintain cell integrity (**Fig. 3b**), allowing for efficient signal acquisition from mammalian cultured cells [13].

### Single-cell LA-ICP-MS analysis

Laser ablation (LA) has become a versatile analytical technique for directly sampling solid samples, providing valuable spatial elemental distribution data across diverse scientific disciplines. Its applications span various fields, including geochemistry, archeology, materials science, environmental science, food science, forensic science, and life science. In biological studies, LA is frequently employed in the two-dimensional elemental mapping of plant and animal tissues, offering insights into the distribution and concentration of elements within specific anatomical regions [40]. In single-cell LA analysis, individual cells are ablated to produce aerosols. Because of the relatively long washout times associated with LA, which are influenced by the sample chamber volume and transport tube length, a fast time-resolved acquisition mode is not required to resolve signals from individual cells. Consequently, the analytical throughput of LA-based single-cell analysis is generally lower than that of techniques employing fast time-resolved measurements. However, LA offers a significant advantage: the ability to selectively target and measure cells based on specific size and morphological characteristics, providing unique insights into heterogeneous cell populations.

### Cell sample preparation

Cell immobilization is crucial for achieving stable ablation and high analytical throughput for effective single-cell LA analysis. Adherent cultured cells can be analyzed directly after removing the culture medium and washing with a rinse solution (e.g., saline). Generating a cell suspension and employing microfluidic devices for cell alignment can further enhance throughput [41]. Alternatively, piezo-acoustic microarrayers offer another effective approach for preparing well-aligned single-cell samples on a substrate, providing precise control over cell positioning [42].

### Quantification protocol

Quantification in LA-ICP-MS typically relies on calibration using solid standard materials. However, matrix effects, arising from differences in composition between the standard and the biological sample, can significantly influence aerosol particle size and elemental composition, leading to inaccuracies [43]. The limited availability of certified reference materials specifically designed for biological matrices exacerbates this issue further [44]. In-house standards, such as homogenized tissues [40] or gelatin [45] spiked with known element concentrations, provide a partial solution in single-cell LA-ICP-MS. Mervič et al. reported that correcting for ablated volume is effective for quantitative LA analysis even when using non-matrix matched standards [46]. Galvanometric optics enable the generation of calibration curves across appropriate concentration ranges, from trace to major components, by mixing standards with low and high elemental concentrations [7]. They also facilitate the homogeneous mixing of solid samples with different matrices, allowing for the application of the standard addition calibration method using commercially available glass standards [47]. However, applying standard addition method to single-cell samples remains challenging, as single-cell samples are entirely ablated in a single analysis. Consequently, accurate quantification of elemental content in single-cell LA-ICP-MS remains a considerable analytical hurdle.

### Cellular applications

While early applications of LA for single-cell elemental analysis were limited, its use has been steadily increasing. Studies investigating the cellular uptake of gold nanoparticles [48] and cisplatin [49] in mammalian cultured cells have demonstrated the technique's potential. Theiner et al. employed two-dimensional mapping on a blood smear, evaluating the elemental content of individual blood cells [50]. Their findings revealed distinct elemental

signatures, with red blood cells exhibiting high Fe content and white blood cells characterized by high P content, demonstrating the capability of LA to differentiate cell types based on their elemental composition.

Using LA-based scICP-MS analysis, we recently investigated the changes in elemental content during cell differentiation [51]. Rat adrenal pheochromocytoma PC12 cells, upon treatment with nerve growth factor (NGF), differentiate into neuron-like cells. However, the expression of differentiation marker proteins remains low after five days of NGF treatment. By distinguishing mature and less mature neuron-like cells by size, we performed separate LA-ICP-MS analyses. Our results revealed a clear correlation between cell size and elemental content: large differentiated cells exhibited significantly higher levels of essential elements than undifferentiated PC12 cells, whereas small differentiated cells showed elemental content comparable to undifferentiated cells (Fig. 4).

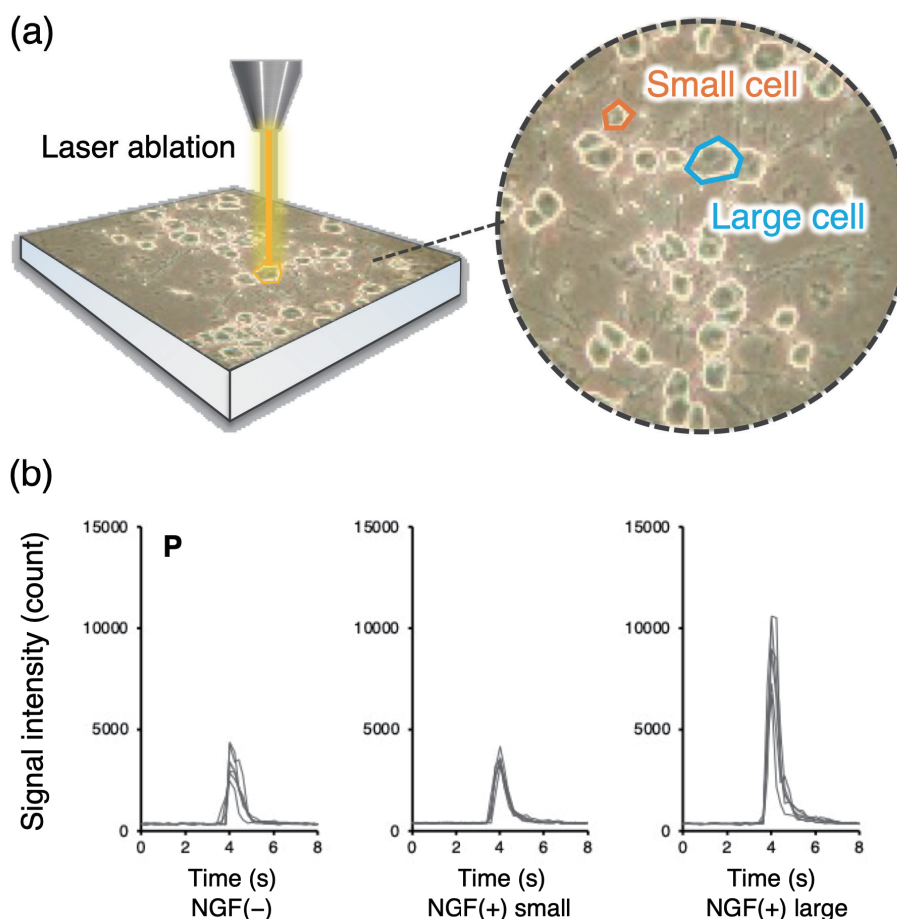


**Fig. 4.** Single-cell-based selection and analysis of PC12 cells by LA-ICP-MS (Data from reference [51]). (a) Schematic diagram illustrating the selective measurement of PC12 cells by size as a differentiation marker. (b) Phosphorus (P) signal intensity measured by LA-ICP-MS. Phosphorus content in small differentiated cells was comparable to that observed in undifferentiated cells.

## Conclusion

We have presented an overview of single-cell elemental analysis using ICP-MS. While fast time-resolved analysis offers broad applicability across various cell types and has facilitated numerous applications, the impact of nebulization on the structural integrity of fragile mammalian cells has not been adequately addressed. Therefore, the development and implementation of standardized sample introduction systems, such as those employing

microdroplet generators, are crucial for the reliable analysis of these cell types. Although LA applications in single-cell analysis are currently limited, ongoing instrumental advancements are promising and offer the potential for robust quantitative single-cell elemental analysis.

### Acknowledgment

This study was financially supported by ACT-UR Grants (#4366, #4489) from Agilent Technologies. The authors are greatly indebted to Mr. Tetsuo Kubota, Ms. Michiko Yamanaka, and Mr. Naoki Sugiyama (Agilent Technologies) for advice on ICP-MS analysis.

### References

- [1] Baker AL, Schmidt RR. Intracellular distribution of phosphorus during synchronous growth of *Chlorella pyrenoidosa*. *Biochimica et Biophysica Acta*. 1963;74:75-83.
- [2] Ogra Y, Tejima A, Hatakeyama N, Shiraiwa M, Wu S, Ishikawa T, Yawata A, Anan Y, Suzuki N. Changes in intracellular copper concentration and copper-regulating gene expression after PC12 differentiation into neurons. *Scientific Reports*. 2016;6:33007.
- [3] Bonneau B, Ando H, Kawaai K, Hirose M, Takahashi-Iwanaga H, Mikoshiba K. IRBIT controls apoptosis by interacting with the Bcl-2 homolog, Bcl2l10, and by promoting ER-mitochondria contact. *eLife*. 2016;5:e19896.
- [4] Homma-Takeda S, Fujishiro H, Tanaka I, Yakumaru H, Ayama K, Uehara A, Oikawa M, Himeno S, Ishihara H. Single-Cell Imaging for Studies of Renal Uranium Transport and Intracellular Behavior. *Minerals* 2021;11:191.
- [5] Shimura M, Shindou H, Szyrwiel L, Tokuoka SM, Hamano F, Matsuyama S, Okamoto M, Matsunaga A, Kita Y, Ishizaka Y, Yamauchi K, Kohmura Y, Lobinski R, Shimizu I, Shimizu T. Imaging of intracellular fatty acids by scanning X-ray fluorescence microscopy. *FASEB J*. 2016;30:4149-4158.
- [6] Müller W, Shelley M, Miller P, Broude S. Initial performance metrics of a new custom-designed ArF excimer LA-ICPMS system coupled to a two-volume laser-ablation cell. *Journal of Analytical Atomic Spectrometry*. 2009;24:209-214.
- [7] Makino Y, Kuroki Y, Hirata T. Determination of major to trace elements in metallic materials based on the solid mixing calibration method using multiple spot-laser ablation-ICP-MS. *Journal of Analytical Atomic Spectrometry*. 2019;34:1794-1799.
- [8] Resano M, Aramendía M, García-Ruiz E, Bazo A, Bolea-Fernandez E, Vanhaecke F. Living in a transient world: ICP-MS reinvented via time-resolved analysis for monitoring single events. *Chemical Science*. 2022;13:4436-4473.
- [9] Yamashita S, Yoshikuni Y, Obayashi H, Suzuki T, Green D, Hirata T. Simultaneous Determination of Size and Position of Silver and Gold Nanoparticles in Onion Cells using Laser Ablation-ICP-MS. *Analytical Chemistry*. 2019;91:4544-4551.
- [10] Á-Fernández García R, Gutiérrez Romero L, Bettmer J, Montes-Bayón M. Capabilities of Single Cell ICP-MS for the Analysis of Cell Suspensions from Solid Tissues. *Nanomaterials*. 2022;13:12.
- [11] Wang H, Wang B, Wang M, Zheng L, Chen H, Chai Z, Zhao Y, Feng W. Time-resolved ICP-MS analysis of mineral element contents and distribution patterns in single cells. *Analyst*. 2015;140:523-531.
- [12] Wang H, Wang M, Wang B, Zheng L, Chen H, Chai Z, Feng W. Interrogating the variation of element masses and distribution patterns in single cells using ICP-MS with a high efficiency cell introduction system. *Analytical and Bioanalytical Chemistry*. 2017;409:1415-1423.
- [13] Tanaka Y-k, Katayama H, Iida R, Ogra Y. Quantitative elemental analysis of human leukemia K562 single cells by inductively coupled plasma mass spectrometry in combination with a microdroplet generator. *Journal of Analytical Atomic Spectrometry*. 2025; 40: 216-225.
- [14] Pace HE, Rogers NJ, Jarolimek C, Coleman VA, Higgins CP, Ranville JF. Determining Transport Efficiency for the Purpose of Counting and Sizing Nanoparticles via Single Particle Inductively Coupled Plasma Mass Spectrometry. *Analytical Chemistry*. 2011;83:9361-9369.
- [15] Tanaka Y-k, Iida R, Takada S, Kubota T, Yamanaka M, Sugiyama N, Abdelnour Y, Ogra Y. Quantitative Elemental Analysis of a Single Cell by Using Inductively Coupled Plasma-Mass Spectrometry in Fast Time-Resolved Analysis Mode. *Chembiochem*. 2020;21:3266-3272.
- [16] Gomez-Gomez B, Corte-Rodríguez M, Perez-Corona MT, Bettmer J, Montes-Bayón M, Madrid Y. Combined single cell and single particle ICP-TQ-MS analysis to quantitatively evaluate the uptake and biotransformation of tellurium nanoparticles in bacteria. *Analytica Chimica Acta*. 2020;1128:116-128.
- [17] Hellmann S, García-Cancela P, Alonso-Fernández S, Corte-Rodríguez M, Bettmer J, Manteca A, Merten D, Gil-Díaz T, Schäfer T, Montes-Bayón M. Single cell ICP-MS to evaluate the interaction behaviour for Cd, Ce and U with *Streptomyces coelicolor* spores. *Chemosphere*. 2024;347:140633.
- [18] Xu L, Sigler A, Chernatynskaya A, Rasmussen L, Lu J, Sahle-Demessie E, Westenberg D, Yang H, Shi H. Study of *Legionella pneumophila* treatment with copper in drinking water by single cell-ICP-MS. *Anal Bioanal Chem*. 2024;416:419-430.
- [19] Liang Y, Liu Q, Zhou Y, Chen S, Yang L, Zhu M, Wang Q. Counting and Recognizing Single Bacterial Cells by a Lanthanide-Encoding Inductively Coupled Plasma Mass Spectrometric Approach. *Analytical Chemistry*. 2019;91:8341-8349.
- [20] Tanaka Y-k, Shimazaki S, Fukumoto Y, Ogra Y. Detection of Histidine-Tagged Protein in *Escherichia coli* by Single-Cell Inductively Coupled Plasma-Mass Spectrometry. *Analytical Chemistry*. 2022;94:7952-7959.
- [21] Wang H, Chen B, He M, Hu B. A Facile Droplet-Chip-Time-Resolved Inductively Coupled Plasma Mass Spectrometry Online System for Determination of Zinc in Single Cell. *Analytical Chemistry*. 2017;89:4931-4938.
- [22] Wei X, Zheng D-H, Cai Y, Jiang R, Chen M-L, Yang T, Xu Z-R, Yu Y-L, Wang J-H. High-Throughput/High-Precision Sampling of Single Cells into ICP-MS for Elucidating Cellular Nanoparticles. *Analytical Chemistry*. 2018;90:14543-14550.
- [23] Chen P, He M, Chen B, Hu B. Size- and dose-dependent cytotoxicity of ZIF-8 based on single cell analysis. *Ecotoxicol Environ Saf*. 2020;205:111110.
- [24] Zheng L-N, Wang M, Zhao L-C, Sun B-Y, Wang B, Chen H-Q, Zhao Y-L, Chai Z-F, Feng W-Y. Quantitative analysis of Gd@C82(OH)22 and cisplatin uptake in single cells by inductively coupled plasma mass spectrometry. *Analytical and Bioanalytical Chemistry*. 2015;407:2383-2391.
- [25] Galé A, Hofmann L, Lüdi N, Hungerbühler MN, Kempf C, Heverhagen JT, von Tengg-Kobligh H, Broekmann P, Ruprecht N. Beyond Single-Cell Analysis of Metallodrugs by ICP-MS: Targeting Cellular Substructures. *International Journal of Molecular Sciences*. 2021;22:9468.

- [26] Gutierrez-Romero L, Blanco-González E, Montes-Bayón M. Single-Cell ICP-MS in Combination with Fluorescence-Activated Cell Sorting for Investigating the Effects of Nanotransported Cisplatin(IV) Prodrugs. *Analytical Chemistry*. 2023;95:11874-11878.
- [27] Zhou Y, Wang H, Tse E, Li H, Sun H. Cell Cycle-Dependent Uptake and Cytotoxicity of Arsenic-Based Drugs in Single Leukemia Cells. *Analytical Chemistry*. 2018;90:10465-10471.
- [28] Zhou Y, Chen Z, Zeng J, Zhang J, Yu D, Zhang B, Yan X, Yang L, Wang Q. Direct Infusion ICP-qMS of Lined-up Single-Cell Using an Oil-Free Passive Microfluidic System. *Analytical Chemistry*. 2020;92:5286-5293.
- [29] Zhang X, Wei X, Men X, Jiang Z, Ye W-Q, Chen M-L, Yang T, Xu Z-R, Wang J-H. Inertial-Force-Assisted, High-Throughput, Droplet-Free, Single-Cell Sampling Coupled with ICP-MS for Real-Time Cell Analysis. *Analytical Chemistry*. 2020;92:6604-6612.
- [30] Chen Z, Chen B, He M, Hu B. Negative Magnetophoresis Focusing Microchips Online-Coupled with ICP-MS for High-Throughput Single-Cell Analysis. *Analytical Chemistry*. 2022;94:6649-6656.
- [31] Wu C, Wei X, Men X, Zhang X, Yu Y-L, Xu Z-R, Chen M-L, Wang J-H. Two-Dimensional Cytometry Platform for Single-Particle/Cell Analysis with Laser-Induced Fluorescence and ICP-MS. *Analytical Chemistry*. 2021;93:8203-8209.
- [32] Wu C, Men X, Liu M, Wei Y, Wei X, Yu Y-L, Xu Z-R, Chen M-L, Wang J-H. Two-Dimensional Multi-parameter Cytometry Platform for Single-Cell Analysis. *Analytical Chemistry*. 2023;95:13297-13304.
- [33] Wang J, Wei X, Wu C-X, Zhang X, Wei Y-J, Liu J-H, Wang Y, Chen M-L, Wang J-H. Interaction of Cellular Uptake of Nanosilver and Metallothionein Stress Expression Elucidated by 2D Single-Cell Analyses Based on LIF and ICP-MS. *Analytical Chemistry*. 2023;95:16176-16184.
- [34] Shigeta K, Traub H, Panne U, Okino A, Rottmann L, Jakubowski N. Application of a micro-droplet generator for an ICP-sector field mass spectrometer – optimization and analytical characterization. *Journal of Analytical Atomic Spectrometry*. 2013;28:646-656.
- [35] Verboket PE, Borovinskaya O, Meyer N, Günther D, Dittrich PS. A New Microfluidics-Based Droplet Dispenser for ICPMS. *Analytical Chemistry*. 2014;86:6012-6018.
- [36] Vonderach T, Günther D. Fundamental studies on droplet throughput and the analysis of single cells using a downward-pointing ICP-time-of-flight mass spectrometer. *Journal of Analytical Atomic Spectrometry*. 2021;36:2617-2630.
- [37] Koch J, Flamigni L, Gschwind S, Allner S, Longerich H, Günther D. Accelerated evaporation of microdroplets at ambient conditions for the on-line analysis of nanoparticles by inductively-coupled plasma mass spectrometry. *Journal of Analytical Atomic Spectrometry*. 2013;28:1707-1717.
- [38] Rosenkranz D, Kriegel FL, Mavrakís E, Pergantis SA, Reichardt P, Tentschert J, Jakubowski N, Laux P, Panne U, Luch A. Improved validation for single particle ICP-MS analysis using a pneumatic nebulizer / microdroplet generator sample introduction system for multi-mode nanoparticle determination. *Anal Chim Acta*. 2020;1099:16-25.
- [39] Kocic J, Günther D, Hattendorf B. Improving detection capability for single particle inductively coupled plasma mass spectrometry with microdroplet sample introduction. *Journal of Analytical Atomic Spectrometry*. 2021;36:233-242.
- [40] Iwase M, Tanaka YK, Suzuki N, Ogra Y. Determination of spatial mercury concentration by laser ablation-inductively coupled plasma mass spectrometry. *J Toxicol Sci*. 2021;46:193-198.
- [41] Zheng L-N, Sang Y-B, Luo R-P, Wang B, Yi F-T, Wang M, Feng W-Y. Determination of silver nanoparticles in single cells by microwell trapping and laser ablation ICP-MS determination. *Journal of Analytical Atomic Spectrometry*. 2019;34:915-921.
- [42] Löhr K, Borovinskaya O, Tourniaire G, Panne U, Jakubowski N. Arraying of Single Cells for Quantitative High Throughput Laser Ablation ICP-TOF-MS. *Analytical Chemistry*. 2019;91:11520-11528.
- [43] Pozebon D, Scheffler GL, Dressler VL, Nunes MAG. Review of the applications of laser ablation inductively coupled plasma mass spectrometry (LA-ICP-MS) to the analysis of biological samples. *Journal of Analytical Atomic Spectrometry*. 2014;29:2204-2228.
- [44] Martinez M, Baudelet M. Calibration strategies for elemental analysis of biological samples by LA-ICP-MS and LIBS – A review. *Analytical and Bioanalytical Chemistry*. 2020;412:27-36.
- [45] Lockwood TE, Bordin DCM, Westerhausen MT, Bishop DP. Preparation of gelatine calibration standards for LA-ICP-MS bioimaging with 266 nm laser ablation systems. *Talanta*. 2025;283:127150.
- [46] Mervič K, Šelih VS, Šala M, van Elteren JT. Non-matrix-matched calibration in bulk multi-element laser ablation-inductively coupled plasma-mass spectrometry analysis of diverse materials. *Talanta*. 2024;271:125712.
- [47] Yokoyama TD, Suzuki T, Kon Y, Hirata T. Determinations of rare earth element abundance and U-Pb age of zircons using multipot laser ablation-inductively coupled plasma mass spectrometry. *Anal Chem*. 2011;83(23):8892-8899.
- [48] Drescher D, Giesen C, Traub H, Panne U, Kneipp J, Jakubowski N. Quantitative Imaging of Gold and Silver Nanoparticles in Single Eukaryotic Cells by Laser Ablation ICP-MS. *Analytical Chemistry*. 2012;84:9684-9688.
- [49] Schoeberl A, Gutmann M, Theiner S, Schaiher M, Schweikert A, Berger W, Koellensperger G. Cisplatin Uptake in Macrophage Subtypes at the Single-Cell Level by LA-ICP-TOFMS Imaging. *Analytical Chemistry*. 2021;93:16456-16465.
- [50] Theiner S, Schweikert A, Van Malderen SJM, Schoeberl A, Neumayer S, Jilma P, Peyrl A, Koellensperger G. Laser Ablation-Inductively Coupled Plasma Time-of-Flight Mass Spectrometry Imaging of Trace Elements at the Single-Cell Level for Clinical Practice. *Analytical Chemistry*. 2019;91:8207-8212.
- [51] Tanaka Y-k, Ogra Y. Single-Cell Analysis of Elemental Contents by Laser Ablation-Inductively Coupled Plasma Mass Spectrometry. *Journal of the American Society for Mass Spectrometry*. 2024;35:2082-2089.

# Selenium-containing $\pi$ -Bond Compounds of Heavier Main-Group Elements

Koh Sugamata<sup>1,\*</sup>, Takahiro Sasamori<sup>2,\*</sup>

<sup>1</sup> Department of Chemistry, College of Science, Rikkyo University

<sup>2</sup> Department of Chemistry, Institute of Pure and Applied Sciences, and Tsukuba Research Center for Energy Materials Sciences (TREMS), University of Tsukuba

## Abstract

This review highlights the unique chemistry of  $\pi$ -bond compounds consisting of both selenium and other heavier main-group element, which exhibit intriguing reactivity and potential applications in catalysis, materials science, and bioinorganic chemistry. While selenium shares similarities with sulfur, its larger atomic size and greater polarizability give Se-containing double bonds distinctive characteristics that often result in higher reactivity. This review will focus on recent advancements of compounds that contain a  $\pi$ -bond containing selenium and other heavier main-group elements as well as unique  $\pi$ -conjugated systems, rather than on well-established compounds such selenoketones and selenoamides.

**Keywords:** Selenium,  $\pi$ -bond, main group element, molecular structure, thermodynamic stabilization, kinetic stabilization

---

## \*Correspondence:

Koh Sugamata  
Department of Chemistry, College of Science, Rikkyo University, 3-34-1 Nishi-Ikebukuro, Toshima-ku, Tokyo 171-8501, Japan  
**e-mail** ; sugamata@rikkyo.ac.jp;

Takahiro Sasamori  
Department of Chemistry, Institute of Pure and Applied Sciences, and Tsukuba Research Center for Energy Materials Sciences (TREMS), University of Tsukuba, 1-1-1 Tennoudai, Tsukuba, Ibaraki 305-8571, Japan  
**e-mail** ; sasamori@chem.tsukuba.ac.jp

Received: November 28, 2024

Accepted: December 24, 2024

Released online: February 28, 2025

## 1. Introduction

### 1.1 General introduction

Selenium, a member of the chalcogen family (group-16 elements), exhibits a rich and versatile chemistry that has garnered significant attention in recent decades[1]. Among its various bonding modes, the formation of double bonds involving selenium is of particular interest due to its implications in a wide array of chemical and biological processes. Indeed, compounds featuring selenium double bonds offer intriguing properties, including unique reactivity patterns and potential applications in catalysis, materials science, and bioinorganic chemistry[1,2]. Despite the structural similarities between selenium and sulfur, the chemistry of selenium double bonds reveals distinct characteristics arising from the larger atomic size, lower electronegativity, and greater polarizability of selenium. These factors influence the stability, electronic properties, and reactivity of selenium-containing double-



This work is licensed under a Creative Commons Attribution 4.0 International License.

©2025 THE AUTHORS. [DOI](https://doi.org/10.11299/metallomicsresearch.MR202411) <https://doi.org/10.11299/metallomicsresearch.MR202411>

bond systems. As a result, selenium double bonds often exhibit reactivity higher than their sulfur counterparts, unlocking avenues for the development of new synthetic methodologies.

This review aims to provide a comprehensive overview of recent advancements in the study of selenium double-bond compounds, focusing on their synthesis, structural features, and fundamental reactivity. By comparing the behavior of selenium-based double-bond systems with systems that contain other group-16 elements, we seek to highlight the unique features of selenium chemistry and its potential for further exploration in both fundamental and applied research. It should be noted here that simple double-bond systems that contain selenium and second-row-elements such as selenoketones and selenoamides have already been introduced and discussed in several reviews/books[2,3], and will thus not be considered in this review. This mini-review focuses on recent examples of compounds with double bonds that contain selenium and other heavier main-group elements as well as unique  $\pi$ -conjugated systems that include selenium. These reactive Se-containing double-bond systems are often stabilized by intermolecular coordination from an electron-donor, which electronically perturbs the intrinsic nature of the Se- $\pi$  bonds.

## 1.2. Theoretical aspects

For many years, it had been commonly accepted that compounds that contain double bonds between heavier main-group elements are most likely unstable species due to their substantially higher reactivity compared to that of their second-row-element analogues (“double-bond rule”)[4]. Although several examples of C=S and C=Se double-bond compounds had been isolated and characterized, examples of selenium-containing double-bond compounds with a heavier main-group element remained elusive. However, following the pioneering reports on the synthesis and isolation of the first stable disilene[5] and diphosphene[6] in 1981 by the groups of West and Yoshifuji, respectively, it was demonstrated that compounds with double bonds between heavier main-group elements can be isolated as stable compounds when sufficiently stabilized by sterically demanding substituents (kinetic stabilization)[7]. After this breakthrough, the so-called heavy ketones (E=Ch double-bond compounds; E = Si, Ge, Sn, Ch = S, Se, Te), i.e., the heavier-element analogues of ketones, were successfully synthesized, isolated, and fully characterized[8].

The predominant reason for the difficulties associated with the isolation of compounds that contain a double bond between heavier main-group elements is that the bonding energy of a  $\pi$ -bond between heavier main-group elements is very small relative to the corresponding  $\sigma$ -bond energy, which causes facile oligomerization even under inert atmospheres. As shown in **Table 1-1**[9], the energy of the Se=E (E = C, Si, Ge, Sn, Pb)  $\pi$ -bonds is significantly lower than the energy of the corresponding  $\sigma$ -bonds and of the (S=E)  $\pi$ -bond energy of the corresponding sulfur analogues.

**Table 1-1.** Energy values (kcal/mol) and lengths (Å) of the  $\sigma$ -bond energy and  $\pi$ -bond energy of Ch=EH<sub>2</sub> (E = C, Si, Ge, Sn, Pb) compounds.

Ch=EH <sub>2</sub>		Ch = O	Ch = S	Ch = Se	Ch = Te
E = C	$\sigma$ -BE <sup>a</sup>	93.6	73.0	65.1	57.5
	$\pi$ -BE <sup>b</sup>	95.3	54.6	43.2	32.0
	distance <sup>c</sup>	1.200	1.617	1.758	1.949
E = Si	$\sigma$ -BE <sup>a</sup>	119.7	81.6	73.7	63.2
	$\pi$ -BE <sup>b</sup>	58.5	47.0	40.7	32.9
	distance <sup>c</sup>	1.514	1.945	2.082	2.288
E = Ge	$\sigma$ -BE <sup>a</sup>	101.5	74.1	67.8	59.1
	$\pi$ -BE <sup>b</sup>	45.9	41.1	36.3	30.3
	distance <sup>c</sup>	1.634	2.042	2.174	2.373
E = Sn	$\sigma$ -BE <sup>a</sup>	94.8	69.3	64.3	56.4
	$\pi$ -BE <sup>b</sup>	32.8	33.5	30.6	26.3
	distance <sup>c</sup>	1.802	2.222	2.346	2.543
E = Pb	$\sigma$ -BE <sup>a</sup>	80.9	60.9	57.0	50.3
	$\pi$ -BE <sup>b</sup>	29.0	30.0	27.8	24.4
	distance <sup>c</sup>	1.853	2.273	2.394	2.590

<sup>a</sup> Ch=E s-bond energy (kcal/mol); <sup>b</sup> Ch=E p-bond energy (kcal/mol); <sup>c</sup> Ch=E distance (Å).

Natural-bond-orbital (NBO) calculations on the bonding character of Se=E double bonds (E = group 13-15 elements)[10], suggested that the Se=E  $\sigma$ -bonds should be composed of a ~60% contribution from the Se atom with its  $sp^n$  hybridized orbital ( $n > 4.7$ ), reflecting the intrinsic nature of unfavorable formation of hybridized orbitals in heavier main-group elements. The  $\pi$ -bonds of Se=E should consist predominantly of contributions from the p-orbital of the Se atom (>60%) probably due to the larger effective nuclear charge for the valence orbitals of the Se atom. Accordingly, the Se atoms should be negatively charged relative to the bonding E atoms. It should also be noted here that a nucleophile, such as a phosphine or alkyl lithium, sometimes attacks the Se atom of Se=E compounds despite the negative charge of the Se atom, which is probably due to the low-lying  $\pi^*$  orbitals of the Se=E bonds that spreading largely around the Se atom. This bonding behavior should result in amphiphilic character of the Se atoms in Se=E compounds.

**Table 1-2.** Bonding characters, bond lengths (Å), and natural charges for Ch=EH<sub>2</sub> (E = C, Si, Ge, Sn, Pb) compounds calculated at the B3PW91-D3(BJ)/def2TZVPP level using Gaussian 16 (rev. C) and NBO 7.0.

<b>E=Se (Å)</b>		group-13	group-14
<b><math>\sigma</math>: E + Se</b>		HE=Se (E = B, Al, Ga, In, Tl)	H <sub>2</sub> E=Se (E = C, Si, Ge, Sn, Pb)
<b><math>\pi</math>: E + Se</b>			
<b>NPA: E, Se</b>			
2 <sup>nd</sup> row	<b>E = B:</b> HB=Se: 1.7279 $\sigma$ : B( $sp^{1.04}$ , 43.5%)+Se( $sp^{2.88}$ , 56.5%) $\pi$ : B(p, 25.3%)+Se(p, 74.7%) $\pi$ : B(p, 25.3%)+Se(p, 74.7%) NPA: B(+0.15), Se(-0.10)		<b>E = C:</b> H <sub>2</sub> C=Se: 1.7441 $\sigma$ : C( $sp^{1.80}$ , 58.1%)+Se( $sp^{4.67}$ , 41.8%) $\pi$ : C(p, 46.3%)+Se(p, 53.7%) NPA: C(-0.54), Se(+0.16)
3 <sup>rd</sup> row	<b>E = Al:</b> HAl=Se: 2.1238 $\sigma$ : Al( $sp^{0.89}$ , 31.5%)+Se( $sp^{4.88}$ , 68.5%) $\pi$ : Al(p, 14.0%)+Se(p, 86.0%) $\pi$ : Al(p, 14.0%)+Se(p, 86.0%) NPA: Al(+1.13), Se(-0.78)		<b>E = Si:</b> H <sub>2</sub> Si=Se: 2.0743 $\sigma$ : Si( $sp^{1.67}$ , 41.2%)+Se( $sp^{4.72}$ , 58.8%) $\pi$ : Si(p, 28.3%)+Se(p, 71.7%) NPA: Si(+0.79), Se(-0.45)
4 <sup>th</sup> row	<b>E = Ga:</b> HGa=Se: 2.1252 $\sigma$ : Ga( $sp^{0.91}$ , 36.1%)+Se( $sp^{5.19}$ , 63.8%) $\pi$ : Ga(p, 14.3%)+Se(p, 85.7%) $\pi$ : Ga(p, 14.3%)+Se(p, 85.7%) NPA: Ga(+0.93), Se(-0.69)		<b>E = Ge:</b> H <sub>2</sub> Ge=Se: 2.1529 $\sigma$ : Ge( $sp^{1.69}$ , 43.0%)+Se( $sp^{5.84}$ , 57.0%) $\pi$ : Ge(p, 28.1%)+Se(p, 71.9%) NPA: Ge(+0.74), Se(-0.45)
5 <sup>th</sup> row	<b>E = In:</b> HIn=Se: 2.2979 $\sigma$ : In( $sp^{0.85}$ , 36.9%)+Se( $sp^{8.20}$ , 63.2%) $\pi$ : In(p, 12.1%)+Se(p, 87.9%) $\pi$ : In(p, 12.1%)+Se(p, 87.9%) NPA: In(+1.03), Se(-0.74)		<b>E = Sn:</b> H <sub>2</sub> Sn=Se: 2.3290 $\sigma$ : Sn( $sp^{1.57}$ , 42.3%)+Se( $sp^{7.70}$ , 57.7%) $\pi$ : Sn(p, 23.7%)+Se(p, 76.3%) NPA: Sn(+0.95), Se(-0.57)
6 <sup>th</sup> row	<b>E = Tl:</b> HTl=Se: 2.3322 $\sigma$ : Se( $sp^{10.5}$ )→Tl(p) (coordination) $\pi$ : Tl(p, 11.4%)+Se(p, 88.6%) $\pi$ : Tl(p, 11.4%)+Se(p, 88.6%) NPA: Tl(+0.90), Se(-0.68)		<b>E = Pb:</b> H <sub>2</sub> Pb=Se: 2.4040 $\sigma$ : Pb( $sp^{1.47}$ , 46.9%)+Se( $sp^{11.28}$ , 53.1%) $\pi$ : Pb(p, 21.2%)+Se(p, 78.8%) NPA: Pb(+0.87), Se(-0.54)
<b>E=Se (Å)</b>		group-15	group-16
<b><math>\sigma</math>: E + Se</b>		HE=Se (E = N, P, As, Sb, Bi)	E=Se (E = O, S, Se, Te, Po)
<b><math>\pi</math>: E + Se</b>			
<b>NPA: E, Se</b>			
2 <sup>nd</sup> row	<b>E = N:</b> HN=Se: 1.7110 $\sigma$ : N( $sp^{3.42}$ , 64.1%)+Se( $sp^{5.96}$ , 35.9%) $\pi$ : N(p, 56.2%)+Se(p, 43.8%) NPA: N(-0.74), Se(+0.42)		<b>E = O:</b> O=Se: 1.6401 $\sigma$ : O( $sp^{4.41}$ , 69.3%)+Se( $sp^{6.81}$ , 30.7%) $\pi$ : O(p, 65.7%)+Se(p, 34.3%) NPA: O(-0.68), Se(+0.68)
3 <sup>rd</sup> row	<b>E = P:</b> HP=Se: 2.0718 $\sigma$ : P( $sp^{5.37}$ , 45.8%)+Se( $sp^{5.95}$ , 54.2%) $\pi$ : P(p, 41.5%)+Se(p, 58.5%) NPA: P(+0.25), Se(-0.18)		<b>E = S:</b> S=Se: 2.0380 $\sigma$ : S( $sp^{6.85}$ , 53.1%)+Se( $sp^{7.71}$ , 46.9%) $\pi$ : S(p, 53.2%)+Se(p, 46.8%) NPA: S(-0.12), Se(+0.12)

4 <sup>th</sup> row	<b>E = As:</b> HAs=Se: 2.1823 $\sigma$ : As(sp <sup>7.07</sup> , 44.0%)+Se(sp <sup>6.71</sup> , 56.0%) $\pi$ : As(p, 39.9%)+Se(p, 60.1%) NPA: As(+0.35), Se(-0.26)	<b>E = Se:</b> Se=Se: 2.1737 $\sigma$ : Se(sp <sup>8.88</sup> , 50.0%)+Se(sp <sup>8.88</sup> , 50.0%) $\pi$ : Se(p, 50.0%)+Se(p, 50.0%) NPA: Se(0.0), Se(0.0)
5 <sup>th</sup> row	<b>E = Sb:</b> HSb=Se: 2.3594 $\sigma$ : Sb(sp <sup>7.98</sup> , 40.1%)+Se(sp <sup>7.64</sup> , 59.9%) $\pi$ : Sb(p, 35.2%)+Se(p, 64.8%) NPA: Sb(+0.61), Se(-0.43)	<b>E = Te:</b> Te=Se: 2.3628 $\sigma$ : Te(sp <sup>10.20</sup> , 45.4%)+Se(sp <sup>9.95</sup> , 54.6%) $\pi$ : Te(p, 44.8%)+Se(p, 55.2%) NPA: Te(+0.19), Se(-0.19)
6 <sup>th</sup> row	<b>E = Bi:</b> HBi=Se: 2.4427 $\sigma$ : Bi(sp <sup>11.7</sup> , 39.4%)+Se(sp <sup>8.81</sup> , 60.6%) $\pi$ : Bi(p, 34.2%)+Se(p, 65.8%) NPA: Bi(+0.66), Se(-0.47)	<b>E = Po:</b> Po=Se: 2.4529 $\sigma$ : Po(sp <sup>14.81</sup> , 44.2%)+Se(sp <sup>11.24</sup> , 55.8%) $\pi$ : Po(p, 43.4%)+Se(p, 56.6%) NPA: Po(+0.25), Se(-0.25)

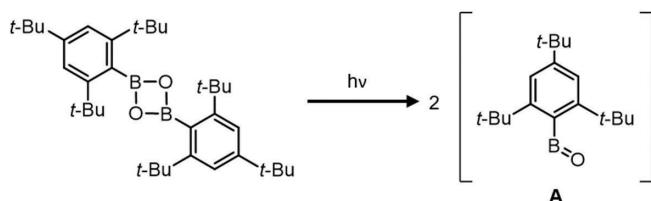
Given that there have recently been reported several examples of Se-containing  $\pi$ -bond compounds with heavier main-group elements, which have been isolated by using kinetic and/or thermodynamic stabilization, we will introduce in the next section the synthesis and structural features of these examples.

## 2. Group-13 – Selenium $\pi$ -bond compounds

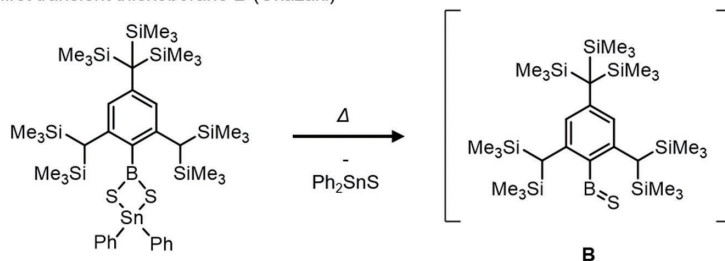


**Figure 2-1.** Isolobal relationship between the carbonyl group and its heavier main-group analogues.

a) The first transient oxoborane **A** (West)



b) The first transient thioxoborane **B** (Okazaki)



c) The first stable oxoborane complex **C** (Cowley)

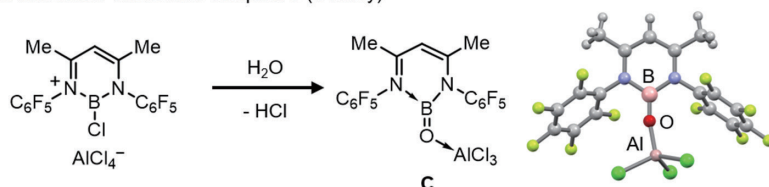


**Figure 2-2.** Pioneering studies on a) oxoborane **A**, b) thioxoborane **B**, and c) oxoborane complex **C**.

Due to the synthetic importance of the carbonyl group, the synthesis of their main-group analogues containing a multiple bond to a group-16 element (Ch = O, S, Se, Te) has been investigated extensively. As group-13 elements ( $E^{13}$  = B, Al, Ga, In, Th) are more electropositive than carbon, the resulting  $E^{13}$ =Ch bonds are highly polarized compared to the carbonyl C=O bond (**Figure 2-1**). Unfortunately, the isolation of compounds with  $E^{13}$ =Ch bonds is usually difficult due to self-oligomerization. A pioneering study on transient oxoborane **A** was reported by West and co-workers, who generated it via the irradiation of 1,3-dioxo-2,4-boretane[11]. The elusive nature of **A**

indicates that the bulky aryl group, Mes\*, is insufficient to kinetically stabilize this highly reactive oxoborane species at ambient temperature (**Figure 2-2a**). The first example of compounds with an  $E^{13}=S$  bond, i.e., thioxoborane **B** with a bulky aryl substituent, was reported by Okazaki and co-workers in 1996 (**Figure 2-2b**)<sup>[12]</sup>. In 2005, Cowley and co-workers reported that the isolation of the first example of a monomeric stable oxoborane bearing a B=O moiety (**C**)<sup>[13]</sup>. The compound was synthesized using a  $\beta$ -diketiminato as a supporting ligand for boron, and it was stabilized by the addition of the Lewis acid  $AlCl_3$ . Further investigations led to the synthesis of several compounds that contain  $E^{13}=Ch$  multiple bonds<sup>[14,15]</sup>. However, examples of  $E^{13}=Se$  compounds are more scarce compared to other chalcogenides due to the high propensity for dimerization of the  $E^{13}=Se$  bond. In this chapter, the synthesis and properties of compounds with an  $E^{13}=Se$  bond are described.

## 2.1. B=Se compounds

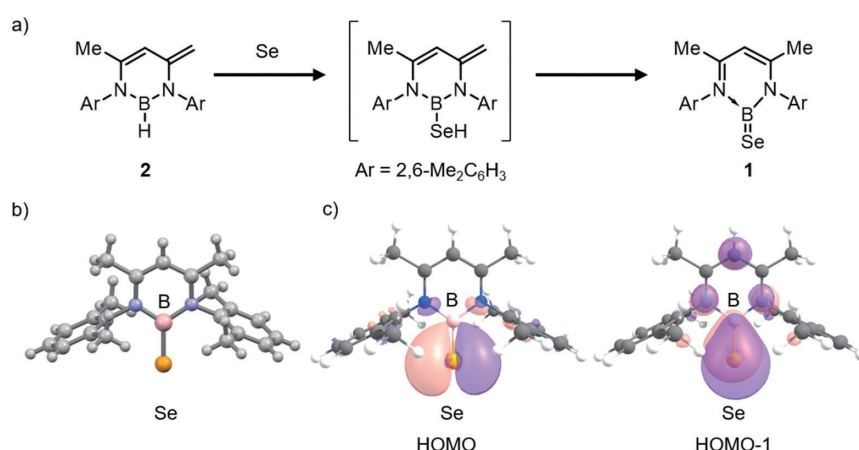


**Figure 2-3.** a) Synthesis of stable selenoxoborane **1**. b) Molecular structure of **1** in the crystalline state. c) Representations of the frontier orbitals of **1**.

In 2010, Cui and co-workers reported the synthesis of stable selenoxoborane **1** as orange crystals from the reaction of hydroborane **2**, which bears a  $\beta$ -diketiminato ligand, with 1 equivalent of elemental selenium at 70 °C in toluene<sup>[16]</sup>. The formation mechanism was interpreted in terms of a B-H bond insertion of selenium, followed by an H-migration to the exocyclic methylene group (**Figure 2-3a**). Selenoxoborane **1** is extremely air- and moisture-sensitive. The <sup>11</sup>B NMR spectrum of **1** exhibits a broad resonance at 40.88 ppm, which is downfield-shifted relative to that of **2** (29.3 ppm). The <sup>77</sup>Se NMR resonance for **1** is observed at -196 ppm. The molecular structure of **1** in the crystalline state revealed that the length of the B-Se bond (1.896(4) Å) is comparable to Pyykkö's standard value for a B-Se double bond (1.85 Å), and significantly shorter than those of reported B-Se single bonds (1.960-2.13 Å) (**Figure 3b**)<sup>[17-22]</sup>. The central boron atom adopts an approximately trigonal-planar coordination geometry. These structural features are consistent with a B-Se multiple bond. The bonding situation was furthermore analyzed by theoretical calculations on the Kohn-Sham orbitals of **1**, which revealed that the HOMO corresponds predominantly to the selenium lone pair and that the HOMO-1 refers to the B-Se  $\pi$ -bond.

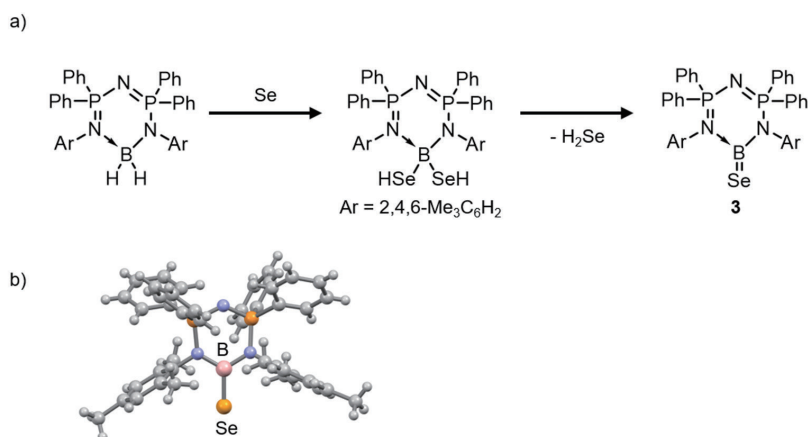
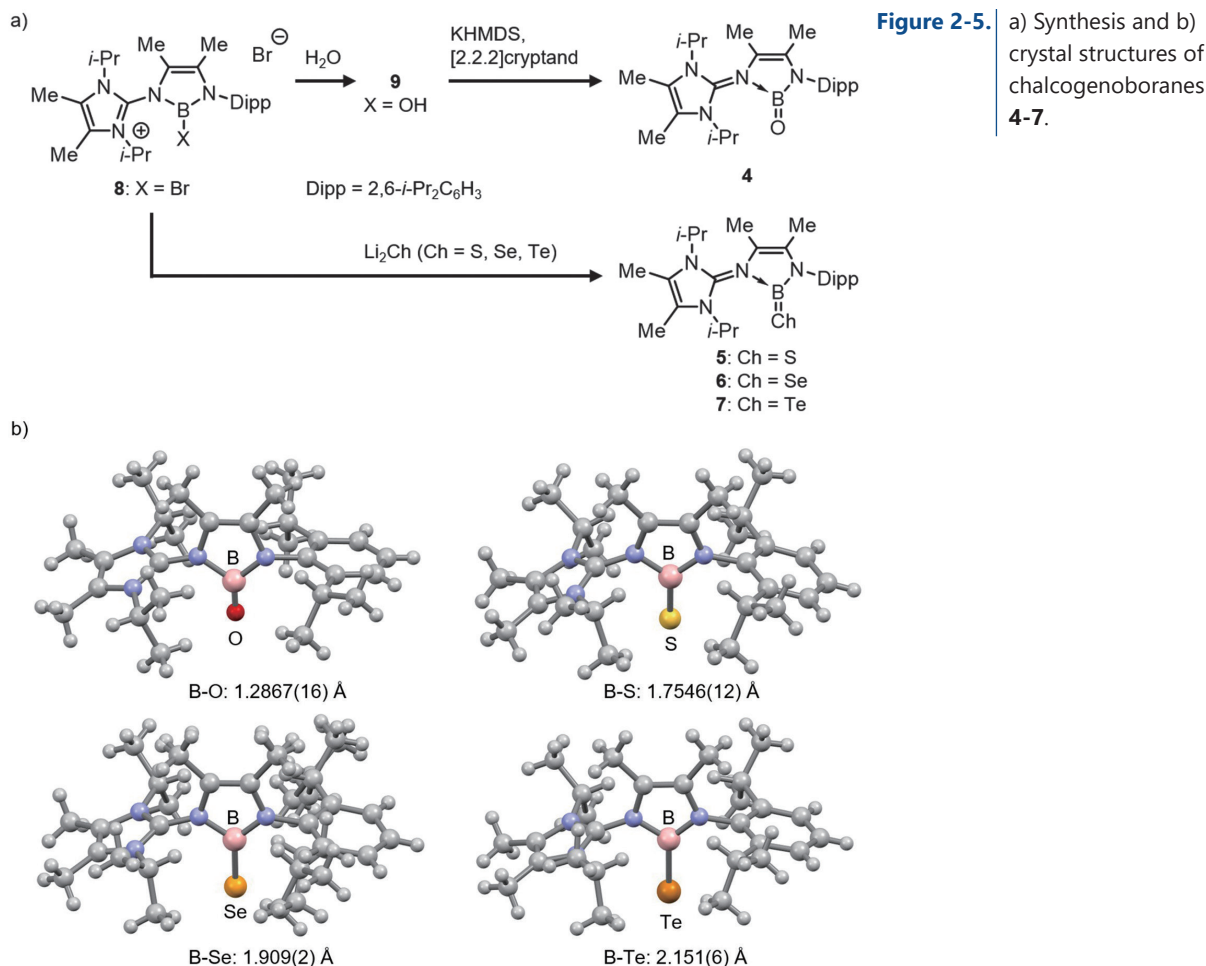


**Figure 2-4.** a) Synthesis of stable selenoxoborane **3**. b) Molecular structure of **3** in the crystalline state.

Singh and co-workers have obtained bis(phosphinimino)amide-substituted selenoxoborane **3** from the reaction of a hydroborane with elemental selenium (**Figure 2-4a**) [23]. Compound **3** exhibits structural features and properties similar to those of **1**. The  $^{11}\text{B}$  NMR spectrum of **3** shows a broad singlet resonance at 45.2 ppm, similar to the shift for **1** (40.88). The length of the B-Se bond (1.871(5) Å) is almost identical to that of **1** (1.896(4) Å).



Trzaskowski and Frank have reported the synthesis of a series of chalcogenoxoboranes (**4-7**) using the same NacNac-type ligand, i.e., HAmIm (**Figure 2-5**) [24]. Oxoborane **4** was obtained from the reaction of bromoborane **8** with  $\text{H}_2\text{O}$  to give the hydroxyborane **9**, followed by a deprotonation reaction with KHMDS in the presence of [2.2.2] cryptand. Heavier B=Ch compounds **5-7** were synthesized by the reaction of bromoborane **8** with the corresponding lithium chalcogenides ( $\text{Li}_2\text{Ch}$ ; Ch = S, Se, Te). The  $^{11}\text{B}$  NMR spectra of **4-7** show similar values (21.4 ppm for **4**, 35.2 ppm for **5**, 35.8 ppm for **6**, and 30.2 ppm for **7**). The crystal structures of **4-7** revealed that all compounds contain a boron center with a trigonal-planar coordination geometry and B-Ch double-bond character. The length of the B=Se bond in **7** (1.909(2) Å) is the longest B=Se distance reported so far. The Wiberg bond indices (WBIs) decrease continuously with increasing atomic number of the chalcogen element from 1.86 in **4** to 1.69 in **7**, which indicates diminished  $\pi$ - $\pi$  interactions between the boron atom and the heavier chalcogen atoms. Meanwhile, the values for **4-7** (>1.60) justify the formulation of the B=Ch bonds as true double bonds.

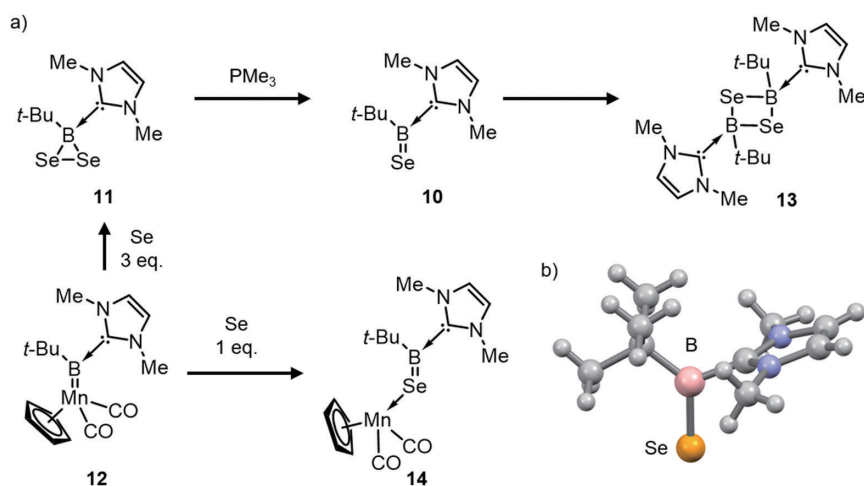


**Figure 2-6.** a) Synthesis of selenoxoborane **10**, its dimer **13**, and Mn complex **14**. b) Crystal structure of **13**.

Braunschweig and co-workers have reported the synthesis of *N*-heterocycliccarbene (NHC)-stabilized selenoxoborane **10** via the deselenization of boradiselenirane **11**, which was obtained from the reaction of borylene complex **12** with elemental selenium (Figure 2-6)[25]. At 60 °C, **10** slowly dimerizes (48 h) to give four-membered cycle **13**. The  $^{11}\text{B}$  NMR spectrum of **10** exhibits a broad resonance at -2.9 ppm, which is upfield-shifted relative to that of **1** (40.88 ppm). The  $^{77}\text{Se}$  NMR resonance of **10** is observed at 250 ppm, which is significantly downfield-shifted compared to that of **1** (-196 ppm) and upfield-shifted relative to that of previous reported selenoxoborane Mn complex **14** (370 ppm)[26]. The crystal structure of **10** revealed a length of the B-Se bond (1.876(4) Å) and a coordination geometry (trigonal planar) of the boron atom that are typical for selenoxoboranes.

## 2.2. Al=Se compounds

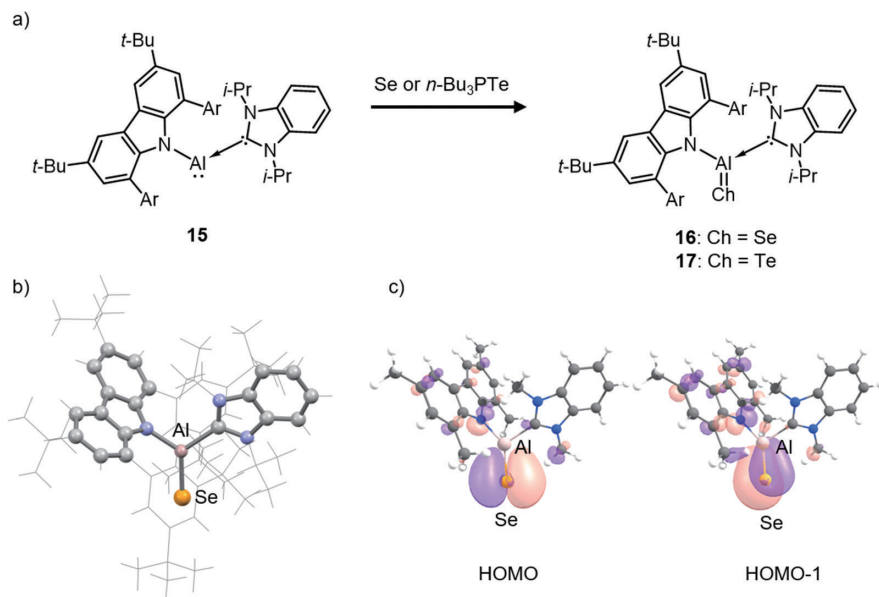


**Figure 2-7.** Synthesis of stable selenoxoalumane **16** and telluroxoalumane **17**. b) Crystal structure of **16**. c) Kohn-Sham frontier orbitals of **16**.

In 2023, Braunschweig and co-workers reported the synthesis of neutral aluminum selenide **16** by reacting NHC-stabilized alumylene **15** with elemental selenium in almost quantitative yield (Figure 2-7)[27]. Inoue and co-workers had previously attempted the synthesis of a neutral aluminum selenide, but obtained only the corresponding dimer[28]. The  $^{77}\text{Se}$  NMR spectrum of **16** exhibits a characteristic resonance signal at -264 ppm, which is up-field shifted compared to those of the compounds with B=Se bonds (Table 1). The crystal structure of **16** revealed that the central Al atom adopts a tricoordinate distorted trigonal-planar coordination geometry with an angle sum

around Al of  $359.8^\circ$ . The Al-Se bond ( $2.1935(8) \text{ \AA}$ ) is currently the shortest reported Al-Se bond, and comparable to Pyykkö's standard value for an Al-Se double bond ( $2.20 \text{ \AA}$ ). The WBI for the Al-Se bond in **16** (1.31) is smaller than that for tellurium derivative **17** (1.47). The Kohn-Sham orbitals of **16** show that the HOMO corresponds mainly to the selenium lone pair and the HOMO-1 to the Al-Se  $\pi$ -bond (**Figure 2-7c**). The NBO charges of Al (+1.56 for **16**, +1.40 for **17**) and Ch ( $-1.05$  for **16**,  $-0.89$  for **17**) suggest a considerable amount of charge separation. The NBO results suggest that the Al-Se bond is more polar than the Al-Te bond, which is consistent with the fact that the electronegativity of Se (2.55) is higher than that of Te (2.12). Furthermore, an intrinsic-bond-orbital (IBO) analysis indicated the presence of a single Al-Ch  $\sigma$ -bond, strengthened by the electrostatic attraction between the  $\text{Al}^+$  and  $\text{Se}^-$  centers as well as a slight donation from the lone pairs of Se to the vacant orbitals at Al. These results suggest multiple-bond character for the Al-Se bond, albeit with an ambiphilic nature.

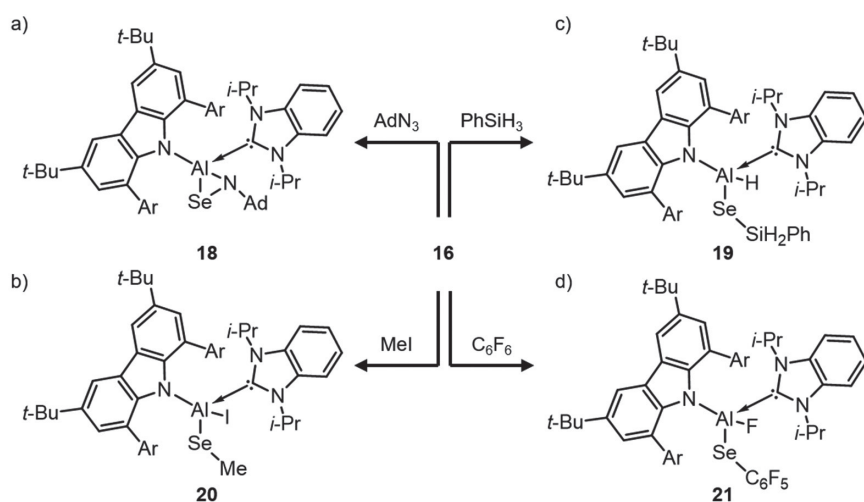


**Figure 2-8.** Reactivity of selenoxoborane **16**.

The reactivity of **16** corroborates its proposed ambiphilic multiple-bond character (**Figure 2-8**). The reaction of **16** with adamantylazide ( $\text{AdN}_3$ ) in toluene at room temperature rapidly afforded **18** with a three-membered Al-N-Se cycle, which is the first example of an aluminum and selenium containing analog of aziridine (**Figure 2-8a**). Compound **18** is likely formed via a [3 + 2] cycloaddition of  $\text{AdN}_3$  with **16** followed by  $\text{N}_2$  elimination. Furthermore, **16** can activate small molecules such as methyl iodide ( $\text{MeI}$ ), phenylsilane ( $\text{PhSiH}_3$ ), and perfluorobenzene ( $\text{C}_6\text{F}_6$ ), whereby the corresponding C-I, Si-H, and C-F bonds are cleaved to furnish addition products **19**, **20**, and **21**, respectively.

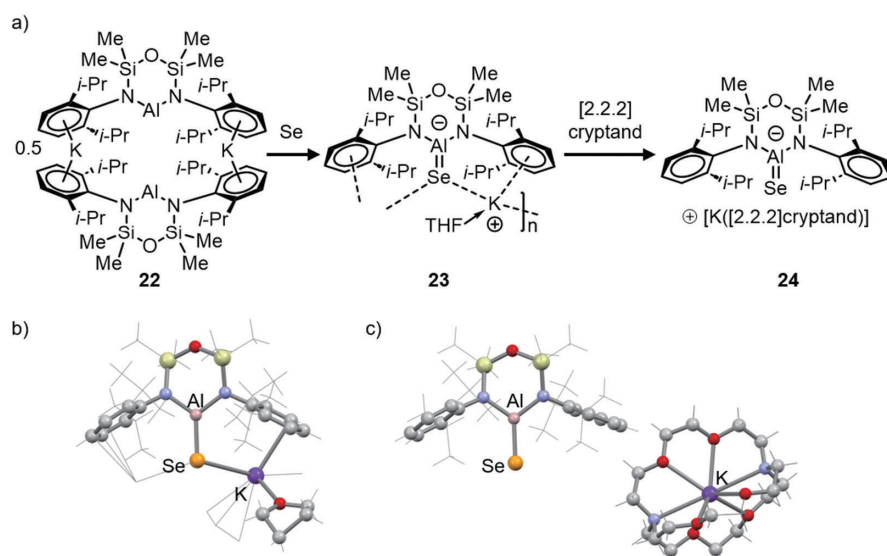


**Figure 2-9.** a) Synthesis and b,c) crystal structures of anionic selenoxoaluminanes **23** and **24**.

In 2019, Coles and co-workers reported the synthesis of anionic selenoxoalumane  $[\text{K}(\text{THF})][\text{Al}(\text{NON}^{\text{Ar}})(\text{Se})]$  ( $\text{NON}^{\text{Ar}} = [\text{O}(\text{SiMe}_2\text{NAr})_2]^{2-}$ ,  $\text{Ar} = 2,6\text{-}i\text{-Pr}_2\text{C}_6\text{H}_3$ ) (**23**) by reacting aluminyl anion  $\text{Al}(\text{NON}^{\text{Ar}})^-$  (**22**) with elemental selenium (**Figure 2-9a**)<sup>[29]</sup>. The crystal structure of **23** revealed the formation of an infinite chain structure by linking  $\text{K}^+$  cations through  $\text{Se}\cdots\text{K}$  and  $\pi$ -arene interactions. In the crystal, the aluminum center adopts a three-coordinate distorted trigonal-planar coordination environment with a short Al-Se bond (2.225(1) Å). The selenium atom interacts with two solvated potassium cations ( $\text{Se}\cdots\text{K}$ : 3.2965(10) Å/3.3730(10) Å) to form a one-dimensional chain. To isolate the aluminum-selenium bond from  $\text{Se}\cdots\text{K}$  interactions, the reaction was performed in the presence of [2.2.2]cryptand, which provided selenoxoalumane **24**, wherein the potassium cation is fully solvated by the [2.2.2] cryptand. The Al-Se bond in **24** (2.2032(6) Å) is shorter than that of **23**, confirming that the  $\text{Se}\cdots\text{K}$  interactions in **24** cause a slight elongation of the bond. The WBI for the Al-Se bond in **24** (1.39) is slightly higher than that of **16** (1.31), which indicates the presence of significant multiple-bond character in **24**. The NBO charges in **24** for Al (+1.61) and Se (-1.06) are indicative of a slightly higher polarization of the Al-Se bond in **24** compared to that in **16**. The spectroscopic analysis of **23** was limited by its low solubility and/or instability in common solvents, whereas **24** allowed for a successful analysis due to its improved solubility. The  $^{77}\text{Se}$  NMR spectrum of **24** displays a singlet at -563 ppm, which is upfield-shifted compared to those of reported  $\text{E}^{13}=\text{Se}$  compounds.

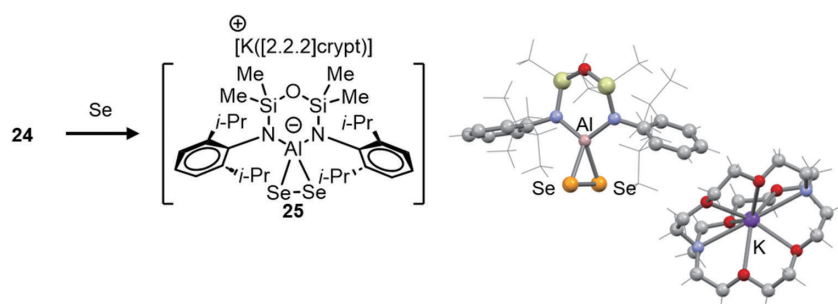


**Figure 2-10.** Reactivity of selenoxoalumane **24**.

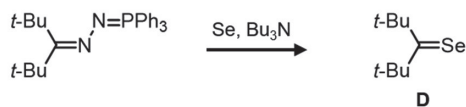
Treatment of selenoxoalumane **24** with an equimolar amount of elemental selenium in THF afforded diselenirane **25** as bright purple crystals (**Figure 2-10**).

### 3. Group-14 – Selenium $\pi$ -bond compounds

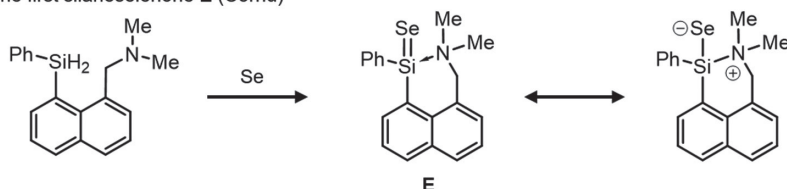
Arguably the most common molecules containing a  $\pi$ -bond between group-14 elements ( $\text{E}^{14} = \text{C}, \text{Si}, \text{Ge}, \text{Sn}, \text{Pb}$ ) and group-16 elements ( $\text{Ch} = \text{O}, \text{S}, \text{Se}, \text{Te}$ ) are ketones. Heavy ketones ( $\text{R}_2\text{E}^{14}=\text{Ch}$ ), which feature a double bond between heavier group-14 and -16 elements, are attractive synthetic targets due to their unique properties and high reactivity. Among these, selenium analogues are particularly valuable because their electronic state in solution can be analyzed using  $^{77}\text{Se}$  NMR spectroscopy. Unfortunately, their isolation is usually difficult due to self-oligomerization (as in the case of  $\text{E}^{13}=\text{Ch}$  species; *vide supra*). The study of selenium-containing heavy ketones has a long history, beginning with Burton and co-workers, who reported in 1975 the synthesis of di-*t*-butylselenoketone (**D**) as the first monomeric compound of this class (**Figure 3-1**)<sup>[30]</sup>. Subsequently, in 1989, Corriu and co-workers reported the first silaneselone derivatives (**E**) stabilized by an intramolecular  $\text{N}\rightarrow\text{Si}$  donor-acceptor interaction (thermodynamic stabilization)<sup>[31]</sup>. This method, remains widely used today and has become one of the strongest tools for stabilizing highly reactive species of main-group elements. Another primary method for stabilizing reactive main-group elements species is the previously mentioned kinetic stabilization by taking advantage of steric protection groups. Pioneering work on stable heavy ketones with a terminal group-16 element has been reported mainly by Okazaki and Tokitoh through the introduction of bulky 2,4,6-tris(bis(trimethylsilyl)methyl)phenyl and 2,6-bis(bis(trimethylsilyl)methyl)-4-(tris(trimethylsilyl)methyl)phenyl groups to group-14 elements<sup>[8]</sup>. The Ge-Se bond in germaneselone **F** (2.180(2) Å) is comparable to Pyykkö's standard value for a Ge-Se double bond (2.18 Å)<sup>[17,32]</sup>, while, those of thermodynamically stabilized germaneselones show slightly longer (2.194(1) Å-2.237(2) Å) due to the effect of zwitterionic canonical structures (**Figure 3-1b**)<sup>[33-54]</sup>. However, such base-stabilization

(thermodynamic stabilization) provides access only to a relatively limited range of heavier analogues of common, small organic molecules such as ketones. In this chapter, notable achievements of new types of  $E^{14}=\text{Se}$  species, such as heavier analogues of carboxylic acids, acylium ions, carbon dioxide, and carbonyl ylides, are described.

a) The first monomeric selenoketone **D** (Barton)



b) The first silaneselenone **E** (Corriu)



c) The first germaneselenone **F** (Okazaki and Tokitoh)

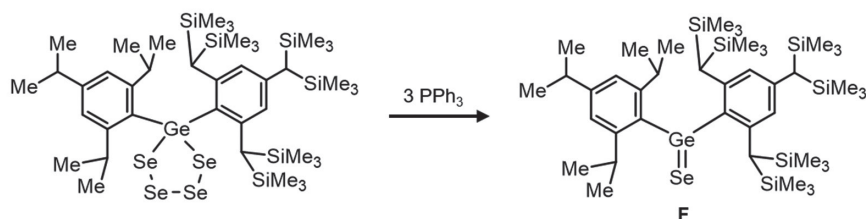


**Figure 3-1.** Pioneering studies on a) selenoketone **D**, b) silaneselone **E**, and c) germaneselone **F**.

### 3.1. Heavier analogues of carboxylic acids

a)

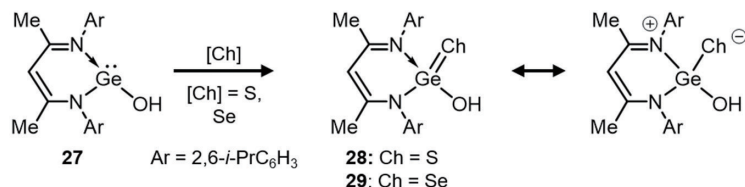
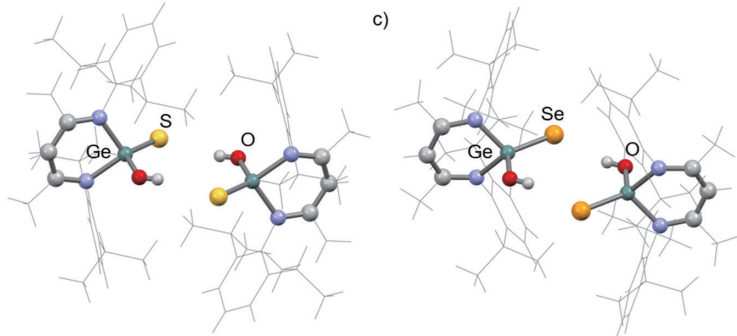
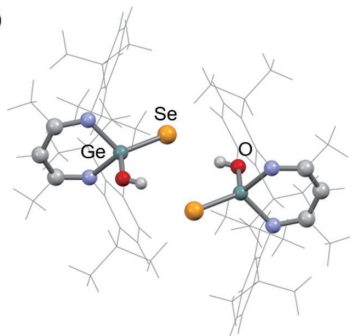


**Figure 3-2.** a) Synthesis of chalcogenogermanoic acids **28** and **29** as well as packing structures for b) **28** and c) **29**.

b)



c)



In 2004, Roesky and co-workers reported the synthesis of thiogermanoic acid **28** as the first heavier carboxylic acid, by reacting hydroxygermylene **27** with elemental sulfur (**Figure 3-2**) [55]. In 2006, selenogermanoic acid **29** was obtained by the same manner using elemental selenium instead of elemental sulfur [37]. The OH stretching frequency of **29** shows a broad absorption at  $3299 \text{ cm}^{-1}$ , which is at slightly higher wavenumber than that of **28** ( $3238 \text{ cm}^{-1}$ ). These values are significantly shifted to lower wavenumbers compared to that of **27** ( $3571 \text{ cm}^{-1}$ ), indicating the formation of hydrogen bonds in **28** and **29**. In the  $^1\text{H}$  NMR spectra of **28** and **29**, their OH protons were observed at 2.30 ppm and 2.19 ppm, respectively, which are significantly upfield-shifted compared to carboxylic acids, indicating the weaker acidity for **28** and **29** than for common carboxylic acids. The  $^{77}\text{Se}$  NMR

resonance of **29** is observed at  $-439$  ppm, which falls within the range of compounds exhibiting ylide-type and multiple-bond character at the germanium-selenium moiety[56]. In the crystal, **29** exists as a selenoxo tautomeric form of hydrogen-bonded dimers with weak intermolecular hydrogen interactions. The length of the Ge-Se bond in **29** ( $2.206(1)$  Å) is comparable to Pyykkö's standard value for a Ge-Se double bond ( $2.18$  Å), and very much consistent with resonance-structure contributions from both a Ge-Se ylide-type bond and a multiple bond rather than a pure germanium-selenium single bond ( $2.37$  Å)[17]. The pKa values of **28** ( $37.2$ ) and **29** ( $38.3$ ) fall in the range expected for aromatic ( $-33$ ) and aliphatic ( $-48$ ) compounds. Importantly, these values are significantly lower than those observed for representative oxygen-containing Brønsted acids ( $-15$ ) [57].

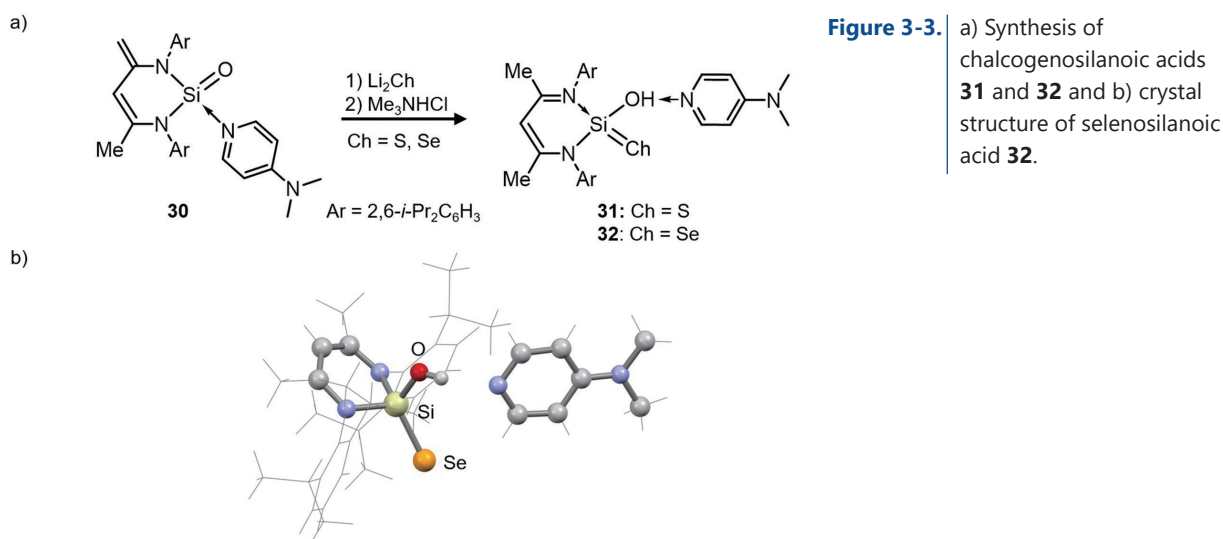


**Figure 3-3.** a) Synthesis of chalcogenosilanoic acids **31** and **32** and b) crystal structure of selenosilanoic acid **32**.

Subsequently, in 2013, Driess and co-workers reported the synthesis of the stable selenosilanoic acid-base adduct of the type [LSi(Se)=OH(dmap)] (**32**) by reacting silanone complex **30** with H<sub>2</sub>Se (**Figure 3-3**) [58]. Compound **32** is the heavier analogue of a carboxylic acid and its sulfur analogue of the type [LSi(S)=OH(dmap)] (**31**), which had been reported by the same group in 2010[59]. In the <sup>1</sup>H NMR spectra of **31** and **32** their OH protons are observed at 6.35 and 6.42 ppm, respectively, which are significantly downfield-shifted compared to those of germanium derivatives **28** and **29**. The <sup>77</sup>Se NMR resonance of **32** is observed at  $-545$  ppm, which is similar to that of germanium derivative **29**. The crystal structures of **31** and **32** show that they are acid-base complexes, wherein one dmap ligand is connected to the chalcogenosilanoic-acid moiety through an O-H $\cdots$ N hydrogen bond. The length of the Si-Se bond in **32** ( $2.1348(7)$  Å) is close to Pyykkö's standard value for a Si-Se double bond ( $2.14$  Å)[17].

### 3.2. Heavier analogues of acylium ions

Koley and Inoue have reported the synthesis of NHC-stabilized germa-acylium ion **34** by reacting germyliumylidene ion **33** with N<sub>2</sub>O[60]. Subsequently, the reaction of **34** with Lawesson's reagent (LR) and Woollins' reagent (WR) afforded the corresponding sulfur (**35**) and selenium analogues (**36**). The driving force of these reactions is the formation of a stable P=O bond in a cycloreversion step that resembles the mechanism of Wittig reactions, indicating that the reactivity of germa-acylium ion **34** is akin to classical acylium-like behavior. The Ge-Se bond in **36** ( $2.2372(5)$  Å) is slightly longer than Pyykkö's standard value for a Ge-Se double bond ( $2.18$  Å), and comparable to those of thermodynamically stabilized germaneselones ( $2.194(1)$  Å- $2.237(2)$  Å)[17, 33-54]. NBO analyses of **34-36** suggested that the Ge-Ch bond becomes less polarized upon descending group-16 (O: 78.9%; S: 60.5%; Se: 55.3%). Furthermore, unlike the Ge-O bond in **33**, the Ge-S and Ge-Se bonds of **35** and **36** exhibit partial double-bond character, as indicated by the calculated WBI values of 1.279 and 1.302, respectively.

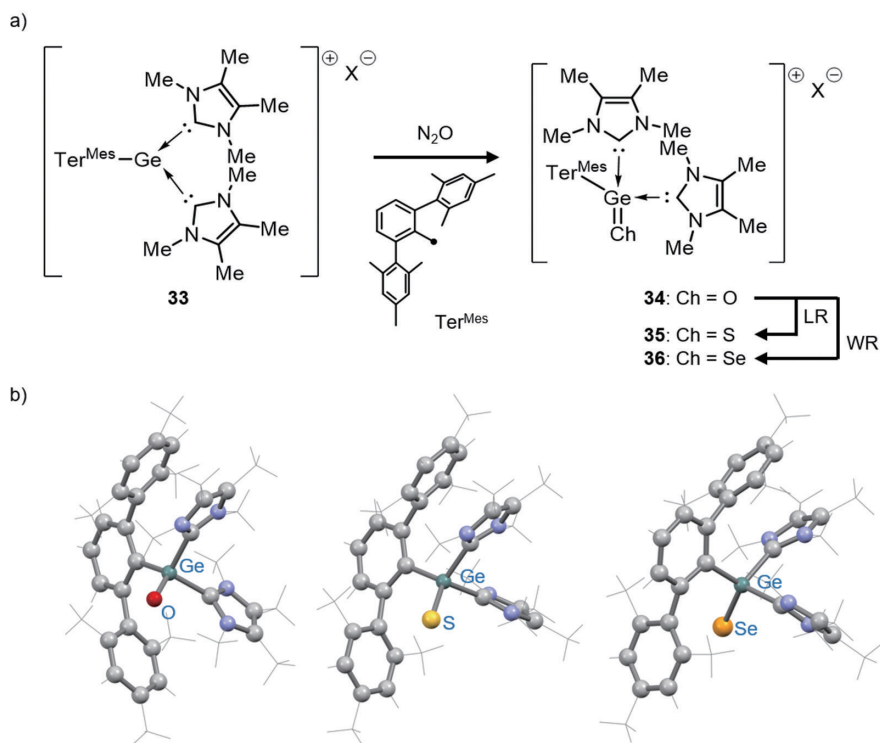


**Figure 3-4.** a) Synthesis of germaacylium ion **34** and its heavier analogues **35** and **36**. b) Crystal structures of **34-36**.

### 3.3. Heavier analogues of CO and CO<sub>2</sub>

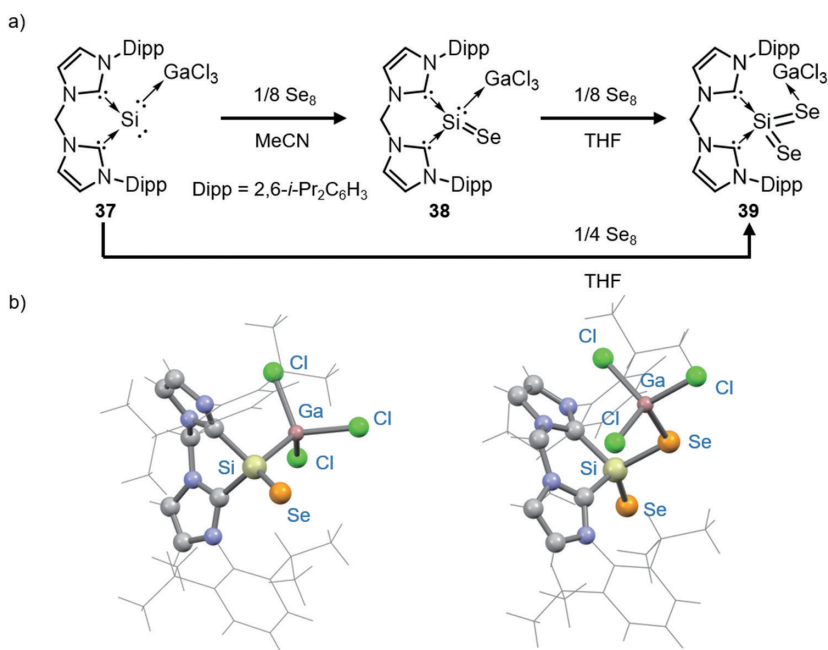


**Figure 3-5.** a) Synthesis of silicon and selenium analogues of CO (**38**) and CO<sub>2</sub> (**39**) together with b) their crystal structures.

Kaupp and Driess have reported the synthesis of bis-NHC-stabilized monomeric silicon chalcogenides. Silicon selenide **38** and diselenide **39** were obtained from the reaction of silylone **37** with elemental selenium<sup>[61]</sup>. Compounds **38** and **39** serve as base-stabilized heavier analogues of CO and CO<sub>2</sub>, respectively. Interestingly, the formation of **38** and **39** is solvent-dependent, i.e., **38** forms in acetonitrile, while **39** forms in THF. Notably, **38** does not react further in acetonitrile with additional Se, while solvent exchange to THF smoothly converts **38** into **39**. The <sup>77</sup>Se NMR resonances of **38** and **39** appear at –655 ppm and –391 ppm, respectively. The length of the Si–Se bonds in **38** (2.135(1) Å/2.1439(9) Å in the two independent molecules) are consistent with Pyykkö's standard value

for a Si=Se double bond (2.14 Å)[17]. In **39**, the longer Si1–Se2 bond (2.241(6) Å) approaches Pyykkö's standard value for a Si–Se single bond (2.32 Å), while the shorter Si1–Se1 bond (2.129(2) Å) resembles that of **38**[17].

### 3.4. Heavier analogues of allenes

a)

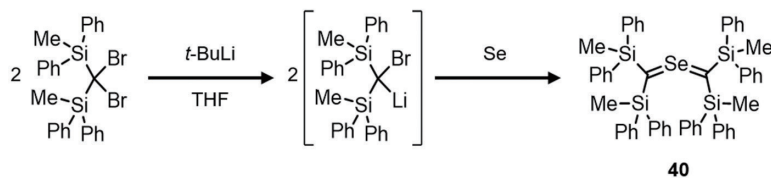
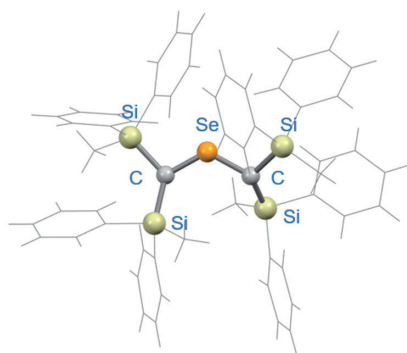


**Figure 3-6.** a) Synthesis of bis(methylene)- $\lambda^4$ -selane **40**, and its b) crystal structure.

b)



Sugamata and co-workers have reported on the synthesis of a series of bis(methylene)- $\lambda^4$ -chalcogenanes, i.e., 2-chalcogenaallene-type molecules, using bulky silyl substituents[62-65]. The selenium analogue, i.e., bis(methylene)- $\lambda^4$ -selane **40**, was obtained from the reaction of a transient bis(silyl)carbenoid with elemental selenium. While **40** represents a heavier analogue of a carbonyl ylide, it is also a significant example of a bent-allene-type structure rather than an ylide, being characterized as a symmetric molecule. The  $^{77}\text{Se}$  NMR resonance of **40** appears at 1501 ppm, which is characteristic for unsaturated organoselenium compounds[66,67]. The crystal structure of **40** exhibits pseudo- $C_2$  symmetry with a bent C–Se–C configuration. The nearly identical, short C–Se bond lengths (1.801(4) Å/1.808(3) Å) in **40** falls between Pyykkö's standard values for a C=Se double bond (1.74 Å) and a C–Se single bond (1.91 Å), indicating significant multiple-bond character[17]. An NBO analysis of **40** revealed two C–Se bonds and a 3-center-4-electron  $\pi$ -bond on the C–Se–C moiety.

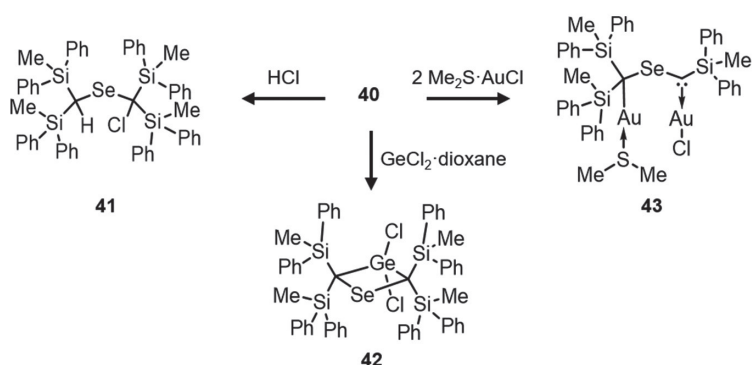


**Figure 3-7.** Reactions of **40**.

Bis(methylene)- $\lambda^4$ -selane **40** is inert toward a variety of alkynes and alkenes, despite being an analogue of carbonyl ylides, which are known as 1,3-dipole reagents. However, the reaction with hydrogen chloride yielded the corresponding 1,3-adduct (**41**) in a quantitative yield. Furthermore, treatment of **40** with  $\text{GeCl}_2$ -dioxane produced unique four-membered ring compound **42**, suggesting that the formal [3 + 1] cycloaddition represents

a specific reactivity pattern of bis(methylene)- $\lambda^4$ -chalcogenanes. The reaction with  $\text{AuCl}\cdot\text{Me}_2\text{S}$  selectively afforded the unexpected dinuclear carbene gold(I) complex **43** *via* the elimination of  $\text{Ph}_2\text{MeSiCl}$ [68].

#### 4. Group-15 – Selenium $\pi$ -bond compounds

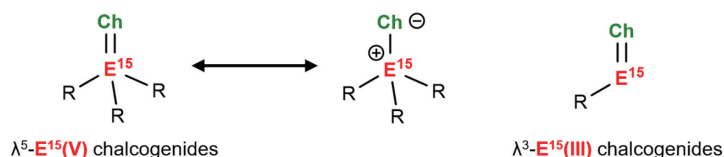


**Figure 4-1.** Compounds with terminal  $\text{E}^{15}=\text{Ch}$  bonds.

The synthesis of compounds with multiple bonds between heavier group-15 elements ( $\text{E}^{15} = \text{P}, \text{As}, \text{Sb}, \text{Bi}$ ) and chalcogens ( $\text{Ch} = \text{S}, \text{Se}, \text{Te}$ ) has received increased attention over the last few decades. Phosphine oxides and their heavier analogues, which are  $\text{P}(\text{V})$  species, are well known as useful reagents in organic synthesis (**Figure 4-1**). Their heavier analogues should be described as polar single-bonded structures[69]. In contrast,  $\text{E}^{15}(\text{III})$  chalcogenides are extremely rare species due to their low stability. The stabilization of such compounds typically requires sterically overcrowded ligands to prevent self-oligomerization. Tokitoh and co-workers have reported the selenization of kinetically stabilized diphosphene (**G** and **J**;  $\text{ArP}=\text{PAr}$ ), distibenes (**H** and **K**;  $\text{ArSb}=\text{SbAr}$ ) and dibismuthenes (**I** and **L**;  $\text{ArBi}=\text{BiAr}$ ) to afford the corresponding  $\text{E}^{15}(\text{III})$  selenides (**M-P**)[70-72], (**Figure 4-2**). Nevertheless, evidence for monomeric compounds that bear an unsupported terminal  $\text{E}^{15}(\text{III})$  chalcogen double bond is still missing. Breunig and co-workers have suggested the presence of a terminal antimony-selenium double bond for tungsten complex **Q** in benzene solution, albeit that **Q** forms a dimer in the solid state. In this chapter, notable achievements of  $\text{E}^{15}(\text{III})$  selenides are described.

##### a) $\text{E}^{15}(\text{III})$ selenides (Tokitoh)

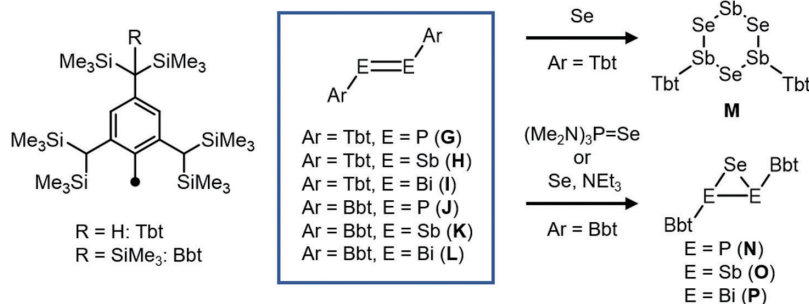
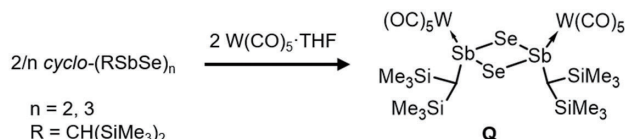


**Figure 4-2.** Pioneering studies on  $\text{E}^{15}(\text{III})$  selenides.

##### b) Antimony(III) selenide dimer complex **Q** (Breunig)



#### 4.1. Antimony(III) selenides

Dostál and co-workers have reported the synthesis of the first stable antimony(III) selenide using an NCN-pincer ligand[73]. The reaction of the cyclic organoantimony compound of the type  $\text{Ar}_4\text{Sb}_4$  (**44**) with an excess of elemental selenium in THF afforded the corresponding antimony(III) selenide (**45**) as a highly air-sensitive yellow crystalline solid[74]. The  $^1\text{H}$  and  $^{13}\text{C}$  NMR spectra of **45** displayed only one set of signals, indicating a highly symmetric structure in solution. A single signal at  $-197$  ppm was observed in the  $^{77}\text{Se}$  spectrum, and the  $^{77}\text{Se}$  CP/MAS NMR spectrum at  $-153$  ppm confirmed that the monomeric structure of **45** in the solid state is retained in solution. In the solid state, **45** is monomeric, with a Sb-Se bond length of  $2.4396(7)$  Å, which is approximately 9% shorter than Pyykkö's standard value for a Sb-Se single bond ( $2.56$  Å), approaching the length of a Sb=Se double bond ( $2.40$

Å)[17]. The Kohn-Sham orbitals of **45** show that the HOMO corresponds mainly to the selenium lone pair and the HOMO-1 to the Sb-Se  $\pi$ -bond (Figure 4-3). The WBI for Sb-Se in **45** is 1.41. An NBO analysis showed notable charge separation, with NBO charges of +0.999 on Sb and -0.788 on Se. Moreover, the NBO analysis revealed a large back-donation from the lone pair on Se into an empty orbital on Sb, suggesting that the terminal Sb-Se bond in **45** exhibits appreciable double-bond character, albeit that the electron density is strongly polarized toward selenium.

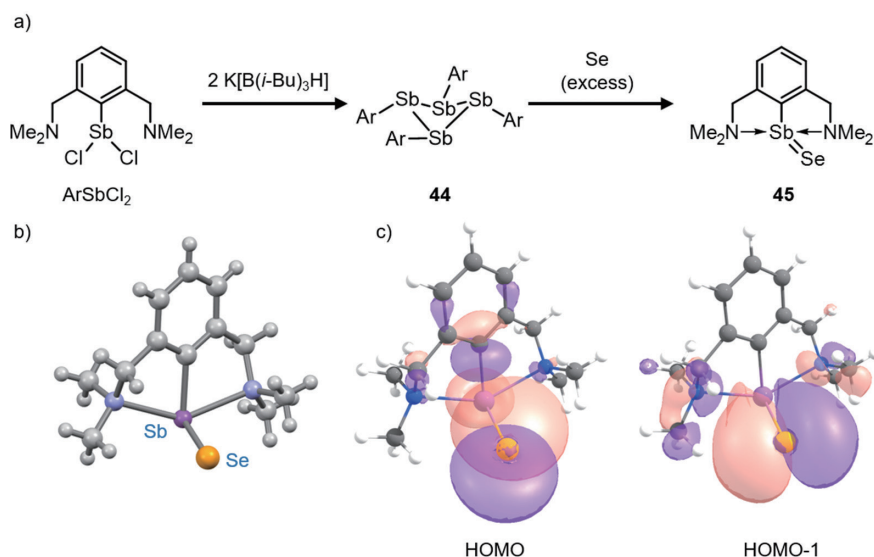


**Figure 4-3.** a) Synthesis of antimony(III) selenide **45** together with b) its crystal structure. c) Kohn-Sham frontier orbitals of **45**.

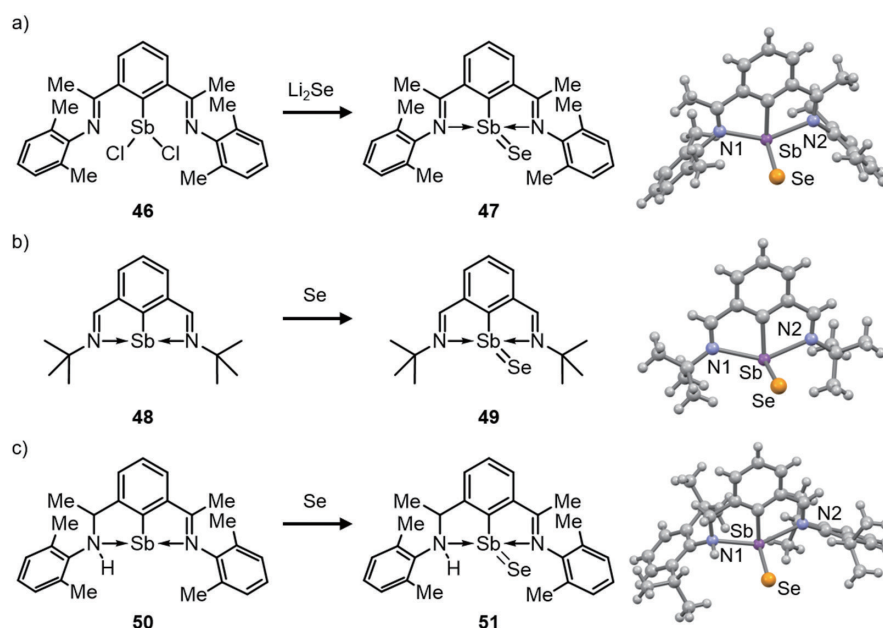


**Figure 4-4.** a) Synthesis and molecular structures of antimony(III) selenides **47**, **49**, **51**.

**Table 4-1.** | Comparisons among the antimony(III) selenides **45**, **47**, **49**, **51**.

	Sb-Se (Å)	C-Sb (Å)	N1-Sb (Å)	Sb-N2 (Å)	WBI <sup>a)</sup>	NBO charge <sup>a)</sup>		$\delta^{77}\text{Se}$	Ref.
						Sb	Se		
<b>45</b>	2.4396(6)	2.135(4)	2.461(3)	2.518(3)	1.376	1.023	-0.807	-197	[74]
<b>47</b>	2.4329(5)	2.124(3)	2.395(2)	2.393(2)	1.288	1.105	-0.779	-140	[75]
<b>49</b>	2.4498(6)	2.129(1)	2.549(1)	2.391(1)	1.242	1.099	-0.807	—	[76]
<b>51</b>	2.4371(5)	2.147(4)	2.536(3)	2.458(3)	1.271	1.096	-0.811	-17.3	[77]

a) Calculated at the B3PW91-D3(BJ)/SDD level for Sb, and the corresponding 6-31G(d) level for all other atoms.

To investigate the impact of donating N atoms on the character of the Sb–Se bond, the same research group synthesized antimony(III) selenides **47**[75], **49**[76], and **51**[77] with different NCN-pincer ligands (**Figure 4-4**). The reaction of antimony chloride **46** with  $\text{Li}_2\text{Se}$  yielded monomeric antimony(III) selenide **47**, while **49** and **51** were obtained from the reactions of elemental selenium with stibinidenes **48** and **50**, respectively. The  $^{77}\text{Se}$  NMR spectra of the antimony(III) selenides showed a single peak at  $-139.6$  ppm (**47**) and  $-17.3$  ppm (**51**), which are slightly downfield shifted from that of **45**; for **49**, no apparent signal was observed. The length of the Sb–Se bonds in **47** ( $2.4329(5)$  Å), **49** ( $2.4497(4)$  Å), and **51** ( $2.4371(5)$  Å) suggest double-bond character similar to that in **45**. NBO calculations were performed to analyze the bonding nature of the Sb–Se bond in these antimony(III) selenides, using a consistent level of calculations (**Table 4-1**). The results indicate that the terminal Sb–Se bonds in these antimony(III) selenides exhibit lower polarity and stronger double-bond character, influenced by the electron-donating strength of the pincer ligands.

#### 4.2. As(III) selenides

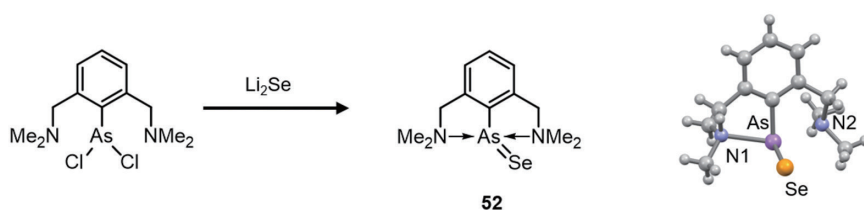


**Figure 4-5.** a) Synthesis and molecular structures of arsenic(III) selenide **52**.

Dostál and co-workers have also reported the synthesis of arsenic(III) selenide **52** using the same NCN-pincer ligand as for the synthesis of **45** (**Figure 4-5**)[78]. The reaction of a dichloroarsine with  $\text{Li}_2\text{Se}$  afforded arsenic(III) selenide **52** as a yellow solid. Its  $^{77}\text{Se}$  NMR spectrum showed a resonance at 0 ppm, which is downfield shifted compared to those of other antimony(III) selenides. The terminal As–Se bond ( $2.2736(5)$  Å) is significantly shorter than Pyykkö's standard value for an As–Se single bond ( $2.37$  Å), approaching the length of a typical As=Se double bond ( $2.21$  Å). The NBO charges on As and Se amount to  $+0.740$  and  $-0.645$ , respectively. The WBI of **52** ( $1.48$ ) is higher than those of antimony analogue **45** ( $1.41$ ).

### 5. Summary

In this mini-review, we have presented recent examples of isolated compounds that feature both selenium and heavier main-group elements in a  $\pi$ -bond, which are stabilized through kinetic and thermodynamic means using judiciously designed substituents. A notable characteristic of these species is the highly electrophilic nature of the selenium atom in the  $\pi$ -bond, due to the presence of a low-lying  $\pi^*$  orbital. This represents a captivating area of study within main-group element chemistry. Despite their remarkable properties, these intriguing compounds remain relatively unexplored, offering significant opportunities for further advancements across various research domains.

#### Acknowledgments:

The authors would like to thank Dr. U.F.J. Mayer from Mayer Scientific Editing (<http://www.mayerscientificediting.com/>) for his assistance during the preparation of this manuscript. Theoretical calculations in this manuscript have been performed with financial support by JSPS KAKENHI grants 21KK0094 and 23H01943 from MEXT (Japan), and JST CREST grant JPMJCR19R4.

#### References

- [1] (a) Guo T, Li Z, Bi L, Fan L, Zhang P. Recent advances in organic synthesis applying elemental selenium. *Tetrahedron* 2022; 112: 132752 (Article number). (b) Sonogo JM, de Diego SI, Szajnman SH, Gallo-Rodriguez C, Rodriguez JB. Organoselenium Compounds: Chemistry and Applications in Organic Synthesis. *Chem. Eur. J.* 2023; 29: e202300030 (Article number). (c) Reich HJ, Hondal RJ. Why Nature Chose Selenium. *ACS Chem. Biol.* 2016; 11: 821-841. (d) Singh FV, Wirth T. Selenium reagents as catalysts *Catal. Sci. Technol.* 2019; 9: 1073-1091.
- [2] (a) Ramírez-Gómez A, Gutiérrez-Hernández AI, Alvarado-Castillo MA, Toscano RA, Ortega-Alfaro MC, López-Cortés JG. Selenoamides as powerful scaffold to build imidazo[1,5-a]pyridines using a grinding protocol. *J. Organomet. Chem.* 2020; 919: 121315 (Article number). (b) Zhao Q, Li G, Nareddy P, Jordan F, Lalancette R, Szostak R, Szostak M. Structures of the Most Twisted Thioamide and Selenoamide: Effect of Higher Chalcogens of Twisted Amides on N–C(X) Resonance. *Angew. Chem. Int. Ed.* 2022; 61: e202207346 (Article number).
- [3] Wirth T. Organoselenium Chemistry: Synthesis and Reactions Wiley-VCH 2011.

- [4] Pitzer KS. Repulsive Forces in Relation to Bond Energies, Distances and Other Properties. *J. Am. Chem. Soc.* 1948; 70: 2140-2145.
- [5] West R, Fink MJ, Michl J. Tetramesityldisilene, a Stable Compound Containing a Silicon-Silicon Double-Bond. *Science* 1981; 214: 1343-1344.
- [6] Yoshifuji M, Shima I, Inamoto N, Hirotsu K, Higuchi T. Synthesis and Structure of Bis(2,4,6-tri-tert-butylphenyl) diphosphene: - Isolation of a True Phosphobenzene. *J. Am. Chem. Soc.* 1981; 103: 4587-4589.
- [7] Fischer RC, Power PP.  $\pi$ -Bonding and the Lone Pair Effect in Multiple Bonds Involving Heavier Main Group Elements: Developments in the New Millennium. *Chem. Rev.* 2010; 110: 3877-3923.
- [8] Okazaki R, Tokitoh N. Heavy Ketones, the Heavier Element Congeners of a Ketone. *Acc. Chem. Res.* 2000; 33: 625-630.
- [9] Suzuki H, Tokitoh N, Okazaki R, Nagase S, Goto M. Synthesis, Structure, and Reactivity of the First Kinetically Stabilized Silanethione. *J. Am. Chem. Soc.* 1998; 120: 11096-11105.
- [10] NBO calculations were performed using the NBO7 program; for details, see: Glendening ED, Landis CR, Weinhold F. NBO 7.0: New vistas in localized and delocalized chemical bonding theory. *J. Comput. Chem.* 2019; 40: 2234-2241.
- [11] Pachaly B, West R. Synthesis of a 1,3-Dioxo-2,4-diboretane, an Oxoborane Precursor. *J. Am. Chem. Soc.* 1985; 107: 2987-2988.
- [12] Tokitoh N, Ito M, Okazaki R. Formation and reactions of a thioxoborane, a novel boron-sulfur double-bond compound. *Tetrahedron Lett.* 1996; 37: 5145-5148.
- [13] Vidovic D, Moore JA, Jones JN, Cowley AH. Synthesis and Characterization of a Coordinated Oxoborane: Lewis Acid Stabilization of a Boron-oxygen Double bond. *J. Am. Chem. Soc.* 2005; 127: 4566-4567.
- [14] Franz D, Inoue S. Advances in the development of complexes that contain a group 13 element chalcogen multiple bond. *Dalton Trans.* 2016; 45: 9385-9397.
- [15] Martínez JP, Trzaskowski B. Structural and Electronic Properties of Boranes Containing Boron-chalcogen Multiple Bonds and Stabilized by Amido Imidazoline-2-imine Ligands. *Chem. Eur. J.* 2022; 28: e202103997 (Article number).
- [16] Wang H, Zhang J, Hu H, Cui C. Access to B=S and B=Se Double Bonds via Sulfur and Selenium Insertion into a B-H Bond and Hydrogen Migration. *J. Am. Chem. Soc.* 2010; 132: 10998-10999.
- [17] Pyykkö P, Atsumi M. Molecular Double-bond Covalent Radii for Elements Li-E112. *Chem. Eur. J.* 2009; 15: 12770-12779.
- [18] Ito M, Tokitoh N, Okazaki R. 1,3,2,4-Diselenastannoboretane, a novel selenium-containing four-membered boracycle: synthesis, structure and thermal cycloreversion into a selenoxoborane. *Chem. Commun.* 1998: 2495-2496.
- [19] Ito M, Tokitoh N, Okazaki R. Syntheses, structures, and properties of novel four-membered stannacycles, 1,3,2,4-dichalcogenastannoboretanes. *Phosphorus Sulfur Silicon Relat. Elem.* 1999; 150: 145-148.
- [20] Ito M, Tokitoh N, Kawashima T, Okazaki R. Formation of a borylene by photolysis of an overcrowded bis(methylseleno) borane. *Tetrahedron Lett.* 1999; 40: 5557-5560.
- [21] Conrad O, Jansen C, Krebs B. Boron-sulfur and Boron-selenium Compounds—from Unique Molecular Structural Principles to Novel Polymeric Materials. *Angew. Chem. Int. Ed.* 1998; 37: 3208-3218.
- [22] Amii H, Vranicar L, Gornitzka H, Bourissou D, Bertrand G. Radical-type Reactivity of the 1,3-Diboro-2,4-diphosphoniocyclobutane-1,3-diyl. *J. Am. Chem. Soc.* 2004; 126: 1344-1345.
- [23] Jaiswal K, Prashanth B, Ravi S, Shamasundar KR, Singh S. Reactivity of a dihydroboron species: synthesis of a hydroborenum complex and an expedient entry into stable thioxo- and selenoxo-boranes. *Dalton Trans.* 2015; 44: 15779-15785.
- [24] Dolati H, Denker L, Trzaskowski B, Frank R. Superseding  $\beta$ -Diketiminato Ligands: An Amido Imidazoline-2-imine Ligand Stabilizes the Exhaustive Series of B=X boranes (X=O, S, Se, Te). *Angew. Chem. Int. Ed.* 2021; 60: 4633-4639.
- [25] Liu S, Légaré MA, Hofmann A, Braunschweig H. A Boradiselenirane and a Boraditellurirane: Isolable Heavy Analogs of Dioxiranes and Dithiiranes. *J. Am. Chem. Soc.* 2018; 140: 11223-11226.
- [26] Liu S, Légaré MA, Auerhammer D, Hofmann A, Braunschweig H. The First Boron-tellurium Double Bond: Direct Insertion of Heavy Chalcogens into a Mn=B Double bond. *Angew. Chem., Int. Ed.* 2017; 56: 15760-15763.
- [27] Zhang X, Liu LL. Crystalline Neutral Aluminum Selenide/Telluride: Isoelectronic Aluminum Analogues of Carbonyls. *J. Am. Chem. Soc.* 2023; 145: 15729-15734.
- [28] Xu H, Kostenko A, Weetman C, Fujimori S, Inoue S. An Aluminum Telluride with a Terminal Al=Te Bond and its Conversion to an Aluminum Tellurocarbonate by CO<sub>2</sub> Reduction. *Angew. Chem., Int. Ed.* 2023; 62: e202216021 (Article number).
- [29] Anker MD, Coles MP. Isoelectronic Aluminium Analogues of Carbonyl and Dioxirane Moieties. *Angew. Chem., Int. Ed.* 2019; 58: 13452-13455.
- [30] Back TG, Barton DHR, Britten-Kelly MR, Guziec FS. Synthesis and properties of monomeric selenoketones. *J. Chem. Soc. Chem. Commun.* 1975; (13): 539.
- [31] Arya P, Boyer J, Carré F, Corriu R, Lanneau G, Lapasset J, Perrot M, Priou C. Formation and Reactivity of Silicon-sulfur and Silicon-selenium Double Bonds. The First X-ray Structure of a Silanethione. *Angew. Chem. Int. Ed.* 1989; 28: 1016-1018.
- [32] Matsumoto T, Tokitoh N, Okazaki R. Synthesis and Structure of the First Stable Germaneselone. *Angew. Chem. Int. Ed.* 1994; 33: 2316-2317.
- [33] Kuchta MC, Parkin G. Terminal Sulfoxo and Selenido Complexes of Tin: Syntheses and Structures of [n<sup>4</sup>-Me<sub>3</sub>taa]SnE (E = S, Se). *J. Am. Chem. Soc.* 1994; 116: 8372-8373.
- [34] Huo SC, Li Y, Zhang DX, Zhou Q, Yang Y, Roesky HW. Synthesis, Characterization, and Reaction of Digermylenes. *Chem. Asian J.* 2022; 17: e202200141 (Article number).
- [35] Soto-Montero T, Flores-Díaz N, Molina D, Soto-Navarro A, Lizano-Villalobos A, Camacho C, Hagfeldt A, Pineda LW. Dopant-free Hole-transport Materials with Germanium Compounds Bearing Pseudohalide and Chalcogenide Moieties for Perovskite Solar Cells. *Inorg. Chem.* 2020; 59: 15154-15166.
- [36] Siwath RK, Nagendran S. Germaester Complexes with a Ge(E)Ot-Bu Moiety (E = S or Se). *Organometallics* 2012; 31: 3389-3394.
- [37] Pineda LW, Jancik V, Oswald RB, Roesky HW. Preparation of LGe(Se)OH: A Germanium Analogue of a Selenocarboxylic Acid (L = HC[(CMe)(NAr)]<sub>2</sub>, Ar = 2,6-iPr<sub>2</sub>C<sub>6</sub>H<sub>3</sub>). *Organometallics* 2006; 25: 2384-2387.
- [38] Harris LM, Tam ECY, Cummins SJW, Coles MP, Fulton JR. The Reactivity of Germanium Phosphanides with Chalcogens. *Inorg. Chem.* 2017; 56: 3087-3094.
- [39] Siwath RK, Karwasara S, Sharma MK, Mondal S, Mukherjee G; Rajaraman G; Nagendran S. Reactivity of LGe-NR<sub>2</sub> and LGe(E)-NR<sub>2</sub> over LGe-Cl and LGe(E)-Cl toward Me<sub>3</sub>SiX (L = Aminotroponimate; NR<sub>2</sub> = N(SiMe<sub>3</sub>)<sub>2</sub>/NC<sub>4</sub>H<sub>4</sub>; E = S/Se; X = Br/CN). *Organometallics* 2016; 35: 429-438.
- [40] Ding Y, Ma Q, Roesky HW, Herbst-Irmer R, Usón I, Noltemeyer M, Schmidt HG. Synthesis, Structures, and Reactivity of Alkylgermanium(II) Compounds Containing a Diketiminato Ligand. *Organometallics* 2002; 21(24): 5216-5220.

- [41] Tam ECY, Harris LM, Borren ES, Smith JD, Lein M, Coles MP, Fulton JR. Why compete when you can share? Competitive reactivity of germanium and phosphorus with selenium. *Chem. Commun.* 2013; 49: 10278–10280.
- [42] Foley SR, Bensimon C, Richeson DS. Facile Formation of Rare Terminal Chalcogenido Germanium Complexes with Alkylamidinates as Supporting Ligands. *J. Am. Chem. Soc.* 1997; 119: 10359–10363.
- [43] Yadav D, Siwatch RK, Mukherjee G, Rajaraman G, Nagendran S. Use of Thio and Seleno Germanones as Ligands: Silver(I) Halide Complexes with Ge=E→Ag-I (E = S, Se) Moieties and Chalcogen-dependent Argentophilic Interaction. *Inorg. Chem.* 2014; 53: 10054–10059.
- [44] Ding Y, Ma Q, Roesky HW, Usón I, Noltemeyer M, Schmidt HG. Syntheses, structures and properties of [HC(CMeNAr)<sub>2</sub>Ge(E)X] (Ar = 2,6-*i*Pr<sub>2</sub>C<sub>6</sub>H<sub>3</sub>; E = S, Se; X = F, Cl). *Dalton Trans.* 2003: 1094–1098.
- [45] Ossig G, Meller A, Brönneke C, Müller O, Schäfer M, Herbst-Irmer R. Bis[(2-pyridyl)bis(trimethylsilyl)methyl-C,N]germanium(II): A Base-stabilized Germylene and the Corresponding Germanethione, Germaneselenone, and Germanetellurone. *Organometallics* 1997; 16: 2116–2120.
- [46] Karwasara S, Siwatch RK, Jha CK, Nagendran S. Aminotroponiminatosilathio- and Siloxygermylenes: Reactivity Comparison. *Organometallics* 2015; 34: 3246–3254.
- [47] Karwasara S, Sharma MK, Tripathi R, Nagendran S. Synthesis and Reactivity of *N*-Aminotroponiminatogermylene-pyrrole and its Derivatives. *Organometallics* 2013; 32: 3830–3836.
- [48] Barman MK, Nembenna S. Mixed guanidinato-amido Ge(IV) and Sn(IV) complexes with Ge=E (E = S, Se) double bond and SnS<sub>4</sub>, Sn<sub>2</sub>Se<sub>2</sub> rings. *RSC Adv.* 2016; 6: 338–345.
- [49] Prashanth B, Singh S. Concise access to iminophosphonamide stabilized heteroleptic germylenes: chemical reactivity and structural investigation. *Dalton Trans.* 2016; 45: 6079–6087.
- [50] Leung WP, Chong KH, Wu YS, So CW, Chan HS, Mak TCW. Synthesis of Chalcogeno[3-(pyrid-2-yl)-1-azaallyl]germanium Complexes. *Eur. J. Inorg. Chem.* 2006; 2006: 808–812.
- [51] Kocsor TG, Matioszek D, Nemeş G, Castel A, Escudé J, Petrar PM, Saffon N, Haiduc I. Chalcogeno[bis(phosphaalkenyl)] Germanium and Tin Compounds. *Inorg. Chem.* 2012; 51: 7782–7787.
- [52] Mahawar P, Shukla P, Chandra Joshi P, Singh D, Kumar H, Mukherjee G, Nagendran S. Air and water stable germacarbonyl compounds. *Chem. Sci.* 2022; 13: 12382–12388.
- [53] Hossain J, Parvin N, Shah BK, Khan S. Four-Coordinate Germylene and Stannylene and their Reactivity towards Se & Te. *Z. Anorg. Allg. Chem.* 2022; 648: e202200164 (Article number).
- [54] Kim HS, Jung EA, Han SH, Han JH, Park BK, Kim CG, Chung TM. Germanium Compounds Containing Ge=E Double Bonds (E = S, Se, Te) as Single-source Precursors for Germanium Chalcogenide Materials. *Inorg. Chem.* 2017; 56: 4084–4092.
- [55] Pineda LW, Jancik V, Roesky HW, Herbst-Irmer R. Germacarbonyl Acid: An Organic-acid Analogue Based on a Heavier Group 14 Element. *Angew. Chem. Int. Ed.* 2004; 43: 5650–5652.
- [56] Ding Y, Ma Q, Roesky HW, Usón I, Noltemeyer M, Schmidt HG. Syntheses, structures and properties of [HC(CMeNAr)<sub>2</sub>Ge(E)X] (Ar = 2,6-*i*Pr<sub>2</sub>C<sub>6</sub>H<sub>3</sub>; E = S, Se; X = F, Cl). *Dalton Trans.* 2003; 1094–1098.
- [57] Bordwell FG. Equilibrium acidities in dimethyl sulfoxide solution. *Acc. Chem. Res.* 1988; 21: 456–463.
- [58] Tan G, Xiong Y, Inoue S, Enthaler S, Blom B, Epping JD, Driess M. From elusive thio- and selenosilanoic acids to copper(I) complexes with intermolecular Si=E→Cu-O-Si coordination modes (E = S, Se). *Chem. Commun.* 2013; 49: 5595–5597.
- [59] Xiong Y, Yao S, Driess M. Silicon Analogues of Carboxylic Acids: Synthesis of Isolable Silanoic Acids by Donor-acceptor Stabilization. *Angew. Chem. Int. Ed.* 2010; 49: 6642–6645.
- [60] Sarkar D, Weetman C, Dutta S, Schubert E, Jandl C, Koley D, Inoue S. *N*-Heterocyclic Carbene-stabilized Germa-acylium Ion: Reactivity and Utility in Catalytic CO<sub>2</sub> Functionalizations. *J. Am. Chem. Soc.* 2020; 142: 15403–15404.
- [61] Burchert A, Müller R, Yao S, Schattnerberg C, Xiong Y, Kaupp M, Driess M. Taming Silicon Congeners of CO and CO<sub>2</sub>: Synthesis of Monomeric Si<sup>II</sup> and Si<sup>IV</sup> Chalcogenide Complexes. *Angew. Chem. Int. Ed.* 2017; 56: 6298–6301.
- [62] Sugamata K, Hashizume D, Suzuki Y, Sasamori T, Ishii S. Synthesis and Structure of a Stable Bis(methylene)- $\lambda^4$ -sulfane. *Chem. Eur. J.* 2018; 24: 6922–6926.
- [63] Sugamata K, Urao Y, Minoura M. A stable bis(methylene)- $\lambda^4$ -selane with a >C=Se=C< bond containing Se(IV). *Chem. Commun.* 2019; 55: 8254–8257.
- [64] Sugamata K, Asakawa T, Urao Y, Minoura M. Tellurium-Centered Bent Allenes: Synthesis, Characterization, and Reactivity. *Inorg. Chem.* 2022; 61: 17641–17645.
- [65] Sugamata K, Sasamori T. 2-Heteroallenes. *Dalton Trans.* 2023; 52: 9882–9892.
- [66] Cullen ER, Guziec FS, Murphy CJ, Wong TC, Andersen KK. Selenium-77 NMR Studies of Some Organoselenium Compounds Containing-selenium Double Bonds. *J. Am. Chem. Soc.* 1981; 103: 7055–7057.
- [67] Maaninen T, Laitinen R, Chivers T. A monomeric selenium(IV) diimide and a dimeric seleninylamine. *Chem. Commun.* 2002; 1812–1813.
- [68] Sugamata K, Urao Y, Minoura M. (Thio)(silyl)carbene and (seleno)(silyl)carbene gold(I) complexes from the reaction of bis(methylene)- $\lambda^4$ -sulfane and bis(methylene)- $\lambda^4$ -selane with chloro(dimethylsulfide)gold(I). *Dalton Trans.* 2020; 49: 7688–7691.
- [69] Heimann S, Bläser D, Wölper C, Haack R, Jansen G, Schulz S. The bonding situation in triethylchalcogenostboranes - polarized single bonds vs. double bonds. *Dalton Trans.* 2014; 43: 14772–14777.
- [70] Tokitoh N, Arai Y, Sasamori T, Okazaki R, Nagase S, Uekusa H, Ohashi Y. A Unique Crystalline-state Reaction of an Overcrowded Distibene with Molecular Oxygen: The First Example of a Single Crystal to a Single Crystal Reaction with an External Reagent. *J. Am. Chem. Soc.* 1998; 120: 433–434.
- [71] Tokitoh N, Sasamori T, Okazaki R. Synthesis of the first stable selenadistibirane and its molecular structure. *Chem. Lett.* 1998; 27: 725–726.
- [72] Sasamori T, Mieda E, Tokitoh N. Chalcogenation reactions of overcrowded doubly bonded systems between heavier group 15 elements. *Bull. Chem. Soc. Jpn.* 2007; 80: 2425–2435.
- [73] Dostál L, Jambor R, Růžička A, Lyčka A, Brus J, de Proft F. Synthesis and Structure of Organoantimony(III) Compounds Containing Antimony–Selenium and –Tellurium Terminal Bonds. *Organometallics* 2008; 27: 6059–6062.
- [74] Dostál L, Jambor R, Růžička A, Holeček J. Syntheses and Structures of Ar<sub>3</sub>Sb<sub>5</sub> and Ar<sub>4</sub>Sb<sub>4</sub> Compounds (Ar = C<sub>6</sub>H<sub>3</sub>-2,6-(CH<sub>2</sub>NMe<sub>2</sub>)<sub>2</sub>). *Organometallics* 2008; 27: 2169–2171.
- [75] Šimon P, Jambor R, Růžička A, Lyčka A, De Proft F, Dostál L. Monomeric organoantimony(III) sulphide and selenide with terminal Sb-E bond (E = S, Se). Synthesis, structure and theoretical consideration. *Dalton Trans.* 2012; 41: 5140–5143.
- [76] Ganesamoorthy C, Wölper C, Dostál L, Schulz S. Syntheses and structures of N,C,N-stabilized antimony chalcogenides. *J. Organomet. Chem.* 2017; 845: 38–43.
- [77] Zechovský J, Kertész E, Kerslake V, Hejda M, Mikysek T, Erben M, Růžička A, Jambor R, Benkó Z, Dostál L. Exploring Differences Between Bis(aldimino)- and Amino-aldimino-*N,C,N*-pincer-stabilized Pnictinidenes: Limits of Synthesis, Structure, and Reversible Tautomerization-controlled Oxidation. *Organometallics* 2022; 41: 2535–2550.
- [78] Vrána J, Jambor R, Růžička A, Lyčka A, De Proft F, Dostál L. *N*→*As* intramolecularly coordinated organoarsenic(III) chalcogenides: Isolation of terminal As–S and As–Se bonds. *J. Organomet. Chem.* 2013; 723: 10–14.

# Mechanisms of Selenoprotein P translation regulation by long noncoding RNA

Yuichiro Mita\*, Yukihiro Inenaga, Noriko Noguchi

Systems Life Sciences Laboratory, Graduate School of Life and Medical Sciences, Doshisha University

## Abstract

Selenium (Se) is one of the essential trace elements in the body. Se is present in proteins in the form of selenocysteine (Sec), in which the sulfur of cysteine (Cys) is replaced by Se. These proteins are referred to as selenoproteins. There are 25 selenoproteins in the human genome, and they play important roles in various physiological functions, including as an antioxidant and in the synthesis of thyroid hormones. Sec is inserted into selenoproteins using the Sec insertion sequence (SECIS), which is located in the 3' untranslated region. We have identified an antisense long noncoding RNA, *CCDC152*, which binds mRNA of selenoprotein P (SELENOP), one of the plasma selenoproteins. *CCDC152* inhibits the binding of SECIS binding protein 2 (SBP2), which is a key protein for selenoprotein translation, to SECIS by direct interaction with *SELENOP* mRNA. Inhibiting the formation of the SBP2 and SECIS complex by *CCDC152* reduces the binding of ribosomes to *SELENOP* mRNA and suppresses the translation step of SELENOP. As a result, *CCDC152* causes a decrease in SELENOP protein levels independent of *SELENOP* mRNA levels. No impact was observed on the protein and mRNA expression levels of other selenoproteins. This review describes the mechanism of SELENOP protein suppression by *CCDC152*.

**Keywords:** Selenoprotein, SELENOP, SECIS, long noncoding RNA, antisense RNA

**Statements about COI:** The authors declare no conflict of interest associated with this manuscript.

## \*Correspondence:

Yuichiro Mita

Systems Life Sciences Laboratory, Graduate School of Life and Medical Sciences, Doshisha University  
1-3 Tatara Miyakodani, Kyotanabe-shi, Kyoto 610-0394  
Japan

**Tel ;** +81 775 65 6258

**E-mail ;** [ymita@mail.doshisha.ac.jp](mailto:ymita@mail.doshisha.ac.jp)

Received: November 29, 2024

Accepted: January 16, 2025

Released online: February 28, 2025

## 1. Introduction

Selenium transport protein selenoprotein P (SELENOP) contains the essential trace element selenium (Se) in the form of selenocysteine (Sec), which is an amino acid in which the sulfur of cysteine is replaced by Se. It has been reported that SELENOP is increased in the blood of patients with type 2 diabetes mellitus (T2DM). Excess SELENOP induces insulin resistance and impairs insulin secretion, resulting in aggravation of T2DM [1,2]. Therefore, SELENOP is expected to become a new therapeutic target of T2DM.

Selenoproteins, including SELENOP, are synthesized by a unique translation mechanism. In the 3' untranslated region (UTR) of the mRNA encoding selenoprotein, there



This work is licensed under a Creative Commons Attribution 4.0 International License.

©2025 THE AUTHORS. [DOI](https://doi.org/10.11299/metallomicsresearch.MR202412) <https://doi.org/10.11299/metallomicsresearch.MR202412>

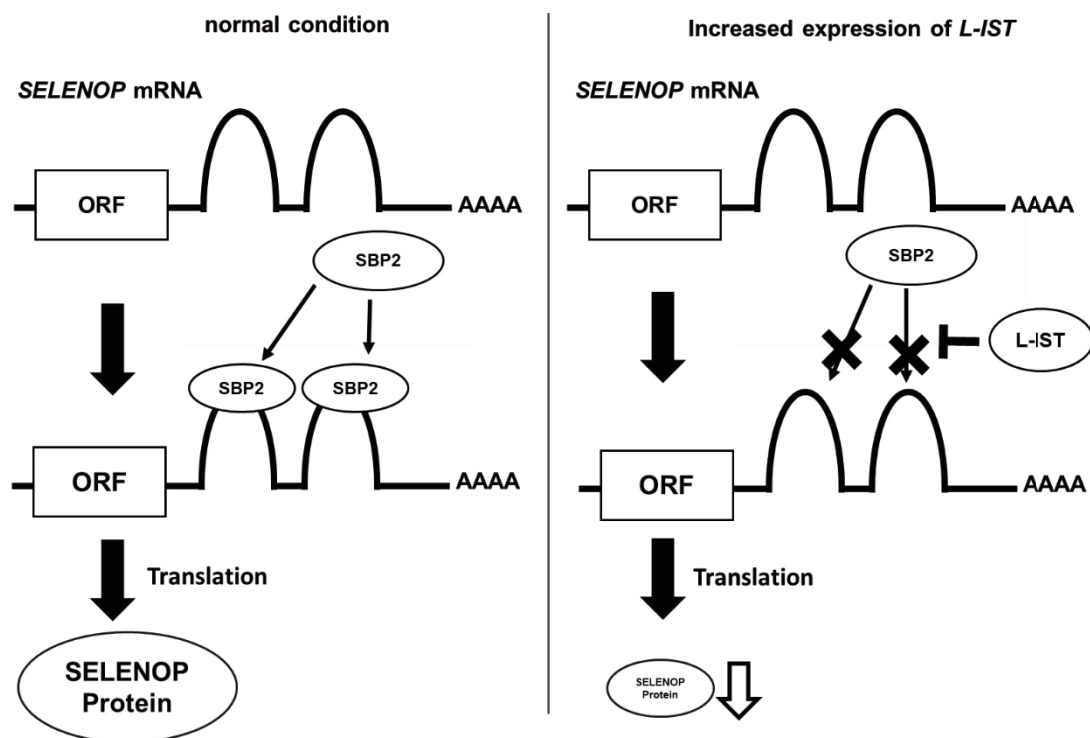


**Figure** | Schematic diagram of the mechanism of SELENOP translation suppression by *CCDC152/L-IST* in hepG2 cells. *CCDC152/L-IST* specifically suppresses SELENOP translation by inhibiting the binding of SBP2 to SECIS of SELENOP mRNA.  
 ORF: Open Reading Frame.  
 SBP2: SECIS Binding Protein 2.

is a Sec insertion sequence (SECIS) forming a stable loop structure. Sec-tRNAs, specific elongation factor eEFSec, and SECIS binding protein 2 (SBP2) bind to SECIS and form a complex. This complex allows for the insertion of Sec into the UGA codon, which is usually recognized as a termination codon [3]. In the process of analyzing the SECIS sequence, we identified a gene of unknown function, *coiled-coil domain-containing protein 152* (*CCDC152*), which has a complementary sequence to the SECIS-containing 3' UTR of *SELENOP* mRNA. The overexpression of *CCDC152* in human hepatocellular carcinoma-derived HepG2 cells expressing SELENOP causes a decrease in protein levels without altering *SELENOP* mRNA levels. Since *CCDC152* is mainly found in the nucleus, the *CCDC152* protein was not detectable when overexpressed in HEK293 cells, which do not express *CCDC152*. In addition, *CCDC152* RNA binds to *SELENOP* mRNA; hence, it is possible that *CCDC152* functions as an RNA. In HepG2 cells overexpressing *CCDC152*, the binding of *SELENOP* mRNA to ribosomes and SBP2 was decreased [4]. Based on these functions, we named *CCDC152* a long noncoding RNA inhibitor of selenoprotein P translation (*L-IST*) (Figure).

In this review, we describe the translation mechanism of selenoprotein in the presence of SECIS and explain the action of *L-IST* that we found. We also describe *L-IST* as a new therapeutic target for reducing the increase of T2DM.

## 2. The mechanisms of selenocysteine insertion

Se deficiency is known to cause severe cardiomyopathy and increase the incidence of cancer [5,6]. There are 25 selenoproteins in the human genome, and they play important roles in various physiological functions. Selenoproteins include antioxidant proteins, such as glutathione peroxidase (GPx) and thioredoxin reductase (TrxR), and proteins related to thyroid hormone synthesis, such as iodothyronine deiodinase. Thus, selenoproteins play an important role in the protection of cells from oxidative stress and in the process of energetic metabolism. The insertion of Sec into proteins occurs during the translation phase, and Sec has also been called the "21st amino acid that can be

translated" [7]. The complex of SBP2 and Sec-tRNA<sup>Sec</sup> binds to a hairpin structure called SECIS, which is essential for Sec translation, and Sec is inserted into the UGA codon [8]. The strength of the binding between SECIS and SBP2 depends on the 3D structure of SECIS [9]. Therefore, it has been suggested that the efficiency of selenoprotein translation is dependent on the 3D structure and not the SECIS sequence [9].

### 3. Identification and functional analysis of *CCDC152*

We compared the SECIS sequences of mRNAs encoding 25 human selenoproteins in SelenoDB 2.0 (<http://selenodb.crg.eu>) [10] with the sequences of all transcripts using BLAST analysis. We found a novel gene, *CCDC152*, containing an antisense sequence to the SECIS sequence of the *SELENOP*. *CCDC152* contains a part of the coding sequence of *SELENOP* and an antisense sequence against the 3' UTR region containing the SECIS sequence, and both sequences were completely complementary to each other. The results of the homology analysis of *CCDC152* show that it is present from fish to mammals.

Analysis of *CCDC152* expression levels in various cultured cells revealed that *CCDC152* was expressed in human neuroblastoma SH-SY5Y cells, glioma U87MG cells, and human T lymphocytoma Jurkat cells, but only slightly in hepatocarcinoma-derived HepG2 cells, which express and secrete *SELENOP*. Comparison of expression levels in various tissues in mice revealed that *SELENOP* was expressed mainly in the liver, small intestine, and kidney and that *CCDC152* was most highly expressed in the testes and also expressed in the liver, kidney, and white fat tissue. In high-fat, high-sucrose diet-induced diabetic model mice, there was an increase in *SELENOP* expression in the liver, while *CCDC152* in the liver tended to be decreased.

*CCDC152* has a complementary sequence to *SELENOP* mRNA; therefore, we overexpressed *CCDC152* in HepG2 cells expressing *SELENOP* and examined its effect on *SELENOP* protein expression. We observed a reduction in *SELENOP* protein levels and no change in mRNA levels. The overexpression of *CCDC152* and *SELENOP* mRNA in HEK293 cells, which express neither *CCDC152* nor *SELENOP* mRNA, also caused a decrease in *SELENOP* protein levels without a change in mRNA levels, as observed in HepG2 cells. Hence, the mRNA level-independent decrease in *SELENOP* protein levels by *CCDC152* was not specific to a particular cell type. Next, we examined the effect of *CCDC152* on other selenoproteins. There were no changes in the protein and mRNA levels of selenoproteins such as Gpx4 and TrxR1 other than *SELENOP*, suggesting that *CCDC152* specifically affects the amount of *SELENOP* protein and mRNA.

There are more than 200 members of the CCDC protein family. It has been reported that CCDC80 and CCDC134 inhibit the activity of ERK [11, 12] which protein suppresses *SELENOP* transcription by promoting FoxO3a translocation out of the nucleus. Therefore, CCDC80 and CCDC134 may enhance the transcription of *SELENOP*. On the other hand, the suppression of *SELENOP* protein expression by *CCDC152* overexpression is not involved in transcriptional regulation. Therefore, it is likely that *SELENOP* protein levels are regulated by a different mechanism than the previously known CCDC protein family. Because of the presence of an open reading frame (ORF) between bases 71 and 835 in the 5' region of *CCDC152*, we investigated whether the CCDC152 protein or RNA could reduce the protein content of *SELENOP*. To validate protein translation from the ORF, we inserted an HA-tag at the 3' end of the ORF. However, western blotting with an antibody against the HA-tag did not detect the CCDC152 encoding protein. Next, we analyzed the effect of the *CCDC152* deletion mutant on the *SELENOP* protein. The *CCDC152* ( $\Delta$ 500) mutant, in which up to 500 bases were deleted from the 5' end, including the putative initiation ATG codon, retained the ability to suppress *SELENOP* protein expression. However, the *CCDC152* ( $\Delta$ 600) mutant, in which up to 600 bases were deleted from the 5' end, did not have the same suppressive effect. Therefore, the *SELENOP*-reducing effect of *CCDC152* is possibly through its action not as a protein but as an RNA.

Next, we focused on the translation step, with particular emphasis on the step involved in the binding of mRNA to ribosomes. Our results showed that *CCDC152* exerts an inhibitory effect on protein synthesis in a manner independent of mRNA levels. Polysome analysis was performed to evaluate the binding of *SELENOP* mRNA to ribosomes. We found that the number of ribosome-bound *SELENOP* mRNAs was markedly diminished in *CCDC152*-overexpressing HepG2 cells. In contrast, *Gpx4* mRNA, another selenoprotein mRNA, did not show a significant

change in its binding to ribosomes when *CCDC152* was overexpressed.

Subsequently, we investigated the binding of *SELENOP* mRNA to SBP2, which is an essential factor for Sec insertion via SECIS, using an RNA pull-down assay. We found that the overexpression of *CCDC152* reduced the binding affinity of *SELENOP* mRNA to SBP2. Thus, these results showed that *CCDC152* inhibits the translational step of *SELENOP* mRNA, especially the binding of SBP2 to SECIS. Based on these functions, we named *CCDC152* a long noncoding RNA inhibitor of selenoprotein P translation [4].

#### 4. Epigallocatechin gallate increases *L-IST* expression and decreases *SELENOP* protein

It has been reported that elevated blood *SELENOP* levels are associated with T2DM [1] and pulmonary hypertension [13]. The development of a method to decrease *SELENOP* would be a novel therapeutic strategy for those diseases. Therefore, we searched for substances that increase *L-IST*. We found that epigallocatechin gallate (EGCg), which is known as the main ingredient of green tea with an antidiabetic effect, increased *L-IST* and decreased *SELENOP* protein levels without changing *SELENOP* mRNA levels. Based on these results, we administered EGCg to mice and found that *L-IST* was increased in the liver of EGCg-treated mice, but *SELENOP* mRNA levels were unchanged. Mice with increased *L-IST* by EGCg also had decreased blood levels of *SELENOP* and blood glucose levels, indicating that *L-IST* could be a promising therapeutic candidate agent for T2DM treatment [4].

#### 5. Translation regulation mechanisms by noncoding RNAs

Most of the intergenic regions in the genome have been called “junk regions,” which are presumed to lack any functional significance. However, in recent years, many noncoding RNAs have been found in these junk regions, and their functions have been clarified. The analysis of noncoding RNAs involved in the regulation of protein quantity has been a prominent area of research.

Protein reduction by short RNAs of approximately 20 mer, such as siRNA and miRNA, is mediated by the AGO family protein [14]. In contrast, different mechanisms of translation regulation by long noncoding RNAs have been reported for different types of RNA. *Antisense BASE-1* has been demonstrated to increase *BASE-1* protein levels by causing mRNA stabilization [15]. Long noncoding RNAs containing *SINEB2* sequences promote the translation of target mRNAs by recruiting ribosomes [16]. Competing endogenous RNAs (ceRNAs) are long noncoding RNAs that do not act directly on mRNAs. These ceRNAs trap miRNAs, thereby inhibiting the binding of miRNAs to their target mRNAs and increasing protein levels [17]. The *L-IST* has a complementary sequence to the SECIS sequence of *SELENOP* mRNA. *L-IST* appears to bind directly to *SELENOP* mRNA, inhibiting the binding of SBP2 to SECIS and of *SELENOP* mRNA to the ribosome. The mechanism of translational suppression of *SELENOP* by *L-IST* differs from the previously reported mechanisms of regulation of protein levels by long noncoding RNAs such as *antisense BASE-1*. However, Long-noncoding RNAs that bind directly to mRNAs, and inhibit the binding of SECIS to SECIS binding proteins such as SBP2 have not been reported. Therefore, the translational suppression of *SELENOP* by *L-IST* is considered to be a novel function of a noncoding RNA.

#### 6. Effects of antisense RNA on selenoproteins other than *SELENOP*

We are currently analyzing the functional sequence of *L-IST* and its effect on the translation of other selenoproteins. We have not yet completely determined the precise functional sequences of *L-IST*. Nevertheless, we have identified the functional sequences that are present in both the 5' and 3' regions and not only sequences complementary to *SELENOP* mRNA [4]. Furthermore, it is becoming obvious that the complementary sequence between *L-IST* and *SELENOP* mRNA is not necessary for the suppression of *SELENOP* mRNA translation by *L-IST*. We replaced the complementary sequence region to *SELENOP* mRNA in *L-IST* with the sequence complementary to the 3' UTR in other selenoprotein mRNA. The available data are preliminary, but they suggest that RNAs containing antisense sequences of 3' UTR may also suppress protein levels of other selenoproteins as well as *SELENOP*. In the future, we will confirm the reproducibility of the study and analyze the effect of antisense long noncoding RNAs on the translation of mRNAs containing SECIS.

## Conclusion

We identified a novel noncoding RNA, *CCDC152/L-IST*, with a sequence complementary to the SECIS sequence of *SELENOP* mRNA. *L-IST* reduced *SELENOP* protein levels by specifically inhibiting the translation step of *SELENOP* mRNA (Figure) [4]. *SELENOP* was originally studied as a Se transport protein, but recent studies have shown that excess *SELENOP* is associated with many diseases, such as T2DM [1,2]. As *L-IST* can specifically decrease *SELENOP* protein levels, therapies that increase *L-IST* may be promising for treating several diseases in patients with high *SELENOP* levels.

## Acknowledgments

The research on *CCDC152/L-IST* described in this manuscript was conducted in collaboration with Professor Yoshiro Saito (Tohoku University) and Professor Toshifumi Inada (Tokyo University). We would like to take this opportunity to thank them.

## References

- [1] Mita Y, Nakayama K, Inari S, Nishito Y, Yoshioka Y, Sakai N, Sotani K, Nagamura T, Kuzuhara Y, Inagaki K, Iwasaki M, Misu H, Ikegawa M, Takamura T, Noguchi N, Saito Y. Selenoprotein P-neutralizing antibodies improve insulin secretion and glucose sensitivity in type 2 diabetes mouse models. *Nature Commun.* 2017; 8: 1658.
- [2] Misu H, Takamura T, Takayama H, Hayashi H, Matsuzawa-Nagata N, Kurita S, Ishikura K, Ando H, Takeshita Y, Ota T, Sakurai M, Yamashita T, Mizukoshi E, Yamashita T, Honda M, Miyamoto K, Kubota T, Kubota N, Kadowaki T, Kim HJ, Lee IK, Minokoshi Y, Saito Y, Takahashi K, Yamada Y, Takakura N, Kaneko S. A liver-derived secretory protein, selenoprotein P, causes insulin resistance. *Cell Metab.* 2010; 12: 483-95.
- [3] Bulteau AL, Chavatte L. Update on Selenoprotein Biosynthesis. (2015) *Antioxid Redox Signal.* 2015; 23: 775-94.
- [4] Mita Y, Uchida R, Yasuhara S, Kishi K, Hoshi T, Matsuo Y, Yokooji T, Shirakawa Y, Toyama T, Urano Y, Inada T, Noguchi N, Saito Y. Identification of a novel endogenous long non-coding RNA that inhibits selenoprotein P translation. *Nucleic Acids Res.* 2021; 49: 6893-6907.
- [5] Duntas LH, Benavente S. Selenium: an element for life. *Endocrine.* 2015; 48: 756-75.
- [6] M. P. Rayman, Selenium and human health, *Lancet.* 2012; 379: 1256-68.
- [7] Vindry C, Ohlmann T, Chavatte L. Translation regulation of mammalian selenoproteins. *Biochim Biophys Acta. Gen. Subj.* 2018; S0304-4165, 30142-9.
- [8] Low SC, Grundner-Culemann E, Harney JW, Berry MJ. SECIS-SBP2 interactions dictate selenocysteine incorporation efficiency and selenoprotein hierarchy. *EMBO J.* 2000; 19: 6882-90.
- [9] Donovan J, Copeland PR. Selenocysteine insertion sequence binding protein 2L is implicated as a novel post-transcriptional regulator of selenoprotein expression. *PLoS One.* 2012; 7: e35581.
- [10] Romagné F, Santesmasses D, White L, Sarangi GK, Mariotti M, Hübler R, Weihmann A, Parra G, Gladyshev VN, Guigó R, Castellano S. SelenoDB 2.0: annotation of selenoprotein genes in animals and their genetic diversity in humans. *Nucleic Acids Res.* 2014; 42: D437-D443.
- [11] Liu Z, Yan W, Liu S, Liu Z, Xu P, Fang W. Regulatory network and targeted interventions for CCDC family in tumor pathogenesis. *Cancer Lett.* 2023; 565: 216225.
- [12] Huang J, Shi T, Ma T, Zhang Y, Ma X, Lu Y, Song Q, Liu W, Ma D, Qiu X. CCDC134, a novel secretory protein, inhibits activation of ERK and JNK, but not p38 MAPK. *Cell Mol Life Sci.* 2008; 65: 338-49.
- [13] Kikuchi N, Satoh K, Kurosawa R, Yaoita N, Elias-Al-Mamun M, Siddique MAH, Omura J, Satoh T, Nogi M, Sunamura S, Miyata S, Saito Y, Hoshikawa Y, Okada Y, Shimokawa H. Selenoprotein P Promotes the Development of Pulmonary Arterial Hypertension. *Circulation.* 2018; 138: 600-623.
- [14] Meister G, Landthaler M, Patkaniowska A, Dorsett Y, Teng G, Tuschl T. Human Argonaute2 Mediates RNA Cleavage Targeted by miRNAs and siRNAs. *Molecular Cell.* 2004; 15(2): 185-197.
- [15] Faghihi MA, Modarresi F, Khalil A, Wood D, Sahagan B, Morgan T, Finch C, St Laurent G 3rd, Kenny P, Wahlestedt C. Expression of a noncoding RNA is elevated in Alzheimer's disease and drives rapid feed-forward regulation of beta-secretase. *Nature Med.* 2008; 14: 723-30.
- [16] Carrieri C, Cimatti L, Biagioli M, Beugnet A, Zucchelli S, Fedele S, Pesce E, Ferrer I, Collavin L, Santoro C, Forrest A, Carninci P, Biffo S, Stupka E, Gustincich S. Long non-coding antisense RNA controls Uchl1 translation through an embedded SINEB2 repeat. *Nature.* 2012; 491: 454-7.
- [17] Tay Y, Kats L, Salmena L, Weiss D, Tan S, Ala U, Karreth F, Poliseno L, Provero P, Cunto F, Lieberman J, Rigoutsos I, Pandolfi P. Coding-independent regulation of the tumor suppressor PTEN by competing endogenous mRNAs. *Cell.* 2011; 147: 344-57.

## Overview of the biochemistry and biology of selenoneine

Takuya Seko<sup>1,\*</sup>, Yumiko Yamashita<sup>1</sup>, Michiaki Yamashita<sup>2</sup>

<sup>1</sup> Fisheries Technology Institute, Japan Fisheries Research and Education Agency

<sup>2</sup> National Fisheries University, Japan Fisheries Research and Education Agency

### Abstract

Selenoneine (SEN) is one of the major organic selenium (Se) species present in fish and was initially identified in the blood of bluefin tuna. SEN is a selenium analog of ergothioneine (EGT), which is well known as a radical scavenger, with SEN exhibiting greater radical scavenging capacity than EGT. SEN is expected to have beneficial health functions due to its radical scavenging capacity, and elucidation of its biochemical and physiological functions *in vivo* may reveal additionally unknown functions. Herein, we systematically review previous SEN studies and comprehensively discuss SEN concentrations observed in various organisms including humans. Moreover, we describe the chemical, biochemical and biological properties of SEN. The current limitations of the research on SEN are shown to indicate the future studies required on understanding SEN.

**Keywords:** selenoneine, ergothioneine, Se-methylselenoneine, OCTN1, erythrocyte, melanin, NAFLD

**Statements about COI:** The authors declare no conflict of interest associated with this manuscript.

### Abbreviations:

**SEN;** selenoneine

**MeSEN;** Se-methylselenoneine

**GPx;** glutathione peroxidase

**OCTN1;** organic cation/carnitine transporter-1

**EGT;** ergothioneine

**SEN-seleninic acid;** selenoneine seleninic acid

**SelP;** selenoprotein P

**NAFLD;** non-alcoholic fatty liver disease

### 1. Introduction

Selenium (Se) is an essential trace element in animals, including humans, and plays an important role in the body's redox system. Most animals consume Se in their diet as selenocysteine (SeCys) or selenomethionine (SeMet). In 2010, Yamashita and Yamashita found a novel organic selenium compound in the erythrocytes of bluefin tuna and identified it as selenoneine (SEN, **Fig. 1a, b**) [1]. Even before the identification of SEN, tunas were known to contain high levels of Se. Yamashita and Yamashita found that the blood and dark muscle of bluefin tuna contained high levels of Se, and in 1993 they started purifying the Se compound, which was thought to be an unknown Se species. They separated an extract from the dark muscle of tuna using gel filtration chromatography and the Se compound was not a protein containing Se

#### \*Correspondence:

Takuya Seko,

Fisheries Technology Institute, Japan Fisheries Research and Education Agency, Kanazawa, Yokohama, Kanagawa 236-8648, Japan

**Tel ;** +81 45 788 7665

**E-mail ;** seko\_takuya65@fra.go.jp

Received: December 05, 2024

Accepted: January 19, 2025

Released online: February 28, 2025



This work is licensed under a Creative Commons Attribution 4.0 International License.

©2025 THE AUTHORS. [DOI](https://doi.org/10.11299/metallomicsresearch.MR202414) <https://doi.org/10.11299/metallomicsresearch.MR202414>

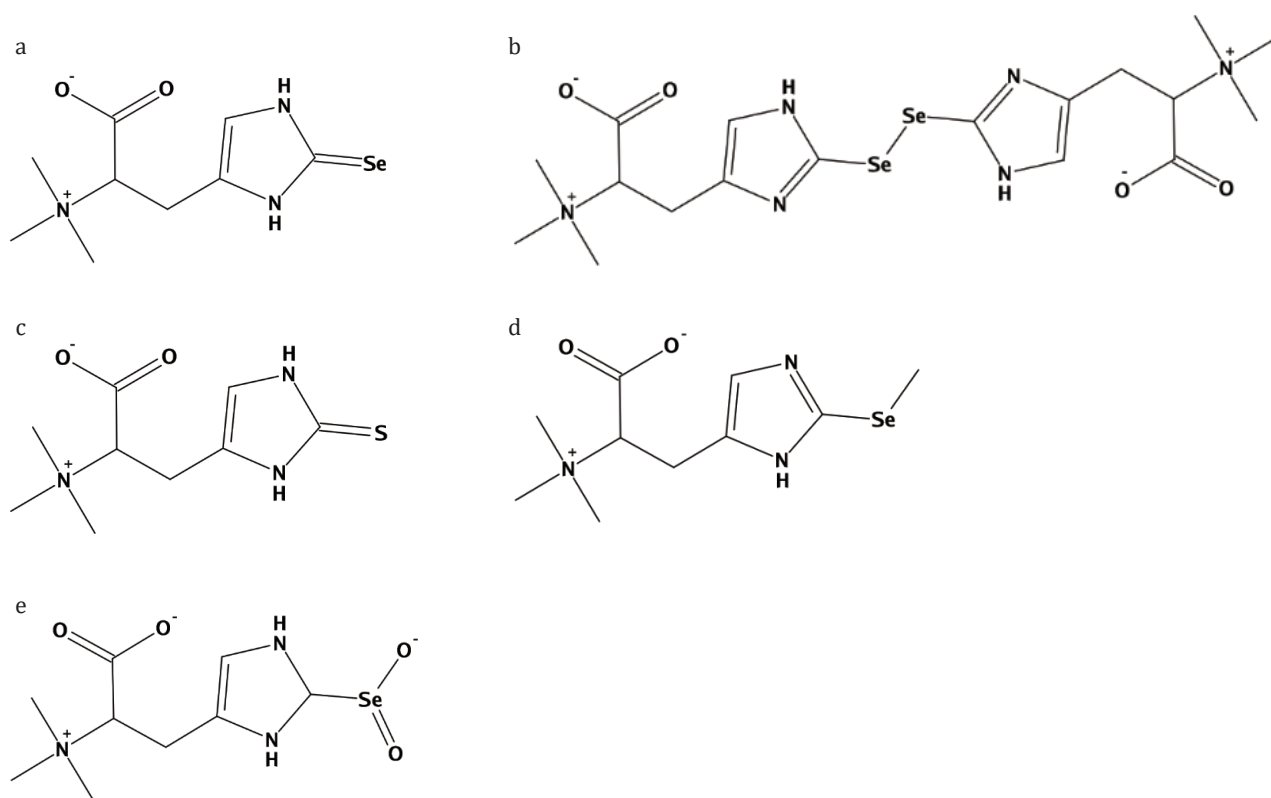


**Fig. 1** | Selenoneine (SEN) and its derivatives are exhibited; SEN monomer (a), SEN dimer (b), ergothioneine (EGT) (c), Se-methylselenoneine (MeSEN) (d) and selenoneine seleninic acid (SEN-seleninic acid) (e).

but a low molecular weight compound below 1000 Da. They purified the low molecular weight compound from the blood of bluefin tuna, and they identified it as  $m/z$  553 and containing two Se atoms using high resolution mass spectrometer (HRMS) [1]. Its structure was determined using nuclear magnetic resonance (NMR) and they named it as “selenoneine” [1] because it is a selenium analogue of ergothioneine (EGT, **Fig. 1c**) that is known as a radical scavenger in fungi [2].

SEN has a strong radical scavenging activity [1]. SEN is one of the major forms of Se in the dietary intake of humans, especially in those who frequently eat fish, and it is predicted to contribute to redox systems and health maintenance. Since the identification of SEN, many studies aiming to elucidate the functions of SEN have been published in diverse disciplines, including chemistry, biochemistry, biology, nutrition and environmental studies. Moreover, analogous pairs of SEN have been identified, such as Se-methylselenoneine (MeSEN, **Fig. 1d**) and selenoneine seleninic acid (SEN-seleninic acid, **Fig. 1e**), and the relationship between their metabolism and function has been actively studied. Herein, we systematically review previous SEN studies across a wide range of disciplines and outline the current status and future prospects of SEN research.

## 2. Selenoneine contents in organisms

The first report of SEN indicated that it was present in the blood of bluefin tuna, with detectable concentrations also present in the blood of other types of fish [1]. SEN is more abundant in the blood of bluefin tuna ( $430 \pm 82 \mu\text{mol Se/kg}$ , **Table 1**) and Pacific mackerel ( $437 \pm 159 \mu\text{mol Se/kg}$ , **Table 1**) than in that of wild bluefin tuna ( $83 \pm 29 \mu\text{mol Se/kg}$ , **Table 1**) [1]. SEN is also detected in the blood of freshwater fish, Tilapia, at  $0.9 \pm 0.6 \mu\text{mol Se/kg}$  (**Table 1**) [1]. Notably, SEN is present in the muscles of fishes, with SEN contents of ordinary and dark muscle of bluefin tuna containing  $2.4 \pm 0.3 \mu\text{mol Se/kg}$  and  $190 \pm 8.0 \mu\text{mol Se/kg}$ , respectively (**Table 1**) [1]. Other types

**Table 1. | SEN concentrations in tissues of organisms**

Species	Tissues	Concentrations per wet weight SEN $\mu\text{mol Se/kg}$ (mg Se/kg)	Total Se $\mu\text{mol/kg}$ (mg/kg)	Reference
Pacific bluefin tuna (Farm-raised) <i>Thunnus orientalis</i>	Whole blood	430 $\pm$ 82 (34 $\pm$ 7)		[1]
	Spleen	41 $\pm$ 16 (3.2 $\pm$ 1.3)	266 $\pm$ 37 (21 $\pm$ 3)	[1], [4]
	Hepatopancreas	39 $\pm$ 7.5 (3.1 $\pm$ 0.6)	165 $\pm$ 38 (13 $\pm$ 3)	
	Heart	15 $\pm$ 15 (1.2 $\pm$ 1.2)	127 $\pm$ 13 (10 $\pm$ 1)	
	Dark muscle	190 $\pm$ 8 (15 $\pm$ 1)	215 $\pm$ 14 (17 $\pm$ 1)	
	Ordinary muscle	2.4 $\pm$ 0.3 (0.19 $\pm$ 0.02)	7.6 $\pm$ 1.1 (0.60 $\pm$ 0.09)	
Pacific bluefin tuna (Wild) <i>Thunnus orientalis</i>	Whole blood	83 $\pm$ 29 (6.6 $\pm$ 2.3)	152 $\pm$ 39 (12 $\pm$ 3)	[4]
Yellowfin tuna <i>Thunnus albacores</i>	Ordinary muscle	1.6 $\pm$ 0.5 (0.13 $\pm$ 0.04)	9.4 $\pm$ 3.9 (0.74 $\pm$ 0.31)	[3]
Albacore <i>Thunnus alalunga</i>	Ordinary muscle	1.7 $\pm$ 0.3 (0.13 $\pm$ 0.03)	19 $\pm$ 8 (1.5 $\pm$ 0.7)	[3]
Bigeye tuna <i>Thunnus obesus</i>	Ordinary muscle	2.6 $\pm$ 1.8 (0.2 $\pm$ 0.1)	14 $\pm$ 7 (1.1 $\pm$ 0.5)	[3]
Skipjack <i>Euthynnus pelamis</i>	Ordinary muscle	1.0 $\pm$ 0.6 (0.05 $\pm$ 0.04)	6.2 $\pm$ 3.4 (0.49 $\pm$ 0.27)	[3]
Swordfish <i>Xiphias gladius</i>	Ordinary muscle	2.8 $\pm$ 0.6 (0.22 $\pm$ 0.05)	6.6 $\pm$ 1.5 (0.52 $\pm$ 0.12)	[3]
Pacific mackerel <i>Scomber japonicus</i>	Whole blood	437 $\pm$ 159 (35 $\pm$ 13)		[1]
	Ordinary muscle	0.6 $\pm$ 0.2 (0.04 $\pm$ 0.01)	3.4 $\pm$ 0.6 (0.27 $\pm$ 0.05)	[3]
Blue mackerel <i>Scomber australasicus</i>	Whole Muscle	2.5 $\pm$ 0.9 (0.20 $\pm$ 0.07)	6.8 $\pm$ 1.5 (0.54 $\pm$ 0.12)	[4]
Japanese Anchovy <i>Engraulis japonica</i>	Ordinary muscle	ND	3.1 $\pm$ 1.8 (0.25 $\pm$ 0.14)	[3]
Pacific sardine <i>Sardinops melanostictus</i>	Ordinary muscle	1.4 $\pm$ 0.6 (0.11 $\pm$ 0.04)	4.1 $\pm$ 0.9 (0.32 $\pm$ 0.07)	[3]
Pacific saury <i>Cololabis saira</i>	Ordinary muscle	ND	2.6 $\pm$ 0.4 (0.21 $\pm$ 0.03)	[3]
	Whole Muscle	0.13 $\pm$ 0.13 (0.01 $\pm$ 0.01)	2.5 $\pm$ 0.3 (0.20 $\pm$ 0.03)	[4]
Horse mackerel <i>Trachurus japonicus</i>	Ordinary muscle	0.5 $\pm$ 0.2 (0.04 $\pm$ 0.02)	5.0 $\pm$ 1.4 (0.40 $\pm$ 0.11)	[3]
Japanese barracuda <i>Sphyræna japonica</i>	Ordinary muscle	0.1 $\pm$ 0.1 (0.008 $\pm$ 0.008)	1.8 $\pm$ 0.2 (0.14 $\pm$ 0.02)	[3]
Japanese conger <i>Conger myriaster</i>	Ordinary muscle	ND	2.5 $\pm$ 1.1 (0.20 $\pm$ 0.09)	[3]
Greeneye <i>Chlorophthalmus albatrossis</i>	Ordinary muscle	1.4 $\pm$ 0.5 (0.11 $\pm$ 0.04)	5.3 $\pm$ 0.6 (0.42 $\pm$ 0.05)	[3]
Alfonsino <i>Beryx splendens</i>	Ordinary muscle	1.3 $\pm$ 0.5 (0.10 $\pm$ 0.04)	18 $\pm$ 13 (1.4 $\pm$ 1.0)	[3]
Red sea bream <i>Pagrus major</i>	Ordinary muscle	0.4 $\pm$ 0.1 (0.03 $\pm$ 0.01)	3.7 $\pm$ 0.3 (0.29 $\pm$ 0.02)	[3]
White croaker <i>Pennahia argentata</i>	Ordinary muscle	ND	3.6 $\pm$ 1.0 (0.28 $\pm$ 0.08)	[3]
Marbled sole <i>Pleuronectes yokohamae</i>	Ordinary muscle	ND	1.4 $\pm$ 0.0 (0.11 $\pm$ 0.00)	[3]
Chum salmon <i>Oncorhynchus keta</i>	Ordinary muscle	ND	3.9 $\pm$ 0.3 (0.30 $\pm$ 0.02)	[3]

Overview of the biochemistry and biology of selenoneine

Species	Tissues	Concentrations per wet weight SEN $\mu\text{mol Se/kg}$ (mg Se/kg)	Total Se $\mu\text{mol/kg}$ (mg/kg)	Reference
Pacific cod <i>Gadus macrocephalus</i>	Muscle	ND	$2.9 \pm 0.5$ ( $0.23 \pm 0.04$ )	[4]
Slime flounder <i>Microstomus achne</i>	Muscle	$2.3 \pm 0.1$ ( $0.18 \pm 0.01$ )	$2.3 \pm 2.3$ ( $0.18 \pm 0.18$ )	[4]
Tilapia <i>Oreochromis niloticus</i>	Whole blood	$0.9 \pm 0.6$ ( $0.07 \pm 0.05$ )		[1]
Japanese common squid <i>Todarodes pacificus</i>	Hepatopancreas	$9.3 \pm 3.5$ ( $0.73 \pm 0.28$ )		[1]
	Muscle	$0.13 \pm 0.00$ ( $0.01 \pm 0.00$ )	$2.7 \pm 0.1$ ( $0.21 \pm 0.01$ )	[4]
Chicken <i>Gallus gallus domesticus</i>	Liver	$0.3 \pm 0.1$ ( $0.02 \pm 0.01$ )		[1]
	Heart	ND		
	Gizzard	ND		
Giant petrel <i>Macronectes</i>	Liver	Range: 165–659 (13–52) per dry weight	Range: 241–5395 (19–426) per dry weight	[5]
	Kidney	Range: 329–1114 (26–88) per dry weight	Range: 519–1659 (41–131) per dry weight	
	Muscle	Range: 25.3–317 (2–25) per dry weight	Range: 51–393 (4–31) per dry weight	
	Brain	Range: 63–443 (5–35) per dry weight	Range: 76–507 (6–40) per dry weight	
	Whole blood	Range: 15–304 (1.2–24)	Range: 38–342 (3–27) per dry weight	
Pig <i>Susscrofa domesticus</i>	Liver	ND		[1]
	Kidney	$0.36 \pm 0.1$ ( $0.03 \pm 0.01$ )		
Minke Whale <i>Balaenoptera acutorostrata</i>	Muscle	$0.63 \pm 0.63$ ( $0.050 \pm 0.050$ )	$5.1 \pm 1.3$ ( $0.40 \pm 0.10$ )	[4]
	Whole blood	$1.6 \pm 0.3$ ( $0.12 \pm 0.02$ )	$11 \pm 1.9$ ( $0.88 \pm 0.15$ )	
Striped Dolphin <i>Stenella coeruleoalba</i>	Blood cells	$56 \pm 14$ ( $4.4 \pm 1.1$ )	$57 \pm 13$ ( $4.6 \pm 1.0$ )	[4]
	Plasma	$0.060 \pm 0.100$ ( $0.0050 \pm 0.0080$ )	$9.6 \pm 1.9$ ( $0.76 \pm 0.15$ )	
	Liver	$4.8 \pm 1.1$ ( $0.38 \pm 0.09$ )	$320 \pm 330$ ( $26 \pm 26$ )	
	Kidney	$35 \pm 1$ ( $2.8 \pm 1.1$ )	$95 \pm 16$ ( $7.5 \pm 1.2$ )	
Risso's Dolphin <i>Grampus griseus</i>	Blood cells	$47 \pm 7$ ( $3.7 \pm 0.6$ )	$57 \pm 6$ ( $4.5 \pm 0.5$ )	[4]
	Plasma	$0.56 \pm 0.05$ ( $0.044 \pm 0.041$ )	$7.6 \pm 1.1$ ( $0.60 \pm 0.09$ )	
	Liver	$5.1 \pm 2.8$ ( $0.40 \pm 0.22$ )	$290 \pm 120$ ( $23 \pm 9$ )	
	Kidney	$25 \pm 10$ ( $2.0 \pm 0.8$ )	$61 \pm 16$ ( $4.9 \pm 1.2$ )	
Pantropical Spotted Dolphin <i>Stenella attenuata</i>	Blood cells	$35 \pm 15$ ( $2.8 \pm 1.2$ )	$37 \pm 10$ ( $2.9 \pm 0.8$ )	[4]
	Plasma	$1.2 \pm 0.4$ ( $0.091 \pm 0.031$ )	$13 \pm 1$ ( $1.0 \pm 0.1$ )	
	Liver	$2.8 \pm 1.0$ ( $0.22 \pm 0.08$ )	$390 \pm 260$ ( $31 \pm 21$ )	
	Kidney	$24 \pm 8$ ( $1.9 \pm 0.6$ )	$95 \pm 15$ ( $7.5 \pm 1.2$ )	
Beluga mattaq <i>Delphinapterus leucas</i>	Skin	Median; 23 (1.8) Range; 15 – 94 (1.2 – 7.4)		[19]

Values are mean  $\pm$  SD. ND < 0.051  $\mu\text{mol Se/kg}$  (0.004 mg Se/kg)

of edible fishes have SEN in their ordinary muscle and their contents are presented in **Table 1** [1,3,4]. Moreover, SEN is present in the spleen ( $41 \pm 16 \mu\text{mol Se/kg}$ , **Table 1**), hepatopancreas ( $39 \pm 7.5 \mu\text{mol Se/kg}$ , **Table 1**) and heart ( $15 \pm 15 \mu\text{mol Se/kg}$ , **Table 1**) [1]. These results indicate that SEN is present more specifically in blood and dark muscle compared to other organs and ordinary muscles. Since SEN is also present at lower levels in ordinary muscle, humans are assumed to routinely consume SEN from eating fish.

Terrestrial organisms are also known to contain SEN. The first report on SEN found that is detected in the liver of chickens ( $0.3 \pm 0.1 \mu\text{mol Se/kg}$ , **Table 1**) and the kidney of pigs ( $0.36 \pm 0.1 \mu\text{mol Se/kg}$ , **Table 1**) [1]. Recently, SEN was reported to be present in seabirds, including giant petrels (*Macronectes sp.*) [5]. SEN was detected in the blood and internal tissues, with the highest concentrations found in the kidneys ( $329\text{--}1114 \mu\text{mol Se/kg}$  in dry weight, **Table 1**) [5]. The study also reports that SEN represents between 78–88% of the total Se in the brain and suggests that it plays a crucial role in the nervous system in the giant petrels [5]. The SEN found in the terrestrial organisms is thought to be derived from their diet because fishmeal is used to some extent in feeds for chickens and pigs, and seabirds consume fish in the ocean. Moreover, an edible mushroom, *Boletus edulis*, is reported to contain SEN at significant levels [6]. More than 80% of the total Se in the mushroom is present as SEN, which reached  $1 \text{ mg Se/kg}$  in wet weight [6]. This suggests that *Boletus edulis* might also represent a natural supply of SEN for terrestrial organisms.

### 3. Synthesis and biosynthesis of selenoneine

#### 3-1. Chemical synthesis of SEN

SEN is a low molecular weight Se species and its chemical synthetic and biosynthetic processes have been investigated. In 2019, a total synthesis method for SEN was reported, which described a method to synthesize an oxidized dimer form of SEN (**Fig. 1**) starting with *L*-histidine methyl ester, converting it to 2-selenoimidazole, followed by oxidation to the diselenide racemic form with a yield of 2% [7].

#### 3-2. Biosynthesis studies of SEN

Biosynthetic methods for SEN were developed prior to the total synthesis method. In 2014, a genetically modified fission yeast (*Schizosaccharomyces pombe*) strain was developed (TP1803) for efficiently synthesizing EGT [8]. TP1803 overexpresses ergothioneine biosynthesis protein 1 (*egt-1*, SPBC1604.1) and synthesizes EGT from hercynylcysteine sulfoxide, which is composed of trimethyl histidine (hercynine) and cysteine [8]. The strain also synthesizes SEN from hercynylselenocysteine, which is composed of hercynine and selenocysteine (SeCys), when the strain is cultured in a medium containing sodium selenate ( $\text{Na}_2\text{SeO}_4$ ) as a source of Se [8]. *Aspergillus sp.* like *A. oryzae*, *A. niger* and *A. sojae* also synthesize SEN by induction of ergothioneine biosynthesis genes [9]. They synthesize SEN in both media containing sodium selenite ( $\text{Na}_2\text{SeO}_3$ ) and selenocystine, and all *Aspergillus sp.* synthesize more SEN with the addition of selenocystine [9]. SeCys is thought to be a Se source for SEN because microorganisms such as *S. pombe* and *Aspergillus sp.* synthesize SEN from selenocystine in the culture media.

However, Secys is not the only source of Se for SEN synthesis. In 2022, a novel SEN biosynthetic pathway in bacteria was reported where SEN is synthesized from selenosugars [10], which are known metabolites of Se species in the body and are detected in the urine of animals [11, 12]. This report indicates that SEN is not only synthesized by the non-specific incorporation of Se into the ergothioneine pathway published in 2014 [8]. The study compares the SEN production in bacteria with a canonical ergothioneine biosynthetic gene cluster (BGC), with or without the selenometabolite BGC corresponding *selD*, which is a selenophosphate synthase gene necessary for selenoprotein synthesis [10, 13]. Although an actinomycete with a selenometabolite BGC (*Amycolatopsis palatopharyngis*, DSM 444832) and a  $\beta$ -proteobacterium with the BGC (*Variovorax paradoxus*, DSM 30034) synthesize SEN in media containing sodium selenite, a genetically similar actinomycete lacking a selenometabolite BGC (*Streptomyces rimosus*, ATCC 10970) and a similar  $\beta$ -proteobacterium lacking the BGC (*Burkholderia thailandensis*, E264) do not synthesize SEN in the media [10]. These results suggest that selenoneine may in fact be the product of a new cluster termed *sen*, composed of *senA*, *senB* and *senC*; moreover, the authors report that SenA (encoded by *senA*)

transfers Se from a selenosugar to hercynine and synthesizes hercynyl-SeGlcNAc selenoxide (GlcNAc-SEN=O) as a precursor of SEN [10]. A recent study exhibited that the SenA forms complexes with hercynine and thioglucose (SGlc), a sulfur analogue of selenoglucose (SeGlc) [14] and it is therefore speculated that the enzyme does not discriminate between S and Se. However, a sulfur analogue of selenosugar has not been detected in organisms and only Se compounds are thought to be used as a substrate by SenA consequently.

#### 4. Purification methods

##### 4-1. Purification of SEN dimer

In the initial report, SEN was extracted in acetonitrile with dithiothreitol (DTT) and purified as a SEN dimer using an ODS column (Atlantis dC18; 300 Å, 19 mm × 150 mm, Waters) and a size exclusion chromatography column (Ultrahydrogel 120; 120 Å, 6 µm, 7.8 mm × 300 mm, Waters) [1]. After the development of the genetically modified fission yeast synthesizing SEN [8], methods for purification of SEN from yeast were developed. In a method published in 2018, SEN dimer was purified from the yeast cell lysate, extracted by sonication and centrifugation in cold methanol [15]. The lysate was evaporated to dryness and dissolved in water, and the SEN dimer was isolated by preparative reverse-phase HPLC with an Atlantis dC18 column (Waters Corporation, Milford, USA) [15]. To isolate SEN monomers from EGT, which has similar polarity, dimerization of SEN monomers in methanol enables the separation of SEN from EGT by an ODS column.

##### 4-1. Purification of SEN monomer

An additional method that permits the separation of SEN monomer from EGT in yeast cells involves using HPLC with a pentabromobenzyl (PBr) column [16]. In this method, SEN monomer and EGT are extracted from the yeast cells using boiling water. The supernatant is collected by centrifugation and concentrated by evaporation, and the concentrated solution is cleaned up using HPLC with a reverse phased column, C30 column (Nomura chemical), with 0.1 % acetic acid as a mobile phase by collecting an elution with early retention time that is barely retained on the column [16]. The eluate is then concentrated and injected into an HPLC with a PBr column and SEN monomer, detected at 260 nm wavelength, is collected with water as the mobile phase following its separation from EGT [16]. The PBr column separates substances by dispersion forces, a type of intermolecular forces, and has been reported to separate pnictogen and halogen compounds [17]. Thus, the column is predicted to separate the chalcogen analogs of SEN monomer and EGT.

#### 5. Distribution and metabolism of selenoneine

##### 5-1. Selenoneine concentrations in humans in epidemiological studies

SEN is one of the major Se compounds humans derive from their diet. Its distribution throughout the body has been examined in epidemiological studies using clinical specimens (**Table 2**) and animal experiments using mice. A study in a remote Japanese island revealed that SEN was present in erythrocytes of the island population with concentrations ranging from 6–2380 µg Se/L with a mean of 212 µg Se/L (n = 167) [18]. The concentrations increase depending on the frequency of fish consumption [18]. In a study of Inuit from Nunavik in Canada, erythrocyte SEN concentrations ranged from 3.20–3230 µg Se/L with a median of 413 µg Se/L (n = 210) [19]. Another study reported that SEN concentrations in erythrocytes of Inuit adults ranged from 1–3226 µg Se/L with a mean of 118 µg Se/L (ages: 18–74, n = 885) [20]. The mean was reported to be significantly higher among women (150.3 µg Se/L, n = 488) than men (87.6 µg Se/L, n = 387) [20]. This result differs from that has been reported that there are no sex differences in blood levels of EGT [21]. While no explanation was provided for why SEN concentrations are different between sexes, the authors speculated that the difference may be attributable to a differential response bias in the food frequency questionnaire [20]. The authors also suspect that there may be biological sex differences in the sequestration and function of SEN [20]. The levels of SEN in erythrocytes are highly correlated with total Se in erythrocytes and whole blood, but only weakly correlated with total Se in plasma [20]. The ratio of SEN : total Se in erythrocytes is also positively correlated with total Se in erythrocytes [20]. These results indicate that increases

**Table 2.** | SEN concentrations in erythrocytes of human

Participants	Tissues	SEN $\mu\text{mol Se/L}$ ( $\mu\text{g Se/L}$ )	Reference
People in remote Japanese islands (n = 167)	Erythrocytes	Mean: 2.68 (212) Range: 0.08–30.1 (6–2380)	[18]
Inuit from Nunavik in Canada (n = 210)	Erythrocytes	Median: 5.23 (413) Range: 0.04–40.9 (3.20–3230)	[19]
Inuit adults (ages: 18–74, n = 885)	Erythrocytes	Mean: 1.49 (118) Range: 0.01–40.9 (1–3226)	[20]
Women (n = 488)		Mean: 1.90 (150.3)	
Men (n = 387)		Mean: 1.11 (87.6)	

in total Se in erythrocytes are found as SEN [20]. However, the association between the ratio of SEN : total Se in erythrocytes is non-linear and the ratio plateaus around 0.8 [20]. The plateaued ratio suggests that there is an upper limit to the accumulation of SEN in erythrocytes and the existence of a SEN clearance mechanism. Notably, methylated SEN, Se-methylselenoneine (MeSEN, **Fig. 1d**), was identified in human urine and blood [22], and is predicted to be the metabolite that is the excreted form of SEN.

### 5-2. Distribution and metabolism of selenoneine in mice

Animal experiments using mice reveal the distribution of SEN in organs. A study reports that SEN is detected in the liver of mice at a concentration of  $8.11 \mu\text{mol Se/kg}$  after 4 months of ingestion of a diet containing  $0.3 \text{ mg Se/kg}$  SEN [23]. Another study detected SEN in the kidney and spleen in addition to the liver in ICR mice after 32 days of ingestion of a  $2.7 \text{ mg Se/kg}$  SEN-containing diet [24]. In this study, SEN was not detected in erythrocytes, and it was suggested that SEN preferentially accumulates in organs such as the liver, kidney and spleen [23]. Concentrations of SEN in the liver (male:  $0.411 \pm 0.121 \mu\text{mol Se/kg}$ , female:  $0.562 \pm 0.203 \mu\text{mol Se/kg}$ ) and spleen (male:  $0.939 \pm 0.092 \mu\text{mol Se/kg}$ , female:  $1.10 \pm 0.35 \mu\text{mol Se/kg}$ ) were not different between sexes, whereas SEN in the kidney of female mice was significantly higher than in male mice (male:  $0.323 \pm 0.091 \mu\text{mol Se/kg}$ , female:  $0.731 \pm 0.151 \mu\text{mol Se/kg}$ ) [24]. The difference between sexes appears to be consistent with the Inuit study in that the blood concentrations of SEN were significantly higher among women than men [20], however, a detailed mechanistic explanation will require further research. An additional study reported SEN accumulation in the liver, kidney and spleen in male Balb/c mice continuously administered  $10 \mu\text{M}$  purified SEN via the drinking water for 6 days [25]. In the study, SEN was detected in erythrocytes at  $3.0 \pm 0.1 \mu\text{mol Se/kg}$ , which was lower than in the liver ( $16.1 \pm 3.3 \mu\text{mol Se/kg}$ ) and kidney ( $13.1 \pm 1.9 \mu\text{mol Se/kg}$ ) [25]. The study also showed that MeSEN was a metabolite of dietary SEN by administering stable isotope-labeled (Se-76) SEN to mice and analyzing their urine [25]. In addition to urine, MeSEN was detected in plasma, liver and kidney, and it was suggested that MeSEN was synthesized in these tissues [25]. Although major Se species in the body, like SeCys and SeMet, are metabolized to selenosugar or trimethylselenonium (TMSe) via selenide ( $\text{HSe}^-$ ) [26], SEN is methylated and retains its original structure (**Fig. 2**). Therefore, SEN is thought to be metabolized by a unique pathway that is distinct from the pathway via  $\text{HSe}^-$  (**Fig. 2**). However, it is necessary to confirm how SEN is metabolized under selenium-deficient conditions because this study was performed under dietary selenium-replete conditions. Indeed, urinary excretion of the major Se species is not affected by SEN administration [27]. Such features of SEN are important when discussing dietary intake of

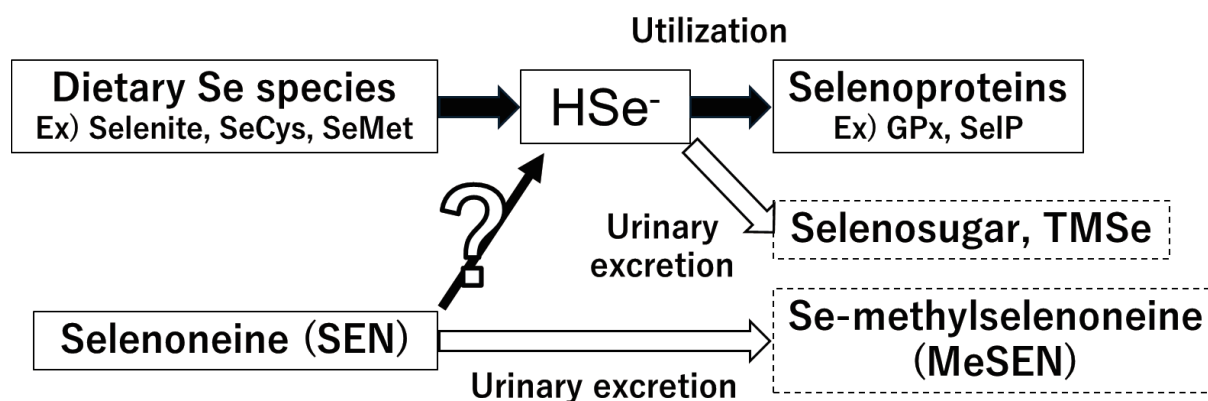


**Fig. 2** | Dietary Se species metabolism and predicted metabolic scheme of SEN. Dietary Se species such as selenite, SeCys and SeMet are converted to utilization forms in the body, selenoproteins, and urinary excretion forms, selenosugar and TMSe via selenide ( $\text{HSe}^-$ ). Selenoneine (SEN) is converted to Se-methylselenoneine (MeSEN) for the urinary excretion.

SEN as a source of Se because most Se species play a role in the body by being synthesized into selenoproteins via selenocysteine. The methylation mechanism of SEN is not fully understood and further studies of SEN metabolism are required. Notably, a methyltransferase for SEN has not been identified, and it is also not known whether SEN is metabolized enzymatically or non-enzymatically.

### 5-3. Absorption of SEN by a transporter, OCTN1

SEN is incorporated into cells via the organic cation/carnitine transporter-1, OCTN1 (SLC22A4), which is a known EGT transporter in animals [28, 29]. SEN was incorporated into human embryonic kidney 293 cells (HEK293) over expressing OCTN1 following transient transfection with an OCTN1 vector [28]. The study also demonstrated that SEN concentrations in zebrafish embryo are increased by addition of SEN from the water, and were decreased to control levels by suppression of OCTN1 expression with an antisense morpholino oligo [28]. A transwell assay using the Caco-2 human colon adenocarcinoma cell line as an *in vitro* absorption model of the small intestine showed that SEN and MeSEN are detected on the basolateral side after the addition of SEN to the apical side [30]. OCTN1 is expressed on the apical side of the small intestine of human and mouse [31], and dietary SEN is thought to be absorbed via small intestine epithelial cells expressing OCTN1. The  $K_m$  value for SEN uptake was reported to be  $13.0 \mu\text{M}$  [28], which is lower than previously reported for EGT uptake by OCTN1 ( $21 \mu\text{M}$ ) in OCTN1 transfected HEK293 cells [29]. The amount of SEN uptake [28] is thought to be derived from SEN monomer because SEN dimer is not a substrate of OCTN1 [7]. SEN is distributed in organs in mice continuously administered SEN dimer [25], suggesting that SEN dimer is reduced in the digestive tract and absorbed into the body via small intestinal epithelial cells that express OCTN1. The ratio of SEN distribution to the kidney and spleen relative to the liver does not change [24] compared to the distribution of EGT [32]. This suggests that SEN distributes to organs expressing OCTN1 similar to the trend of EGT and the distribution can be predicted by referring to EGT distribution. EGT distributes to the brain [32] and it has been reported to improve cognitive functions [33, 34]. SEN has been detected in the brains of seabirds [5], but it has not yet been detected in mammals. Notably, SEN has been reported to cross an *in vitro* blood-brain barrier model [35], and SEN is expected to improve cognitive function by its radical scavenging capacity upon distribution to the brain. In section 5-2, it states that SEN in the kidney of female mice was significantly higher than in male mice [24], the difference is suspected to be derived from the difference of the expression of OCTN1. However, mRNA expression of OCTN1 in the kidney of mice does not change between male and female [36]. Therefore, the difference in the concentration of SEN in the kidney of mice [24] is thought

to be caused by mechanisms other than the expression of OCTN1.

## 6. Functions of selenoneine in organisms

### 6-1. Antioxidative capacity of SEN

In the first report of SEN, the radical scavenging capacity of SEN was evaluated using the DPPH (2,2-diphenyl-1-picrylhydrazyl) radical scavenging assay, and the capacity of SEN was greater than that of EGT and a water-soluble vitamin E, Trolox [1]. SEN is oxidized by hydrogen peroxide ( $H_2O_2$ ) and converted to selenoneine-seleninic acid (SEN-seleninic acid, **Fig. 1e**) unlike EGT, which is converted to mercynine or sulfonic acid [7]. The difference between SEN and EGT against oxidants is thought to be related to the difference in antioxidative capacity between them. Another study shows that SEN-inspired selenohydantoin derivatives exhibit glutathione peroxidase (GPx)-like activity, reducing hydroperoxides [37].

In a study using *Caenorhabditis elegans* (*C. elegans*), SEN did not diminish ROS induced by *tert*-butyl hydroperoxide immediately after SEN treatment, but an improvement in oxidative stress was observed 48 h after SEN treatment [38]. This study suggests that the protective effect may not be explained by the direct radical scavenging capacity of SEN, but that the delayed protection may rather involve the activation of a molecular signaling cascade corresponding to oxidative stress. Few papers have reported the response of SEN and ROS *in vitro* or *in cellulo*, and further studies are required to understand the antioxidant mechanism of SEN.

### 6-2. Interactions of SEN with metals

Previous studies have shown that dietary Se intake from fish reduces methylmercury (MeHg) toxicity [39-44], and SEN has been implicated in reducing MeHg toxicity. A study demonstrated that 1.6  $\mu$ M SEN reduced MeHg toxicity in zebrafish embryos and was associated with the SEN transporter, OCTN1, because the protective effect was eliminated by the inhibition of OCTN1 expression [28]. This study also showed a decrease of MeHg and an increase of inorganic Hg in the presence of SEN in the embryo [28]. The study speculated that SEN forms a SEN-MeHg complex and that the complex can be converted to mercury selenide (HgSe), which is found in the liver of marine mammals and is thought to be a detoxified form of MeHg [45, 46], by translocation into lysosomal secretory vesicles by OCTN1 [28]. In seabirds, SEN is thought to play a role in MeHg detoxication because SEN levels decrease dramatically (from 68 to 3%) with increasing Hg concentrations in the liver [5]. However, a SEN-MeHg complex has not been found in previous studies. Another study showed that SEN did not interact with inorganic Hg and MeHg in the liver homogenate of marine turtles [47]. Further studies are needed to elucidate the MeHg detoxication mechanism of SEN.

Other studies demonstrate interactions between SEN and metalloenzymes. SEN inhibited a zinc-containing metalloprotease, angiotensin converting enzyme (ACE, EC 3.4.15.1), in an *in vitro* assay and the enzyme kinetics indicated that the inhibition is competitive [48]. *In silico* docking simulation suggested that SEN interacts with the catalytic  $Zn^{2+}$  located at the active center of ACE; however, the Se atom of SEN does not interact with  $Zn^{2+}$ , unlike captopril or selenocaptopril, which inhibit ACE by direct interaction of their thiol or selenol group with  $Zn^{2+}$  [49, 50]. SEN also inhibits a copper-containing enzyme tyrosinase (EC 1.14.18.1), which is involved in melanogenesis [51]. In a human 3D epidermal model containing functional melanocytes, melanin synthesis was suppressed by the addition of SEN to the media [51].

### 6-3. Effect of SEN on disease

SEN is expected to have beneficial health effects due to its strong radical scavenging capacity. In a study using azoxymethane (AOM) and dextran sodium sulfate (DSS)-induced colitis-associated cancer model mice, a diet containing SEN (0.28 mg Se/100 g) from tuna dark muscle extract reduced the pathology of experimental colorectal cancers [52]. The number of macroscopic polyps and tumor diameters were decreased after 74 days of dietary supplementation [52]. The AOM/DSS-induced colitis-associated cancer model corresponds to ROS-induced inflammation and SEN is speculated to improve the pathology through its radical scavenging capacity [52]. However,

an extract from tuna dark muscle was used in this experiment rather than purified SEN. Therefore, the influence of other substances derived from the dark muscle cannot be ignored.

Another study showed an ameliorating effect of SEN against hepatocellular injury and hepatic steatosis in non-alcoholic fatty liver disease (NAFLD) model mice; these mice lack the farnesoid X receptor, which plays an important role in the regulation of lipid and glucose metabolism [23]. The study supplied purified SEN at 0.3 mg Se/kg in the diet for 4 months and SEN-fed mice exhibited reductions of the hepatic damage associated diagnostic markers AST, total bilirubin and total bile acid [23]. Hepatic triacylglycerol levels were suppressed in SEN-fed mice, but the levels did not change in the serum [23]. Interestingly, hepatic mRNA expressions of the selenoproteins, *Gpx1* and *SelP*, were significantly decreased in SEN-fed mice [23]. The production of glutathione peroxidase 1 (GPx1) and selenoprotein P (SelP) were stimulated by excessive consumptions of Se [53-56]. The results in the SEN-fed study suggest that *Gpx1* and *SelP* mRNA expressions are induced by oxidative stress resulting from hepatic steatosis in NAFLD model mice, and SEN supplementation counteracts the induction by reducing ROS and decreasing oxidative stress. However, the mechanism of regulation of selenoprotein expressions by SEN is not clear and should be elucidated to understand SEN function and nutrition in Se metabolism.

## 7. Future prospects

SEN is a compound with potential health benefits due to its strong radical scavenging capacity. Research on the health functions of EGT is accelerating, and in recent years clinical research has even been conducted on dementia [57]. For SEN, animal studies using purified SEN and clinical studies using supplements or tuna dark muscle containing high concentrations of SEN are required to investigate the effects of SEN against various diseases caused by oxidative stress. These studies will demonstrate the efficacy of SEN on human health and contribute to the growing body of evidence on the relationship between fish diets and health.

Se is known to be a trace element with a narrow range of biologically acceptable levels, which raises concerns about the safety of SEN. SEN is thought to be safe in terms of dietary experience, as some people consume large amounts of SEN by eating marine organisms [18-20]. On the other hand, if SEN derived from extracts from fish processing residues, etc. is taken as a supplement, its safety should be carefully assessed, as it may be highly concentrated. SEN is also believed to be methylated and excreted in the urine [25] and not via the central metabolic pathways of selenium, such as selenoproteins synthesis and selenosugars synthesis, so it needs to be carefully considered whether it should be uniformly considered under conventional selenium intake standards and it is an important research topic in Se nutrition.

## 8. Conclusion

Since the identification of SEN in 2010, SEN studies have progressed in several areas. Chemical and biological synthetic studies and the development of SEN purification methods allow us to obtain SEN standards easily compared to those obtained from fish, and contribute to studies on SEN functions in organisms, especially mammals. On the other hand, the metabolism and biological functions of SEN in mammals are not sufficiently elucidated because such studies require abundant purified SEN. In the future, the development of such studies will be enabled by the establishment of mass production methods and market availability of SEN standards. Advances in SEN research not only provide new insights into the relationship between fish consumption and human health, but are also leading to the discovery of new redox mechanisms in organisms that accumulate SEN.

## Author contributions

Takuya Seko: Conceptualization, Writing-Original draft preparation. Yumiko Yamashita: Visualization, Supervision. Michiaki Yamashita: Supervision, Writing-review and editing.

## Acknowledgements

The authors are grateful to the co-authors who were involved in writing our original papers.

## References

- [1] Yamashita Y, Yamashita M. Identification of a novel selenium-containing compound, selenoneine, as the predominant chemical form of organic selenium in the blood of bluefin tuna. *J Biol Chem*. 2010; 285(24): 18134-18138.
- [2] Borodina I, Kenny LC, McCarthy CM, Paramasivan K, Pretorius E, Roberts TJ, van der Hoek SA, Kell DB. The biology of ergothioneine, an antioxidant nutraceutical. *Nutr Res Rev*. 2020; 33(2): 190-217.
- [3] Yamashita Y, Amlund H, Suzuki T, Hara T, Hossain MA, Yabu T, Touhata K, Yamashita M. Selenoneine, total selenium, and total mercury content in the muscle of fishes. *Fish Sci*. 2011; 77: 679-686.
- [4] Yamashita M, Suzuki T, Yokoyama Y. *Fish Consumption and Health —Biological Effects of Methylmercury Exposure*. Tokyo: Koseisyu Koseikaku; 2014.
- [5] El Hanafi K, Pedrero Z, Ouerdane L, Marchán Moreno C, Queipo-Abad S, Bueno M, Pannier F, Corns WT, Cherel Y, Bustamante P, Amouroux D. First time identification of selenoneine in seabirds and its potential role in mercury detoxification. *Environ Sci Technol*. 2022; 56(5): 3288-3298.
- [6] Peer F, Kuehnelt D. High levels of the health-relevant antioxidant selenoneine identified in the edible mushroom *Boletus edulis*. *J Trace Elem Med Biol*. 2024; 127536.
- [7] Lim D, Gründemann D, Seebeck FP. Total synthesis and functional characterization of selenoneine. *Angew Chem Int*. 2019; 58(42): 15026-15030.
- [8] Pluskal T, Ueno M, Yanagida M. Genetic and metabolomic dissection of the ergothioneine and selenoneine biosynthetic pathway in the fission yeast, *S. pombe*, and construction of an overproduction system. *PLoS one*. 2014; 9(5): e97774.
- [9] Ichikawa K, Shinohara Y, Hara S, Kurosawa K, Yamashita Y, Yamashita M. Method for producing selenoneine, U. S. Patent Application. 2018; No. 15: 750-792.
- [10] Kayrouz CM, Huang J, Hauser N, Seyedsayamdost MR. Biosynthesis of selenium-containing small molecules in diverse microorganisms. *Nature*. 2022; 610(7930): 199-204.
- [11] Kobayashi Y, Ogra Y, Ishiwata K, Takayama H, Aimi N, Suzuki KT. Selenosugars are key and urinary metabolites for selenium excretion within the required to low-toxic range. *Proc Natl Acad Sci*. 2002; 99: 15932-15936.
- [12] Kuehnelt D, Kienzl N, Traar P, Le NH, Francesconi KA, Ochi T. Selenium metabolites in human urine after ingestion of selenite, L-selenomethionine, or DL-selenomethionine: a quantitative case study by HPLC/ICPMS. *Anal Bioanal Chem*. 2005; 383: 235-246.
- [13] Böck A, Rother M. *Selenium metabolism in prokaryotes*. Hatfield DL, Berry MJ, Gladyshev VN (eds) : *Selenium : its molecular biology and role in human health, Second Edition*. New York: Springer: 2006; 9-28.
- [14] Liu M, Yang Y, Huang JW, Dai L, Zheng Y, Cheng S, He H, Chen CC, Guo RT. Structural insights into a novel nonheme iron-dependent oxygenase in selenoneine biosynthesis. *Int J Biol Macromol*. 2024; 256: 128428.
- [15] Turrini NG, Kroepfl N, Jensen KB, Reiter TC, Francesconi KA, Schwerdtle T, Kroutil W, Kuehnelt D. Biosynthesis and isolation of selenoneine from genetically modified fission yeast. *Metallomics*. 2018; 10(10): 1532-1538.
- [16] Seko T, Uchida H, Yamashita Y, Yamashita M. Novel method for separating selenoneine reduced monomer and ergothioneine from fission yeast extracts. *Sep Purif Technol*. 2021; 254: 117607.
- [17] Turowski M, Morimoto T, Kimata K, Monde H, Ikegami T, Hosoya K, Tanaka N. Selectivity of stationary phases in reversed-phase liquid chromatography based on the dispersion interactions. *J Chromatogr A*. 2001; 911(2): 177-190.
- [18] Yamashita M, Yamashita Y, Ando T, Wakamiya J, Akiba S. Identification and determination of selenoneine, 2-selenyl- $N_{\alpha}$ ,  $N_{\alpha}$ ,  $N_{\alpha}$ -trimethyl-L-histidine, as the major organic selenium in blood cells in a fish-eating population on remote Japanese Islands. *Biol Trace Elem Res*. 2013; 156: 36-44.
- [19] Achouba A, Dumas P, Ouellet N, Little M, Lemire M, Ayotte P. Selenoneine is a major selenium species in beluga skin and red blood cells of Inuit from Nunavik. *Chemosphere*. 2019; 229: 549-558.
- [20] Little M, Achouba A, Dumas P, Ouellet N, Ayotte P, Lemire M. Determinants of selenoneine concentration in red blood cells of Inuit from Nunavik (Northern Québec, Canada). *Environ Int*. 2019; 127: 243-252.
- [21] Lee S, Mun S, Lee YR, Lee J, Kang HG. Validation of the metabolite ergothioneine as a forensic marker in bloodstains. *Molecules*. 2022; 27(24): 8885.
- [22] Klein M, Ouerdane L, Bueno M, Pannier F. Identification in human urine and blood of a novel seleniummetabolite, Se-methylselenoneine, a potential biomarker of metabolization in mammals of the naturally occurring selenoneine, by HPLC coupled to electrospray hybrid linear ion trap-orbital ion trap MS. *Metallomics*. 2011; 3(5): 513-520.
- [23] Miyata M, Matsushita K, Shindo R, Shimokawa Y, Sugiura Y, Yamashita M. Selenoneine ameliorates hepatocellular injury and hepatic steatosis in a mouse model of NAFLD. *Nutrients*. 2020; 12(6): 1898.
- [24] Seko T, Sato Y, Kuniyoshi M, Murata Y, Ishihara K, Yamashita Y, Fujiwara S, Ueda T, Yamashita M. Distribution and Effects of Selenoneine by Ingestion of Extract from Mackerel Processing Residue in Mice. *Mar Biotechnol*. 2023; 25(6): 1020-1030.
- [25] Seko T, Uchida H, Sato Y, Imamura S, Ishihara K, Yamashita Y, Yamashita M. Selenoneine is methylated in the bodies of mice and then excreted in urine as Se-methylselenoneine. *Biol Trace Elem Res*. 2024; 202(8): 3672-3685.
- [26] Navarro-Alarcon M, Cabrera-Vique C. Selenium in food and the human body: a review. *Sci Total Environ*. 2008; 400(1-3): 115-141.
- [27] Seko T. Studies on the biological functions and metabolism of selenoneine. Kyoto University. 2024; Ph. D. thesis, *in publication*
- [28] Yamashita M, Yamashita Y, Suzuki T, Kani Y, Mizusawa N, Imamura S, Takemoto K, Hara T, Anwar H, Yabu T, Touhata K. Selenoneine, a novel selenium-containing compound, mediates detoxification mechanisms against methylmercury accumulation and toxicity in zebrafish embryo. *Mar Biotechnol*. 2013; 15: 559-570. <https://doi.org/10.1007/s10126-013-9508-1>
- [29] Gründemann D, Harlfinger S, Golz S, Geerts A, Lazar A, Berkels R, Jung N, Rubbert A, Schömig E. Discovery of the ergothioneine transporter. *Proc Natl Acad Sci*. 2005; 102: 5256-5261.
- [30] Rohn I, Kroepfl N, Bornhorst J, Kuehnelt D, Schwerdtle T. Side-directed transfer and presystemic metabolism of selenoneine in a human intestinal barrier model. *Mol Nutr Food Res*. 2019; 63:1900080.
- [31] Sugiura T, Kato S, Shimizu T, Wakayama T, Nakamichi N, Kubo Y, Iwata D, Suzuki K, Soga T, Asano M, Iseki S, Tamai I, Tsuji A, Kato Y. Functional expression of carnitine/organic cation transporter OCTN1/SLC22A4 in mouse small intestine and liver. *Drug Metab Dispos*. 2010; 38: 16651672.
- [32] Tang RMY, Cheah IKM, Yew TSK, Halliwell B. Distribution and accumulation of dietary ergothioneine and its metabolites in mouse tissues. *Sci Rep*. 2018; 8: 1-15.
- [33] Yang NC, Lin HC, Wu JH, Ou HC, Chai YC, Tseng CY, Liao JW, Song TY. Ergothioneine protects against neuronal injury induced by  $\beta$ -amyloid in mice. *Food Chem Toxicol*. 2012; 50(11): 3902-3911.

- [34] Yau YF, Cheah IK, Mahendran R, Tang RM, Chua RY, Goh RES, Feng L, Li J, Kua EH, Chen C, Halliwell B. Investigating the efficacy of ergothioneine to delay cognitive decline in mild cognitively impaired subjects: A pilot study. *J Alzheimers Dis*. 2024; 13872877241291253.
- [35] Drobyshev E, Raschke S, Glabonjat RA, Bornhorst J, Ebert F, Kuehnelt D, Schwerdtle T. Capabilities of selenoneine to cross the in vitro blood-brain barrier model. *Metallomics*. 2021; 13(1): mfaa007.
- [36] Alnouti Y, Petrick JS, Klaassen CD. Tissue distribution and ontogeny of organic cation transporters in mice. *Drug Metab Dispos*. 2006; 34(3): 477-482.
- [37] Alhasan R, Martins GM, de Castro PP, Saleem RSZ, Zaiter A, Fries-Raeth I, Kleinclaus A, Perrin-Sarrado C, Chaimbault P, da Silva Júnior EN, Gaucher C, Jacob C. Selenoneine-inspired selenohydantoins with glutathione peroxidase-like activity. *Bioorg Med Chem*. 2023; 94: 117479.
- [38] Rohn I, Kroepfl N, Aschner M, Bornhorst J, Kuehnelt D, Schwerdtle T. Selenoneine ameliorates peroxide-induced oxidative stress in *C. elegans*. *J Trace Elem Med Biol*. 2019; 55: 78-81.
- [39] Friedman MA, Eaton LR, Carter WH. Protective effects of freeze dried swordfish on methylmercury chloride toxicity in rats. *Bull Environ Cont Toxicol*. 1978; 19: 436-443.
- [40] Ganther HE, Sunde ML. Effect of tuna fish and selenium on the toxicity of methylmercury. *J Food Sci*. 1974; 39: 1-5.
- [41] Ganther H, Goudie C, Sunde M, Kopeckey M, Wagner S, Hoekstra W. Selenium: relation to decreased toxicity of methylmercury added to diets containing tuna. *Science*. 1972; 175: 1122-1124.
- [42] Ohi G, Nishigaki S, Seki H, Tamura Y, Maki T, Minowa K, Shimamura Y, Mizoguchi I, Inaba Y, Takizawa Y, Kawanishi Y. The protective potency of marine animal meat against the neurotoxicity of methylmercury: its relationship with the organ distribution of mercury and selenium in the rat. *Food Cosmet Toxicol*. 1980; 18: 139-145.
- [43] Raymond LJ, Ralston NV. Mercury:selenium interactions and health implications. *SMDJ Seychelles Med Dent J*. 2004; 7: 52-56.
- [44] Raymond LJ, Seale LA, Ralston NV. *Seafood selenium in relation to assessments of methylmercury exposure risks*. In: Hatfield DL, Berry MJ, Gladyshev VN (eds) *Selenium: its molecular biology and role in human health, Third edn*. New York: Springer; 2012.
- [45] Martoja R, Berry JP. Identification of tiemannite as a probable product of demethylation of mercury by selenium in cetaceans. A complement to the scheme of the biological cycle of mercury. *Vie et Milieu/Life Environ*. 1980; 30: 7-10.
- [46] Ng PS, Ji H, Matsumoto K, Yamazaki S, Kogure T, Takagi T, Nagasawa H. Striped dolphin detoxifies mercury as insoluble Hg (S, Se) in the liver. *Proc Japan Acad*. 2001; 77: 178-183.
- [47] Anan Y, Tanabe S, Ogra Y. Comparison of selenoneine found in marine organisms with selenite in the interaction with mercury compounds in vitro. *J Toxicol Sci*. 2011; 36(6): 725-731.
- [48] Seko T, Imamura S, Ishihara K, Yamashita Y, Yamashita M. Inhibition of angiotensin-converting enzyme by selenoneine. *Fish Sci*. 2019; 85: 731-736.
- [49] Natesh R, Schwager SL, Evans HR, Sturrock ED, Acharya KR. Structural details on the binding of antihypertensive drugs captopril and enalaprilat to human testicular angiotensin I-converting enzyme. *Biochemistry*. 2004; 43: 8718-8724.
- [50] Akif M, Masuyer G, Schwager SL, Bhuyan BJ, Mugesh G, Isaac RE, Sturrock ED, Acharya KR. Structural characterization of angiotensin I-converting enzyme in complex with a selenium analogue of captopril. *FEBS J*. 2011; 278: 3644-3650.
- [51] Seko T, Imamura S, Ishihara K, Yamashita Y, Yamashita M. Selenoneine suppresses melanin synthesis by inhibiting tyrosinase in murine B16 melanoma cells and 3D-cultured human melanocytes. *Fish Sci*. 2020; 86: 171-179.
- [52] Masuda J, Umemura C, Yokozawa M, Yamauchi K, Seko T, Yamashita M, Yamashita Y. Dietary supplementation of selenoneine-containing tuna dark muscle extract effectively reduces pathology of experimental colorectal cancers in mice. *Nutrients*. 2018; 10(10): 1380.
- [53] Qin S, Huang K, Gao J, Huang D, Cai T, Pan C. Comparison of glutathione peroxidase 1 and iodothyronine deiodinase 1 mRNA expression in murine liver after feeding selenite or selenized yeast. *J Trace Elem Med Biol*. 2009; 23(1): 29-35.
- [54] Stranges S, Marshall JR, Natarajan R, Donahue RP, Trevisan M, Combs GF, Cappuccio FP, Ceriello A, Reid ME. Effects of long-term selenium supplementation on the incidence of type 2 diabetes: A randomized trial. *Ann Intern Med*. 2007; 147: 217-223.
- [55] Steinbrenner H, Speckmann B, Pinto A, Sies H. High selenium intake and increased diabetes risk: Experimental evidence for interplay between selenium and carbohydrate metabolism. *J Clin Biochem Nutr*. 2011; 48: 40-45.
- [56] Rayman MP, Stranges S. Epidemiology of selenium and type 2 diabetes: Can we make sense of it? *Free Radic Biol Med*. 2013; 65: 1557-1564.
- [57] Yau YF, Cheah IK, Mahendran R, Tang RM, Chua RY, Goh RE, Feng L, Li J, Kua EH, Chen C, Halliwell B. Investigating the efficacy of ergothioneine to delay cognitive decline in mild cognitively impaired subjects: A pilot study. *J Alzheimer's Dis*. 2024; 102(3): 841-854.

# Interaction of selenite and arsenite on erythrocytes uptake of each metalloid: Possible mechanism mediated by extracellularly generated selenium-arsenic complexes

Yayoi Kobayashi<sup>1,2\*</sup>, Seishiro Hirano<sup>1</sup>

<sup>1</sup> Health and Environmental Risk Division, National Institute for Environmental Studies

<sup>2</sup> Graduate School and Faculty of Pharmaceutical Sciences, Chiba University

## Abstract

It has been demonstrated that selenium (Se) and arsenic (As) interact in living organisms. The elucidation of the interaction mechanisms of these toxic metalloids is believed to be of great importance for understanding their effects on humans and animals. The seleno-bis(S-glutathionyl) arsinium ion  $[(GS)_2AsSe]^-$  has been identified as the major As metabolite present in the bile of rabbits and rats co-treated with selenite (iSeIV) and arsenite (iAsIII). Selenide ( $HSe^-$ ), a reduced form of iSeIV, is a crucial component in the As-Se-GSH conjugate formation. This study aimed to shed light on  $HSe^-$  released from erythrocytes and propose a novel mechanism for the uptake of As and Se into erythrocytes via Se-As complexes, in addition to a previously reported mechanism for  $[(GS)_2AsSe]^-$  formation. Erythrocytes from rats that had been fed As-depleted rodent chow for at least 7 weeks after weaning were used in the experiments. iAsIII and/or iSeIV were added to the erythrocyte suspension (final 10%) and incubated at 37°C for up to 180 min or 10 min. The uptake of both elements into the erythrocytes was assessed by measuring the attenuation of each element in the supernatant.  $HSe^-$  was detected by measuring the syn-(methyl,-methyl) bimane produced from the reaction of monochlorobimane with  $HSe^-$ . We observed that iAsIII was slightly taken up by erythrocytes. Furthermore, iSeIV was rapidly taken up by erythrocytes. Simultaneous exposure to both iSeIV and iAsIII increased Se and As uptake by erythrocytes. In addition, a temporal delay occurred in the uptake of both compounds. In conclusion, our study revealed that  $HSe^-$  release is more pronounced in selenite-treated erythrocytes and successfully proposed a novel mechanism for Se and As uptake.

## Keywords:

Selenium, Arsenic, Selenide, As-Se complex, erythrocytes

## COI:

The authors declare no conflict of interest associated with this study.

## Introduction

Selenium (Se) is a sulfur analog that exists in nature in four oxidation states: selenate (iSeVI) (+6), selenite (iSeIV) (+4), elemental selenium ( $Se^0$ ) (0), and selenide ( $HSe^-$ ) (-2) [1]. Se is an essential trace element, yet it is well known that this substance is highly toxic, with a very

## \*Correspondence

Yayoi Kobayashi

Health and Environmental Risk Division, National Institute for Environmental Studies,  
16-2 Onogawa, Tsukuba, Ibaraki 305-8506, JAPAN

Tel ; +81 29 850 2893

E-mail ; [kobayashi.yayoi@nies.go.jp](mailto:kobayashi.yayoi@nies.go.jp)

Received: November 27, 2024

Accepted: January 14, 2025

Released online: February 28, 2025



This work is licensed under a Creative Commons Attribution 4.0 International License.

©2025 THE AUTHORS. [DOI](https://doi.org/10.11299/metallomicsresearch.MR202410) <https://doi.org/10.11299/metallomicsresearch.MR202410>

narrow margin between safe and toxic levels. Se nutritional supply depends on its concentration in food. Both inorganic (iSeIV and iSeVI) and organic Se forms, such as selenocysteine and selenomethionine, can be used as dietary sources. Ingested Se compounds are reduced to  $\text{HSe}^-$ , which is subsequently used in selenoprotein synthesis [2]. Excess Se is methylated to form mono-, di-, or trimethyl-Se, which is then excreted from the body [3, 4].

Arsenic (As) is ubiquitous in the environment and has four oxidation states: arsenate (iAsV) (+5), arsenite (iAsIII) (+3), elemental As (0), and arsine (-3). It causes adverse health effects in humans, including cancer and multiorgan diseases. Millions of people worldwide suffer from chronic As poisoning [5]. However, As has been used to treat acute promyelocytic leukemia in humans [6]. Like Se, As is methylated in the body and excreted [7].

It has been established that Se and As interact in vivo. Understanding the interaction mechanisms of the toxic metalloids Se and As is crucial for elucidating their effects on animal and human health. The chemical properties of Se and As are analogous, and both are conjugated to glutathione (GSH) and methylated within the body [4, 8, 9]. It has been reported that co-treatment of rats with iSeIV and iAsIII resulted in the accumulation of both compounds in the blood and their excretion in the bile [10, 11]. The seleno-bis(S-glutathionyl) arsinium ion  $[(\text{GS})_2\text{AsSe}]^-$  has been identified as the major As metabolite present in the bile of rabbits and rats co-treated with iSeIV and iAsIII [12-14]. Erythrocytes have been identified as the production site of this excretory product in vivo [15, 16]. iSeIV is rapidly and selectively taken up by erythrocytes, where it is reduced to  $\text{HSe}^-$  [17, 18]. Following this reduction,  $\text{HSe}^-$  is transported to the plasma, where it selectively binds to albumin [18, 19]. The specific molecular mechanisms underlying the interaction between Se and As in erythrocytes remain unclear. Therefore, this study aimed to shed light on  $\text{HSe}^-$  released from erythrocytes and propose a mechanism for the erythrocyte uptake of As and Se via the Se-As complex, in addition to the  $[(\text{GS})_2\text{AsSe}]^-$  production mechanism proposed by Kaur et al. [16].

## Materials and Methods

### Chemicals and Reagents

Sodium arsenite ( $\text{NaAsO}_2$ ; iAsIII: 97.0%), sodium selenite ( $\text{Na}_2\text{SeO}_3$ ; iSeIV: 99.0%), monochlorobimane (MCB), syn-(methyl,-methyl) bimane, Trizma<sup>®</sup>base, and bovine serum albumin (BSA), were purchased from Sigma (St. Louis, MO, USA). 4,4'-Diisothiocyanatostilbene-2,2'-disulfonic acid (DIDS) was purchased from Tocris Biosciences (Bristol, UK). Standard solutions containing As and S (100  $\mu\text{g}$  As/mL and 100  $\mu\text{g}$  Se/mL; Accustandard<sup>®</sup>, New Haven, CT, USA) and rhodium (internal standard, 1.01 mg Rh/mL; Wako Pure Chemical Industries, Osaka, Japan) were used for total As and Se analysis. Working standard solutions (10 ng As/mL) were prepared daily using Milli-Q SP water (Yamato Millipore, Tokyo, Japan). GSH, nitric acid ( $\text{HNO}_3$ ), hydrogen peroxide ( $\text{H}_2\text{O}_2$ ), and other chemicals were purchased from FUJIFILM Wako Pure Chemical Corporation (Osaka, Japan).

### Animals and preparation of erythrocyte

Rats are one of the most tolerant animal species to As, and As is known to accumulate in rat erythrocytes following administration of iAs in the form of dimethylarsenical [20] [21]. It has also been reported that large amounts of As accumulate in erythrocytes after dimethylarsinic acid (DMAV) administration [22]. The commercial standard rodent chow (CE-2, Clea Japan Co., Tokyo, Japan) contained fishmeal as a protein source. Arsenobetaine was the major chemical form of As in the standard diet; however, small amounts of arsenocoline, iAsIII, DMAV, and iAsV were also detected [22]. To avoid As compound accumulation in red blood cell diets, pre-weaned rats were used. Male Sprague-Dawley rats (aged 2 weeks) and lactating female rats were obtained from Charles River Japan (Kanagawa, Japan). Following arrival, the lactating rats (with pups) were provided ad libitum access to As-depleted rodent chow (AIN-93G) [23], which used casein as the protein source instead of fish, purchased from Oriental Yeast Co. (Tokyo, Japan), along with sterilized deionized distilled water. Rats were maintained in an air-conditioned, clean room at 22–25°C, 50%–55% relative humidity, and a 12-h light-dark cycle. After 1 week of lactation, weanling male rats (3 weeks old) were separated from the dams and maintained on the same diet for at least 7 weeks until blood collection. This study was conducted in accordance with the Guide for the Care and Use of Laboratory Animals and approved by the Animal Care and Use Committee of the National Institute for Environmental Studies (NIES).

Animals (>10 weeks old) were sacrificed by collecting whole blood from the abdominal aorta in heparin-coated evacuated blood collection tubes under anesthesia (sodium pentobarbital administration). Whole blood was centrifuged at 1,600 *g* for 10 min to remove the buffy coat and plasma. The erythrocytes were rinsed three times with tris-buffered saline (TBS, pH 7.4), and a 20% hematocrit erythrocyte suspension was prepared with TBS.

#### Procedure for total elemental analysis

A 100  $\mu\text{L}$  of each sample was wet-digested with 0.6 mL nitric acid and 0.2 mL hydrogen peroxide at 90°C overnight and then at 130°C for 2 h in an aluminum block bath. The samples were diluted with Milli-Q water, and the concentrations of total As and Se were determined using the internal standard (Rh; *m/z* 103) method with inductively coupled argon plasma mass spectrometry (ICP-MS) (Agilent 7500cx or 8800; Agilent, Japan). The analytical method was validated by measuring As (7500cx (He reaction mode); *m/z* 75:  $^{75}\text{As}^+$  or 8800 ( $\text{O}_2$  reaction mode); *m/z* 91:  $^{75}\text{As}^{16}\text{O}^+$ ) and Se (7500cx ( $\text{H}_2$  reaction mode); *m/z* 78:  $^{78}\text{Se}^+$  or 8800 ( $\text{H}_2$  reaction mode); *m/z* 78:  $^{78}\text{Se}^+$ ) concentrations in the reference samples (NIES CRM No. 18 human urine [NIES, Tsukuba, Japan, *n* = 5]). The certified and measured values for total As and Se in CRM No. 18 human urine were 0.137 and 0.133 As mg/L and 0.059 and 0.057 Se mg/L, respectively.

#### iAsIII and/or iSeIV uptake in erythrocytes with or without GSH or DIDS

iAsIII (final 10  $\mu\text{M}$ ) and/or iSeIV (final 10  $\mu\text{M}$ ) with or without GSH (final 5 mM) or DIDS (final 50  $\mu\text{M}$ ) were added to the erythrocyte suspension (final 10%) and incubated at 37°C for up to 180 or 10 min. Erythrocytes and supernatants were separated by centrifugation (8,000 *g*, 10 s). Each supernatant (*n*=3) was digested with  $\text{HNO}_3$  and  $\text{H}_2\text{O}_2$ , and As and Se concentrations in the supernatant were determined using ICP-MS.

#### Se release from iSeIV-pre-treated erythrocytes and albumin and iAsIII effect on released Se reuptake

iSeIV (final 10  $\mu\text{M}$ ) was added to the erythrocyte suspension (final 10%) and incubated at 37°C for 10 min. The erythrocytes and supernatants were separated by centrifugation (2,000 *g*, 10 min) to prepare the iSeIV-pre-treated erythrocytes. The iSeIV-pre-treated erythrocytes were rinsed three times with TBS (pH 7.4), and a 20% hematocrit erythrocyte suspension was prepared with TBS. The untreated 10% and iSeIV-pre-treated erythrocytes used in this experiment contained  $68.2 \pm 3.68$   $\mu\text{g}/\text{mL}$  and  $513 \pm 18.4$   $\mu\text{g}/\text{mL}$  Se, respectively. BSA (final 50 mg/mL) and/or iAsIII (final 10  $\mu\text{M}$ ) were added to the erythrocyte suspension (final 10%) and incubated at 37°C for up to 10 min. TBS was added instead of BSA or iAsIII to serve as a control. The iSeIV-pre-treated erythrocytes and supernatants were separated by centrifugation (8,000 *g*, 10 s). Each supernatant (*n*=3) was digested with  $\text{HNO}_3$  and  $\text{H}_2\text{O}_2$ , and As and Se concentrations in the supernatant were determined using ICP-MS. The same procedure was performed on erythrocyte suspensions that were not previously treated with iSeIV.

#### Detection of MCB reaction products with $\text{HSe}^-$

Untreated and iSeIV-pre-treated erythrocytes were suspended in TBS solution at a concentration of 10% and incubated at 37°C for 10 min. Erythrocytes and supernatants were separated by centrifugation (8,000 *g*, 10 s). The resulting supernatant was used for  $\text{HSe}^-$  measurement.  $\text{HSe}^-$  levels were measured according to the method described by Imai et al. [24]. Briefly, MCB (final 100  $\mu\text{M}$ ) was added to the supernatant and incubated at 37°C for 1 h. Then, an aliquot of 1 mL sample was extracted with 500  $\mu\text{L}$  ethyl acetate. After dilution with 10 vol.% water, the extracted compounds were subjected to high-performance liquid chromatography (HPLC) analysis. The HPLC system (Shimadzu, Kyoto, Japan) consisted of a CTO-20AC column oven, LC-20AD solvent delivery module, DGU-20A3 degasser, RF-20A Fluorescence detector, and 7125 six-port injection valve with a 20 mL injection loop (Rheodyne, CA, USA). An aliquot of the sample (10  $\mu\text{L}$ ) was applied to a reversed-phase Luna C18(2) column (50 mm  $\times$  3.0 mm; GL Science, Tokyo, Japan) and eluted with 20 mM ammonium formate involving 50% acetonitrile as elution solution (flow rate of 1 mL/min). The samples were analyzed using a fluorometer at excitation and emission wavelengths of 380 and 480 nm, respectively.

## Statistical analysis

Values are presented as the means  $\pm$  SD of three samples. An unpaired multiple *t*-test was used to test the differences between the two means. To test the difference between multiple means, a two-way ANOVA followed by Tukey's multiple comparison test was performed. Statistical significance was set at  $P < 0.05$ . All analyses were performed using GraphPad Prism version 10.3.1 for Windows (GraphPad Software, Boston, Massachusetts, USA, www.graphpad.com).

## Results

### Distribution of arsenic and selenium in erythrocytes, erythrocyte lysates, erythrocyte ghost, and supernatants of erythrocyte suspensions

The total recovery rates of Se and As in 10% erythrocytes and the supernatant were satisfactory, with values ranging from 90.6 to 99.0% (**Table S1**). The recovery rates of both elements from the erythrocyte membrane (ghosts) exhibited a range of 0.456 to 4.10%, with the majority of these elements present in the erythrocytes or the supernatant (**Table S1**). Consequently, in this study, the uptake of both elements into the erythrocytes was assessed based on the attenuation of each element in the supernatant.

### Effects of simultaneous exposure to iAsIII on erythrocytes uptake of Se compounds, and vice-versa

In this study, consistent with previous reports [16, 17], iSeIV was rapidly taken up by erythrocytes (**Fig. S1a**). Except for iSeIV, Se compounds, such as iSeVI, selenomethionine, and selenocyanate, were infrequently incorporated into erythrocytes (**Fig. S1a**). Compared with the uptake levels observed for each Se compound, only iSeIV exhibited increased erythrocyte uptake in iAsIII presence (**Fig. S1a**). iAsIII was slightly taken up by erythrocytes; however, its uptake was elevated in iSeIV presence (**Fig. S1b**). In contrast, the coexistence of Se compounds other than iSeIV did not change iAsIII uptake compared with exposure to iAsIII alone (**Fig. S1b**).

### GSH effect on erythrocyte uptake of As and Se compounds

**Fig. 1** shows iAsIII (**Fig. 1a and b**) and iSeIV (**Fig. 1c and d**) uptake and the simultaneous exposure of iAsIII and iSeIV (**Fig. 1e and f**) in erythrocytes with or without GSH for up to 180 min in vitro. When exposed to iAsIII without GSH, iAsIII was slightly taken up by erythrocytes, and its uptake was inhibited in GSH presence. (**Fig. 1a and b**). Regarding iSeIV, approximately 30% and 67.3% of the added iSeIV was taken up by the erythrocytes immediately after the start of the reaction and within 5 min, respectively, in the absence of GSH (**Fig. 1c and d**). Se recovery from the supernatant decreased up to 5 min, increased slightly from 10 to 30 min, and then decreased gradually (**Fig. 1c**). GSH inhibited iSeIV uptake by the erythrocytes (**Fig. 1c and d**). However, approximately 40% of the added iSeIV was taken up by erythrocytes in GSH presence (**Fig. 1c and d**). In contrast, concurrent exposure to iAsIII and iSeIV in GSH presence significantly impeded the uptake of both elements by erythrocytes. (**Fig. 1e and f**). Compared with the uptake observed when each element was administered individually in GSH absence, iSeIV uptake increased, and iAsIII uptake was significantly enhanced when both elements were present concurrently (**Fig. 1**). Moreover, a time lag occurred between iAsIII and iSeIV uptake: iAsIII was taken up slightly later than iSeIV (**Fig. 1e and f**).

### DIDS effect on erythrocyte uptake of As and Se compounds

iSeIV is transported into erythrocytes via band 3 anion transport proteins, also known as anion exchanger 1 (AE1) or band 3 [17]. As previously reported [16, 17], the iSeIV uptake was inhibited by DIDS (**Fig. 2b**). iAsIII uptake rate by erythrocytes did not change significantly in DIDS presence or absence (**Fig. 2a**). When erythrocytes were simultaneously exposed to iAsIII and iSeIV, the uptake of both elements was almost entirely suppressed in DIDS presence (**Fig. 2c**).

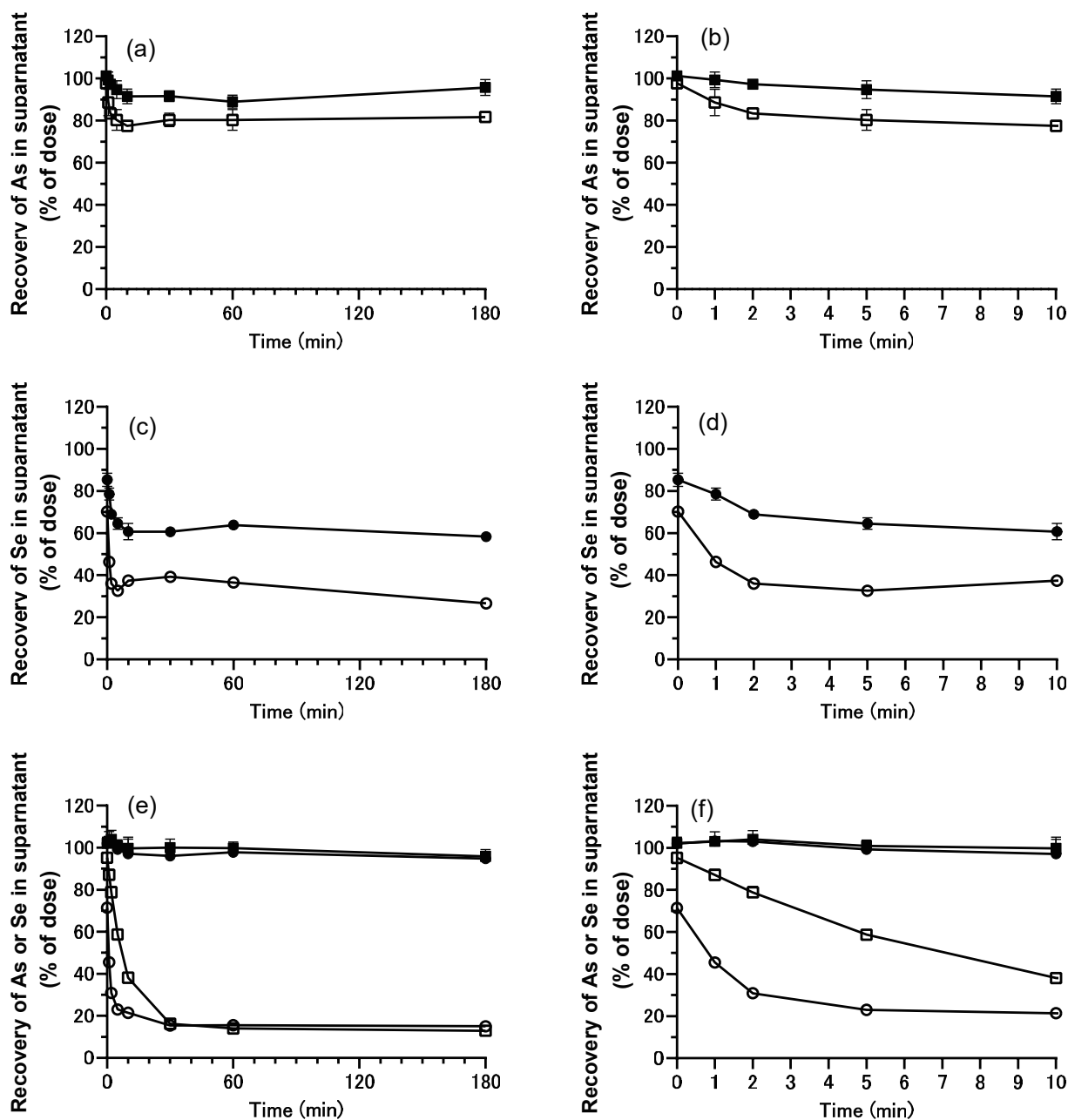


**Fig. 1** Time-course of changes in uptake of As and Se with or without GSH in erythrocytes up to (a, c, and e) 180 min, and (b, d, and f) results for a, c, and e up to 10 min.

iAsIII (final 10  $\mu$ M), iSeIV (final 10  $\mu$ M), and iAsIII and iSeIV (final 10  $\mu$ M of each) with (final 5 mM) or without GSH were added to the erythrocyte suspension (final 10%), and the mixtures were incubated at 37°C for up to 180 min. Erythrocytes and supernatants were separated by centrifugation (8,000  $g$ , 10 s) and total As ( $m/z=75$ ) and Se ( $m/z=78$ ) contents in supernatant were determined by ICP-MS. (a and b) Changes in As recovery rate of supernatant in the presence or absence of 5 mM GSH. (c and d) Changes in Se recovery rate of supernatant in the presence or absence of 5 mM GSH. (e and f) Changes in As and Se recovery rate of supernatant in the presence or absence of 5 mM GSH. Vertical bars indicate As or Se recovery (% of dose) from the supernatant. Open squares and circles represent As and Se without GSH, respectively. Closed squares and circles represent As and Se with GSH, respectively. Values are presented as the mean  $\pm$ SD ( $n = 3$ ).

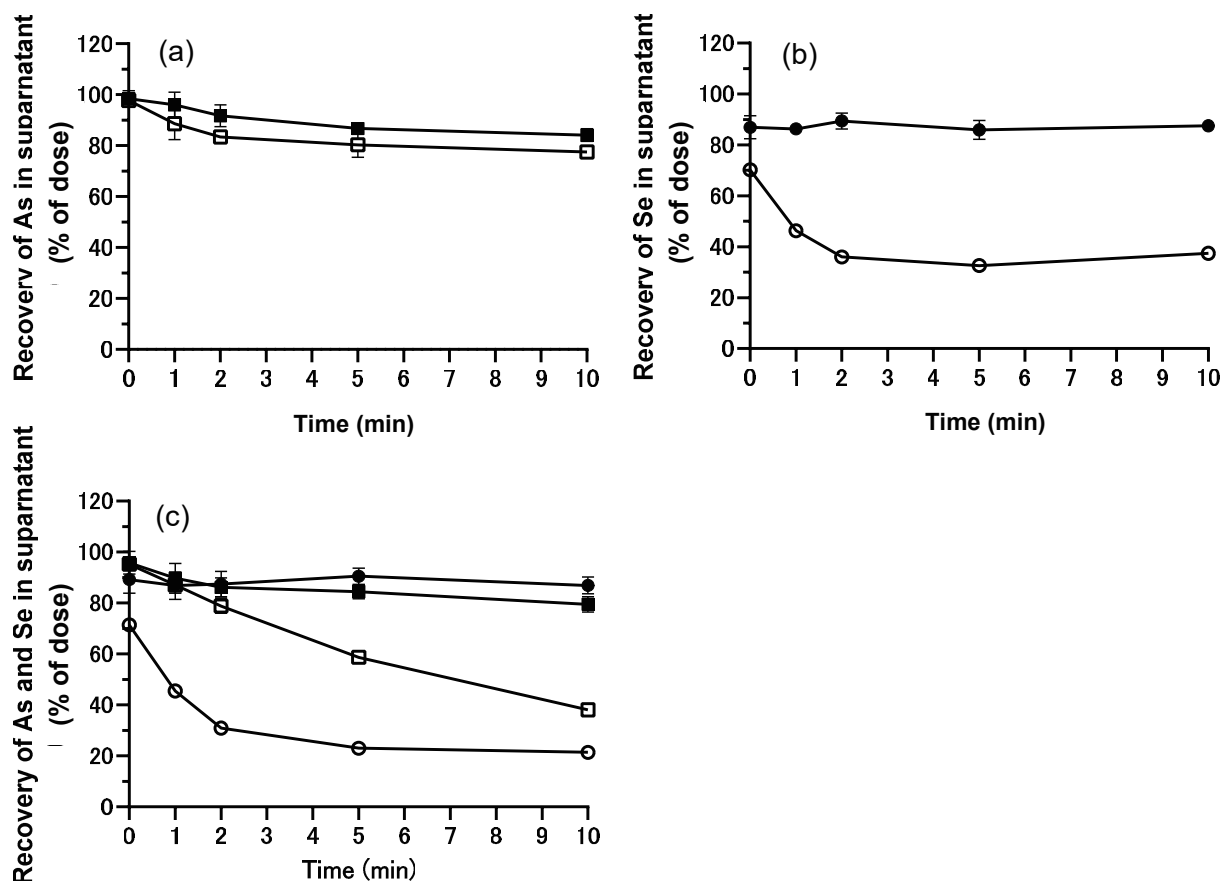


**Fig. 2** Time-course of changes in the uptake of As and Se with or without DIDS in erythrocytes up to 10 min.

**(a) iAsIII, (b) iSeIV, and (c) iAsIII and iSeIV**

iAsIII (final 10 μM), iSeIV (final 10 μM), and iAsIII and iSeIV (final 10 μM of each) with (final 50 μM) or without DIDS were added to the erythrocyte suspension (final 10%), and the mixtures were incubated at 37°C for up to 10 min. Erythrocytes and supernatants were separated by centrifugation (8,000 *g*, 10 s) and total As (*m/z*=75) and Se (*m/z*=78) contents in supernatant were determined by ICP-MS. (a) Changes in As recovery rate of supernatant in the presence or absence of 50 μM DIDS. (b) Changes in Se recovery rate of supernatant in the presence or absence of 50 μM DIDS. (c) Changes in As and Se recovery rate of supernatant in the presence or absence of 50 μM DIDS. Vertical bars indicate As or Se recovery (% of dose) from the supernatant. Open squares and circles, the same data as in Fig 1, represent As and Se without DIDS, respectively. Closed squares and circles represent As and Se with DIDS, respectively. Values are presented as the mean ±SD (*n* = 3).

### Effect of albumin and iAsIII on released Se reuptake from iSeIV-pre-treated erythrocytes

iSeIV, which is taken up by erythrocytes and subsequently chemically modified within erythrocytes, selectively binds to albumin when released [17]. Consequently, plasma proteins, particularly albumin, may influence Se reuptake. iAsIII uptake into iSeIV-pre-treated erythrocytes was significantly enhanced compared with that in untreated erythrocytes (Fig. 3a). iAsIII uptake into erythrocytes was not affected by BSA, with or without iSeIV treatment (Fig. 3a). In BSA presence, Se recovery from the supernatant of the iSeIV-pre-treated erythrocyte suspensions was higher than that in the control group, whereas in iAsIII presence, the recovery was lower than that in the control group (Fig. 3b). In the presence of BSA and iAsIII, Se recovery from the supernatant of iSeIV-pre-treated erythrocyte suspension was lower than that observed in BSA presence and higher than that observed in iAsIII presence (Fig. 3b).

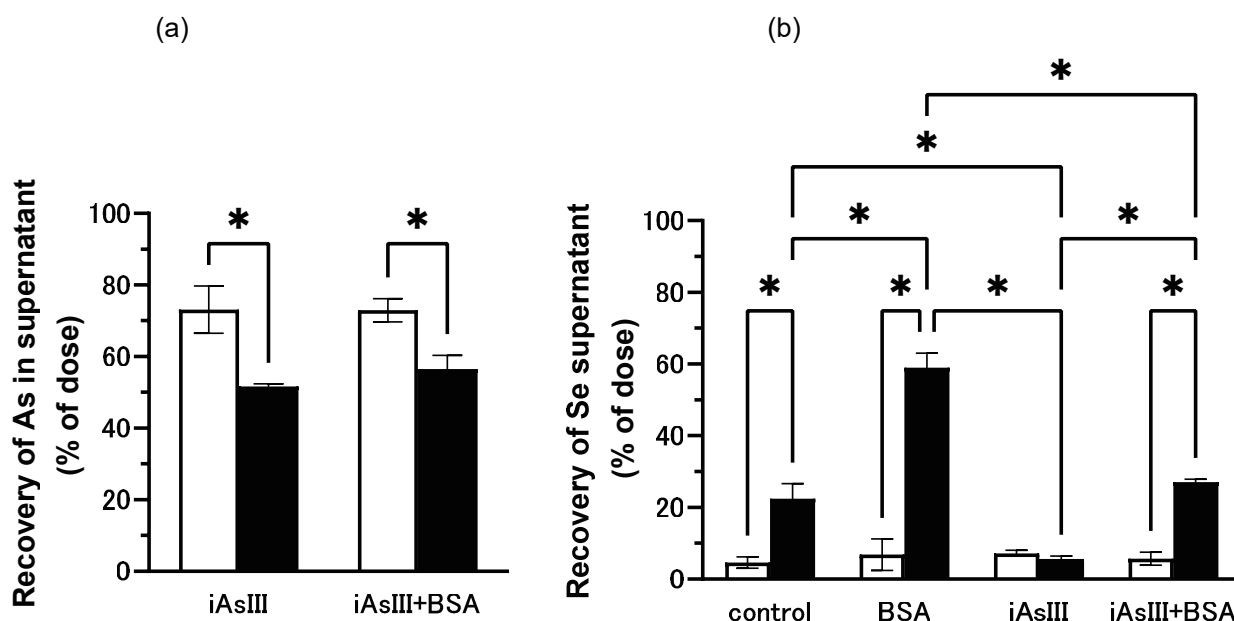


**Fig. 3** Recovery of (a) As with or without BSA and (b) effect of BSA and iAsIII on released Se uptake from untreated and iSeIV-pre-treated erythrocytes.

iAsIII (final 10  $\mu$ M) was added to the untreated or iSeIV-pre-treated erythrocyte (final 10%) with or without BSA (final 50 mg/mL) and then incubated at 37°C for up to 10 min. As another experiment, BSA (final 50 mg/mL) and/or iAsIII (final 10  $\mu$ M) were added to the untreated or iSeIV-pre-treated erythrocyte suspension (final 10%) and incubated at 37°C for up to 10 min. TBS was added instead of BSA or iAsIII to serve as a control. Erythrocytes and supernatants were separated by centrifugation (8,000  $g$ , 10 s). Vertical bars indicate As or Se recovery (% of dose) from the supernatant. Open and closed bars represent untreated and iSeIV-pre-treated erythrocytes, respectively. Values are presented as the mean  $\pm$ SD ( $n = 3$ ). Asterisks indicate significant differences between the samples.

### Identification of Se compounds released extracellularly from erythrocytes

In the bloodstream, iSeIV is rapidly taken up by erythrocytes and subsequently reduced to  $\text{HSe}^-$  [17-19]. Recently, a sensitive, selective, quantitative, and simple method for selenol and  $\text{HSe}^-$  detection has been reported [24]. This method involves MCB reaction, followed by the extraction of the product, syn(methyl, methyl)bimane (*syn*-MMB), using ethyl acetate. Under the conditions used in this study (see Materials and Methods for details), MCB peaks were detected at approximately 1.8, 2.8, and 2.2 min, in order of height. *Syn*-MMB was detected after approximately 2.2 min (Fig. 4a). Although an overlapping peak was observed at approximately 2.2 min, the MCB peak at this time accounts for approximately 8% of the total peak area. Consequently, it was concluded that this peak has a minimal impact on  $\text{HSe}^-$  detection. iSeIV did not react with MCB (Fig. 4b). The enhanced fluorescence intensity of *syn*-MMB in iSeIV-pre-treated erythrocytes, compared with untreated erythrocytes, indicated that  $\text{HSe}^-$  was released from the erythrocytes (Fig. 4c and d).

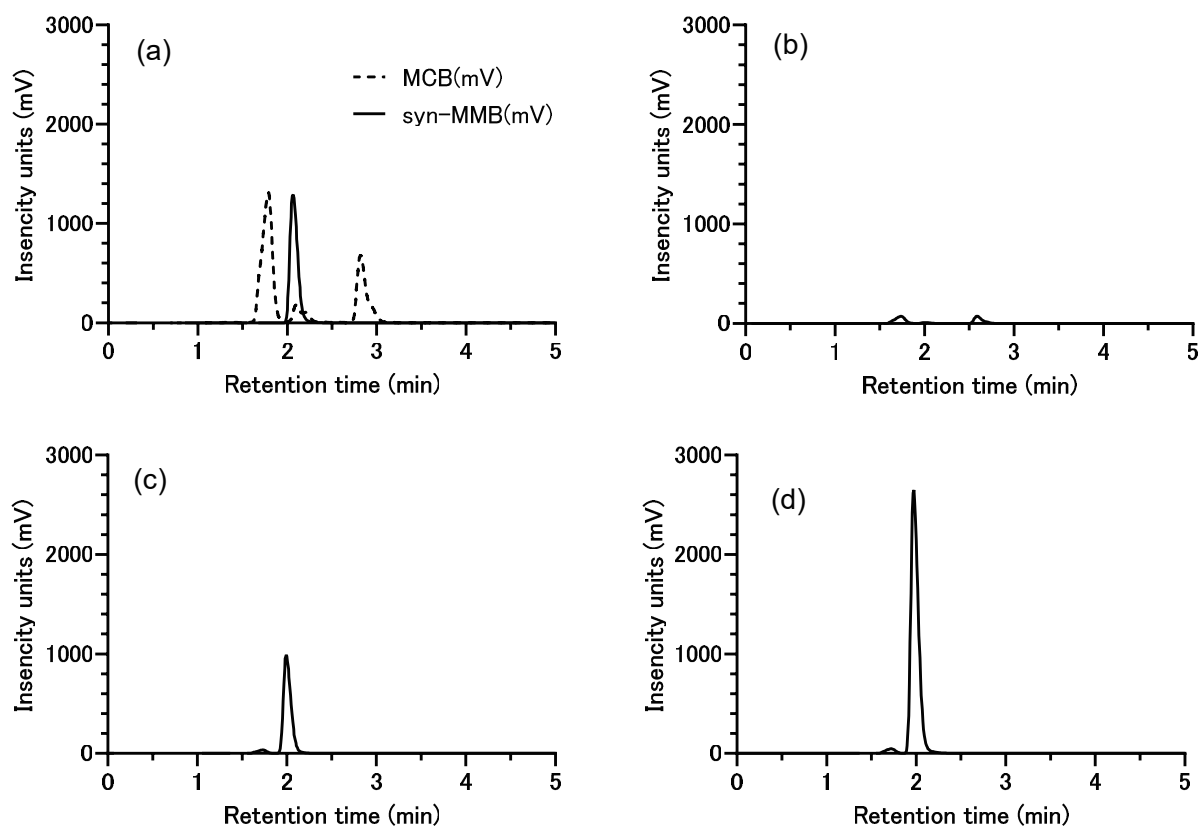


**Fig. 4** Elution profiles of MCB and syn-MMB from (a) standard solutions (0.1 mM MCB and 0.01 mM syn-MMB, respectively), samples reacted with (b) iSeIV, (c) untreated, or (d) iSeIV-pre-treated erythrocytes.

A 10  $\mu\text{L}$  sample was applied to a reversed-phase column and eluted with mobile phase (20 mM ammonium formate / acetonitrile = 50/50) at a flow rate of 1  $\text{mL min}^{-1}$ . Vertical bars indicate intensity units (mV). The dashed line indicates MCB, and the solid line indicates syn-MMB, which is generated by the reaction of MCB with selenol or  $\text{HSe}^-$ .

## Discussion

In this study, iAsIII was slightly taken up by erythrocytes (**Fig. 1a and b**). iAsIII uptake by human erythrocytes is partially inhibited by the aquaporin 3 (AQP3) inhibitors, indicating that AQP3 may play a significant role in iAsIII uptake [16]. AQP3 has been recognized as the primary channel responsible for glycerol transport in both human and rat erythrocytes [25, 26]. Consequently, it has been suggested that AQP3 plays a role in iAsIII uptake by erythrocytes in rats. As triglutathione ( $\text{As}(\text{GS})_3$ ) is generated non-enzymatically [8] and stabilized by GSH [27]. iAsIII uptake into the erythrocytes was inhibited in GSH presence (**Fig. 1a and b**). It is proposed that this phenomenon is the result of the non-enzymatic  $\text{As}(\text{GS})_3$  production as well as a shift in the equilibrium in favor of  $\text{As}(\text{GS})_3$  production by GSH.

Approximately 30% of the added iSeIV was taken up by the erythrocytes immediately after the start of the reaction (**Fig. 1c and d**). The addition of the sample to the erythrocyte suspension and the subsequent separation of the supernatant required approximately 30 s. The results of this study indicate that iSeIV uptake into erythrocytes occurred during this time, i.e., iSeIV was rapidly taken up by the erythrocytes. iSeIV is transported into erythrocytes through band 3 anion transport proteins [16, 17], and its uptake was inhibited by DIDS (**Fig. 2b**). In contrast, iAsIII

uptake by erythrocytes was unaffected by DIDS (**Fig. 2a**). Se recovery in the supernatant exhibited a biphasic pattern, initially decreasing for up to 5 min, then increasing slightly from 10 to 30 min, and subsequently decreasing gradually (**Fig. 1c**), suggesting that Se taken up by erythrocytes is released outside the erythrocytes and then reabsorbed. iSeIV uptake into the erythrocytes was inhibited in GSH presence (**Fig. 1c and d**). Painter first reported that iSeIV reacts with thiol-containing compounds in vitro to produce  $\text{RSSeSR}'$  ( $\text{H}_2\text{SeO}_3 + 4\text{RSH} \rightarrow \text{RSSeSR} + \text{RSSR} + 3\text{H}_2\text{O}$ ) [28]. Subsequently, a series of experiments were conducted to investigate the reaction between iSeIV and GSH [29]. The results demonstrated that the redox reaction of GSH with iSeIV occurs according to the following equation:  $2\text{H}^+ + 4\text{GSH} + \text{SeO}_3^{2-} \rightarrow \text{GSSG} + \text{GSSeSG} + 3\text{H}_2\text{O}$  [30].

GSSeSG has been proposed as an intermediate and major inorganic Se metabolite [31]. Subsequent GSH reduction produces GSH selenopersulfide ( $\text{GSSe}^-$ ) from GSSeSG, which can be readily decomposed to produce  $\text{Se}^0$  as the end product or further reduced to  $\text{HSe}^-$  in the presence of a large excess of GSH [30, 31]. It has been suggested that the production of these Se compounds reduces iSeIV uptake by erythrocytes.

Consistent with previous reports [16], simultaneous exposure to both elements increased iSeIV uptake and significantly enhanced iAsIII uptake into erythrocytes compared with the uptake observed when each element was exposed individually in GSH absence (**Fig. 1**). A temporal delay occurred in iAsIII and iSeIV uptake, with iAsIII being absorbed marginally later than iSeIV (**Fig. 1e and f**). We concentrated on this aspect and predicted the pathway through which  $[\text{AsSe}(\text{OH})_2]^-$  is generated via the reaction between  $\text{HSe}^-$  and iAsIII outside of erythrocytes (**Fig. 5b**). The untreated 10% erythrocytes used in this experiment contained  $68.2 \pm 3.68 \mu\text{g/mL}$  Se, and the iSeIV-pre-treated erythrocytes contained  $513 \pm 18.4 \mu\text{g/mL}$  Se. In this study,  $\text{HSe}^-$  release from untreated erythrocytes was observed; however, the release was significantly more pronounced in erythrocytes treated with iSeIV (**Fig. 4c and d**).  $\text{HSe}^-$  is produced by GSH reduction in erythrocytes, selectively binds to albumin, and is transported to the liver [17, 18, 32]. Se release from iSeIV-pre-treated erythrocytes was markedly enhanced in BSA presence compared with that in its absence (**Fig. 3b**).  $\text{HSe}^-$  was released from erythrocytes and rapidly re-uptaken into the erythrocytes. In the presence of albumin, most of the released Se was rapidly bound to albumin, suggesting that reabsorption into erythrocytes was inhibited (**Fig. 5b**). Conversely, Se release from iSeIV-pre-treated erythrocytes in iAsIII presence was markedly lower than in its absence (**Fig. 3b**). In contrast, iAsIII uptake was significantly increased in iSeIV-pre-treated erythrocytes compared with that in untreated cells (**Fig. 3a**). This phenomenon indicates that  $\text{HSe}^-$  reacts with iAsIII, resulting in the formation of an As-Se compound that is subsequently taken up by erythrocytes, and then conjugated with GSH to produce  $[(\text{GS})_2\text{AsSe}]^-$ . Furthermore, the fact that the uptake of Se and As into erythrocytes when iSeIV and iAsIII were added simultaneously was inhibited by GSH (**Fig. 1e and f**) suggests that  $[\text{AsSe}(\text{OH})_2]^-$  generated outside erythrocytes reacted with excess GSH outside erythrocytes to generate  $[(\text{GS})_2\text{AsSe}]^-$ .

Harper et al. [33] used density functional theory (DFT) and solvent-assisted proton exchange (SAPE) to model the reaction mechanism of iAsIII and iSeIV with thiols and the formation of the As-Se species  $(\text{RS})_2\text{AsSeH}$ . Based on the DFT-SAPE results, the reaction of  $\text{HSe}^-$  with  $\text{As}(\text{SR})_2(\text{OH})$  was reported to be the most favorable mechanism for As-Se bond formation [33]. It has been reported that the pathway where  $\text{HSe}^-$  attacks iAsIII to form intermediate  $\text{As}(\text{OH})_2\text{SeH}$ , followed by RSH as a nucleophile to form  $\text{As}(\text{RS})_2\text{SeH}$ , requires more energy and depends on the rates of iAsIII consumption and  $\text{RSSeH}$  and  $\text{HSe}^-$  formation [33]. The limitation of this study is the inability to identify As-Se compounds, such as  $[\text{AsSe}(\text{OH})_2]^-$  and  $[(\text{GS})_2\text{AsSe}]^-$  (**Fig. 5b**). We have attempted to detect As-Se complexes but have not succeeded yet.

In conclusion, it is highly likely that the pathway presented in **Fig. 5a** is the main pathway for  $[(\text{GS})_2\text{AsSe}]^-$  formation; however, the possibility that the pathway presented in **Fig. 5b** is an alternative pathway cannot be ruled out. Further research is needed to clarify these issues, including the isolation of As-Se compounds, which are thought to be reaction intermediates and kinetic studies.

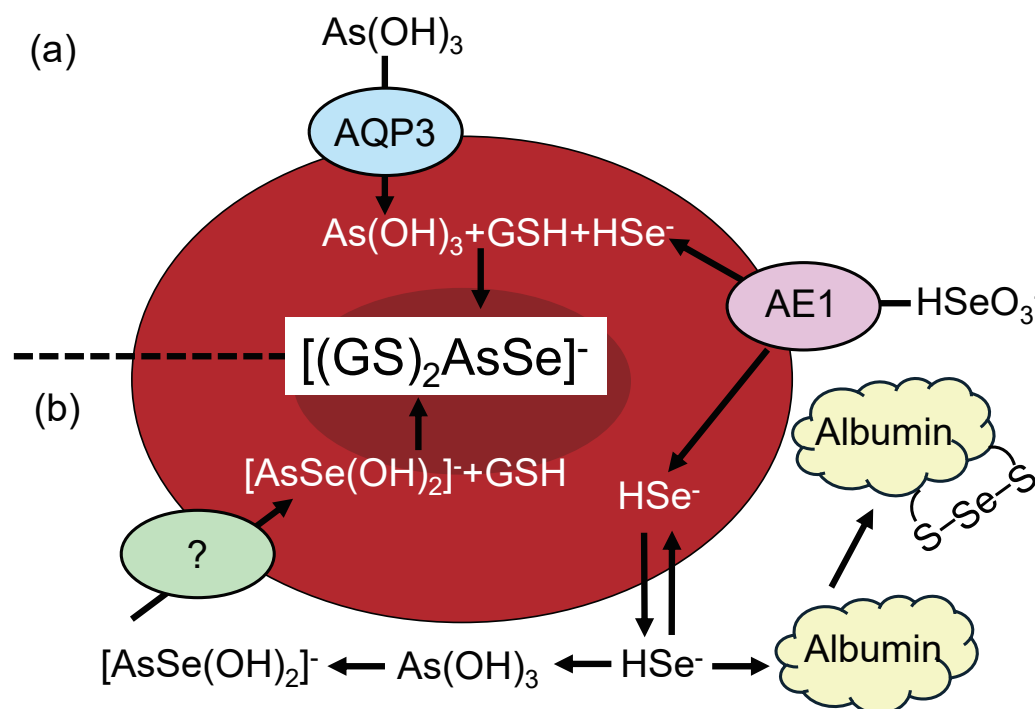


**Fig. 5** Two putative pathways for the enhancement of iAsIII and iSeIV uptake in erythrocytes when these two metalloids are doped simultaneously. (a) proposed by Kaur G et al. [16] and (b) proposed in the present study.

### Acknowledgments

This study was conducted with intramural funding from the National Institute for Environmental Studies.

### Author's contribution

Conceptualization: Y. K. and S. H.; methodology: Y. K. and S. H.; investigation: Y. K.; validation: Y. K. and S. H.; formal analysis: Y. K.; writing of the original draft: Y. K.; review and editing: S. H. and Y. K.; funding acquisition: Y. K.; supervision: S. H.

### References

- [1] Barceloux DG. Selenium. *J Toxicol Clin Toxicol.* 1999; 37 (2): 145-172.
- [2] Low SC, Harney JW, Berry MJ. Cloning and functional characterization of human selenophosphate synthetase, an essential component of selenoprotein synthesis. *J Biol Chem.* 1995; 270 (37): 21659-21664.
- [3] Itoh M, Suzuki KT. Effects of dose on the methylation of selenium to monomethylselenol and trimethylselenonium ion in rats. *Arch Toxicol.* 1997; 71 (7): 461-466.
- [4] Kobayashi Y, Ogra Y, Ishiwata K, Takayama H, Aimi N, Suzuki KT. Selenosugars are key and urinary metabolites for selenium excretion within the required to low-toxic range. *P Natl Acad Sci USA.* 2002; 99 (25): 15932-15936.
- [5] Rodriguez-Lado L, Sun G, Berg M, Zhang Q, Xue H, Zheng Q, Johnson CA. Groundwater arsenic contamination throughout China. *Science.* 2013; 341 (6148): 866-868.
- [6] Miller WH, Jr., Schipper HM, Lee JS, Singer J, Waxman S. Mechanisms of action of arsenic trioxide. *Cancer Res.* 2002; 62 (14): 3893-3903.
- [7] Lin S, Shi Q, Nix FB, Styblo M, Beck MA, Herbin-Davis KM, Hall LL, Simeonsson JB, Thomas DJ. A novel S-adenosyl-L-methionine:arsenic(III) methyltransferase from rat liver cytosol. *J Biol Chem.* 2002; 277 (13): 10795-10803.
- [8] Hayakawa T, Kobayashi Y, Cui X, Hirano S. A new metabolic pathway of arsenite: arsenic-glutathione complexes are substrates for human arsenic methyltransferase Cyt19. *Arch Toxicol.* 2005; 79 (4): 183-191.
- [9] Sun HJ, Rathinasabapathi B, Wu B, Luo J, Pu LP, Ma LQ. Arsenic and selenium toxicity and their interactive effects in humans. *Environment International.* 2014; 69: 148-158.
- [10] Csanaky I, Gregus Z. Effect of selenite on the disposition of arsenate and arsenite in rats. *Toxicology.* 2003; 186 (1-2): 33-50.
- [11] Gregus Z, Gyurasics A, Koszorús L. Interactions between selenium and group Va-metalloids (arsenic, antimony and bismuth) in the biliary excretion. *Environ Toxicol Phar.* 1998; 5 (2): 89-99.

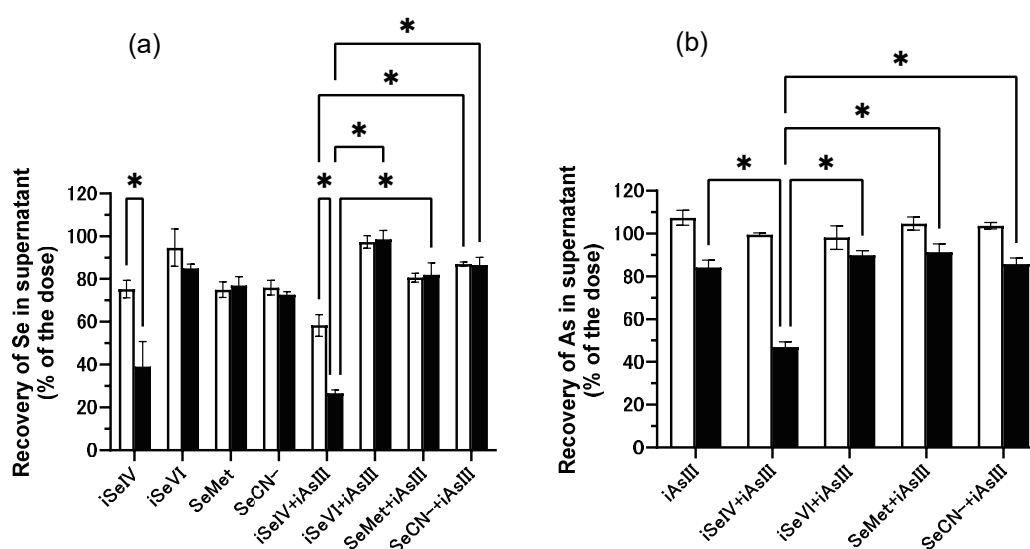
- [12] Gailer J, George GN, Pickering IJ, Prince RC, Younis HS, Winzerling JJ. Biliary excretion of [(GS)(2)AsSe](-) after intravenous injection of rabbits with arsenite and selenite. *Chem Res Toxicol*. 2002; 15 (11): 1466-1471.
- [13] Gailer J, Madden S, Buttigieg GA, Denton MB, Younis HS. Identification of [(GS)AsSe] in rabbit bile by size-exclusion chromatography and simultaneous multielement-specific detection by inductively coupled plasma atomic emission spectroscopy. *Appl Organomet Chem*. 2002; 16 (2): 72-75.
- [14] George GN, Gailer J, Ponomarenko O, La Porte PF, Strait K, Alauddin M, Ahsan H, Ahmed S, Spallholz J, Pickering IJ. Observation of the seleno bis-(S-glutathionyl) arsinium anion in rat bile. *J Inorg Biochem*. 2016; 158: 24-29.
- [15] Manley SA, George GN, Pickering IJ, Glass RS, Prenner EJ, Yamdagni R, Wu Q, Gailer J. The seleno bis(-glutathionyl) arsinium ion is assembled in erythrocyte lysate. *Chem Res Toxicol*. 2006; 19 (4): 601-607.
- [16] Kaur G, Javed W, Ponomarenko O, Shekh K, Swanlund DP, Zhou JR, Summers KL, Casini A, Wenzel MN, Casey JR, Cordat E, Pickering IJ, George GN, Leslie EM. Human red blood cell uptake and sequestration of arsenite and selenite: Evidence of seleno-bis(S-glutathionyl) arsinium ion formation in human cells. *Biochem Pharmacol*. 2020; 180: 114141.
- [17] Suzuki KT, Shiobara Y, Itoh M, Ohmichi M. Selective uptake of selenite by red blood cells. *Analyst*. 1998; 123 (1): 63-67.
- [18] Kobayashi Y, Ogra Y, Suzuki KT. Speciation and metabolism of selenium injected with <sup>82</sup>Se-enriched selenite and selenate in rats. *J Chromatogr B Biomed Sci Appl*. 2001; 760 (1): 73-81.
- [19] Shiobara Y, Suzuki KT. Binding of selenium (administered as selenite) to albumin after efflux from red blood cells. *J Chromatogr B*. 1998; 710 (1-2): 49-56.
- [20] Lerman S, Clarkson TW. The Metabolism of Arsenite and Arsenate by the Rat. *Fund Appl Toxicol*. 1983; 3 (4): 309-314.
- [21] Vahter M, Marafante E, Dencker L. Tissue distribution and retention of <sup>74</sup>As-dimethylarsinic acid in mice and rats. *Arch Environ Contam Toxicol*. 1984; 13 (3): 259-264.
- [22] Kobayashi Y, Hirano S. Distribution and Excretion of Arsenic Metabolites after Oral Administration of Seafood-Related Organoarsenicals in Rats. *Metals*. 2016; 6 (10): 231.
- [23] Reeves PG, Nielsen FH, Fahey GC. AIN-93 Purified Diets for Laboratory Rodents - Final Report of the American Institute of Nutrition Ad Hoc Writing Committee on the Reformulation of the AIN-76a Rodent Diet. *J Nutr*. 1993; 123 (11): 1939-1951.
- [24] Imai T, Kurihara T, Esaki N, Mihara H. Selective fluorescence detection method for selenide and selenol using monochlorobimane. *Anal Biochem*. 2017; 532: 1-8.
- [25] Roudier N, Verbavatz JM, Maurel C, Ripoche P, Tacnet F. Evidence for the presence of aquaporin-3 in human red blood cells. *J Biol Chem*. 1998; 273 (14): 8407-8412.
- [26] Liu YJ, Promeneur D, Rojek A, Kumar N, Frokizer J, Nielsen S, King LS, Agre P, Carbrey JM. Aquaporin 9 is the major pathway for glycerol uptake by mouse erythrocytes, with implications for malarial virulence. *P Natl Acad Sci USA*. 2007; 104 (30): 12560-12564.
- [27] Kobayashi Y, Cui X, Hirano S. Stability of arsenic metabolites, arsenic triglutathione [As(GS)<sub>3</sub>] and methylarsenic diglutathione [CH<sub>3</sub>As(GS)<sub>2</sub>], in rat bile. *Toxicology*. 2005; 211 (1-2): 115-123.
- [28] Painter EP. The chemistry and toxicity of selenium compounds, with special reference to the selenium problem. *Chem Rev*. 1941; 28 (2): 179-213.
- [29] Kessi J, Hanselmann KW. Similarities between the abiotic reduction of selenite with glutathione and the dissimilatory reaction mediated by and. *J Biol Chem*. 2004; 279 (49): 50662-50669.
- [30] Qiao Y, Huang X, Chen B, He M, Hu B. In vitro study on antagonism mechanism of glutathione, sodium selenite and mercuric chloride. *Talanta*. 2017; 171: 262-269.
- [31] Hsieh HS, Ganther HE. Acid-volatile selenium formation catalyzed by glutathione reductase. *Biochemistry*. 1975; 14 (8): 1632-1636.
- [32] Sandholm M. The initial fate of a trace amount of intravenously administered selenite. *Acta Pharmacol Toxicol (Copenh)*. 1973; 33 (1): 1-5.
- [33] Harper LK, Antony S, Bayse CA. Thiol Reduction of Arsenite and Selenite: DFT Modeling of the Pathways to an As-Se Bond. *Chem Res Toxicol*. 2014; 27 (12): 2119-2127.

## Supplemental Information

**Table S1** Arsenic and selenium recovered from each sample.

Selenite (iSeIV) (final 10  $\mu$ M) and/or arsenite (iAsIII) (final 10  $\mu$ M) were added to the erythrocyte suspension (final 10%) and then incubated at 37°C for up to 10 min. Values are presented as the mean  $\pm$ SD (n = 3).

	(a) 10% erythrocytes	(b) 10% lysate	(c) 10% ghost	(d) supernatant	(e) Total (a+d)	(f) Total (b+c+d)
Recovery of Se (% of the dose)						
iSeIV	69.4 $\pm$ 1.70	57.7 $\pm$ 3.40	2.45 $\pm$ 0.770	21.2 $\pm$ 0.90	90.6	81.4
iSeIV+iAsIII	83.7 $\pm$ 1.87	67.0 $\pm$ 3.09	4.10 $\pm$ 1.15	12.5 $\pm$ 0.392	96.2	102
Recovery of As (% of the dose)						
iAsIII	14.4 $\pm$ 1.15	6.63 $\pm$ 0.190	0.456 $\pm$ 0.194	84.5 $\pm$ 1.88	98.9	91.6
iSeIV+iAsIII	84.8 $\pm$ 2.00	66.2 $\pm$ 3.37	3.48 $\pm$ 1.18	14.2 $\pm$ 0.629	99.0	83.9

**Fig. S1** Accumulation of (a) Se and (b) As in the erythrocytes.

Se compounds (final 10  $\mu$ M), such as selenite (iSeIV), selenate (iSeVI), selenomethionine (SeMet), selenocyanate (SeCN-), and/or arsenite (iAsIII) (final 10  $\mu$ M) were added to the erythrocyte suspension (final 10%) and then incubated at 37°C for up to 10 min. Erythrocytes and supernatants were separated by centrifugation (8,000 *g*, 10 s). Vertical bars indicate As or Se recovery (% of dose) from the supernatant. Open and closed bars represent before and after incubation, respectively. Values are presented as the mean  $\pm$ SD (n = 3). Asterisks indicate significant differences between the samples. The experiment was performed in duplicate to ensure reproducibility.

# A suppressive effect of selenium on amyloid- $\beta$ plaque deposition in Tg2576 transgenic mice brain

Sakura Yoshida<sup>1\*</sup>, Takeshi Fuchigami<sup>2</sup>, Morio Nakayama<sup>1</sup>, Mamoru Haratake<sup>3\*</sup>

<sup>1</sup> Graduate School of Biomedical Sciences, Nagasaki University

<sup>2</sup> Graduate School of Medical Sciences, Kanazawa University

<sup>3</sup> Faculty of Pharmaceutical Sciences, Sojo University

## Abstract

Alzheimer's disease (AD) is a chronic neurodegenerative disease and characterized by deposition of the amyloid- $\beta$  (A $\beta$ ) peptide in the brain. Reactive oxygen species (ROS) are thought to be associated with the onset and/or progression of AD. Selenium-dependent glutathione peroxidases (GPxs) play a critical role in the brain in the extinction of ROS. The selenium concentration in the brain is kept higher than those of other organs/tissues even when dietary selenium is limited, which suggests the importance of this element in the brain. We previously reported that a dietary selenium deficiency caused the elevated deposition of A $\beta$  plaques in the brain of Tg2576 transgenic mice, which is frequently used as a model of AD. In this study, we analyzed the GPx activity and lipid peroxidation of brain tissues after the feeding of a selenium-deficient diet to Tg2576 transgenic mice. We also investigated the effect of seleno-L-methionine (SeMet) supplementation on the A $\beta$  plaque deposition in the brain. After feeding for 72 weeks, the selenium concentration and GPx activity in the brain of the selenium-deficient diet-fed mice was lower than those in the selenium-adequate diet-fed mice and SeMet-supplemented diet-fed mice. The deposition of A $\beta$  plaques and lipid peroxidation in the SeMet-supplemented diet-fed mice brain appeared to decrease compared to those in the selenium-deficient diet-fed mice. Supplementation of SeMet might have a suppressive effect on the brain A $\beta$  plaque deposition in the Tg2576 transgenic mice.

**Key words:** selenium, Alzheimer's disease, amyloid- $\beta$ , seleno-L-methionine, Tg2576 mouse

**Statements about COI:** The authors declare no conflict of interest associated with this manuscript.

## \*Correspondence

Sakura Yoshida, Ph.D. Assistant professor  
Department of Hygienic Chemistry, Graduate School of  
Biomedical Sciences, Nagasaki University  
1-14 Bunkyo-machi, Nagasaki 852-8521, Japan  
**Tel ;** +81 95 819 2443  
**E-mail ;** yoshida-s@nagasaki-u.ac.jp

Mamoru Haratake, Ph.D. Professor  
Faculty of Pharmaceutical Sciences, Sojo University  
4-22-1 Ikeda, Kumamoto 860-0082, Japan  
**Tel ;** +81 96 326 3816  
**E-mail ;** haratake@ph.sojo-u.ac.jp

Received: November 30, 2024

Accepted: February 05, 2025

Released online: March 13, 2025



This work is licensed under a Creative Commons Attribution 4.0 International License.

©2025 THE AUTHORS. [DOI](https://doi.org/10.11299/metallomicsresearch.MR202413) <https://doi.org/10.11299/metallomicsresearch.MR202413>

## Introduction

Alzheimer's disease (AD) is a neurodegenerative disease and the most common type of dementia in elderly people. Currently, about 50 million people are suffering from AD around the world and the number is estimated to triple by 2050 [1].

The deposition of amyloid  $\beta$  (A $\beta$ ) peptides and aggregation of tau proteins in a patient's brain are the pathological hallmarks of AD, and these are supposed to impair multiple cellular functions [2, 3]. However, the detailed underlying etiological mechanisms causing the AD clinical symptoms, such as memorial damage and cognitive decline, have still not been completely understood. Despite extensive research, few treatments are currently available for AD [4]. Cholinesterase inhibitors and antagonist of the *N*-methyl-D-aspartate receptor are commonly used for the treatment of AD patients, although these medicines only slow down the development of the AD symptoms. Recently, the monoclonal antibody against A $\beta$ , aducanumab and lecanemab, has been developed and used for the treatment of AD [5, 6]. These A $\beta$ -targeting drugs has successively reduced the A $\beta$  plaque deposition in AD patients' brain, however, improvement of the cognitive function by these reagents is limited and sometimes caused severe side effects [7, 8].

A $\beta$  peptide deposition is predicted to cause a neurotoxic effect such as synaptic dysfunction and neuronal loss in the brain [2, 9]. Understanding of the molecular pathogenesis underlying the onset and progression of AD is necessary for the development of an effective strategy of prevention or treatment of the disease. Increasing evidence indicates that various factors, such as genetic background, environmental pollution, lifestyles and accumulation of heavy metals, are involved in the cause of AD [4, 10, 11].

The accumulation of reactive oxygen species (ROS) was reported to cause cytotoxic oxidation and was thought to be related to the onset and progression of AD [3, 10, 12]. Because selenium is a crucial factor of several antioxidative enzymes, such as selenium dependent glutathione peroxidases (GPxs), which reduces peroxides inevitably generated in organisms, selenium has been suggested to be related to the AD pathogenesis [13, 14]. However, the biological effect of selenium on AD pathology is currently complicated [15, 16]. Some studies have shown a lower selenium status associated with the decreasing cognitive function [17, 18]. On the other hand, a large scale placebo-controlled, randomized clinical trial, PREADViSE, showed no effect of selenium supplementation on the prevention of AD [19]. Several selenoproteins, proteins containing one or more seleno-L-cysteine in their amino acid sequence, including GPxs, selenoprotein P, selenoprotein K and selenoprotein W are reported to be involved in the AD pathology, A $\beta$  metabolism and toxicity caused by A $\beta$  fibrils [20–24]. In our previous research, a selenium deficient diet was fed to Tg2576 transgenic mice for 76 weeks which resulted in a more than 2 times increase of the A $\beta$  plaque deposition in the brains of selenium-deficient diet-fed mice compared to the control selenium-adequate diet-fed mice [25]. This result suggested that selenium in the brain is involved in the metabolism of brain A $\beta$  in Tg2576 transgenic mice. In this study, we evaluated the suppressive effect of dietary selenium against the deposition of A $\beta$  plaques in the Tg2576 transgenic mice brain. We compared the effect of dietary selenium on the A $\beta$  plaque deposition in brains by feeding 3 different diets to Tg2576 transgenic mice, i.e., a selenium-adequate normal diet, selenium-deficient diet, or seleno-L-methionine (SeMet)-supplemented diet.

## Materials and Methods

### Materials

Seleno-L-methionine (SeMet), glutathione in the reduced form (GSH), hydrogen peroxide, 2-thiobarbituric acid (TBA) and thioflavin T (Th-T) were purchased from Nacalai Tesque, Inc. (Kyoto, Japan). 2,3-Diaminonaphthalene (DAN) was from Dojindo Molecular Technologies, Inc. (Kumamoto, Japan). Nicotinamide adenine dinucleotide phosphate in the reduced form (NADPH) and glutathione reductase (GR) were from the FUJIFILM Wako Pure Chemical Corporation (Osaka, Japan). The water used throughout this study ( $>18$  M $\Omega$  cm) was generated by a Milli-Q Reference system (Millipore Corp., Billerica, MA, USA). All other chemicals were of commercial reagent or special grade and used as received.

### Animals and diets

Female 16-week-old Tg2576 transgenic mice were purchased from Taconic Farms, Inc. (Germantown, NY, USA). They were cared for in accordance with the guidelines of the Nagasaki University on Animal Care. Animals were randomly assigned to 3 groups (5 in each) and kept one per cage. The mice were housed on a 12 h light-12 h dark schedule at  $23 \pm 2$  °C and 60% relative humidity and freely fed the selenium-adequate regular breeding diet (CE-2, Clea Japan, Inc., Tokyo, Japan), selenium-deficient diet (F2SeDD, Oriental Yeast Co., Ltd., Tokyo, Japan), or SeMet-supplemented diet for 72 weeks. The Torula yeast-based selenium deficient diet was prepared to contain 0.4  $\mu\text{gSe/g}$  or less by the manufacturer and the actual selenium content was 0.007  $\mu\text{gSe/g}$ . The CE-2 regular diet was reported to contain 0.4-0.6  $\mu\text{gSe/g}$ . The SeMet-supplemented diet was prepared every 30 days by the addition of SeMet to the selenium-deficient diet to make the selenium concentration 2  $\mu\text{gSe/g}$ . SeMet was dissolved in Milli-Q water and sprayed on the selenium-deficient diet.

After feeding for 72 weeks, the selected organs/tissues were obtained from the mice under isoflurane anesthesia. The harvested tissues were thoroughly rinsed with 66 mM phosphate buffer (pH 7.4) and stored at  $-80$  °C until used. Blood was collected into heparin-coated tubes and centrifuged at 1,000 *g* for 10 min to separate the plasma and hemocytes. The left hemisphere of the mice brain was immersed in an optimal cutting temperature (OCT) compound (Tissue-Tek O. C. T. Compound, Sakura Finetek USA, Inc., CA, USA) and frozen on dry ice for preparation of the brain slices.

### Preparation of tissue lysate

Tissues were homogenized in 66 mM phosphate buffer using a Polytron PT1200E (Kinematica AG, Luzern, Switzerland) on ice. The homogenate was then sonicated at an acoustic power level of 20 W using a probe-type sonicator 250D (Branson Ultrasonic Corp., Danbury, CT, USA). The suspension was subsequently centrifuged in a rotor 70.1Ti using an Optima L-80 Ultracentrifuge (Beckman Coulter, Inc., Indianapolis, IN, USA) at 30,200 *g*, 4 °C for 1 h. The obtained supernatant was used for the determination of the protein concentration and measurement of the GPx activity.

### Preparation of brain slice and its staining with thioflavin T

The OCT compound embedded brain was cut into 10- $\mu\text{m}$  thick slices by a cryostat CM1950 (Leica Microsystems, Wetzlar, Germany). For staining of the A $\beta$  plaque, the Tg2576 mice brain slices were covered with a 10  $\mu\text{M}$  Th-T in 50% ethanol solution for 5 min at room temperature, then washed 5 times with 50% ethanol for 1 min. The fluorescence image was captured by an inverted microscope BZ-8100 (KEYENCE Corporation, Osaka, Japan) using a filter set with 450-470 nm excitation and 515-565 nm emission. MetaMorph (Premier) software (Molecular Devices, LLC, Sunnyvale, CA, USA) was used for the qualitative analysis of the obtained fluorescence images of the mice brain slices.

### Determination of selenium

After acid digestion with a 1 : 4 mixture by volume of perchloric acid and nitric acid, the selenium concentrations in the specimens were fluorometrically determined using DAN [26]. The digested samples were reacted with DAN in a 0.1 M HCl solution containing 0.1 M EDTA and 0.1 M NaF at 60 °C for 20 min with 120 str/min followed by extraction with cyclohexane. The fluorescent intensity (Ex: 375 nm, Em: 520 nm) was measured by a FP-6600 fluorometer (Jasco Corporation, Tokyo, Japan). The selenium standard solution for the atomic absorption spectrometry (1000 mg/L in 0.1 mol/L nitric acid, Kanto Chemical Co., Inc., Tokyo, Japan) was used as the standard material for preparation of the calibration curve (0.1-1000 ng Se/mL).

### Determination of glutathione peroxidase activity and protein concentrations

The protein concentrations in the specimens were measured by the Lowry method using bovine serum albumin (Nacalai Tesque, Inc.) as the standard [27].

The tissue GPx activity was measured by monitoring the absorbance at 340 nm due to the NADPH [28]. The tissue lysate was combined with sodium azide (1 mM), a GR solution (1 unit/mL), a reduced GSH solution (1 mM) and an NADPH solution (0.2 mM) in 66 mM phosphate buffer (pH 7.4). The reaction was initiated by the addition of a hydrogen peroxide solution (0.25 mM). The absorbance at 340 nm was recorded every 1 min just after mixing by inversion using a V-660 spectrometer (JASCO Corp.). The GPx activity was calculated using the following equation (1) as  $\mu$ moles of NADPH oxidized per minute, where  $\Delta A_{\text{SAM}}$  is the decrease in the absorbance at 340 nm of the sample solutions between 15 and 75 s after the addition of the substrates,  $\Delta A_{\text{BLK}}$  is the decrease in absorbance at 340 nm per minute of the solutions using the 66 mM phosphate buffer instead of the sample solutions, 10 is the dilution factor,  $\epsilon_{\text{mM}}$  is the extinction coefficient for the 1 mM NADPH solution ( $6.22 \text{ mM}^{-1} \text{ cm}^{-1}$ ), and  $c$  is the protein content (mg/mL).

$$\text{GPx activity} = (\Delta A_{\text{SAM}} - \Delta A_{\text{BLK}}) \times 10 / \epsilon_{\text{mM}} / c \quad (1)$$

### Determination of TBA reactive substance (TBARS)

The TBARS was measured according to the method of Tien & Aust [29]. The 2 $\times$  amount of TBA reagent solution (0.375% TBA, 15% butyl hydroxytoluene, 0.4% trichloroacetic acid in 0.25 M HCl) was mixed with the brain cell lysate and boiled for 15 min. After centrifugation at 3,000 rpm for 10 min at room temperature, the absorbance at 535 nm of the supernatant was measured by a V-660 spectrometer (JASCO Corp.). The TBARS was calculated by equation (2) as moles of red pigment produced by the reaction, where  $A_{\text{SAM}}$  is the absorbance at 535 nm of the sample solutions,  $A_{\text{BLK}}$  is the absorbance at 535 nm of the solutions using the 66 mM phosphate buffer instead of the sample solutions, 6 is the dilution factor, and  $1.56 \times 10^5$  is the molar extinction coefficient of the produced red pigment after the reaction.

$$\text{TBARS (mol/g)} = (A_{\text{SAM}} - A_{\text{BLK}}) \times 6 / (1.65 \times 10^5 \times \text{brain tissue weight}) \quad (2)$$

### Statistical analysis

All the data are presented as the mean and standard error (SE). Statistical analyses were performed using PRISM 10 (GraphPad Software, Inc., La Jolla, CA, USA). Statistically significant differences between the feeding groups were determined by a one-way ANOVA using the Tukey method. Comparisons were considered to be statistically significant at  $P < 0.05$ .

### Results and discussion

Selenium concentrations in the organs/tissues of selenium-deficient diet-fed Tg2576 mice substantially decreased compared to those of the selenium-adequate diet-fed mice after feeding for 72 weeks (**Figure 1**). Selenium concentrations of the livers, kidneys, hearts and muscles in the selenium-deficient diet-fed mice were 8.2%, 20.0%, 10.7% and 9.3% of those in the selenium-adequate diet-fed mice, respectively. On the other hand, the brain selenium concentration in the selenium-deficient diet-fed mice decreased to 50% of that in the selenium-adequate diet-fed mice. A similar selenium status in the organs/tissues after selenium-deficient diet feeding was observed in our previous research using the ICR and Tg2576 transgenic mice [25, 30]. The selenium concentration in the brain is far less variable than those in other peripheral organs/tissues when the selenium intake from the diets is limited [31, 32]. This brain specific selenium retention suggested the vital role of selenium in the brain. Feeding of the SeMet-supplemented diet increased the selenium concentrations in the organs/tissues of the Tg2576 mice 1.5-5.6 times in comparison to the selenium-adequate diet feeding. Selenium concentrations of the brains, livers, kidneys, hearts and muscles in the SeMet-supplemented diet-fed mice were 3.7, 2.1, 1.6, 4.3 and 5.6 times higher than those in selenium-adequate diet-fed mice, respectively. Because SeMet is non-specifically incorporated into proteins in the position of Met, it is known to be incorporated into organs/tissues with high rates of protein synthesis such as the skeletal muscles, pancreas, erythrocytes, livers and kidneys [33, 34]. SeMet was also reported to be retained

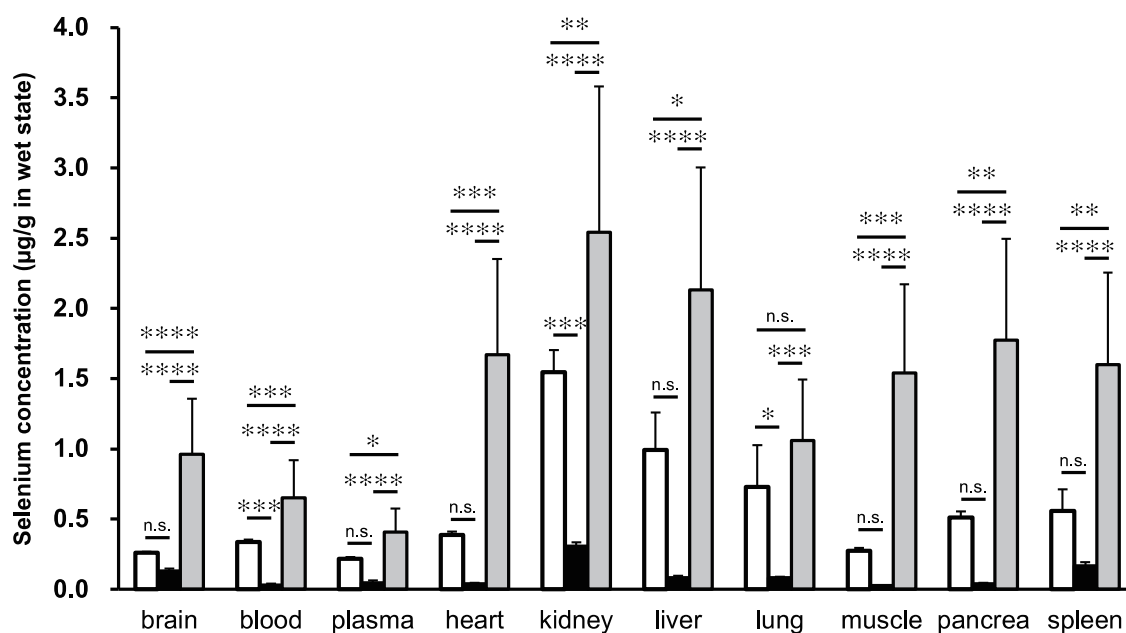


**Figure 1.** Selenium concentration in organs/tissues of Tg2576 transgenic mice after the feeding. White column, selenium-adequate diet-fed mice; black column, selenium-deficient diet-fed mice; grey column, SeMet-supplemented diet-fed mice. Data express mean  $\pm$  SE ( $n = 3-6$ ). \*, \*\*, \*\*\*, \*\*\*\*: significantly different between the diets with  $P < 0.05$ ,  $< 0.01$ ,  $< 0.001$ ,  $< 0.0001$ , respectively (ANOVA with a Tukey test), n. s.: not significantly different from each other.

by the brain.

The Tg2576 transgenic mice overexpress a human amyloid precursor protein (APP) containing a Lys670Asn and Met671Leu mutation which was found in familial AD patients and significantly elevated amounts of A $\beta$  peptides were detected in the 11–13 month-old Tg2576 mice brain [35]. In this study, we compared the extent of A $\beta$  plaque deposition in the Tg2576 mice brain among the different selenium statuses. Th-T, a commonly used amyloid staining fluorescent dye, was used for the detection of A $\beta$  plaque deposition in the Tg2576 mice brain slices in this study. The obtained fluorescent images of the Th-T-treated mice brain slices were qualitatively analyzed using MetaMorph software (Figures S1). Although it is not statistically significant, feeding of both the selenium-deficient diet and SeMet-supplemented diet changed the A $\beta$  plaque deposition in the Tg2576 mice brain (Figure 2). In the selenium-deficient diet-fed mice brain, the deposition of A $\beta$  plaques appeared to have increased. On the other hand, a slightly decreased A $\beta$  deposition was detected in the SeMet-supplemented diet-fed Tg2576 mice brain. In our previous research, A $\beta$  plaque deposition in the selenium-deficient diet-fed Tg2576 mice brain significantly increased after the 76 weeks-feeding compared to the selenium-adequate diet-fed Tg2576 mice [25]. This difference between the two studies might be caused by the interindividual difference of the Tg2576 mice used in both studies.

Because the selenium concentration in organs/tissues substantially changed by the feeding of selenium-deficient or SeMet-supplemented diets, the influence of feeding these diets on the selenoprotein activity in the brain was examined (Figure 3). GPxs are the major selenoprotein family and play pivotal roles by reducing hydrogen peroxide and lipid peroxides [36]. The GPx activity against both inorganic (H<sub>2</sub>O<sub>2</sub>) and organic (TBHP) peroxides of the selenium-deficient diet-fed Tg2576 mice brain tissue lysate was lower than that of the selenium-adequate diet-fed mice. On the other hand, the brain GPx activity of the SeMet-supplemented diet-fed mice was at the same

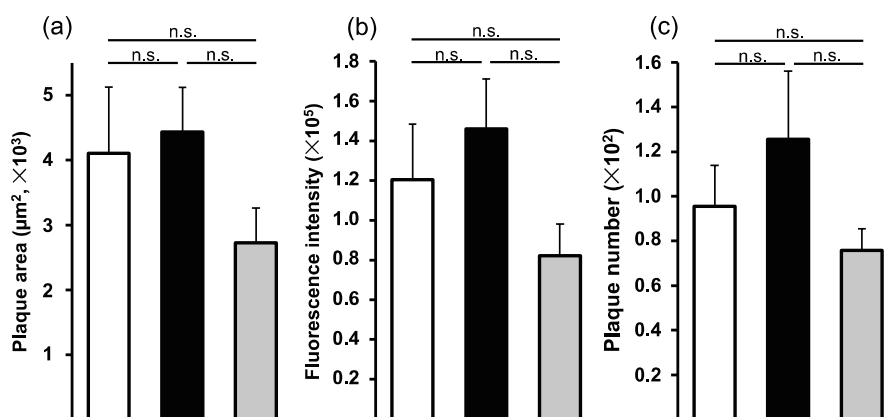


**Figure 2.** Image analysis of Th-T fluorescence in the brain slices of the Tg2576 transgenic mice. (a) Total area stained with Th-T per brain slice; (b) total fluorescence intensity of stained area; (c) the plaque number. White column, selenium-adequate diet-fed mice; black column, selenium-deficient diet-fed mice; gray column, SeMet-supplemented diet-fed mice. Data express mean  $\pm$  SE (n = 13-15). n. s.: not significantly different from each other.

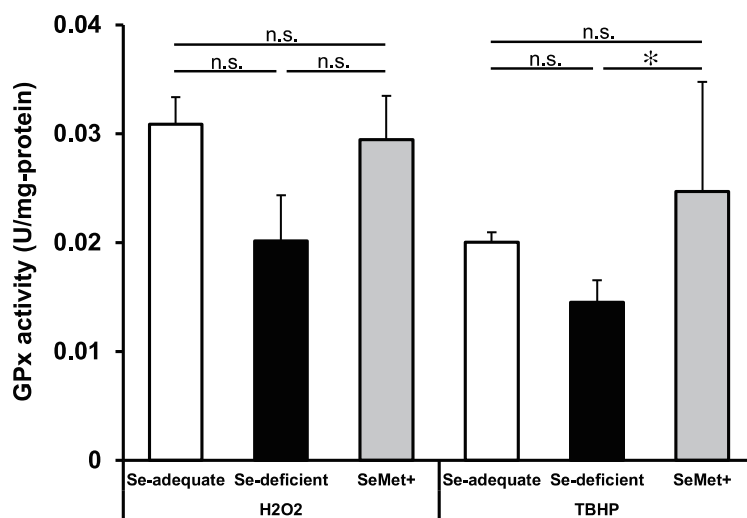


**Figure 3.** GPx activity of brain tissue lysate of Tg2576 transgenic mice. White column, selenium-adequate diet-fed mice; black column, selenium-deficient diet-fed mice; gray column, SeMet-supplemented diet-fed mice. Data express mean  $\pm$  SE (n = 3-6). \*: significantly different between the diets with P < 0.05 (ANOVA with a Tukey test), n. s.: not significantly different from each other.

level as that of the selenium-adequate diet-fed mice. Although the brain selenium concentration of the SeMet-supplemented diet-fed mice was nearly 3 times higher than that of selenium-adequate diet-fed mice, the change in the brain GPx activity was small. This suggested that the GPx activity in the brain was saturated by the feeding of the selenium-adequate diet and the additional supply of selenium did not have an influence on the GPx activity in the SeMet-supplemented diet-fed mice.

Tg2576 transgenic mice are commonly used as a model of familial AD. It was reported that the generation of ROS in the Tg2576 mice brain was increased and this caused cerebrovascular dysfunction [37, 38]. To examine the extent of lipid peroxidation in the brain of the Tg2576 mice, TBARS in the brain tissue lysates was measured (Figure 4). The value of TBARS in the selenium-deficient diet-fed Tg2576 mice brain was almost twice that of the selenium-adequate diet-fed Tg2576 mice brain. On the other hand, a decreasing tendency of the TBARS value was observed in the brain tissues of the SeMet-supplemented diet-fed Tg2576 mice. These results suggested that the reduced brain GPx activity in the selenium-deficient diet-fed mice led to the increased lipid peroxidation. The reduced GPx activity and increased lipid peroxidation in the Tg2576 transgenic mice were also reported in previous studies [38]. In this study, about a 5 times higher content of selenium as SeMet was supplied to the SeMet-supplemented diet-fed mice compared to the selenium-adequate diet-fed mice and this treatment resulted in a 3.7 times higher selenium concentration in the brain of the SeMet-supplemented diet-fed mice than that of the selenium-adequate diet-fed mice. However, the brain GPx activity of the SeMet-supplemented diet-fed mice was almost the same as that of the selenium-adequate diet-fed mice. These facts suggested that an excess amount of SeMet was randomly incorporated into the Met position of proteins rather than being used to make the brain GPx activity higher than that of the selenium-adequate diet-fed mice. Met substitution by SeMet sometimes changes the protein stability due to the increased hydrophobicity and distinct oxidation susceptibility of SeMet compared to Met [39–43]. Martinez et al. prepared the SeMet substituted A $\beta$ 40 peptide in the position of Met35 and it resulted in inhibition of the peptide fibrillation and decrease in the cytotoxicity [44]. The reduced tendency of A $\beta$  plaque deposition in the SeMet-supplemented diet-fed mice might be caused by substitution of Met in APP by SeMet.

In this study, the feeding of the selenium-deficient diet reduced the selenium concentration in the brain of the Tg2576 transgenic mice and it was presumed to cause the reduced GPx activity in the brain tissues. On the other hand, the SeMet-supplemented diet feeding significantly increased the brain selenium concentration of the Tg2576 transgenic mice, and it was effective in maintaining the brain GPx activity. Although it was not significant, the increased lipid peroxidation in the selenium-deficient diet-fed mice brain was observed and the lipid peroxidation

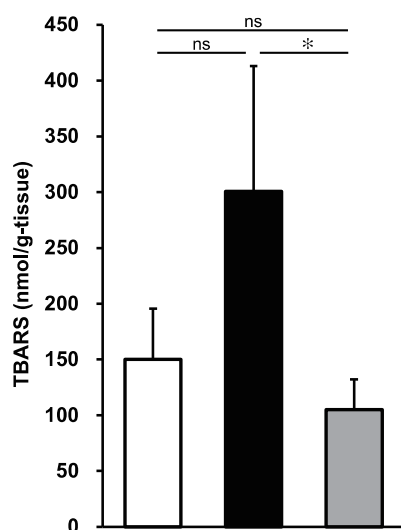


**Figure 4.** TBARS of brain tissue lysate of Tg2576 transgenic mice. White column, selenium-adequate diet-fed mice; black column, selenium-deficient diet-fed mice; gray column, SeMet-supplemented diet-fed mice. Data express mean  $\pm$  SE (n = 3). \*: significantly different between the diets with P < 0.05 (ANOVA with a Tukey test), n. s.: not significantly different from each other.

was reduced in the SeMet-supplemented diet-fed mice brain. These results were presumed to be partially caused by the difference in the brain GPx activity. Additionally, the decreased tendency of the A $\beta$  deposition in the SeMet-supplemented diet-fed Tg2576 mice brain compared to the selenium-deficient diet-fed mice might be the effect of the increased brain GPx activity and reduced lipid peroxidation. Although we need a further investigation, there is the possibility that supplementation of SeMet to selenium deficient mice suppresses the deposition of A $\beta$  in the Tg2576 transgenic mice brain. The analysis of the expression levels of GPxs and the ROS generation in brain tissues after feeding of selenium species into AD model mice would be helpful for elucidation of the mechanisms of the suppressive effect of selenium on A $\beta$  deposition in future experiment.

Considering the average amount of the diets the Tg2576 mice had in this study (5–7 g/day), selenium intakes of the selenium-adequate diet-fed mice and the SeMet-supplemented diet-fed mice were about 200 and 1,000 times higher than that of recommended dietary allowance established in Dietary Reference Intakes for Japanese (25–30  $\mu$ g/day for adults) [45], respectively. Because feeding C57BL/6J mouse with the excess amount SeMet (8 mgSe/kg diet) did not cause apparent toxic symptom of selenium [46], mouse seemed to have higher tolerance for SeMet compared to human. Selenium concentration in food is highly dependent on the selenium concentration in the soil [47]. Therefore, human dietary selenium intake also geographically varies, which range from 3 to 6,690  $\mu$ g/day [48]. It is reported that about 1 billion people are affected by insufficient selenium intake worldwide [49]. More detailed research on the relevance of selenium intakes to various disease including AD is needed.

Despite the numerous efforts for developing medications with the aim of the complete cure of AD for many decades, the option and the efficacy of medications currently used for the treatment of AD is limited. This is probably attributed to the complicated pathology of AD [50]. Although the relevance of AD onset/progression and selenium is still controversial, various selenium species have been developed for the prevention and treatment of AD [21, 51, 52]. The administration of inorganic and organic selenium species, including SeMet, have been reported to be effective for the improvement of the cognitive function and the reduced neurotoxicity of A $\beta$  and tau protein in the transgenic AD model mice [53–56]. Zheng et al. administered sodium selenate with drinking water to AD model mice. Treatment with 7.5–10.0  $\mu$ gSe/day for 10 months significantly reduced the A $\beta$  deposition and neurofibrillary tangles and increased the activity of GPxs and thioredoxin reductases in the mice brain [57]. The results obtained from these research studies will contribute to a further understanding of AD pathology and help us to develop effective medicine for the prevention and treatment of AD [24, 58–62].

In conclusion, reduced GPx activity in the selenium-deficient diet-fed Tg2576 mice brain was predicted to increase lipid peroxidation, which may be related to the enhanced deposition of A $\beta$  plaques in the brain. SeMet supplementation raised the brain selenium concentration and was effective in maintaining the brain GPx activity at the same level as that of the selenium-adequate diet-fed mice which appeared to prevent the production of lipid peroxides.

### Acknowledgement

This study was partially supported by JSPS KAKENHI Grant number JP16K18921. This study was the result of using research equipment shared in the MEXT Project for promoting public utilization of the advanced research infrastructure (Program for supporting introduction of the new sharing system) Grant number JPMXS0422500320.

### References

- [1] Evans-Lacko S, Aguzzoli E, Read S, Comas-Herrera A, Farina N. *World Alzheimer Report 2024: Global changes in attitudes to dementia*. Alzheimer's Disease International; 2024; 1-176.
- [2] Master CL, Bateman R, Blennow K, Rowe CC, Sperling RA, Cummings JL. Alzheimer's disease. *Nat Rev Dis Primers*. 2015; 1: 15056.
- [3] Cheignon C, Tomas M, Bonnefont-Rousselot D, Faller P, Hureau C, Collin F. Oxidative stress and the amyloid beta peptide in Alzheimer's disease. *Redox Biol*. 2018; 14: 450-464.
- [4] Scheltens P, Strooper BD, Kivipelto M, Holstege H, Ch  telat G, Teunissen CE, Cummings J, van der Flier WM. Alzheimer's disease. *Lancet*. 2021; 397: 1577-1590.
- [5] Sevigny J, Chiao P, Bussi  re T, Weinreb PH, Williams L, Maier M, Dunstan R, Salloway S, Chen T, Ling Y, O'Gorman J, Qian F, Arastu M, Li M, Chollate S, Brennan MS, Quintero-Monzon O, Scannevin RH, Arnold HM, Engber T, Rhodes K, Ferrero J, Hang Y, Mikulskis A, Grimm J, Hock C, Nitsch RM, Sandrock A. The antibody aducanumab reduces A $\beta$  plaques in Alzheimer's disease. *Nature*. 2016; 537: 50-56.
- [6] Karran E, Strooper BD. The amyloid hypothesis in Alzheimer disease: new insights from new therapeutics. *Nat Rev Drug Discov*. 2022; 21: 306-318.

- [7] Shi M, Chu F, Zhu F, Zhu J. Impact of anti-amyloid- $\beta$  monoclonal antibodies on the pathology and clinical profile of Alzheimer's disease: A focus on aducanumab and lecanemab. *Front Aging Neurosci.* 2022; 14: 870517.
- [8] Høiland-Carlsen PF, Alavi A, Barrio JR, Castellani RJ, Costa T, Herrup K, Kepp KP, Neve RL, Perry G, Revheim ME, Robakis NK, Sensi SL, Vissel B. Donanemab, another anti-Alzheimer's drug with risk and uncertain benefit. *Ageing Res Rev.* 2024; 99: 102348.
- [9] Polanco JC, Li C, Bodea LG, Martinez-Marmol R, Meunier FA, Götz J. Amyloid- $\beta$  and tau complexity—towards improved biomarkers and targeted therapies. *Nat Rev Neurol.* 2018; 14: 22-39.
- [10] Kepp KP. Bioinorganic chemistry of Alzheimer's disease. *Chem Rev.* 2012; 112: 5193-5239.
- [11] Mateo D, Marquès M, Torrente M. Metals linked with the most prevalent primary neurodegenerative dementias in the elderly: A narrative review. *Environ Res.* 2023; 236: 116722.
- [12] Sonnen JA, Breitner JC, Lovell MA, Markesbery WR, Wuinn JF, Montine TJ. Free radical-mediated damage to brain in Alzheimer's disease and its transgenic mouse models. *Free Radic Biol Med.* 2008; 45: 219-230.
- [13] Cardoso BR, Ong TP, Jacob-Filho W, Jaluul O, Freitas MI, Cozzolino SM. Nutritional status of selenium in Alzheimer's disease patients. *Br J Nutr.* 2010; 103: 803-806.
- [14] Varikasuvu SR, Prasad VS, Kothapalli J, Manne M. Brain selenium in Alzheimer's disease (BRAIN SEAD Study): a systematic review and meta-analysis. *Biol Trace Elem Res.* 2019; 189: 361-369.
- [15] Zhang S, Rocourt C, Cheng WH. Selenoproteins and the aging brain. *Mech Ageing Dev.* 2010; 131: 253-260.
- [16] Loeff M, Shrauzer GN, Walach H. Selenium and Alzheimer's disease: A systematic review. *J Alzheimers Dis.* 2011; 26: 81-104.
- [17] Gao S, Jin Y, Hall KS, Liang C, Unverzagt FW, Ji R, Murrell JR, Cao J, Shen J, Ma F, Matesan J, Ying B, Cheng Y, Bian J, Li P, Hendrie HC. Selenium level and cognitive function in rural elderly Chinese. *Am J Epidemiol.* 2007; 165: 955-965.
- [18] Pereira ME, Souza JV, Galicioli MEA, Sare F, Vieira GS, Kruk IL, Oliveira CS. Effects of selenium supplementation in patients with mild cognitive impairment or Alzheimer's disease: A systematic review and meta-analysis. *Nutrients.* 2022; 14: 3205.
- [19] Kryscio RJ, Abner EL, Caban-Holt A, Lovell M, Goodman P, Darke AK, Yee M, Crowley J, Schmitt FA. Association of antioxidant supplement use and dementia in the prevention of Alzheimer's disease by vitamin E and selenium trial (PREADViSE). *JAMA Neurol.* 2017; 74: 567-573.
- [20] Du X, Wang Z, Zheng Y, Li H, Ni J, Liu Q. Inhibitory effect of selenoprotein P on Cu(+)/Cu(2+)-induced A $\beta$ 42 aggregation and toxicity. *Inorg Chem.* 2014; 53: 1672-1678.
- [21] Solovyev N. Selenoprotein P and its potential role in Alzheimer's disease. *Hormones.* 2020; 19: 73-79.
- [22] Ouyang P, Cai Z, Peng J, Lin S, Chen X, Chen C, Feng Z, Wang L, Song G, Zhang Z. SELENOK-dependent CD36 palmitoylation regulates microglial functions and A $\beta$  phagocytosis. *Redox Biol.* 2024; 70: 103064.
- [23] Ren B, Situ J, Huang X, Tan Q, Xiao S, Li N, Tian J, Du X, Ni J, Liu Q. Selenoprotein W modulates tau homeostasis in an Alzheimer's disease mouse model. *Commun Biol.* 2024; 7: 872.
- [24] Shen Y, Zhang G, Wei C, Zhao P, Wang Y, Li M, Sun L. Potential role and therapeutic implications of glutathione peroxidase 4 in the treatment of Alzheimer's disease. *Neural Regen Res.* 2025; 20: 613-631.
- [25] Haratake M, Yoshida S, Mandai M, Fuchigami T, Nakayama M. Elevated amyloid- $\beta$  plaque deposition in dietary selenium-deficient Tg2576 transgenic mice. *Metallomics.* 2013; 5: 479-483.
- [26] Watkinson JH. Fluorometric determination of selenium in biological material with 2,3-diaminonaphthalene. *Anal Chem.* 1966; 38: 92-97.
- [27] Lowry OH, Resebrough NJ, Farr AL, Randall RJ. Protein measurement with the Folin phenol reagent. *J Biol Chem.* 1951; 193: 265-275.
- [28] Flohe L, Gunzler WW. Assay of glutathione peroxidase. *Methods Enzymol.* 1984; 105: 114-121.
- [29] Tien M, Aust SD. Rabbit liver microsomal lipid peroxidation. The effect of lipid on the rate of peroxidation. *Biochim Biophys Acta.* 1982; 712: 1-9.
- [30] Haratake M, Ono M, Nakayama M. Penicillamine selenotrisulfide as a selenium-source in mice. *J Health Sci.* 2004; 50: 366-371.
- [31] Behne D, Hilmert H, Scheid S, Gessner H, Elger W. Evidence for specific selenium target tissues and new biologically important selenoproteins. *Biochim Biophys Acta.* 1988; 966: 12-21.
- [32] Nakayama A, Hill KE, Austin LM, Motley AK, Burk RF. All regions of mouse brain are dependent on selenoprotein P for maintenance of selenium. *J Nutr.* 2007; 137: 690-693.
- [33] Whanger PD, Butler JA. Effects of various dietary levels of selenium as selenite or selenomethionine on tissue selenium levels and glutathione peroxidase activity in rats. *J Nutr.* 1988; 118: 846-852.
- [34] Schrauzer GN. Selenomethionine: a review of its nutritional significance, metabolism and toxicity. *J Nutr.* 2000; 130: 1653-1656.
- [35] Hsiao K, Chapman P, Nilsen S, Eckman C, Harigaya Y, Younkin S, Cole G. Correlative memory deficits, A $\beta$  elevation, and amyloid plaques in transgenic mice. *Science.* 1996; 274: 99-102.
- [36] Brigelius-Flohé R, Maiorino M. Glutathione peroxidases. *Biochim Biophys Acta.* 2013; 1830: 3239-3303.
- [37] Han BH, Zhou MI, Johnson AW, Singh I, Liao F, Vellimana AK, Nelson JW, Milner E, Cirrito JR, Basak J, Yoo M, Dietrich HH, Holtzman DM, Zipfel GJ. Contribution of reactive oxygen species to cerebral amyloid angiopathy, vasomotor dysfunction, and microhemorrhage in aged Tg2576 mice. *Proc Natl Acad Sci USA.* 2015; 112: E881-E890.
- [38] Boonruamkaew P, Chonpathompikunlert P, Vong LB, Sakaue H, Tomidokoro Y, Ishii K, Tamaoka A, Nagasaki Y. Chronic treatment with a smart antioxidative nanoparticle for inhibition of amyloid plaque propagation in Tg2576 mouse model of Alzheimer's disease. *Sci Rep.* 2017; 7: 3785.
- [39] Budisa N, Huber R, Golbik R, Minks C, Weyher E, Moroder L. Atomic mutations in annexin V—Thermodynamic studies of isomorphous protein variants. *Eur J Biochem.* 1998; 253: 1-9.
- [40] Gassner NC, Baase WA, Hausrath AC, Matthews BW. Substitution with selenomethionine can enhance the stability of methionine-rich proteins. *J Mol Biol.* 1999; 294: 17-20.
- [41] Wernimont AK, Huffman DL, Finney LA, Demeler B, O'Halloran TV, Rosenzweig AC. Crystal structure and dimerization equilibria of PcoC, a methionine-rich copper resistance protein from Escherichia coli. *J Biol Inorg Chem.* 2003; 8: 185-194.
- [42] Le DT, Liang X, Fomenko DE, Raza AS, Chong CK, Carlson BA, Hatfield DL, Gladyshev VN. Analysis of methionine/selenomethionine oxidation and methionine sulfoxide reductase function using methionine-rich proteins and antibodies against their oxidized forms. *Biochemistry.* 2008; 47: 6685-6694.
- [43] Yamniuk AP, Ishida H, Lippert D, Vogel HJ. Thermodynamic effects of noncoded and coded methionine substitutions in calmodulin. *Biophys J.* 2009; 96: 1495-1507.
- [44] Martínez J, Lisa S, Sánchez R, Kowalczyk W, Zurita E, Teixidó M, Giral E, Andreu D, Avila J, Gasset M. Selenomethionine incorporation into amyloid sequences regulates fibrillogenesis and toxicity. *PLoS One.* 2011; 6: e27999.

- [45] *Dietary Reference Intakes for Japanese, 2020*. JAPAN: Health Service Bureau, Ministry of Health, Labour and Welfare; 2020.
- [46] Akahoshi N, Anan Y, Hashimoto Y, Tokoro N, Mizuno R, Hayashi S, Yamamoto S, Shimada K, Kamata S, Ishii I. Dietary selenium deficiency or selenomethionine excess drastically alters organ selenium contents without altering the expression of most selenoproteins in mice. *J Nutr Biochem*. 2019; 69: 120-129.
- [47] Navarro-Alarcon M, Cabrera-Vique C. Selenium in food and the human body: A review. *Sci Total Environ*. 2008; 400: 115-141.
- [48] Dumont E, Vanhaecke F, Cornelis R. Selenium speciation from food source to metabolites: a critical review. *Anal Bioanal Chem*. 2006; 285: 1304-1323.
- [49] Jones GD, Droz B, Greve P, Gottschalk P, Poffet D, McGrath SP, Seneviratne SI, Smith P, Winkel LHE. Selenium deficiency risk predicted to increase under future climate change. *Proc Natl Acad Sci USA*. 2017; 114: 2848-2853.
- [50] Wang J, Gu BJ, Masters CL, Wang YJ. A systemic view of Alzheimer disease—insights from amyloid- $\beta$  metabolism beyond the brain. *Nat Rev Neurol*. 2017; 13: 612-623.
- [51] Umar M, Rehman Y, Ambreen S, Mumtaz SM, Shaquuzzaman M, Alam MM, Ali R. Innovative approaches to Alzheimer's therapy: Harnessing the power of heterocycles, oxidative stress management, and nanomaterial drug delivery system. *Ageing Res Rev*. 2024; 97: 102298.
- [52] Vicente-Zurdo D, Rosales-Conrado N, León-González ME. Unravelling the in vitro and in vivo potential of selenium nanoparticles in Alzheimer's disease: A bioanalytical review. *Talanta*. 2024; 269: 125519.
- [53] Zhang ZH, Wu QY, Zheng R, Chen C, Chen Y, Liu Q, Hoffman PR, Ni JZ, Song GL. Selenomethionine mitigates cognitive decline by targeting both tau hyperphosphorylation and autophagic clearance in an Alzheimer's disease mouse model. *J Neurosci*. 2017; 37: 2449-2462.
- [54] van der Jeugd A, Parra-Damas A, Baeta-Corral R, Soto-Faguás CM, Ahmed T, LaFerla FM, Giménez-Llort L, D'Hooge R, Saura CA. Reversal of memory and neuropsychiatric symptoms and reduced tau pathology by selenium in 3xTg-AD mice. *Sci Rep*. 2018; 8: 6431.
- [55] Du X, Shi Q, Zhao Y, Xie Y, Li X, Liu Q, Iqbal J, Zhang H, Liu X, Shen L. Se-methylselenocysteine (SMC) improves cognitive deficits by attenuating synaptic and metabolic abnormalities in Alzheimer's mice model: A proteomic study. *ACS Chem Neurosci*. 2021; 12: 1112-1132.
- [56] Guo X, Lie Q, Liu Y, Jia Z, Gong Y, Yuan X, Liu J. Multifunctional selenium quantum dots for the treatment of Alzheimer's disease by reducing A $\beta$ -neurotoxicity and oxidative stress and alleviate neuroinflammation. *ACS Appl Mater Interfaces*. 2021; 13: 30261-30273.
- [57] Zheng L, Zhu HZ, Wang BT, Zhao QH, Du XB, Zheng Y, Jiang L, Ni JZ, Zhang Y, Liu Q. Sodium selenate regulates the brain ionome in a transgenic mouse model of Alzheimer's disease. *Sci Rep*. 2016; 6: 39290.
- [58] Landgraf AD, Alsegiani AS, Alaql S, Thanna S, Shah ZA, Sucheck SJ. Neuroprotective and anti-neuroinflammatory properties of ebselen derivatives and their potential to inhibit neurodegeneration. *ACS Chem Neurosci*. 2020; 11: 3008-3016.
- [59] Behera A, Pradhan SP, Tejaswani P, Sa N, Pattnaik S, Sahu PK. Ameliorative and neuroprotective effect of core-shell type Se@Au conjugated hesperidin nanoparticles in diabetes-induced cognitive impairment. *Mol Neurobiol*. 2023; 60: 7329-7345.
- [60] Fu C, Wang X, Zhou W, Gao Q, Luo J, Li Y. Exploring the mechanism of chondroitin sulfate-selenium nanoparticles in improving Alzheimer's disease: Insights from intestinal flora evaluation. *Heliyon*. 2024; 10: e38635.
- [61] Bai YZ, Zhang Y, Zhang SQ. New horizons for the role of selenium on cognitive function: advances and challenges. *Metab Brain Dis*. 2024; 39: 1255-1268.
- [62] Pyka P, Haberek W, Więcek M, Szymanska E, Ali W, Cios A, Jastrzębska-Więsek M, Satała G, Podlewska S, Giacomo SD, Sotito AD, Garbo S, Karcz T, Lambona C, Marocco F, Latacz G, Sudoł-Tałaj S, Mordyl B, Głuch-Lutwin M, Siwek A, Czarnota-Łydka K, Gogola D, Olejarz-Maciej A, Wilczyńska-Zawal N, Honkisz-Orzechowska E, Starek M, Dąbrowska M, Kucwaj-Brysz K, Fioravanti R, Nasim MJ, Hittinger M, Partyka A, Wesołowska A, Battistelli C, Zwergel C, Handzlik J. First-in-class selenium-containing potent serotonin receptor 5-HT $_6$  agents with a beneficial neuroprotective profile against Alzheimer's disease. *J Med Chem*. 2024; 67: 1580-1610.

Supplemental information

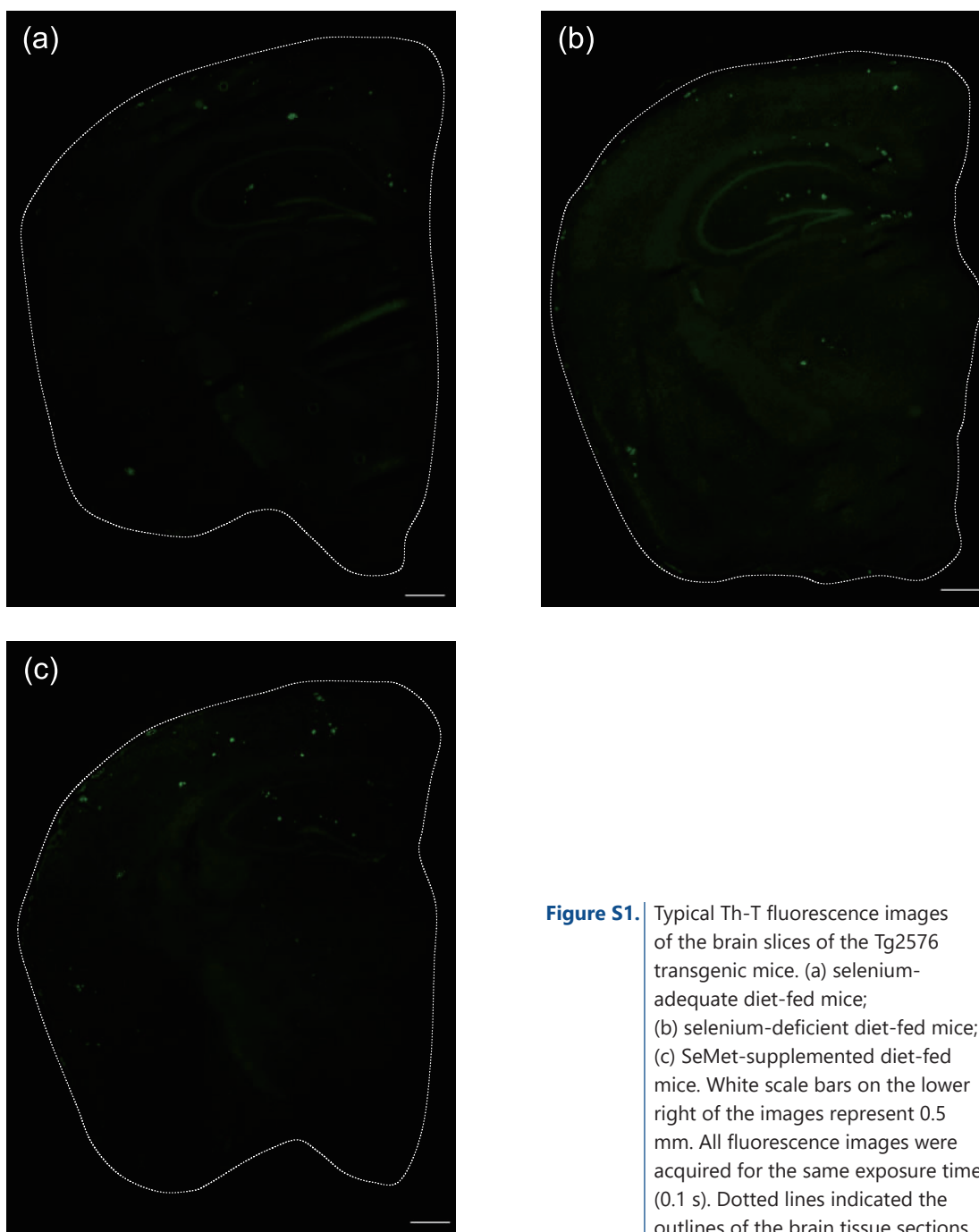


**Figure S1.** Typical Th-T fluorescence images of the brain slices of the Tg2576 transgenic mice. (a) selenium-adequate diet-fed mice; (b) selenium-deficient diet-fed mice; (c) SeMet-supplemented diet-fed mice. White scale bars on the lower right of the images represent 0.5 mm. All fluorescence images were acquired for the same exposure time (0.1 s). Dotted lines indicated the outlines of the brain tissue sections.

## The distribution and chemical form of selenium in the tissue of ferns were visualized using a synchrotron radiation X-ray microbeam.

Shota Yuzawa<sup>1</sup>, Koichi Nambu<sup>1</sup>, Kazuaki Takahashi<sup>2</sup>, Yasumitsu Ogra<sup>3†</sup>, Akiko Hokura<sup>1\*</sup>

<sup>1</sup> Department of Applied Chemistry, Tokyo Denki University

<sup>2</sup> Graduate School of Horticulture, Chiba University

<sup>3</sup> Graduate School of Pharmaceutical Sciences, Chiba University

### Abstract

In this study, *Pteris vittata* L. was cultivated *via* hydroponics by incorporating inorganic selenate (selenium concentration of 5 mg/kg or 50 mg/kg). The growth of the plants was not impaired when they were grown for three weeks with a selenium concentration of 5 ppm. Furthermore, selenium accumulated in the roots (389 mg/kg), stems (85 mg/kg), and leaves (166 mg/kg). Selenium accumulation and metabolism were observed in the roots. As the cultivation period increased, the proportion of Se(-II) in the above-ground parts increased. After three weeks, more than 80 % of the accumulated selenium had been metabolized into Se(-II) compounds. This phenomenon was particularly pronounced under conditions of low selenium concentration, with 5 mg/kg added. Moreover, an analysis conducted using a synchrotron radiation X-ray microbeam demonstrated that the metabolized selenium was present in specific tissues, including the root epidermis and central cylinder. Conversely, the extraction of selenium compounds from each tissue revealed the presence of Se-methyl selenocysteine and selenomethionine as soluble components among the selenium compounds produced by metabolism. It is hypothesized that these methylated selenium compounds accumulate in the plant body as low-toxicity chemical species. The extraction rate of selenium in the above-ground parts, such as stems and leaves, was relatively low, and it is postulated that it was metabolized into chemical species, such as selenium-containing proteins.

**Keywords:** selenate, fern, chemical speciation, X-ray absorption spectrometry, accumulation, extraction

**Statements about COI:** The authors have no conflicts of interest associated with this manuscript to declare.

### \*Correspondence

Akiko Hokura

5 Senju-Asahicho, Adachi, Tokyo 120-8551 Japan

Tel ; +81 3 5284 5440

E-mail ; [hokura@mail.dendai.ac.jp](mailto:hokura@mail.dendai.ac.jp)

Received: December 21, 2024

Accepted: March 17, 2025

Released online: March 31, 2025

### Introduction

The environmental remediation technology that uses plants is called phytoremediation [1]. Phytoremediation is a process that removes contaminants from soil by using uptake by plant roots, transport to above-ground parts, and accumulation of pollutants. Phytoremediation is attracting attention as a new environmentally friendly remediation technology because it uses little energy for decontamination and has little impact on the ecosystem. Phytoremediation is applied to plants that



This work is licensed under a Creative Commons Attribution 4.0 International License.

©2025 THE AUTHORS. [DOI](https://doi.org/10.11299/metallomicsresearch.MR202416) <https://doi.org/10.11299/metallomicsresearch.MR202416>

hyperaccumulate heavy metals and metalloids [1, 2].

*Pteris vittata* L. is a fern reported to hyperaccumulate arsenic in 2001 [3] and attracted attention. When cultivated for 6 weeks in soil containing 1,500 mg/kg (ppm) arsenic, it accumulated approximately 22,000 mg/kg (dry weight) arsenic in the aerial parts. In addition, it has been reported in recent years that selenium has a beneficial effect on the accumulation of arsenic in *P. vittata* [4, 5].

Selenium is an essential trace element for humans and animals [6]. Selenium is found in proteins as an element of the amino acid selenocysteine (SeCys) [7]. In contrast, there is debate about whether selenium is essential for plants, as no known plant enzymes require selenium. However, it is known that trace amounts of selenium promote plant growth, and it is positioned as a beneficial element in plants. Low doses of selenium are thought to protect plants from stresses such as cold, drought, and metal stress [8, 9]. However, the mechanism is complex and not fully understood.

Selenium is a rare metal used in various applications, including electronic materials such as photoreceptors, glass colorants and decolorants, and chemical catalysts. It is released into the environment in wastewater and waste from these industrial activities. In general, it is present in the soil at concentrations ranging from sub-ppm to a few ppm, mainly in the form of inorganic selenate and selenite and, to a lesser extent, in organic selenomethionine (SeMet) [10]. The main area where selenium has a significant impact on the environment is in the aquatic environment. Because inorganic selenium exhibits chronic and acute toxicity to living organisms, Japan has set a National effluent standard of 0.1 mg/L or less for selenium and selenium compounds [11]. The World Health Organization (WHO) has recommended 10 µg/L as the lower intake limit of Se in drinking water [12]. There are almost no selenium-contaminated areas in Japan. Still, the effects of selenium contamination on livestock and humans have been reported in some regions of China, India, the United States, etc. [13, 14].

Plants known to accumulate high levels of selenium include *Brassica pinnata*, which is native to North America, and wheat (*Triticum aestivum*) and Indian mustard (*Brassica juncea*), which are found in the Punjab region of India. There is a tendency for plants in the Brassica family to accumulate high levels of selenium [10, 15]. When the soil selenium concentration was 6 ppm, the amount of selenium accumulated in the leaves of these plants was extremely high, about 3,000 ppm. In wheat (*T. aestivum*), when the soil selenium concentration was 13.1 ppm, the selenium accumulation in the leaves was about 390 ppm, and in mustard (*B. juncea*), when the soil selenium concentration was 6.8 ppm, the selenium accumulation in the leaves was about 935 ppm [16, 17].

These plants take up the highly toxic inorganic ion of selenium and metabolize them to less toxic organic selenium compounds in the plant body [14]. In wheat and Indian mustard, selenate is added and metabolized *via* the intermediate SeCys to *Se*-methylselenocysteine (MeSeCys). It is characteristic of plants that accumulate high levels of selenium that MeSeCys is further metabolized to  $\gamma$ -glutamyl-methyl-selenocysteine ( $\gamma$ -GluMeSeCys), which is the final metabolite of selenium. Another pathway has also been proposed in which SeCys is metabolized to selenocystathionine, SeCys, SeMet, selenohomolanthionine (SeHLan), and other compounds [18-20].

There are several methods to study the chemical form of selenium in plants, and high-performance liquid chromatography (HPLC) combined with inductively coupled plasma mass spectrometry (ICP-MS) is commonly used [21, 22]. The sample is a solution extracted from plant tissue. On the other hand, X-ray absorption spectroscopy using synchrotron radiation X-rays is also helpful in studying the chemical form of plant elements [23]. Regardless of the state of the sample, non-destructive analysis is possible, whether the sample is liquid or solid (powder).

We applied X-ray absorption spectroscopy to *P. vittata* L. growing in arsenic-contaminated soil while alive in a pot. Although the arsenic in the soil was pentavalent, As(+V) and As(+III) coexisted in the stem, and almost all of the arsenic in the leaves was trivalent [24]. In addition, when the chemical form of arsenic taken up by the roots was examined, it was found that trivalent arsenic was more abundant at the root tips, and pentavalent arsenic became dominant as one moved toward the base of the roots [25, 26]. These results suggest that arsenic is actively reduced at the root tips.

The fern of *P. vittata* L. is well-known for its ability to hyperaccumulate arsenic, but it has also been found to take up and accumulate other elements [27, 28]. When grown with added Cr(+VI), it accumulated to high concentrations

in the roots, around 40,000 ppm, while when grown with added Cr(+III), it accumulated to high concentrations in the roots, around 20,000 ppm. With Cr(+III), almost none are collected in the above-ground parts, and nearly all are collected in the roots. In addition, using synchrotron radiation X-ray absorption spectroscopy, it was found that the accumulated Cr was in the trivalent chemical form, regardless of whether Cr(+VI) or Cr(+III) was added [28].

To carry out phytoremediation effectively, it is necessary to elucidate the accumulation mechanism of metals and metalloids in hyperaccumulator plants. Therefore, in this study, we added selenate to *P. vittata* and aimed to clarify the chemical form in which selenium accumulates and where it accumulates in the roots, stems, and leaves. We also extracted soluble components from each part of the fern and attempted to identify the chemical species. We focused on the changes in chemical form to determine what chemical form the selenium taken up by the fern moves to the aboveground part.

## Experimental

### Reagents

*Pteris vittata* L. was provided by Fujita Corporation (Japan). The sodium selenate ( $\text{Na}_2\text{SeO}_4$ ) and potassium selenite ( $\text{K}_2\text{SeO}_3$ ) were procured from Kanto Chemical Co. The cellulose powder, with a particle size of 38  $\mu\text{m}$  (400 mesh), was procured from Wako Pure Chemical Industries, Ltd. Tris(hydroxymethyl)aminomethane and MeSeCys were procured from Tokyo Chemical Industry Co. Boron nitride (BN), Driselase<sup>®</sup> from *Basidiomycetes* sp., and Protease from bovine pancreas were obtained from Sigma-Aldrich Japan.

Sodium selenate was diluted with cellulose as required, and tablets with a diameter of 5 mm were formed, which were employed as samples for the calibration curve when quantifying selenium using X-ray fluorescence (XRF) spectroscopy.  $\text{Na}_2\text{SeO}_4$ ,  $\text{K}_2\text{SeO}_3$ , and Se-methyl selenocysteine were each mixed with BN as necessary, and tablets were formed. These were utilized as reference materials for selenium compounds with known valence in chemical speciation analysis of selenium by X-ray absorption spectroscopy.

Tris(hydroxymethyl)aminomethane was dissolved in pure water to a concentration of 30 mmol/L to prepare a buffer solution (Tris-HCl buffer) with a pH of 7.2 using 0.1 mol/L hydrochloric acid (HCl). This solution was employed to extract soluble selenium compounds from fern plants.

The authentic standards for HPLC-ICP-MS were obtained as below. Sodium selenite, SeMet, and MeSeCys were purchased from Nacalai Tesque (Kyoto, Japan). Sodium selenate was purchased from Wako Pure Chemical Industries, Ltd. (Osaka, Japan).  $\gamma$ -GluMeSeCys was synthesized in our laboratory [29]. Ammonium acetate was purchased from Sigma Aldrich (St. Louis, MO, USA).

### Cultivation of *Pteris vittata* L. and addition of selenate

The sporophytes of the fern, cultivated in soil, were removed from the soil and transferred to a culture solution for acclimatization. The culture solution was a 10-fold dilution of the culture solution described in **Table S1** (modified Hoagland nutrient solution [30]). The fern with culture solution was agitated in an incubator, and the culture solution was replaced every two days for two weeks. Sodium selenate was dissolved in the culture solution to prepare the selenium-added solution. The concentration of selenium added to the culture solution was set at 5 ppm (63.3  $\mu\text{mol/L}$ ), based on the selenium concentration observed in soil from polluted areas such as China [31]. A higher concentration of 50 ppm (633  $\mu\text{mol/L}$ ) Se was also prepared. In the selenium addition experiment, the fern plant bodies were cultured in an incubator for either three weeks using the 5 ppm solution or two weeks using the 50 ppm solution. During incubation, the selenium addition solution was replaced with a new one every two days.

### Sample preparation of slice cross-sections for XRF imaging and X-ray absorption spectrometry using X-ray microbeam

The roots, stems, and leaves of the *P. vittata* L, which had been treated with selenate, were embedded in OCT compound (Sakura<sup>®</sup> Finetek) and 60  $\mu\text{m}$ -thick sections were cut perpendicular to the elongation direction using a cryomicrotome (LEICA CM1900). Subsequently, the sections underwent a freeze-drying process, producing freeze-

dried sections [32, 33]. The section samples were mounted in a 40 mm square acrylic holder using double-sided tape [34] and subjected to XRF imaging and X-ray absorption spectrometry for selenium.

### Sample preparation as bulk for determination of selenium concentration and chemical speciation of selenium

After adding selenate, the plant bodies were separated into three parts: roots, stems, and leaves. Each part was freeze-dried, ground, and then homogenized. 0.1 g of the resulting powdered samples were weighed out and formed into tablets with a diameter of 5 mm, which were subsequently utilized for the quantification and chemical form analysis of selenium.

### Extraction procedure of soluble selenium compounds accumulated in various parts of ferns

The extraction of soluble selenium compounds from the freeze-dried powder of the roots, stems, and leaves of plants to which selenate had been added was conducted in the following manner [18-20]. Two hundred milligrams of powder were added to 5 mL of Tris-HCl buffer solution and homogenized by ultrasonic crushing for 5 minutes, with 30/30 pulses and 50 % output power. Subsequently, 30 mg of Driselase was added and allowed to stand for 24 hours at 37 °C, followed by 30 mg of Protease and another 24 hours of standing at the same temperature. This was done to break down the cell walls and proteins. The supernatant was then filtered through a 0.45 µm mesh filter, and the soluble selenium extract was prepared for each part.

Meanwhile, the residue resulting from the extraction process was subjected to a washing, freeze-drying, and molding procedure to create tablets for utilization in XRF and XAFS analyses, respectively, to determine the selenium concentration present in the extraction residue and investigate the chemical form of the selenium.

### Determination of Se concentrations in various parts of ferns using XRF analysis

The concentration of selenium in various parts of ferns cultivated with the addition of selenate was quantified by XRF analysis. The analysis was carried out using the energy-dispersive X-ray fluorescence spectrometer (Epsilon 5, PANalytical) equipped with a three-dimensional polarization optical system. The instrument has the Cartesian arrangement of the X-ray tube, secondary target, sample, and detector. Selecting a secondary target material appropriate for the target element makes it possible to perform a more sensitive analysis than conventional X-ray fluorescence spectrometers [35]. Zirconium was selected as the secondary target material, and the measurement time per sample was 600 seconds. A calibration curve for selenium was prepared and quantified using it.

### Chemical speciation of selenium in various parts of ferns by X-ray absorption spectroscopy

X-ray absorption near edge structure (XANES) spectra of the Se K-edge were obtained at BL-12C of the Photon Factory (PF) of the High Energy Accelerator Research Organization (Tsukuba, Ibaraki). Following the monochromatization of the synchrotron radiation emitted from the bending magnet using a Si (111) double-crystal monochromator, the beam was focused using a curved cylindrical mirror, resulting in an X-ray beam with a diameter of approximately 1 mm (vertical direction, V) × 1 mm (horizontal direction, H) [36]. In the transmission method, the ionization chambers I<sub>0</sub> and I were filled with 100% N<sub>2</sub> and 15 % Ar + 85% N<sub>2</sub> gases, respectively, and employed as X-ray detectors. In the fluorescence method, a 19-elements germanium semiconductor detector was utilized, and an arsenic filter and a latticed soller slit were incorporated to mitigate the background interference caused by scattered X-rays from the sample. The maximum value of the first derivative curve of the XANES spectrum of Na<sub>2</sub>SeO<sub>4</sub> was employed as the energy calibration for the K absorption edge of selenium at 12654.5 eV (8.9886 deg). The REX (2000) ver. 2.57 software (RIGAKU) was utilized to analyze the spectra obtained from the measurements.

The valence ratio of selenium in the samples was calculated using the XANES spectra of reference materials with known chemical forms (oxidation states). Specifically, three reference materials were employed: sodium selenate, potassium selenite, and MeSeCys. Pattern fitting analysis was conducted for the energy range (12620 eV – 12680 eV). The relative abundance of each oxidation state of selenium (Se(+VI), Se(+IV), Se(-II)) was determined.

### XRF imaging and X-ray absorption spectroscopy using X-ray microbeams

The micro-XRF imaging and micro-XANES spectra of selenium were obtained using BL-4A at PF. A monochromatic synchrotron X-ray beam, which was monochromatized by a Si(111) double crystal monochromator, was focused to a 5.0  $\mu\text{m}$  (vertical, V)  $\times$  5.0  $\mu\text{m}$  (horizontal, H) spot [37]. In XRF imaging, the X-ray energy was set to 13.5 keV, which has an optimal excitation efficiency for selenium and is minimally affected by Compton scattering. The fluorescent X-rays emitted from the sample were detected using a Silicon Drift Detector (SDD). The sample was scanned in two dimensions using a pulse motor control, and a two-dimensional elemental map was created from the XRF intensity of each element at each position.

Subsequently, energy scans were conducted at designated locations on the cross-section to obtain  $\mu$ -XANES spectra of selenium, thereby facilitating the analysis of its chemical form.

### Identification of soluble selenium compounds in each part of the fern

To identify soluble selenium compounds, we analyzed the extracts from each part using a combination of HPLC and ICP-MS/MS (Agilent 8800, Agilent Technologies, Hachiouji, Japan). HPLC-ICP-MS was used to analyze the extracts from each part [18-20]. The multi-mode size exclusion column (Shodex Asahipak GS-320HQ, 7.5 i.d.  $\times$  300 mm with a guard column, 7.5 i.d.  $\times$  75, Showa Denko, Tokyo) was used in this study. This column was eluted with 50 mM ammonium acetate, pH 6.5, at a 0.6 mL/min flow rate. The ICP-MS/MS was equipped with an octapole reaction cell (ORC), which serves to mitigate the impact of multi-atomic ion interference. For detecting selenium, the ion was selected at  $m/z$  80 in Q1, and was reacted with oxygen in Q2, and then, the reacted ion was detected at  $m/z$  96 in Q3. Additionally, for the identification of selenium compounds, authentic standards, including selenate, selenite,  $\gamma$ -GluMeSeCys, SeMeCys, and SeMet, were employed. The sample introduction volume was 20  $\mu\text{L}$  for each.

## Results and discussion

### Quantitative results of selenium concentration accumulated in each part of the fern

**Table 1** illustrates the selenium concentration in the various parts of the fern plant cultivated with the addition of selenate (at selenium concentrations of 5 ppm or 50 ppm). The table presents the mean values of the results obtained from the repeated independent experiments conducted on the fern plant body. While there is considerable

**Table 1.** Changes in selenium concentration over time in the roots, stems and leaves of the *P. vittata* L. cultivated with the addition of selenate

Addition conditions	Concentration of selenium (mg/kg DW)		
	Roots	Stems	Leaves
5 mg/kg Se			
7 days	280 $\pm$ 123	22 $\pm$ 4	38 $\pm$ 5
14 days	392 $\pm$ 48	63 $\pm$ 17	92 $\pm$ 31
21 days	389 $\pm$ 135	85 $\pm$ 25	166 $\pm$ 25
50 mg/kg Se			
1 day	226 $\pm$ 206	24 $\pm$ 22	24 $\pm$ 20
3 days	372 $\pm$ 71	266 $\pm$ 139	109 $\pm$ 109
7 days	978 $\pm$ 661	188 $\pm$ 28	415 $\pm$ 177
14 days	1299 $\pm$ 656	889 $\pm$ 31	396 $\pm$ 176

Average of  $n = 3$  samples

variation overall, the general trend can nonetheless be discerned. When the concentration of added selenium was 5 ppm, the selenium concentration in the roots reached 280 ppm after 7 days and approximately 400 ppm after 14 and 21 days. Furthermore, a gradual accumulation of selenium concentration was observed in the above-ground parts until 21 days after addition. In the above-ground parts, a more significant selenium accumulation was observed in the leaves than in the stems. After 21 days of addition, the selenium concentration in the leaves reached 166 ppm. Consequently, when 5 ppm of Se was added, the roots reached saturation after 14 days, while the concentration in the above-ground parts continued to increase, indicating that the concentration in the above-ground parts continued to increase.

Conversely, when 50 ppm of selenium was added for one day, the roots accumulated 226 ppm of selenium, while the above-ground parts (stems and leaves) accumulated 24 ppm. Subsequently, the concentration in the above-ground parts gradually increased over 14 days. Additionally, the roots demonstrated the highest selenium accumulation, reaching approximately 1,300 ppm after 14 days. The selenium concentration in the leaves decreased slightly after 21 days compared to 14 days. The decrease in selenium concentration in the stems and leaves due to long-term addition of 50 ppm selenium (**Table 1**) may be due to multiple reasons, including: 1) plant damage, 2) a decrease in selenium concentration due to an increase in biomass, and 3) the loss of selenium from the plant body due to its conversion into volatile compounds. Indeed, when 50 ppm of selenium was administered for a period of 14 days, some of the leaf veins exhibited a slight discoloration. However, no such changes were observed at 5 ppm addition.

Plants have been classified as hyperaccumulators, secondary accumulators, and non-accumulators depending upon Se accumulation inside their cells [14, 38]. Hyperaccumulators accumulate higher amounts of Se in their cells, i.e., > 1,000 mg Se/kg DW, and thrive well in Se-rich regions of the world. They have methylated forms of SeCys and SeMet, which confer the Se tolerance of these plants and can be vaporized further as dimethyldiselenide (DMDS<sub>2</sub>). Secondary accumulators accumulate Se and show no signs of toxicity up to 100-1,000 mg Se/kg DW, for e.g., *Brassica juncea*, *Brassica napus*, Broccoli, etc. These Se concentrations in **Table 1** indicate that *P. vittata* is classified as a secondary-hyperaccumulator plant of Se.

In contrast, *Pteris vittata* L. has been identified as a plant species that accumulates significant levels of arsenic. When cultivated in soil contaminated with arsenic, high concentrations accumulate in the plant's above-ground parts [3]. The pentavalent arsenic absorbed by the roots is rapidly transported to the plant's above-ground parts, accumulating in high concentrations as trivalent arsenic [24, 39]. The addition of 50 ppm chromium to the hydroponic culture resulted in the accumulation of this element in the roots at concentrations of tens of thousands of ppm [28], which is the opposite of what was observed with arsenic. Concurrently, the accumulation in the above-ground parts was constrained to a few parts per million. In other words, the transport of chromium from the roots to the above-ground parts was impeded. From these findings, it has been postulated that biological processes regulate chromium uptake. The findings of this study indicate that, despite the addition of selenium, the concentration of selenium accumulated in the roots exceeded that observed in the above-ground parts, suggesting that, in contrast to arsenic, the transport of selenium from the roots to the above-ground parts is restricted. Selenium is assumed to be taken into cells as selenate *via* sulfur transporters on the root cell membrane [40]. When the concentration added was 5 ppm, the leaf concentration was higher than in the stems, indicating that selenium migrated to the leaves and accumulated there.

### Results in chemical speciation of selenium in various parts of fern plants cultivated with the addition of selenate

The results of K-edge XANES spectrum measurements of selenium in the roots, stems, and leaves of ferns to which selenate (selenium concentration: 5 ppm) was added are presented in **Figure 1A**. In contrast, the results for the fern plants that were cultivated with the addition of selenate (selenium concentration: 50 ppm) are presented in **Figure S1**. The chemical forms of sodium selenate, potassium selenite, and MeSeCys are offered as reference samples. The oxidation state of selenium can be estimated from the peak position of the spectrum. The spectrum of

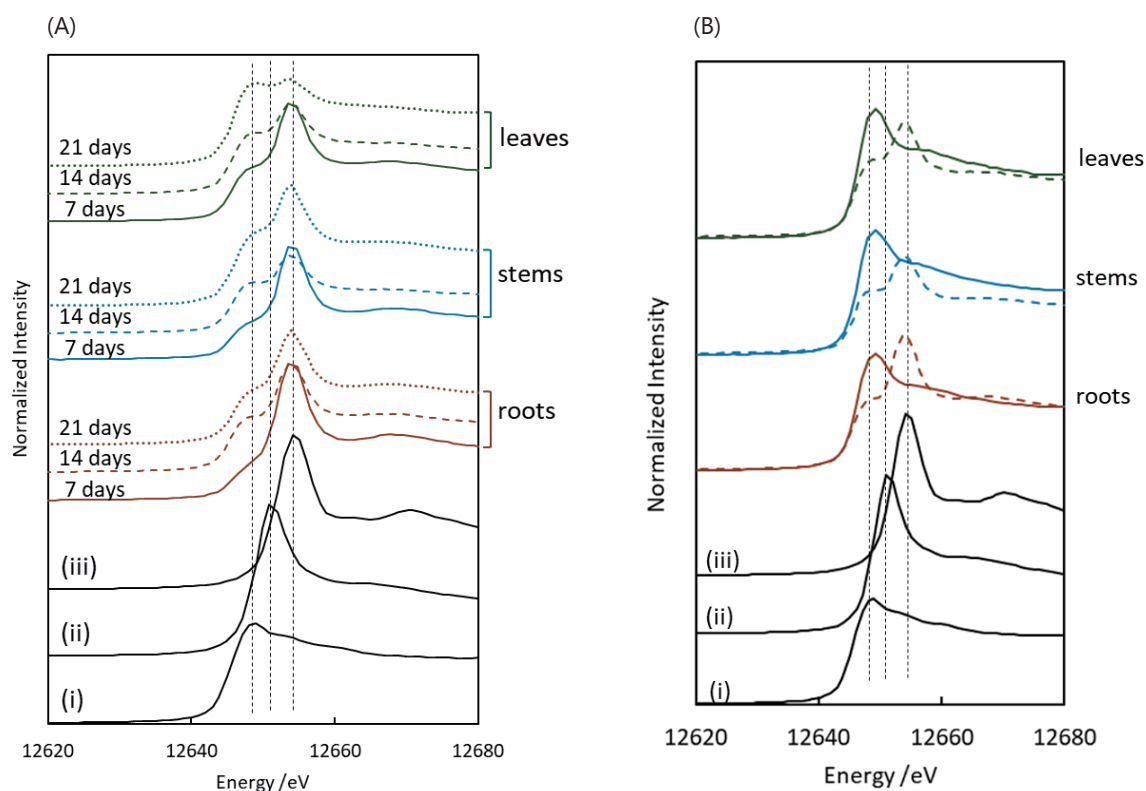


**Figure 1.** Selenium K-edge XANES spectra obtained from various parts of the *P. vittata* L.

Addition conditions: selenium was added as selenate (selenium concentration; 5 ppm) for a certain time

(A) Spectra for the roots, stems, and leaves of the fern over time

(B) Spectra of the roots, stems, and leaves after 14 days of addition (dotted line) and spectra obtained from the residue of each part after extracting the soluble components (solid line)

Reference materials; (i) *Se*-methylseleno cysteine (MeSeCys), (ii) potassium selenite ( $K_2SeO_3$ ), (iii) sodium selenate ( $Na_2SeO_4$ ).

the culture medium containing dissolved selenate is not shown here. Still, the addition of selenate was confirmed to result in forming Se(+VI) in the culture medium.

The spectrum of the selenate (selenium concentration 5 ppm) added to the roots after 7 days (illustrated in **Figure 1A**) is nearly identical to Se(+VI) selenate. However, when the addition was prolonged to 14 and 21 days, a substantial shift in the spectrum was observed. Specifically, the intensity of the Se(+VI)-derived peak decreased, while the Se(-II)-derived peak increased, indicating a shift in selenate metabolism. This shift suggests that some of the added selenate (Se(+VI)) was reduced, and the Se(-II) metabolites SeMet and SeHLan were produced. The toxicity of organic selenium compounds, such as SeMet (a selenium-containing amino acid found in plants), is considerably lower than inorganic selenium compounds [6, 7, 17]. This suggests that the fern metabolizes selenate (Se(+VI)) to convert it to organic selenium compounds (Se(-II)), detoxifying and accumulating selenium.

As the XANES spectrum is additive, it is possible to calculate the percentage of each compound present when multiple compounds are mixed using the spectrum of a reference material [41]. Therefore, the ratio of each component of selenium in each part of the fern was calculated using the spectra of reference materials for selenate (Se(+VI)), selenite (Se(+IV)), and organic selenium compounds (Se(-II)) as shown in **Figure 2**.

Following seven days, approximately 70 % of the selenium taken up by the roots remained in the form of selenate (Se(+VI)). However, after 14 days, the proportion of Se(+VI) had decreased to 44 %, with around 40 % of the selenium forming the reduced chemical species as selenium (Se(-II)). As observed in the stems and leaves, the Se(-II) ratio increased over time. Approximately 85 % of the accumulated selenium was Se(-II) in the leaves

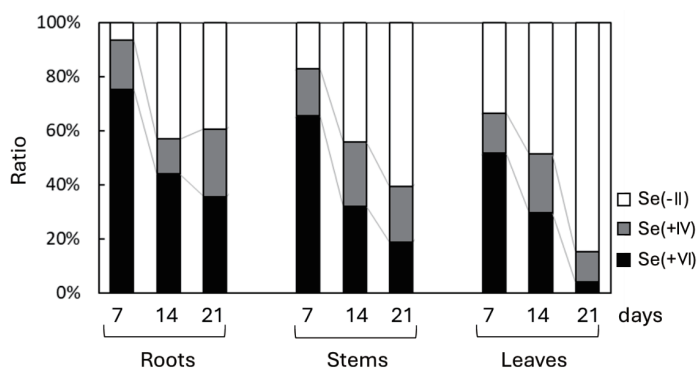


**Figure 2.** Results in chemical speciation of selenium accumulated in each part of the fern. Addition conditions: Selenate (selenium concentration: 5 ppm) was added for a certain time. The values were calculated from the pattern-fitting spectra analysis in **Figure 1A**.

after 21 days of addition.

In contrast, the XANES spectra for each part and the proportion of the respective oxidation states when 50 ppm of selenium were added are presented in **Figure S2**. Approximately 30-40% of Se(-II) was produced in the roots, whereas, in the stem, which serves as the primary conduit for transporting selenium from the roots to the leaves, predominant selenium existed as Se(+VI). This is consistent with the understanding that the homologous element sulfur is taken up by the plant body as a sulfate ion and transported within the plant [14, 40]. It is postulated that the added selenate is transported in the state of Se(+VI). As illustrated in **Figure 1A**, adding 5 ppm of selenium resulted in a high proportion of Se(-II) in the stems and leaves. However, when the concentration of the additive was increased to 50 ppm, as demonstrated in **Figure S2**, the proportion of Se(-II) reduced was low. This suggests the reduction reaction may not keep pace with the selenium uptake. It is postulated that this is due to the reduced stress on the plant when 5 ppm of selenium is added, facilitating the reduction and metabolism processes within the body.

### Results in selenium distribution and selenium chemical form obtained using X-ray microbeams

Elemental distribution measurements were performed on root, stem, and leaf section samples of *P. vittata* after adding selenium at a concentration of 5 ppm for 14 days. The obtained  $\mu$ -XRF imaging results are shown in **Figure 3 (I)**. The results obtained by adding 50 ppm selenium are shown in **Figure S3**. As shown in **Figure 3(a)** and **Figures S3(a) (b)**, selenium accumulated in the epidermis, cortex, and vascular bundles with the central cylinder of the root. The cell shape was visible in these figures, and selenium was highly concentrated in the cell wall.

There are two pathways for water and mineral transport in roots: apoplast (outside the cell membrane) and symplast (inside the cell membrane) [42]. Substances moving from the soil by diffusion through the extracellular (apoplastic) pathway are blocked by the Caspary strip in the root endodermis. The transporters transport substances from the non-specifically blocked substances in a substrate-specific manner, allowing the plant to take the necessary substances (nutrients) into the plant body. Both transporters and barriers enable plants to take up only specific nutrients.

The distribution of selenium in roots suggests that the apoplast mainly transports it to the vascular bundles of the central cylinder since its concentration is high in the cell wall. In the aboveground stem, selenium distribution was also observed in the vascular bundles (which appear U-shaped in this section) and throughout the tissue. In the leaf cross-section, Se was detected in the vascular bundles around the central veins and the leaf flesh.

The results of the  $\mu$ -XANES analysis at points A-E in **Figure 3 (I)** are shown in **Figure 3 (II)**, together with the spectra (bulk) data obtained from the tablets shown in **Figure 1A**. In the XANES spectrum of the root cortex layer (point A), the Se(-II) peak can be seen in **Figure 3 (II)**, indicating that the selenium taken up by the root has already been reduced in the cortex layer. The XANES spectrum of selenium in the root tablets (**Figure 1A**) represents the average state of the bulk sample. In contrast, points A and B in **Figure 3 (II)** show the local chemical speciation of selenium in the points of high selenium concentration (A cortex layer and B central cylinder) in the root section.

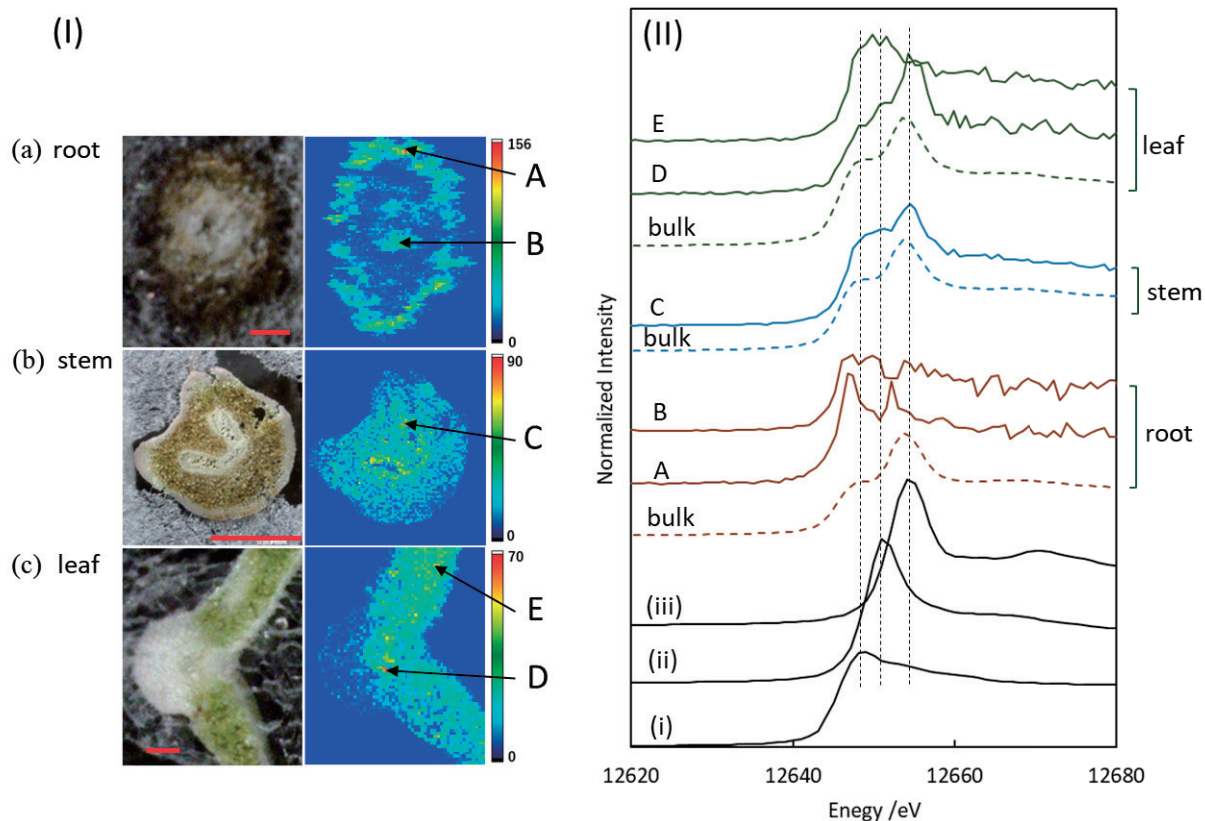


**Figure 3. Distribution and chemical form of selenium obtained by X-ray microbeam analysis**

Addition conditions: Selenate (selenium concentration: 5 ppm) was added for 14 days

X-ray beam size; 5  $\mu\text{m}$  (H)  $\times$  5  $\mu\text{m}$  (V)

(I) Distribution of selenium in fern root, stem and leaf sections

Measurement area and step size; 355  $\mu\text{m}$  (H)  $\times$  405  $\mu\text{m}$  (V), step size 5  $\mu\text{m}$  for root section

1620  $\mu\text{m}$  (H)  $\times$  1720  $\mu\text{m}$  (V), step size 20  $\mu\text{m}$  for stem section

560  $\mu\text{m}$  (H)  $\times$  660  $\mu\text{m}$  (V), step size 10  $\mu\text{m}$  for leaf section

Scale bar; 10  $\mu\text{m}$  in (a) and (c), and 1000  $\mu\text{m}$  in (b)

(II) Micro XANES spectra of the selenium K-edge obtained from the measurement points in the sections

Reference materials; (i) Se-Methylseleno cysteine (MeSeCys), (ii) potassium selenite (K<sub>2</sub>SeO<sub>3</sub>), (iii) sodium selenate (Na<sub>2</sub>SeO<sub>4</sub>).

It was shown that there are localized points of high selenium intensity in the root tissue, such as the cortex layer and the central cylinder, where a high percentage of Se(-II) is present.

At point C in the stem section, Se(+VI) and Se(-II) coexisted in the spectrum, like the bulk spectrum obtained from the tablets. At point C, which is the vascular bundle of the stem, the percentage of Se(-II) was 56%, indicating a slightly higher rate of Se(-II) than in the bulk (44%).

Point D, near the central vein in the leaf section, shows a spectrum like the stem vascular bundles (Point C). On the other hand, at point E in the mesophyll of the leaf section, Se(-II) and Se(+IV) were 62% and 42%, respectively, while Se(+VI) was negligible. Thus, although the bulk analysis of the whole leaf did not reveal it, the Se(-II) content differed significantly between the central vein and the mesophyll, indicating that reduced chemical species, i.e., metabolized selenium compounds, accumulate in the mesophyll.

### Identification of soluble selenium compounds extracted from *P. vittata* L.

**Figure 4A** illustrates the HPLC chromatograms of the extracts prepared from the samples' roots, stems, and leaves with 5 ppm selenium for 14 days. **Figure 4B** has been enlarged slightly to visualize the minor peaks. The reference materials employed were selenate (i),  $\gamma$ -GluMeSeCys (ii), selenite (iii), MeSeCys (iv), and SeMet (v). The respective retention times were 14.5 minutes (i), 15.8 minutes (ii), 16.7 minutes (iii), 19.3 minutes (iv), and 20.3 minutes (v), respectively. The selenate peak was unambiguously identified in all extracts of roots, stems, and leaves. In contrast, MeSeCys (iv) and SeMet (v) were identified in the roots, albeit at an intensity of less than a few tenths of that observed for the selenate peak. Additionally, a minor peak was observed at a retention time of 21.8 minutes; however, it was not identified due to a lack of correspondence with the retention time of the reference substance. Furthermore, in addition to selenate (i), a selenite (iii) peak was detected in the stem and leaf extracts.

The same HPLC-ICP-MS analysis of the sample with 50 ppm selenium added for 7 days demonstrated that the extracts from the roots, stems, and leaves parts exhibited predominantly selenate peaks. It can be inferred that almost selenate was extracted from the roots, stems, and leaves. The results suggest that Se(-II) accumulated in the roots, stems, and leaves are not easily extracted.

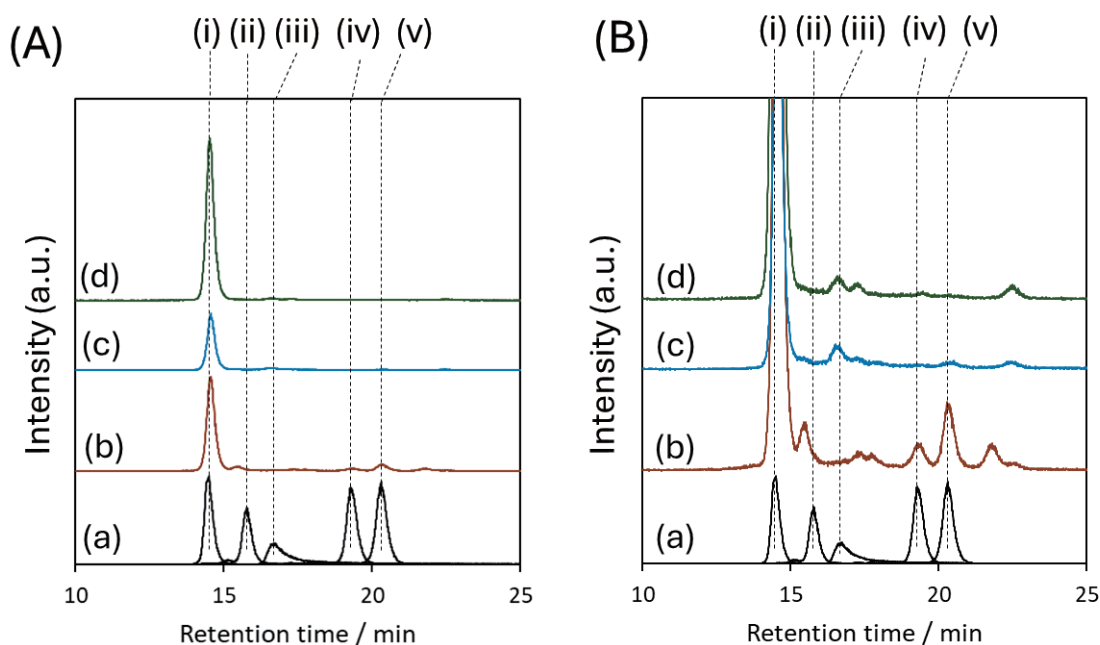


**Figure 4.** Elution profiles of Se in the extracts from each part of the fern cultivated with the addition of selenate.

Cultivation conditions: selenate (the concentration of selenium 5 ppm) for 14 days.

A 20  $\mu$ L aliquot of the extract was subjected to HPLC coupled with ICP-MS.

The profiles for (b)-(d) in **Fig 4(B)** are a 10-fold magnification of the vertical axis in **Fig. 4(A)**.

(a) authentic standards; (i) selenate (14.5 min), (ii)  $\gamma$ -glutamyl-methyl-selenocysteine ( $\gamma$ -GluMeSeCys) (15.8 min), (iii) selenite (16.7 min), (iv) Se-methylselenocysteine (MeSeCys) (19.3 min), (v) selenomethionine (SeMet) (20.3 min).  
(b) root extract, (c) stem extract, (d) leaf extract.

### Results in Chemical Speciation of Selenium in Extraction Residues

Following a 14-day period during which selenate (5 ppm selenium concentration) was added, soluble constituents were extracted from the roots, stems, and leaves of *P. vittata* L. **Table 2** illustrates the concentrations of selenium present in the pre-extraction sample and the residue obtained following the extraction process. By employing

these selenium concentrations ( $C_{pre-extraction}$  and  $C_{residue}$ ) and the dry weights of the sample before and following the extraction ( $W_{pre-extraction}$  and  $W_{residue}$ ), respectively, the percentage of selenium extracted from each part was calculated using the following equation:

$$\text{Extraction efficiency (\%)} = \left( 1 - \frac{C_{residue} \times W_{residue}}{C_{pre-extraction} \times W_{pre-extraction}} \right) \times 100$$

The highest selenium extraction rate was approximately 51 % for the roots, indicating that approximately half of the accumulated selenium was extracted. In contrast, the selenium extraction rate in the above-ground parts (i.e., stems and leaves) was approximately 30 %, with more than half of the remaining unextracted. Our initial hypothesis was that most selenium would be extracted from the root, stem, and leaf samples of *P. vittata*, as previously described in the literature [18-20]. However, the observed extraction rate was lower than anticipated.

**Figure 1B** illustrates the K-edge XANES spectra of selenium in the roots, stems, and leaves before and after extraction. Dotted lines represent the spectra before extraction, while the spectra of the residue following extraction are shown as solid lines. Before extraction, the spectra of the roots, stems, and leaves exhibited a coexistence of Se(+VI) and Se(-II). However, the peaks shifted to the low energy following extraction, indicating the presence of Se(-II) in significant quantities. Furthermore, the ratios of the components Se(+VI), Se(+IV), and Se(-II) were calculated for the XANES spectra of the extraction residue. Consequently, the proportion of Se(-II) in the residue of each component was 78.8% for the roots, 92.3 % for the stems, and 84.3 % for the leaves. The proportion of Se(+VI) was minimal in all cases, indicating that Se(+VI) was effectively extracted and that only a minimal amount remained in the residue. The results of the extracted soluble components (**Figure 4**) correspond with the finding that the main component was selenate.

As can be observed, the extraction process was successful in extracting selenate (Se(+VI)) as a soluble component, but less effective in removing organic selenium compounds (Se(-II)). The inability to extract organic compounds can be attributed to two primary factors: their strong binding within plant tissue and the ineffectiveness of the enzymes utilized for their extraction. Further clarification is necessary to elucidate the underlying mechanisms. By integrating extraction operations with X-ray absorption spectroscopy, as demonstrated in this study, we gained insights into the behavior of selenium accumulated within plants.

**Table 2.** Selenium concentrations before and after extraction for each part of the fern and the selenium extraction efficiencies calculated from these values

Parts	Se concentration (mg/kg DW)		Se extraction efficiency (%)
	Pre-extraction	Residue	
Roots	184.4	88.7	51.9
Stems	26.7	19.1	28.5
Leaves	25.0	16.4	34.4

The following equation calculated selenium extraction efficiency.

$$\text{Extraction efficiency (\%)} = \left( 1 - \frac{C_{residue} \times W_{residue}}{C_{pre-extraction} \times W_{pre-extraction}} \right) \times 100$$

$C_{pre-extraction}$  and  $C_{residue}$  were Se concentrations ( $\mu\text{g/g}$ ) before and after extraction, respectively.  $W_{pre-extraction}$  and  $W_{residue}$  were sample dry weights (g) before and after extraction.

## Conclusions

The addition of low concentrations of selenate (5 ppm selenium) resulted in the uptake of selenium by the fern through its roots, with subsequent transport to the above-ground parts of the plant. This process was observed to persist for 21 days following the initial addition. Adding a high concentration of selenate solution (50 ppm selenium) resulted in the transport of selenium to the plant's above-ground parts. However, most of the selenium accumulated in the roots, indicating limited transport to the above-ground parts. In previous research, it was reported that adding arsenic to *P. vittata* resulted in rapid transport to the plant's above-ground parts, with concentrations reaching tens of thousands of ppm [43]. Furthermore, adding hexavalent chromium resulted in its accumulation in the roots at tens of thousands of ppm [28]. In comparison, the concentration of selenium accumulation in the fern plant was relatively low, and it is postulated that there is a defense mechanism against selenium uptake.

In this study, adding inorganic selenate to *P. vittata* resulted in the uptake and metabolism of selenium in the roots. As the cultivation period was extended, the proportion of Se(-II) in the above-ground parts increased. This phenomenon was particularly evident under conditions of low selenium concentration. Moreover, synchrotron radiation X-ray microbeams demonstrated that metabolized selenium was present in specific tissues, including the root epidermis and central cylinder. Among the selenium compounds produced by metabolism, MeSeCys and SeMet were identified as soluble components. It is hypothesized that these methylated selenium compounds accumulate in the plant body as low-toxicity chemical species. The extraction rate of selenium in the above-ground parts, such as the stems and leaves, was relatively low. It is hypothesized that this is due to selenium being metabolized into more significant selenium compounds, such as proteins. This study employed protease as the most prevalent method for extracting organic selenium compounds. However, by examining the extraction conditions in greater detail and identifying the selenium compounds that were not extracted on this occasion, it is anticipated that a more profound comprehension of the intricacies of the selenium metabolic pathway in *P. vittata* will be achieved.

Synchrotron radiation X-ray absorption spectroscopy is a technique that enables the acquisition of information on chemical forms without the necessity for chemical pretreatment or disruption of the sample. Although this approach has certain advantages for analysis, it is challenging to identify specific substances when multiple compounds are present. This study employed a combined extraction and HPLC-ICP-MS to measure soluble components. We anticipate that this methodology will prove valuable for investigating selenium metabolism in samples subjected to diverse selenium addition conditions and competition with the uptake of other elements, such as sulfur.

## Acknowledgments

This work was performed under the approval of the Photon Factory Program Advisory Committee (Proposal Nos. 2016G580 and 2020G608). A part of the measurements was supported by the Analysis Center of Tokyo Denki University.

## References

- [1] Raskin I, Ensley BD. *Phytoremediation of Toxic Metals Using Plants to Clean Up the Environment*. New Jersey: John Wiley & Sons Inc.; 1999.
- [2] Sarwar N, Imran M, Shaheen MR, Ishaque W, Kamran MA, Matloob A, Rehim A, Hussain S. Phytoremediation strategies for soils contaminated with heavy metals: Modifications and future perspectives. *Chemosphere*. 2017; 171: 710-721.
- [3] Ma LQ, Komar KM, Tu C, Zhang WH, Cai Y, Kennelley ED. A fern that hyperaccumulates arsenic - A hardy, versatile, fast-growing plant helps to remove arsenic from contaminated soils. *Nature*. 2001; 409: 579.
- [4] Dai Z-H, Ding S, Chen J-Y, Han R, Cao Y, Liu X, Tu S, Guan D-X, Ma LQ. Selenate increased plant growth and arsenic uptake in As-hyperaccumulator *Pteris vittata* via glutathione-enhanced arsenic reduction and translocation. *Journal of Hazardous Materials*. 2022; 424: 127581.
- [5] Dai Z-H, Peng Y-J, Ding S, Chen J-Y, He S-X, Hu C-Y, Cao Y, Guan D-X, Ma LQ. Selenium increased arsenic accumulation by upregulating the expression of genes responsible for arsenic reduction, translocation, and sequestration in arsenic hyperaccumulator *Pteris vittata*. *Environmental Science & Technology*. 2022; 56: 14146-14153.
- [6] Roman M, Jitaru P, Barbante C. Selenium biochemistry and its role for human health. *Metallomics*. 2014; 6(1): 25-54.
- [7] Tapiero H, Townsend DM, Tew KD. The antioxidant role of selenium and seleno-compounds. *Biomedicine & Pharmacotherapy*. 2003; 57(3-4): 134-144.
- [8] Kumar M, Bijo AJ, Baghel RS, Reddy CRK, Jha B. Selenium and spermine alleviate cadmium induced toxicity in the red seaweed *Gracilaria dura* by regulating antioxidants and DNA methylation. *Plant Physiology and Biochemistry*. 2012; 51: 129-138.
- [9] Feng R, Wei C, Tu S. The roles of selenium in protecting plants against abiotic stress. *Environmental and Experimental Botany*. 2013; 87: 58-68.
- [10] Ullah H, Lun L, Rashid A, Zada N, Chen B, Shahab A, Li P, Ali MU, Lin S, Wong MH. A critical analysis of sources, pollution, and remediation of selenium, an emerging contaminant. *Environmental Geochemistry Health*. 2023; 45:1359-1389.

- [11] Ministry of the Environment Government of Japan. *National Effluent Standards*. 2015. <https://www.env.go.jp/en/water/wq/nes.html> [accessed 2024.11.30]
- [12] World Health Organization. *Guidelines for drinking-water quality: fourth edition incorporating the first and second addenda*. Chapter 12 Chemical fact sheets. Selenium 2022; 413-415. ISBN: 978-92-4-004506-4. <https://www.who.int/publications/i/item/9789240045064>
- [13] Bajaj M, Eiche E, Neumann T, Winter J, Gallert C. Hazardous concentrations of selenium in soil and groundwater in North-West India. *Journal of Hazardous Materials*. 2011; 189: 640–646.
- [14] Gupta M, Gupta S. An overview of selenium uptake, metabolism, and toxicity in plants. *Frontiers in Plant Science*. 2017; 7: article 2074. <https://doi.org/10.3389/fpls.2016.02074>
- [15] Yawata A, Oishi Y, Anan Y, Ogra Y. Comparison of selenium metabolism in three Brassicaceae plants. *Journal of Health Science*. 2010; 56(6): 699-704.
- [16] Lindblom SD, Fakra SC, Landon J, Schulz P, Tracy B, Pilon-Smits EAH. Inoculation of selenium hyperaccumulator *Stanleya pinnata* and related non-accumulator *Stanleya elata* with hyperaccumulator rhizosphere fungi – investigation of effects on Se accumulation and speciation. *Physiologia Plantarum*. 2014; 150: 107-118.
- [17] Eiche E, Bardelli F, Nothsteina AK, Charlet L, Göttlicher J, Steining R, Dhillond KS, Sadana US. Selenium distribution and speciation in plant parts of wheat (*Triticum aestivum*) and Indian mustard (*Brassica juncea*). *Science of the Total Environment*. 2015; 505: 952-961.
- [18] Kitaguchi T, Ogra Y, Iwashita Y, Suzuki KT. Speciation of selenium in selenium-enriched seeds, buckwheat (*Fagopyrum esculentum* Moench) and quinoa (*Chenopodium quinoa* Willdenow). *European Food Research and Technology*. 2008; 227: 1445-1460.
- [19] Ogra Y, Katayama A, Ogihara Y, Yawata A, Anan Y. Analysis of animal and plant selenometabolites in roots of a selenium accumulator, *Brassica rapa* var. *peruviridis*, by speciation. *Metallomics*. 2013; 5: 429-436.
- [20] Ogra Y, Ogihara Y, Anan Y. Comparison of the metabolism of inorganic and organic selenium species between two selenium accumulator plants, garlic and Indian mustard. *Metallomics*. 2017; 9: 61-68.
- [21] Husted S, Persson DP, Laursen KH, Hansen TH, Pedas P, Schiller M, Hegelunda JN, Schjoerring JK. Review: the role of atomic spectrometry in plant science. *Journal of Analytical Atomic Spectrometry*. 2011; 26: 52-79.
- [22] Polatajko A, Jakubowski N, Szpunar J. State of the art report of selenium speciation in biological samples. *Journal of Analytical Atomic Spectrometry*. 2006; 21: 639-654.
- [23] Wu B, Becker JS. Imaging techniques for elements and element species in plant science. *Metallomics*. 2012; 4: 403-416.
- [24] Hokura A, Omuma R, Terada Y, Kitajima N, Abe T, Saito H, Yoshida S, Nakai I. Arsenic distribution and speciation in an arsenic hyperaccumulator fern by X-ray spectrometry utilizing a synchrotron radiation source. *Journal of Analytical Atomic Spectrometry*. 2006; 21: 321-328.
- [25] Kashiwabara T, Hokura A, Kitajima N, Onuma R, Saito H, Abe T, Nakai I. Distribution and Oxidation State of Arsenic in Root of Arsenic-Hyperaccumulator Fern, *Pteris vittata* L., by Using Synchrotron Radiation X-Ray Fluorescence Analysis *BUNSEKIKAGAKU*. 2006; 55(10): 743-748.
- [26] Kashiwabara T, Kitajima N, Onuma R, Fukuda N, Endo S, Terada Y, Abe T, Hokura A, Nakai I. Synchrotron micro-X-ray fluorescence imaging of arsenic in frozen-hydrated sections of a root of *Pteris vittata*. *Metallomics*. 2021; 13(4): mfab009 <https://doi.org/10.1093/mtomcs/mfab009>
- [27] Koller CE, Patrick JW, Rose RJ, Offler CE, MacFarlane GR. Arsenic and Heavy Metal Accumulation by *Pteris vittata* L. and *P. umbrosa* R. Br. *Bulletin of Environmental Contamination and Toxicology*. 2008; 80: 128-133.
- [28] Honda M, Kitajima N, Abe T, Umemura T, Hokura A. Study on chromium accumulation mechanism of Chinese break fern (*Pteris vittata* L.) by synchrotron radiation X-ray fluorescence analysis. *BUNSEKIKAGAKU*. 2015; 64(11): 801-810.
- [29] Ronan Power, Zi-Jian Lan, Alexandros Yiannikouris. Compositions of selenoorganic compounds and methods of use thereof. U.S. Patent US20160361338A1, 2016.
- [30] Asao T, Kitazawa H, Washizu K, Ban T, Pramanik MHR. Effect of different nutrient levels on anthocyanin and nitrate-N contents in turnip grown in hydroponics. *Journal of Applied Horticulture*. 2005; 7(2): 87-89.
- [31] Dinh QT, Cui Z, Huang J, Tran TAT, Wang D, Yang W, Zhou F, Wang M, Yu D, Liang D. Selenium distribution in the Chinese environment and its relationship with human health: A review. *Environmental International*. 2018; 112: 294-309.
- [32] Kitajima N, Onuma R, Hokura A, Terada Y, Nakai I.  $\mu$ -XRF Imaging and  $\mu$ -XANES Analysis of Root of Arsenic Hyperaccumulator Fern (*Pteris vittata* L. ) by Using Synchrotron Radiation. *Advances in X-Ray Chemical Analysis, Japan*. 2006; 37: 301-310.
- [33] Fukuda N, Kitajima N, Terada Y, Abe T, Nakai I, Hokura A. Visible cellular distribution of cadmium and zinc in the hyperaccumulator *Arabidopsis halleri* ssp. *gemmifera* determined by 2-D X-ray fluorescence imaging using high-energy synchrotron radiation. *Metallomics*. 2019; 12: 193-203.
- [34] Hokura A, Harada E. Chapter 6 Synchrotron Radiation X-Ray Analysis of Metal-Accumulating Plants. *Metallomics Recent Analytical Techniques and Applications*. Springer Tokyo. 2017. <https://doi.org/10.1007/978-4-431-56463-8>
- [35] Bisgård KM, Laursen J, Nielsen BS. Energy-dispersive XRF spectrometry using secondary radiation in a cartesian geometry. *X-ray Spectrometry*. 1981; 10(1): 17-24.
- [36] BL-12C XAFS (High-Throughput) Experiments. <https://www2.kek.jp/imss/pf/eng/apparatus/bl/bl12c.html>
- [37] BL-4A Trace element analysis/X-ray microbeam station. [https://pfwww.kek.jp/users\\_info/users\\_guide\\_e/station\\_spec\\_e/bl04/bl4a.html](https://pfwww.kek.jp/users_info/users_guide_e/station_spec_e/bl04/bl4a.html)
- [38] Galeas ML, Zhang LH, Freeman JL, Wegner M, Pilon-Smits EAH. Seasonal fluctuations of selenium and sulfur accumulation in selenium hyperaccumulators and related nonaccumulators. *New Phytologist*. 2007; 173(3): 517-525.
- [39] Pickering IJ, Gumaelius L, Harris HH, Prince RC, Hirsch G, Banks JA, Salt DE, George GN. Localizing the Biochemical Transformations of Arsenate in a Hyperaccumulating Fern. *Environmental Science & Technology*. 2006; 40: 5010-5014.
- [40] Schiavon M, Pilon-Smits EAH. The fascinating facets of plant selenium accumulation – biochemistry, physiology, evolution and ecology. *New Phytologist*. 2017; 213: 1582-1596.
- [41] Calvin S. *XAFS for Everyone*. Florida: CRC Press; 2014.
- [42] Taiz L, Zeiger E. *Plant Physiology. The third edition*. Oxford University Press Inc. 2002.
- [43] Kitajima N, Kashiwabara T, Fukuda N, Endo S, Hokura A, Terada Y, Nakai I. Observation of Arsenic Transfer in Leaf Tissue of Hyperaccumulator Fern by Utilizing Synchrotron Radiation Micro-XRF Imaging. *Chemistry Letters*. 2008; 37(1): 32-33.

## Supplementary materials

### Cultivation of fern

The plants were transferred to plastic cups containing pure water with the soil still attached and then covered with a plastic bag with two holes in the top to maintain a high-humidity environment. They were then cultivated in an incubator. The cultivation environment conditions were 12 hours of cyclic light irradiation, light intensity of approximately 10,000/400 lx day/night, humidity of 70~80 %, and room temperature of  $25 \pm 3$  °C. After about two weeks, the soil attached to the roots was gently washed away with pure water, and the plants were transferred to a polyethylene bottle wrapped in aluminum foil to prevent light from reaching them and grown hydroponically. At this time, the plants were shaken (100 rpm) using a shaker.

The culture solution was changed once every two days.

**Table S1.** Composition of the culture solution by modified Hoagland nutrient solution [30]

Compound	Concentration (mg L <sup>-1</sup> )
KNO <sub>3</sub>	81
Ca(NO <sub>3</sub> ) <sub>2</sub> ·4H <sub>2</sub> O	95
MgSO <sub>4</sub> ·7H <sub>2</sub> O	50
NH <sub>4</sub> H <sub>2</sub> PO <sub>4</sub>	15.5
NaFe-EDTA	2
H <sub>3</sub> BO <sub>3</sub>	0.3
MnCl <sub>2</sub> ·4H <sub>2</sub> O	0.181
CuSO <sub>4</sub> ·5H <sub>2</sub> O	0.005
Na <sub>2</sub> MoO <sub>4</sub> ·2H <sub>2</sub> O	0.002
ZnSO <sub>4</sub> ·7H <sub>2</sub> O	0.022

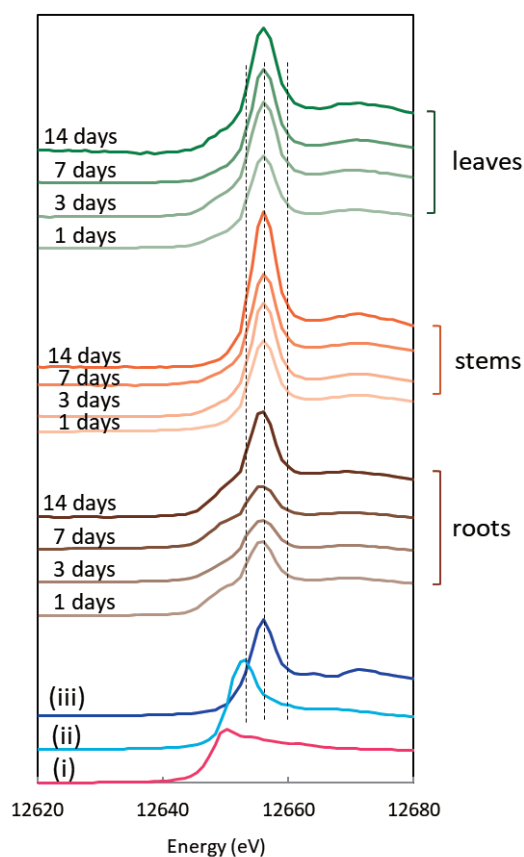


**Figure S1.** Selenium K-edge XANES spectra obtained from various parts of the *P. vittata* L.

Addition conditions: selenium was added as selenate (selenium concentration; 50 ppm) for a certain time  
Spectra for the roots, stems, and leaves of the fern over time  
Reference materials; (i) Se-methyl selenocysteine (MeSeCys), (ii) potassium selenite (K<sub>2</sub>SeO<sub>3</sub>), (iii) sodium selenate (Na<sub>2</sub>SeO<sub>4</sub>).

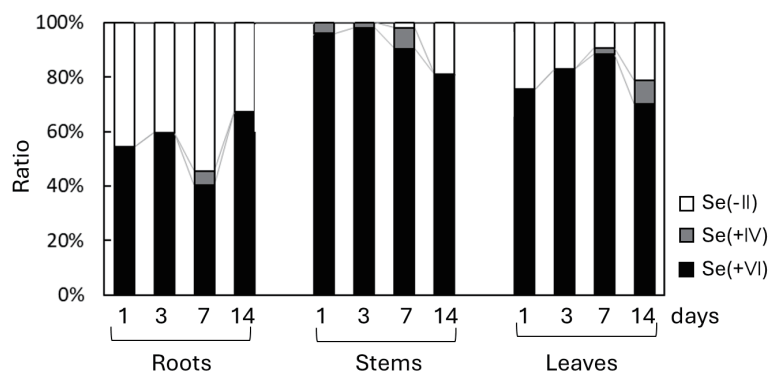


**Figure S2.** Results in chemical speciation of selenium accumulated in each part of the fern  
 Addition conditions: Selenate (selenium concentration: 50 ppm) was added for a certain time  
 The values were calculated from the pattern-fitting spectra analysis in **Figure S1**.

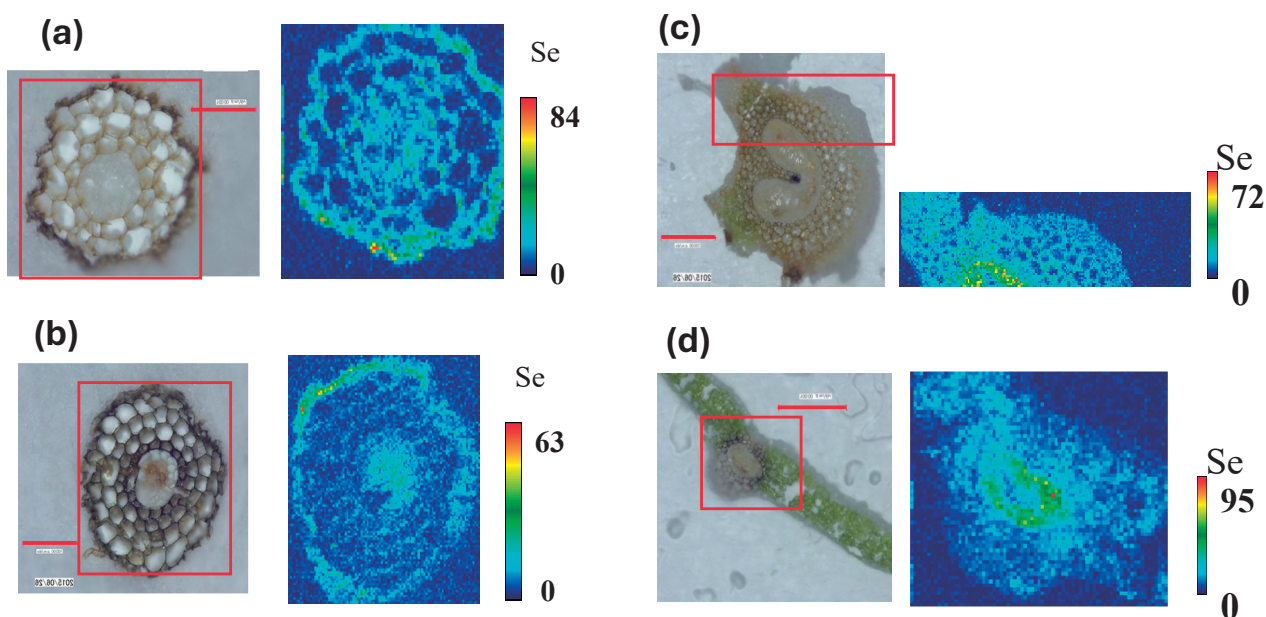


**Figure S3.** Distribution of selenium in fern root, stem and leaf sections  
 X-ray beam size; 5  $\mu\text{m}$  (H)  $\times$  5  $\mu\text{m}$  (V)  
 Measurement area and step size; 365  $\mu\text{m}$  (H)  $\times$  355  $\mu\text{m}$  (V), step size 5  $\mu\text{m}$  for root section (a)  
 475  $\mu\text{m}$  (H)  $\times$  525  $\mu\text{m}$  (V), step size 5  $\mu\text{m}$  for root section (b)  
 850  $\mu\text{m}$  (H)  $\times$  240  $\mu\text{m}$  (V), step size 20  $\mu\text{m}$  for stem section (c)  
 375  $\mu\text{m}$  (H)  $\times$  300  $\mu\text{m}$  (V), step size 10  $\mu\text{m}$  for leaf section (d)  
 Addition conditions: Selenate (selenium concentration: 50 ppm) was added for 7 days.  
 Scale bar; 100  $\mu\text{m}$

# Phosphine-mediated Reduction of a Selenocysteine Selenenyl Iodide to a Selenocysteine Selenol

Satoru Kuwano, Ko Fujisaki, Kei Goto\*

Department of Chemistry, School of Science, Institute of Science Tokyo

## Abstract

Trivalent phosphorus compounds are widely used for the reduction of biologically relevant sulfur- and selenium-containing species due to its strong redox potential, broad pH stability, and ability to minimize unwanted side reactions or competitive interactions with other thiol- or selenol-containing compounds. Selenocysteine selenenyl iodides (Sec-SeIs) have attracted increasing attention as key intermediates in the enzymatic functions of iodothyronine deiodinases. Investigating whether Sec-SeIs can serve as substrates for reduction by trivalent phosphorus compounds could provide valuable insights into the existence and behavior of Sec-SeI in proteins. However, to date, there have been no studies examining the reactivity between trivalent phosphorus compounds and selenenyl iodides. In this study, phosphine-mediated reduction of a selenocysteine selenenyl iodide to a selenocysteine selenol was developed using isolable model compounds stabilized by nanosized molecular cradle. The present study demonstrates that phosphines serve as excellent non-thiol reducing agents for selenenyl iodides, particularly in terms of their high reduction efficiency and lack of interfering thiol or selenol groups.

**Keywords:** Selenocysteine, Selenenyl iodide, Selenol, Phosphine, Reduction

**Statement about COI:** The authors declare no conflict of interest associated with this manuscript.

**Dedication:** Dedicated to Professor Takayuki Kawashima on the occasion of his 77th birthday.

## Introduction

Trivalent phosphorus compounds are widely used for the reduction of sulfur- and selenium-containing species in biological systems. A representative example is tris(2-carboxyethyl)phosphine (TCEP), which is often preferred over alternative reducing agents, such as dithiothreitol (DTT), due to its strong redox potential, broad pH stability, and ability to minimize unwanted side reactions or competitive interactions with other thiol- or selenol-containing compounds [1-4]. It has also been reported that trivalent phosphorus compounds can reduce reactive intermediates formed by the oxidative modification of thiols, such as sulfenic acids (R-SOH) [5-12, 13-15]. For instance, the reduction of cysteine sulfenic acid (Cys-SOH) to cysteine thiol (Cys-SH) by TCEP has been considered experimental evidence supporting the presence of Cys-SOH (**Scheme 1**) [16].

---

## Correspondence ;

Kei Goto

2-12-1 Ookayama, Meguro-ku, Tokyo 152-8550, Japan

**Tel ;** +81-3-5734-3543

**e-mail ;** goto@chem.titech.ac.jp

---

Received: February 14, 2025

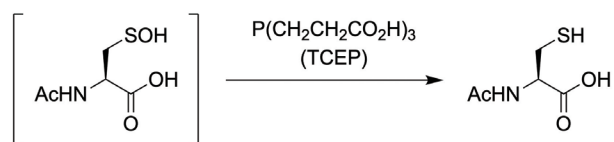
Accepted: April 02, 2025

Released online: April 15, 2025



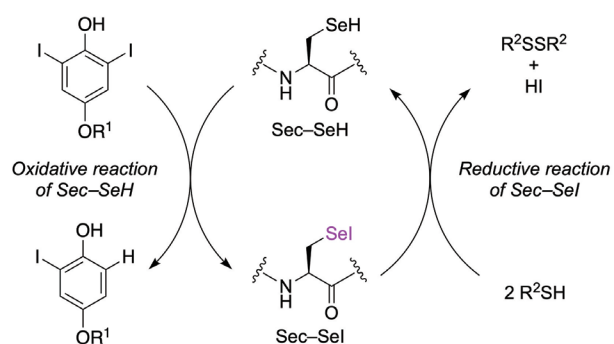
This work is licensed under a Creative Commons Attribution 4.0 International License.

©2025 THE AUTHORS. [DOI](https://doi.org/10.11299/metallomicsresearch.MR202501) <https://doi.org/10.11299/metallomicsresearch.MR202501>



**Scheme 1.** Reduction of a transiently generated sulfenic acid by TCEP.

Selenocysteine selenenyl iodides (Sec–SeI) have attracted increasing attention as key intermediates in the enzymatic functions of iodothyronine deiodinases (Dios). These enzymes regulate the concentration of active thyroid hormones through the deiodination of iodothyronines, a process mediated by selenocysteine selenols (Sec–SeH) at the catalytic site, which is believed to involve the formation of Sec–SeI intermediates (**Scheme 2**) [17–31]. Investigating whether Sec–SeIs can serve as substrates for reduction by trivalent phosphorus compounds could provide valuable insights into the existence and behavior of Sec–SeI in proteins. However, to date, there have been no studies examining the reactivity between trivalent phosphorus compounds and selenenyl iodides, including non-selenocysteinyl derivatives [32–34]. This is largely due to the inherent instability of selenenyl iodides, which readily undergo disproportionation to diselenides and elemental iodine (**Scheme 3**) [35, 36].



**Scheme 2.** Proposed catalytic mechanism of iodothyronine deiodinases.



**Scheme 3.** Disproportionation of selenenyl iodides.

As a protective group to stabilize the biologically relevant reactive intermediates, we have developed a nanosized molecular cradle that can accommodate a reactive amino acid residue [37–42]. By using the molecular cradle as an *N*-terminal protecting group (henceforth denoted as “Bpsc”), we recently succeeded in the synthesis and isolation of selenocysteine-derived selenenyl iodide **1** (**Figure 1**) [38–43]. Here, we report the reduction of the stably isolated Sec–SeI to the corresponding Sec–SeH by phosphines, providing direct experimental evidence of this reaction.

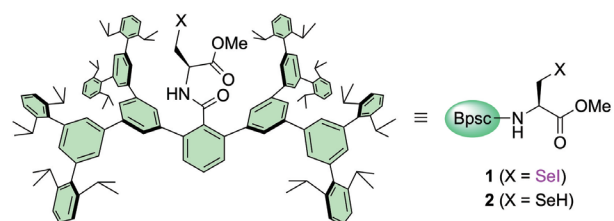


**Figure 1.** Isolable Sec–SeI (**1**) and Sec–SeH (**2**) stabilized by a molecular cradle.

## Materials and methods

### General

All synthetic experiments were performed under argon atmosphere. Selenocysteine selenenyl iodide **1** was prepared according to the reported procedure [42]. Anhydrous THF was purchased from Kanto Chemical and passed through a Kayama Oxygen solvent purification system prior to use. Other chemicals were purchased from commercial sources and used as received.  $^1\text{H}$  NMR spectra were recorded on a JEOL ECS-400, and the chemical shifts of  $^1\text{H}$  are referenced to the residual proton signal of  $\text{CDCl}_3$  ( $\delta$  7.26).  $^{31}\text{P}$  NMR spectra were recorded on JEOL ECX-500 using  $\text{CDCl}_3$  as a solvent, and the chemical shifts of  $^{31}\text{P}$  were referenced to  $\text{PPh}_3$  ( $\delta$  –5.65) as an external standard.

### Reductive transformation from selenocysteine selenenyl iodide **1** to selenocysteine selenol **2** promoted by $\text{Ph}_3\text{P}$ .

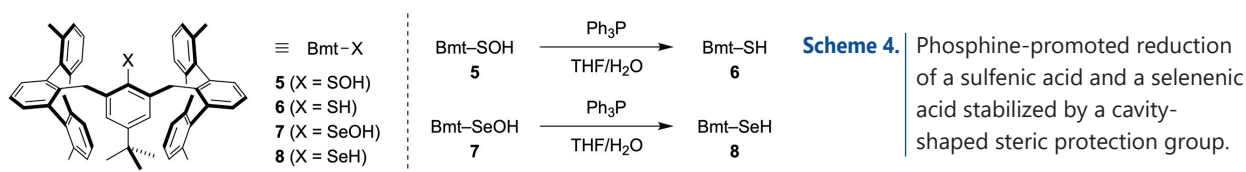
To the mixture of THF (0.8 mL) and  $\text{H}_2\text{O}$  (0.2 mL) in Schlenk flask, solution of  $\text{Ph}_3\text{P}$  in THF (0.111 M, 50.0  $\mu\text{L}$ , 5.58  $\mu\text{mol}$ , 1.20 eq) and solution of selenenyl iodide **1** in THF (0.0186 M, 250  $\mu\text{L}$ , 4.65  $\mu\text{mol}$ ) were added. The resulting mixture was stirred for 10 seconds at room temperature. To the Schlenk flask,  $\text{H}_2\text{O}$  (2.0 mL) was added, and the aqueous layer was extracted with  $\text{Et}_2\text{O}$ . Combined organic layers were concentrated to give crude white solids. The crude mixture was washed with MeCN and dried. By  $^1\text{H}$  NMR spectroscopy, the content of selenocysteine selenol **2**, the corresponding diselenide **3** and the corresponding dehydroalanine **4** was estimated to be 72%, 15% and 3%, respectively. The filtrate was concentrated to yield white solids, in whose  $^{31}\text{P}$  NMR spectrum triphenylphosphine oxide was the only detectable  $\text{Ph}_3\text{P}$ -derived product, along with the remaining  $\text{Ph}_3\text{P}$ .

### Reductive transformation from selenocysteine selenenyl iodide **1** to selenocysteine selenol **2** promoted by $^t\text{Bu}_3\text{P}$ .

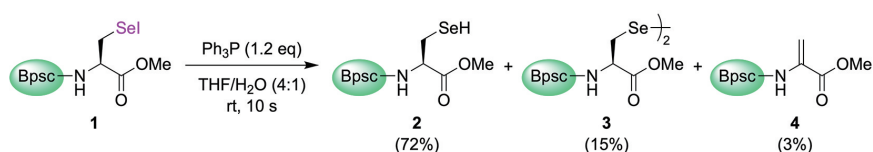
To the mixture of THF (0.8 mL) and  $\text{H}_2\text{O}$  (0.2 mL) in Schlenk flask, solution of  $^t\text{Bu}_3\text{P}$  in THF (0.100 M, 55.0  $\mu\text{L}$ , 5.50  $\mu\text{mol}$ , 1.19 eq) and solution of selenenyl iodide **1** in THF (0.0186 M, 250  $\mu\text{L}$ , 4.64  $\mu\text{mol}$ ) were added. The resulting mixture was stirred for 10 seconds at room temperature. To the Schlenk flask,  $\text{H}_2\text{O}$  (2.0 mL) was added, and the aqueous layer was extracted with  $\text{Et}_2\text{O}$ . Combined organic layers were concentrated to give crude white solids. The crude mixture was washed with MeCN and dried. By  $^1\text{H}$  NMR spectroscopy, the content of selenocysteine selenol **2**, the corresponding diselenide **3** and the corresponding dehydroalanine **4** was estimated to be 67%, 31% and 2%, respectively.

## Results and discussion

While there have been several reports on the reductions of sulfenic acids by trivalent phosphorus compounds, these reactions have been limited to transiently generated R-SOHs [13-15], as sulfenic acids are inherently unstable due to their tendency to undergo self-condensation. In contrast, we have synthesized a stable sulfenic acid **5** bearing a cavity-shaped steric protecting group (a Bmt group) and demonstrated its reduction to the corresponding thiol **6** by triphenylphosphine in a mixed solvent of THF and  $\text{H}_2\text{O}$  (Scheme 4) [44]. We have also demonstrated the phosphine-mediated reduction of a selenenic acid (R-SeOH) through the reaction of selenenic acid **7** stabilized by a Bmt group with triphenylphosphine, yielding selenol **8**.

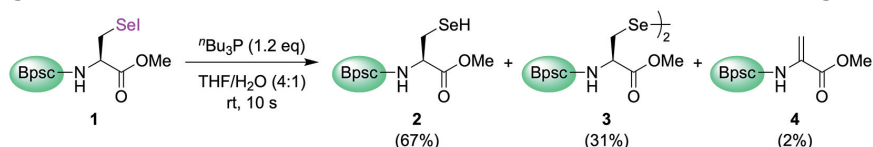


Based on these findings, Sec-SeI **1** was treated with 1.2 equivalents of triphenylphosphine in a mixed solvent of THF and  $\text{H}_2\text{O}$  at room temperature (Scheme 5). Within 10 seconds, purple color of the Sec-SeI **1** disappeared, and compound **1** was completely consumed.  $^1\text{H}$  NMR spectroscopic analysis revealed that Sec-SeH **2** was obtained as the major product in 72% yield, indicating that triphenylphosphine reduces selenenyl iodides very efficiently. In addition to the target Sec-SeH **2**, the corresponding diselenide **3** and dehydroalanine **4** were produced in 15% and 3% yields, respectively. The formation of diselenide **3** may be attributed to the reaction between the starting material, Sec-SeI **1**, and the generated product, Sec-SeH **2**. The small amount of dehydroalanine **4** is likely derived from thermal deselenation of Sec-SeOH [38], which is produced by hydrolysis of Sec-SeI **1** in a water-containing solvent [42]. However, because the hydrolysis is very sluggish under neutral conditions, the amounts of the resulting Sec-SeOH and its deselenation product **4** are considered to be very low.  $^{31}\text{P}$  NMR spectroscopic analysis revealed that triphenylphosphine oxide, which is considered to be formed by the hydrolysis of an initially generated phosphonium salt, was the only detectable triphenylphosphine-derived product, along with the remaining triphenylphosphine.



**Scheme 5.** Ph<sub>3</sub>P-promoted reductive transformation of Sec-Sel **1** to Sec-SeH **2**.

In addition to the triarylphosphine, we also investigated trialkylphosphine as a reductant for selenenyl iodides. When Sec-Sel **1** was treated with tributylphosphine under the same conditions, Sec-SeH **2** was obtained as the major product in 67% yield, along with diselenide **3** and dehydroalanine **4** (**Scheme 6**). These results demonstrate that trialkylphosphine is also a good reducing agent for selenenyl iodides, and strongly suggests that phosphine reagents such as TCEP will be useful for the efficient reduction of Sec-Sels generated in proteins.



**Scheme 6.** <sup>t</sup>Bu<sub>3</sub>P-promoted reductive transformation of Sec-Sel **1** to Sec-SeH **2**.

In conclusion, we have demonstrated for the first time the phosphine-mediated reduction of selenocysteine selenenyl iodide to selenocysteine selenol. In the catalytic cycle of Dios, selenenyl iodide intermediates are postulated to be reduced to their parent selenols by thiol cofactors. We previously reported thiol-mediated reductions of selenenyl iodides bearing both selenocysteiny and nonselenocysteiny backbones [38-43, 45, 46]. The present study clearly shows that phosphines serve as excellent non-thiol reducing agents for selenenyl iodides, particularly in terms of their high reduction efficiency and lack of interfering thiol or selenol groups.

## Acknowledgements

This work was partly supported by JSPS KAKENHI Grant Numbers JP22K05063 (S.K.) and JP23H01946 (K.G.).

## References

- Burns JA, Butler JC, Moran J, Whitesides GM. Selective reduction of disulfides by tris(2-carboxyethyl)phosphine. *J Org Chem*. 1991; 56: 2648-2650.
- Gray WR. Disulfide structures of highly bridged peptides: A new strategy for analysis. *Protein Sci*. 1993; 2: 1732-1748.
- Getz EB, Xiao M, Chakrabarty T, Cooke R, Selvin PR. A Comparison between the Sulfhydryl Reductants Tris(2-carboxyethyl)phosphine and Dithiothreitol for Use in Protein Biochemistry. *Anal Biochem*. 1999; 273: 73-80.
- Barry AN, Blackburn NJ. A Selenocysteine Variant of the Human Copper Chaperone for Superoxide Dismutase. A Se-XAS Probe of Cluster Composition at the Domain 3-Domain 3 Dimer Interface. *Biochemistry*. 2008; 47: 4916-4928.
- Allison WS. Formation and reactions of sulfenic acids in proteins. *Acc Chem Res*. 1976; 9: 293-299.
- Poole LB, Karplus PA, Claiborne A. Protein Sulfenic Acids in Redox Signaling. *Annu Rev Pharmacol Toxicol*. 2004; 44: 325-347.
- Poole LB, Nelson KJ. Discovering mechanisms of signaling-mediated cysteine oxidation. *Curr Opin Chem Biol*. 2008; 12: 18-24.
- Paulsen CE, Carroll KS. Orchestrating Redox Signaling Networks through Regulatory Cysteine Switches. *ACS Chem Biol*. 2010; 5: 47-62.
- Paulsen CE, Carroll KS. Cysteine-Mediated Redox Signaling: Chemistry, Biology, and Tools for Discovery. *Chem Rev*. 2013; 113: 4633-4679.
- Gupta V, Carroll KS. Sulfenic acid chemistry, detection and cellular lifetime. *Biochim Biophys Acta Gen Subj*. 2014; 1840: 847-875.
- Bak DW, Weerapana E. Cysteine-mediated redox signalling in the mitochondria. *Mol BioSyst*. 2015; 11: 678-697.
- Devarie-Baez NO, Lopez EIS, Furdul CM. Biological chemistry and functionality of protein sulfenic acids and related thiol modifications. *Free Radical Res*. 2016; 50: 172-194.
- Cooper RDG, Jose FL. Structural studies on penicillin derivatives. IV. Novel rearrangement of penicillin V sulfoxide. *J Am Chem Soc*. 1970; 92: 2575-2576.
- Hatfield LD, Fisher J, Jose FL, Cooper RDG. Structural studies on penicillin derivatives: Part VII rearrangement of penicillin sulfoxides with trimethylphosphite-acetic anhydride. *Tetrahedron Lett*. 1970; 11: 4897-4900.
- Trost BM, Salzmann TN, Hiroi K. New synthetic reactions. Sulfenylations and dehydrosulfenylations of esters and ketones. *J Am Chem Soc*. 1976; 98: 4887-4902.
- Hazra S, Bhandari DM, Krishnamoorthy K, Sekowska A, Danchin A, Begley TP. Cysteine Dealkylation in *Bacillus subtilis* by a Novel Flavin-Dependent Monooxygenase. *Biochemistry*. 2022; 61: 952-955.
- Berry MJ, Banu L, Larsen PR. Type-I Iodothyronine Deiodinase Is a Selenocysteine-Containing Enzyme. *Nature*. 1991; 349: 438-440.
- Köhrle J. Local activation and inactivation of thyroid hormones: The deiodinase family. *Mol Cell Endocrinol*. 1999; 151: 103-119.
- Bianco AC, Salvatore D, Gereben B, Berry MJ, Larsen PR. Biochemistry, cellular and molecular biology, and physiological roles of the iodothyronine selenodeiodinases. *Endocr Rev*. 2002; 23: 38-89.
- Köhrle J. Iodothyronine deiodinases. *Methods Enzymol*. 2002; 347: 125-167.
- Kuiper GGJM, Kester MHA, Peeters RP, Visser TJ. Biochemical Mechanisms of Thyroid Hormone Deiodination. *Thyroid*. 2005; 15: 787-798.

- [22] Bianco AC, Kim BW. Deiodinases: Implications of the local control of thyroid hormone action. *J Clin Investig.* 2006; 116: 2571-2579.
- [23] Schweizer U, Schlicker C, Braun D, Koehrl J, Steegborn C. Crystal structure of mammalian selenocysteine-dependent iodothyronine deiodinase suggests a peroxiredoxin-like catalytic mechanism. *Proc Natl Acad Sci USA.* 2014; 111: 10526-10531.
- [24] Mondal S, Raja K, Schweizer U, Mugesh G. Chemistry and Biology in the Biosynthesis and Action of Thyroid Hormones. *Angew Chem Int Ed.* 2016; 55: 7606-7630.
- [25] Schweizer U, Towell H, Vit A, Rodriguez-Ruiz A, Steegborn C. Structural aspects of thyroid hormone binding to proteins and competitive interactions with natural and synthetic compounds. *Mol Cell Endocrinol.* 2017; 458: 57-67.
- [26] van der Spek AH, Fliers E, Boelen A. The classic pathways of thyroid hormone metabolism. *Mol Cell Endocrinol.* 2017; 458: 29-38.
- [27] Bayse CA, Marsan ES, Garcia JR, Tran-Thompson AT. Thyroxine binding to type III iodothyronine deiodinase. *Sci Rep.* 2020; 10: 15401.
- [28] Steegborn C, Schweizer U. Structure and Mechanism of Iodothyronine Deiodinases—What We Know, What We Don't Know, and What Would Be Nice to Know. *Exp Clin Endocrinol Diabetes.* 2020; 128: 375-378.
- [29] Rodriguez-Ruiz A, Braun D, Pflug S, Brol A, Sylvester M, Steegborn C, Schweizer U. Insights into the Mechanism of Human Deiodinase 1. *Int J Mol Sci.* 2022; 23: 5361.
- [30] Köhrl J, Fradrich C. Deiodinases control local cellular and systemic thyroid hormone availability. *Free Radic Biol Med.* 2022; 193: 59-79.
- [31] Arai K, Toba H, Yamamoto N, Ito M, Mikami R. Modeling Type-1 Iodothyronine Deiodinase with Peptide-Based Aliphatic Diselenides: Potential Role of Highly Conserved His and Cys Residues as a General Acid Catalyst. *Chem Eur J.* 2023; 29: e202202387.
- [32] du Mont WW, Kubiniok S, Peters K, Vonschnering HG. Synthesis and Structure of a Stable Iodoselenide. *Angew Chem Int Ed Engl.* 1987; 26: 780-781.
- [33] du Mont WW, Wagner I. Iodo[tris(trimethylsilyl)methyl]selane: synthesis of the alkylselenenyl iodide. *Chem Ber.* 1988; 121: 2109-2110.
- [34] Mugesh G, Panda A, Singh HB, Butcher RJ. Intramolecular Se···N nonbonding interactions in low-valent organoselenium derivatives: a detailed study by <sup>1</sup>H and <sup>77</sup>Se NMR spectroscopy and X-ray crystallography. *Chem Eur J.* 1999; 5: 1411-1421.
- [35] Du Mont WW, Martens A, Pohl S, Saak W. Reversible dismutation and coordination of bis(2,4,6-triisopropylphenyl) diselenide with iodine. A model study that relates to iodine intercalation between selenium chains. *Inorg Chem.* 1990; 29: 4847-4848.
- [36] Martens-Von Salzen A, Meyer HU, Du Mont WW. Diselenides and iodine: Influence of solution equilibria between covalent compounds and charge-transfer complexes. *Phosphorus Sulfur Silicon Relat Elem.* 1992; 67: 67-71.
- [37] Sano T, Masuda R, Sase S, Goto K. Isolable small-molecule cysteine sulfenic acid. *Chem Commun.* 2021; 57: 2479-2482.
- [38] Masuda R, Kimura R, Karasaki T, Sase S, Goto K. Modeling the catalytic cycle of glutathione peroxidase by nuclear magnetic resonance spectroscopic analysis of selenocysteine selenenic acids. *J Am Chem Soc.* 2021; 143: 6345-6350.
- [39] Masuda R, Kuwano S, Sase S, Bortoli M, Madabeni A, Orian L, Goto K. Model study on the catalytic cycle of glutathione peroxidase utilizing selenocysteine-containing tripeptides: Elucidation of the protective bypass mechanism involving selenocysteine selenenic acids. *Bull Chem Soc Jpn.* 2022; 95: 1360-1379.
- [40] Masuda R, Kuwano S, Goto K. Modeling Selenoprotein Se-Nitrosation: Synthesis of a Se-Nitrososelenocysteine with Persistent Stability. *J Am Chem Soc.* 2023; 145: 14184-14189.
- [41] Masuda R, Karasaki T, Sase S, Kuwano S, Goto K. Highly Electrophilic Intermediates in the Bypass Mechanism of Glutathione Peroxidase: Synthesis, Reactivity, and Structures of Selenocysteine-Derived Cyclic Selenenyl Amides. *Chem Eur J.* 2023; 29: e202302615.
- [42] Goto K, Kimura R, Masuda R, Karasaki T, Sase S. Demonstration of the Formation of a Selenocysteine Selenenic Acid through Hydrolysis of a Selenocysteine Selenenyl Iodide Utilizing a Protective Molecular Cradle. *Molecules.* 2023; 28: 7972.
- [43] Masuda R, Goto K. Modeling of selenocysteine-derived reactive intermediates utilizing a nano-sized molecular cavity as a protective cradle. *Methods Enzymol.* 2022; 662: 331-361.
- [44] Goto K, Shimada K, Nagahama M, Okazaki R, Kawashima T. Reaction of Stable Sulfenic and Selenenic Acids Containing a Bowl-type Steric Protection Group with a Phosphine. Elucidation of the Mechanism of Reduction of Sulfenic and Selenenic Acids. *Chem Lett.* 2003; 32: 1080-1081.
- [45] Goto K, Sonoda D, Shimada K, Sase S, Kawashima T. Modeling of the 5'-deiodination of thyroxine by iodothyronine deiodinase: Chemical corroboration of a selenenyl iodide intermediate. *Angew Chem Int Ed.* 2010; 49: 545-547.
- [46] Sase S, Kakimoto R, Kimura R, Goto K. Synthesis of a Stable Primary-Alkyl-Substituted Selenenyl Iodide and Its Hydrolytic Conversion to the Corresponding Selenenic Acid. *Molecules.* 2015; 20: 21415-21420.